

---

Electronic Thesis and Dissertation Repository

---

12-14-2017 2:30 PM


## Fabrication and Modification of Titania Nanotube Arrays for Harvesting Solar Energy and Drug Delivery Applications

Ahmed El Ruby Abdel Rahman Mohamed  
*The University of Western Ontario*

Supervisor  
Rohani, Sohrab  
*The University of Western Ontario*

Graduate Program in Chemical and Biochemical Engineering  
A thesis submitted in partial fulfillment of the requirements for the degree in Doctor of Philosophy  
© Ahmed El Ruby Abdel Rahman Mohamed 2017

Follow this and additional works at: <https://ir.lib.uwo.ca/etd>

 Part of the [Biology and Biomimetic Materials Commons](#), [Biomaterials Commons](#), [Catalysis and Reaction Engineering Commons](#), [Ceramic Materials Commons](#), [Environmental Engineering Commons](#), [Inorganic Chemicals Commons](#), [Inorganic Chemistry Commons](#), [Nanomedicine Commons](#), [Nanoscience and Nanotechnology Commons](#), [Other Chemical Engineering Commons](#), [Other Chemicals and Drugs Commons](#), [Semiconductor and Optical Materials Commons](#), and the [Sustainability Commons](#)

---

### Recommended Citation

Mohamed, Ahmed El Ruby Abdel Rahman, "Fabrication and Modification of Titania Nanotube Arrays for Harvesting Solar Energy and Drug Delivery Applications" (2017). *Electronic Thesis and Dissertation Repository*. 5176.  
<https://ir.lib.uwo.ca/etd/5176>

This Dissertation/Thesis is brought to you for free and open access by Scholarship@Western. It has been accepted for inclusion in Electronic Thesis and Dissertation Repository by an authorized administrator of Scholarship@Western. For more information, please contact [wlsadmin@uwo.ca](mailto:wlsadmin@uwo.ca).

## Abstract

The fast diminishing of fossil fuels in the near future, as well as the global warming caused by increasing greenhouse gases have motivated the urgent quest to develop advanced materials as cost-effective photoanodes for solar light harvesting and many other photocatalytic applications. Recently, titania nanotube arrays (TNTAs) fabricated by anodization process has attracted great interest due to their excellent properties such as: high surface area, vertically oriented, highly organized, one-dimensional, nanotubular structure, photoactivity, chemical stability and biocompatibility. This unique combination of excellent properties makes TNTAs an excellent photoanode for solar light harvesting. However, the relatively wide band gap energy of titania limits its photoactivity to the UV spectra which accounts only for 5 % of solar light spectra. The specific objectives of this thesis are to: First, fabricate reproducible well-organized, vertically-oriented TNTAs in different viscous electrolytes and optimize the fabrication parameters. Second, modify the TNTAs by doping nitrogen and carbon and study the effect of modification on optical properties and photoelectrochemical performance. And third, functionalizing the TNTAs surface by monodispersed magnetic ferrite nanoparticles for improved solar light harvesting and drug delivery application in cancer treatment. The effect of each fabrication parameter such as electric potential, pH, water content, anodization time and electrolyte composition was discussed. TNTAs were successfully fabricated in an inexpensive viscous electrolyte composed of 2 wt.% sodium carboxy methylcellulose (CMC). TNTAs were successfully fabricated on both sides of a Ti disc with total tube length of 9.5  $\mu\text{m}$  with a unique structure composed of conducting Ti metal sandwiched between two semiconducting layers of TNTAs on each side with a new potential electronic and photocatalytic applications.

A new, facile, low cost, environment-friendly and nanoarchitecture-safe method was introduced to fabricate N- and C-modified  $\text{TiO}_2$  nanotube arrays. Modified optical properties with narrow band gap energy,  $E_g$ , of 2.65 eV was obtained after annealing the modified TNTAs at 550°C. Modified TNTAs showed enhanced photoelectrochemical performance. Photoconversion efficiency (PCE) was increased from 4.35% for pristine (unmodified) TNTAs to 5.18% for modified TNTAs, an increase of 19%. Effect of nanotubes length of modified

TNTAs on photoelectrochemical performance was also studied. Photocurrent density and PCE were increased by increasing nanotube length with a maximum PCE of 6.38% for nanotube length of 55  $\mu\text{m}$ . This implies an excellent light penetration up to 55  $\mu\text{m}$  depth into photoanode which is about 3.6 times higher than the maximum penetration depth (15  $\mu\text{m}$ ) in the nanoparticulate photoanode. This increasing pattern of photoconversion efficiency with increasing nanotubes length also implied a high charge separation rate and lower charge recombination rate. This high PCE value was attributed to: band gap reduction due to N- and C-modification of TNTAs surface, increased surface area of long TNTAs compared with short TNTAs, investigated in previous studies, and the excellent light penetration and harvesting properties.

Ferrite NPs-encapsulated TNTAs were fabricated for the first time using a facile and efficient method. Ferrite nanoparticles of  $13 \pm 3$  nm diameters were successfully distributed all over the top and inner surface of the nanotubes. UV-Vis reflectance spectra showed excellent visible light absorbance up to wave length of 660 nm ( $E_g = 1.88$  eV). The prepared magnetic nanocomposite showed their potential capability to controlling the drug release of an anti-cancer drug (5-fluorouracil). The drug release of 5-fluorouracil by diffusion was sustained with controlled initial burst effect. The suitability of magnetic nanocomposite for cancer drug delivery was confirmed by in vitro cytotoxicity study.

## Keywords

Titania nanotube arrays, N- and C-modification, photocurrent, photoconversion efficiency, ferrite nanoparticles, ferrite-encapsulated titania nanotube arrays, magnetic titania nanotube arrays, drug delivery, 5-fluorouracil, anti-cancer.

## Co-Authorship Statement (where applicable)

**Chapter 2:** A version of this chapter has been published in the highly ranked journal;

*Energy and Environmental Science*, (impact Factor: 29.518), as:

**Ahmed El Ruby Mohamed** and Sohrab Rohani, “Modified TiO<sub>2</sub> nanotube arrays (TNTAs): progressive strategies toward visible light responsive photoanode, a review”, *Energy Environ. Sci.* 4, (2011), pp. 1065-1086. (143 citation so far according to CrossRef and RSC Journals).

### **Chapter 3:**

1. A paper based on this chapter has been published in *Journal of Nanoscience and Nanotechnology* as: **Ahmed El Ruby Mohamed**, Nualjarose Kasemphaibulsuk, Sohrab Rohani and Shahzad Barghi, “Fabrication of titania nanotube arrays in viscous electrolytes”, *J. Nanosci. Nanotechnol.* 10, (3), (2010), pp.1998-2008.
2. A paper based of this chapter has been published as: **Ahmed El Ruby Mohamed** and Sohrab Rohani, “Synthesis of Titania Nanotube Arrays by Anodization”, *AIDIC Conference Series Vol. 9*, (2009) pp. 121-130. [DOI:10.3303/ACOS090915](https://doi.org/10.3303/ACOS090915).
3. A paper based on this chapter has been published as: Sohrab Rohani and **Ahmed El Ruby**, “ Synthesis of Titania Nanotube Arrays by Anodization”, *Chemical Engineering Transactions* 17, (2009), pp. 963-968. [DOI:10.3303CET0917161](https://doi.org/10.3303CET0917161).

**Chapter 4:** A paper based on this chapter is under final revision as: **Ahmed El Ruby Mohamed** and Sohrab Rohani, “N and C Modified TiO<sub>2</sub> Nanotube Arrays: Enhanced Photoelectrochemical Properties and Effect of Nanotubes length on Photoconversion Efficiency” to be submitted for possible publication.

**Chapter 5:** A paper based on this chapter is under final revision as: **Ahmed El Ruby Mohamed** and Sohrab Rohani, “Multifunctional Magnetic Ferrite-encapsulated Self-organized TiO<sub>2</sub> Nanotubes Nanocomposite: Fabrication, Properties and Drug Release Control” to be submitted for possible publication.

## Dedication

*To*

*My Parents (Lord mercy be upon them), my lovely wife and My Kids: Mennat  
Alrahman, Mahmoud, Mariam and Mayar*

## Acknowledgments

Praise be to ALLAH, The Almighty, for guiding and helping me to complete this work.

I would like to express my deep gratitude and sincere appreciation to Prof. Sohrab Rohani for his instructive supervision, constant advice, valuable help and continuous encouragement to accomplish the work.

I would like to extend my gratitude and appreciation to Dr. Shahzad Barghi for his continuous support, deep advice and willing of assistance during the course of this work.

I would like to express my gratitude to Prof. A. Ray for his constant advice, help and support.

I would like to thank Dr. Doaa Ragab for collaboration in drug release and cytotoxicity experiments in chapter 5. I am also grateful to all my colleagues in Prof. S. Rohani research group in both Zeolites and Nanomaterials Laboratory and the Crystallization and Control of Pharmaceuticals laboratory, for their kind help and cooperation, special thanks to Dr. Davood Karami, Dr. Sameen Zaidi and Mrs. Sally Sabra. I am also send my appreciation to all faculty and staff members in Chemical and biochemical engineering Depart., at Western University.

I am pleased to express my gratitude to Arabic Republic of Egypt and Central Metallurgical Research and Development Institute (CMRDI) for funding my Ph.D. study at Western University and to the members of The Egyptian Bureau of Cultural and Educational Affairs in Canada for their help and cooperation during my study period.

My deepest appreciation and sincere gratitude are extended to my wife, my kids and my big family for their unconditional love and support.

## Table of Contents

|  |           |
|--|-----------|
| Abstract.....  | i         |
| Co-Authorship Statement (where applicable).....  | iii       |
| Dedication.....  | v         |
| Acknowledgments.....   | vi        |
| Table of Contents.....   | vii       |
| List of Tables.....  | xii       |
| List of Figures.....   | xiii      |
| List of Abbreviations and Symbols.....   | xix       |
| Chapter 1 : Introduction.....  | 1         |
| 1 Introduction.....  | 2         |
| 1.1 Background.....  | 2         |
| 1.2 Motivation.....  | 3         |
| 1.3 Why Titania Nanotube Arrays?.....  | 4         |
| 1.4 Challenges.....  | 5         |
| 1.5 Objectives.....  | 6         |
| 1.6 Approach and Methodology.....  | 6         |
| 1.7 Thesis Organization.....   | 7         |
| 1.8 Novelty and major contributions.....   | 9         |
| 1.9 References.....  | 11        |
| Chapter 2 :.....   | 14        |
| <b>2 Modified TiO<sub>2</sub> Nanotube Arrays (TNTAs): Progressive Strategies Towards<br/>Visible Light Responsive Photoanode, A Review.....</b> | <b>14</b> |



|                |  |     |
|----------------|--|-----|
| 2.1            | Abstract .....   | 15  |
| 2.2            | Introduction.....  | 15  |
| 2.3            | TNTAs versus TiO <sub>2</sub> nanoparticles .....                                  | 19  |
| 2.4            | Fabrication of TNTAs.....  | 22  |
| 2.4.1          | Fabrication of TiO <sub>2</sub> Nanotube Arrays (TNTAs) in Aqueous Electrolytes    | 23  |
| 2.4.2          | Fabrication of TNTAs in organic electrolytes .....                                 | 32  |
| 2.5            | TNTAs formation mechanism .....  | 48  |
| 2.6            | Modification of TNTAs Electronic and Photoelectrochemical Properties .....         | 52  |
| 2.6.1          | Non-metal doping .....   | 52  |
| 2.6.2          | Metal Ions Doping .....  | 64  |
| 2.6.3          | CdS Nanoparticle Sensitization .....   | 70  |
| 2.6.4          | Loading of Precious Metals Nanoparticles .....                                     | 72  |
| 2.7            | Advantages of TiO <sub>2</sub> Nanotube Arrays (TNTAs) Over Nonowires and Nanorods | 73  |
| 2.8            | Applications of TiO <sub>2</sub> Nanotube Arrays (TNTAs) Photoanodes .....         | 75  |
| 2.9            | Concluding Remarks.....  | 80  |
| 2.10           | References.....  | 82  |
| Chapter 3..... |  | 101 |
| 3              | Fabrication of Titania Nanotube Arrays in Viscous Electrolytes .....               | 101 |
| 3.1            | Abstract.....  | 102 |
| 3.2            | Introduction.....  | 103 |
| 3.3            | Experimental setup and methods .....   | 110 |
| 3.4            | Results and Discussion .....   | 113 |
| 3.4.1          | Effect of Anodization Voltage .....  | 113 |
| 3.4.2          | Effect of Electrolyte pH.....  | 116 |
| 3.4.3          | Effect of Water Content .....  | 118 |
| 3.4.4          | Effect of Anodization Time .....   | 121 |

|           |  |            |
|-----------|--|------------|
| 3.4.5     | Anodization in Ethylene Glycol Electrolyte .....   | 125        |
| 3.4.6     | Double-sided Nanotube Arrays Fabrication .....   | 127        |
| 3.4.7     | Anodization in CMC Aqueous Electrolyte .....   | 127        |
| 3.5       | Conclusions.....   | 131        |
| 3.6       | References.....  | 133        |
| Chapter 4 | .....  | 138        |
| <b>4</b>  | <b>N and C Modified TiO<sub>2</sub> Nanotube Arrays: Enhanced Photoelectrochemical Properties and Effect of Nanotubes length on Photoconversion Efficiency .....</b> | <b>138</b> |
| 4.1       | Abstract.....  | 139        |
| 4.2       | Introduction.....  | 140        |
| 4.3       | Experimental setup and methods .....   | 142        |
| 4.3.1     | Preparation of Modified TiO <sub>2</sub> Nanotube Arrays (TNTAs).....  | 142        |
| 4.3.2     | Characterization of Modified TNTAs.....  | 143        |
| 4.3.3     | Photoelectrochemical Properties.....   | 144        |
| 4.4       | Results and Discussion .....   | 145        |
| 4.4.1     | FESEM and XRD Studies.....   | 145        |
| 4.4.2     | EDX and XPS Results .....  | 150        |
| 4.4.3     | Optical Properties.....  | 153        |
| 4.4.4     | Photoelectrochemical Properties.....   | 155        |
| 4.5       | Conclusions.....   | 163        |
| 4.6       | References.....  | 164        |
| Chapter 5 | .....  | 170        |
| <b>5</b>  | <b>Multifunctional Magnetic Ferrite-encapsulated Self-organized TiO<sub>2</sub> Nanotubes Nanocomposite: Fabrication, Properties and Drug Release Control .....</b>  | <b>170</b> |
| 5.1       | Abstract.....  | 171        |
| 5.2       | Introduction.....  | 172        |
| 5.3       | Materials and Methods.....   | 173        |

|           |   |            |
|-----------|---|------------|
| 5.3.1     | Fabrication of TiO <sub>2</sub> nanotube arrays.....  | 173        |
| 5.3.2     | Synthesis of Ferrite nanoparticles.....   | 174        |
| 5.3.3     | Ferrite drug loading.....   | 175        |
| 5.3.4     | Encapsulation of Ferrite nanoparticles into titania nanotube arrays.....                    | 175        |
| 5.3.5     | Characterization.....   | 176        |
| 5.3.6     | Drug release.....   | 177        |
| 5.4       | Results and Discussion.....   | 179        |
| 5.4.1     | Structure and Morphology.....   | 179        |
| 5.4.2     | Magnetic and Optical Properties.....  | 183        |
| 5.4.3     | Photoelectrochemical Performance of Ferrite-encapsulated TNTAs.....                         | 185        |
| 5.4.4     | Drug release study.....   | 188        |
| 5.4.5     | Cytotoxicity of ferrite encapsulated TNTAs.....   | 192        |
| 5.5       | Conclusions.....  | 193        |
| 5.6       | References.....   | 195        |
| Chapter 6 | .....   | 197        |
| <b>6</b>  | <b>Conclusions and Recommendations</b> .....  | <b>197</b> |
| 6.1       | 198   |            |
| 6.1       | Challenges and limitations.....   | 199        |
| 6.2       | Objectives.....   | 199        |
| 6.3       | Methodology.....  | 200        |
| 6.4       | Conclusions.....  | 201        |
| 6.4.1     | Fabrication of reproducible self-organized titania nanotube arrays.....                     | 201        |
| 6.4.2     | N- and C-modification of titania nanotube arrays.....                                       | 202        |
| 6.4.3     | Multifunctional Magnetic Ferrite-encapsulated TiO <sub>2</sub> Nanotubes Nanocomposite..... | 203        |
| 6.5       | Novelty and major contributions.....  | 204        |

|  |     |
|--|-----|
| 6.6. Recommendations and future works..... | 206 |
| Curriculum Vitae .....                     | 207 |

## List of Tables

|   |     |
|---|-----|
| Table 3- 1 Electrolyte compositions at different water content.....   | 112 |
| Table 3-2 Effect of water content on nanotube arrays formation and their nanoarchitecture<br>.....  | 120 |
| Table 3-3 Anodization in Ethylene Glycol: Fabrication conditions and nanotubes dimensions<br>.....  | 126 |
| Table 3-4 Diameter, wall thickness and length of titania nanotube arrays synthesized in CMC<br>aqueous electrolyte.....                             | 129 |
| Table 4-1 The band gap energies ( $E_g$ ) and corresponding absorbance edges of $TiO_2$ nanotube<br>arrays annealed at different temperatures ..... | 155 |
| Table 4-2 Nanotubes lengths anodized for different times.....   | 159 |

## List of Figures

|   |    |
|---|----|
| Figure 2-1 The number of publications per year and accumulated publications on the topic of titania nanotube arrays in the last decade. (Statistics analysis was obtained from Scopus database on January 21 <sup>st</sup> , 2018). .....   | 19 |
| Figure 2-2 Illustrative drawing of a two-electrode electrochemical cell for anodization. ....   | 23 |
| Figure 2-3 Effect of anodization potential on TNTAs formation and morphology in 1 M H <sub>2</sub> SO <sub>4</sub> and 0.1 M HF aqueous electrolyte at 01) 5 V, 02) 10 V, 03) 15 V, 04) 20 V, 05) 25 V and 06) 30 V (reprinted with permission from ref. [62] © 2005 Materials Research Society).<br>.....  | 26 |
| Figure 2-4 Effect of anodization potential on titania nanotube morphology (SEM top view and cross-section images) formed in 1 M H <sub>3</sub> PO <sub>4</sub> + 0.3 wt.% HF at: 1 V (a), 2.5 V (b), 5 V (c), 10 V (d), 15 V (e), 20 V (f) and 25 V (g) for 1 h. (Reprinted with permission from ref. [64] © 2006 Elsevier B.V.).....   | 28 |
| Figure 2-5 Lateral views of TNTAs formed in different pH solutions (preprinted with permission from ref. [62] © 2005 Materials Research Society).....   | 29 |
| Figure 2-6 SEM top views of titania nanotube arrays anodized at 20 V in 0.5 wt.% HF aqueous electrolyte at different anodization times: (a) 10 s, (b) 30 s, (c) 60 s, (d) 200 s, (e) 800 s, and (f) 1,800 s (Reprinted with permission from ref. [66] © Springer Science + Business Media, LLC 2008). .....   | 31 |
| Figure 2-7 (a) The tube length as a function of anodization time of samples formed during different times in glycerol + 0.5 wt.% NH <sub>4</sub> F and 1 M (NH <sub>4</sub> ) <sub>2</sub> SO <sub>4</sub> + 0.5 wt. %NH <sub>4</sub> F at 20 V at 20 °C. SEM images of (b) cross-section, (c) top view and (d) bottom view of self-organized TiO <sub>2</sub> nanotubes of length of 6.1 μm formed after 18 hrs anodization in glycerol electrolyte. (Reprinted with premission from ref. [72] ©2006 Elsevier Ltd.)..... | 35 |
| Figure 2-8 SEM top and cross sectional of the TNTAs grown in water/glycerol (1:1 v/v)/0.27 M NH <sub>4</sub> F for 3 h anodization time at different potentials. (Reprinted with permission from ref. [78] ©2008 Elsevier B. V. All rights reserved) .....  | 37 |

|   |    |
|---|----|
| Figure 2-9 SEM images of TNTAs fabricated in DMSO containing 2% HF at 40 V for 69 h: a) cross sectional view, b) lateral view and c) top view (reprinted with permission from ref. [81], ©2006 American Chemical Society.) .....  | 40 |
| Figure 2-10 TNTAs length as a function of (a) anodization potential for 70 h anodization in 2% HF-DMSO with and without a pre-anodization step, (b) HF concentration in DMSO for 40V and 60 V for 70 h, (c) H <sub>2</sub> O concentration in 2% HF DMSO (at 40 V and 40 h), and (d) anodization duration time for 40 V in 2% HF-DMSO electrolytes with 0%, 3%, and 5% deionized water content (reprinted with permission from ref. [82], ©2006 American Chemical Society)..... | 41 |
| Figure 2-11 FESEM images of cross sectional views indicating the lengths of TNTAs as a function of time at 60 V in ethylene glycol, 0.3 wt. % NH <sub>4</sub> F and 2 vol. % H <sub>2</sub> O. (Reprinted with permission from ref. [90], © 2007 American Chemical Society) .....   | 47 |
| Figure 2-12 The chemical dissolution rate in c), depends on the pH-value as in b), caused..   | 49 |
| Figure 2-13 Illustrative diagram of the evolution of a nanotube array at constant anodization voltage: (a) oxide layer formation, (b) pit formation on the oxide layer, (c) growth of the pit into scallop shaped pores, (d) metallic part between the pores undergoes oxidation and field assisted dissolution, and (e) fully developed nanotube array with a corresponding top view. Redrawn with permission from ref. [56], © 2006 Elsevier B. V. All rights reserved. ....  | 50 |
| Figure 2-14 UV-vis absorption spectra of TNTAs and carbon –modified TNTAs reprinted from [133] © 2008 Elsevier B. V. all rights reserved.....   | 60 |
| Figure 2-15 Change of MB concentration with irradiation time under different photocatalysts (reprinted from [133] © 2008 Elsevier B. V. all rights reserved).....   | 61 |
| Figure 2-16 UV-vis DR spectra of sulfur-doped TNTAs and un-doped annealed TNTAs (reprinted from ref. [137], © 2008 American Chemical Society) .....   | 63 |
| Figure 2-17 Illustrative diagram for the charges transfer in Fe-doped TiO <sub>2</sub> .....  | 68 |

|   |     |
|---|-----|
| Figure 2-18 Illustrative diagram for the charge injection from excited CdS into TiO <sub>2</sub> . CB and VB refer to the energy levels of conduction and valence bands respectively. (Reprinted with permission from ref. [165] © 2005 Elsevier B. V. All rights reserved). .....  | 71  |
| Figure 2-19 (a) Schematic representation of dye-sensitized solar cells based on TNTAs (a), electron path through a percolated nanoparticulate and oriented TNTAs structures (b) and I–V characteristic of DSSCs based on different diameter nanotubes (empty symbols correspond to 8 μm and filled symbols to 16 μm nanotubes length) (c). (Reprinted with permission from ref. [12] © The Royal Society of Chemistry 2009). .....          | 78  |
| Figure 3-1 Figure 3-1 Schematic diagram of the evolution of a nanotube array at constant anodization voltage: (a) oxide layer formation, (b) pit formation on the oxide layer, (c) growth of the pit into scallop shaped pores, (d) metallic part between the pores undergoes oxidation and field assisted dissolution, and (e) fully developed nanotube array with a corresponding top view. (Redrawn with permission from Ref. [7])...... | 109 |
| Figure 3-2 Schematic drawing of an electrochemical cell in which the Ti electrode is anodized. Titania nanotube arrays are grown on the Ti metal electrode surface which is in contact with the electrolyte. ....   | 112 |
| Figure 3-3 FESEM images for samples anodized at different voltage: a) 5V, b) 10V, c) 20V, d) 30V, e) 40V at sample edge, and f) 40V at sample center. ....  | 115 |
| Figure 3-4 Effect of voltage on titania nanotubes diameter: a comparison between results in this study and previous studies. ....   | 115 |
| Figure 3-5 Effect of voltage on wall thickness of nanotubes.....  | 116 |
| 3-6 FESEM top view images taken for samples anodized at different pH values.....  | 117 |
| Figure 3-7: FESEM top view images taken for samples anodized at different pH values. ..   | 118 |
| Figure 3-8 SEM topview images for samples anodized at 20 V, pH: 6 and anodization time 1.5 h and H <sub>2</sub> O wt.%: a) 0, b) 5, c)16, d) 30, e) 50, f) 70, and g) 90, h) 99.5 .....   | 119 |
| Figure 3-9 Effect of water content on inner diameter of nanotubes. ....   | 121 |



|   |     |
|---|-----|
| Figure 3-10 SEM images of top view and lateral view of TNTAs, fabricated in glycerol-based electrolyte at 10 V, pH: 6, H <sub>2</sub> O : 16 wt.% and various time intervals: a) 0.5 h, b) 1.5 h, c) 4 h and d) 10 h. ....  | 124 |
| Figure 3-11 Effect of anodization time on length, diameter and wall thickness of TNTAs fabricated in glycerol-based electrolyte at 10 V, 16 wt.% H <sub>2</sub> O, pH: 6 and 0.5 wt.% NH <sub>4</sub> F   | 125 |
| Figure 3-12 FESEM top and cross-sectional views of double-sided titania nanotube arrays anodized in 0.5 wt.% NH <sub>4</sub> F + 1 wt. % urea in ethylene glycol .....  | 128 |
| Figure 3-13 SEM image of titania nanotube arrays fabricated in 2 wt. % CMC aqueous solution at 20 V, pH: 6, 0.5 wt.% NH <sub>4</sub> F, and 1.5 h: a) top view and b) lateral view .....  | 130 |
| Figure 3-14 Comparison among different electrolyte compositions in terms of diameter and length of nanotubes (see electrolyte composition details in text). ....  | 131 |
| Figure 4-1 FESEM images for TNTAs synthesized in ethylene glycol electrolyte containing 1wt% H <sub>2</sub> O and 0.4 wt.% NH <sub>4</sub> F at constant potential of 60V; a) and b) Top view and cross sectional view of TNTAs anodized for 6 h and then sonicated in water for 5 min to clean surface and remove debris, c) and d) are top and cross sectional views of TNTAs anodized at the same conditions for 10 h, and e) and f) are high magnification of top and lateral views of TNTAs in (a), respectively. .... | 146 |
| Figure 4-2 FESEM images of pristine (unmodified)and modified TNTAs: a) and c) top view and high magnified top view of pristine TNTAs, b) and d) top view and high magnified top view of modified TNTAs.....   | 148 |
| Figure 4-3 X-ray diffraction patterns for a) Ti-metal foil, b) as-anodized TNTAs, c) TNTAs annealed at: 350°C, d) 450°C, e) 550°C and f) 650°C, all for 3 h in air. ....  | 149 |
| Figure 4-4 The EDX spectra of modified TNTAs indicating the elemental composition Ti and O with a ratio of Ti:O = 1:2 and the presence of carbon in TNTAs. ....   | 150 |
| Figure 4-5 The XPS spectra of TiO <sub>2</sub> nanotube arrays: a) Wide range survey spectra, b) High resolution XPS spectra over N 1s peak at 399.75 eV, and c) High resolution XPS spectra over C 1s peak.....  | 152 |

|   |     |
|---|-----|
| Figure 4-6 UV-Vis diffuse reflectance absorbance of TiO <sub>2</sub> annealed at different temperatures.<br>.....   | 153 |
| Figure 4-7 Kubelka-Munk transferred diffuse reflectance spectra of samples annealed at 350, 450, 550 and 650°C. The intersections of red rows with X-axis represent the values of band gap energy.....  | 154 |
| Figure 4-8 Photocurrent density of modified TNTAs compared with that of pristine (unmodified) TNTAs. Both samples were anodized in the same conditions with identical nanoarchitectures. ....   | 157 |
| Figure 4-9 Photoconversion efficiency of modified TNTAs and pristine (unmodified) TNTAs .....   | 158 |
| Figure 4-10 Effect of nanotubes length on photocurrent as a function of applied potential.  | 160 |
| Figure 4-11 Effect of nanotube length on photoconversion Efficiency, PCE, as a function of applied potential.....   | 161 |
| Figure 4-12 Linear dependence of photoconversion efficiency on nanotube length of modified TNTAs in the range from 18 to 55 μm.....   | 162 |
| Figure 5-1 FESEM images of pristine TNTAs and ferrite-encapsulated TNTAs fabricated using in-situ encapsulation method; a) and b) top view and lateral view, of pristine TNTAs, c) top view of in-situ ferrite-encapsulated TNTAs and d) high magnification of image c... | 181 |
| Figure 5-2 X-Ray spectra of: ferrite nanoparticles (above chart) and ferrite-encapsulated TNTAs (below). All assigned peaks of ferrite nanoparticles in the above chart existed in ferrite-encapsulated TNTAs x-ray spectra (below chart). ....                           | 182 |
| Figure 5-3 Hysteresis loops of ferrite-encapsulated TNTAs (solid green lines) compared to ferrite nanoparticles (dotted red line).....  | 183 |
| Figure 5-4 UV-vis. Diffuse reflectance spectra of ferrite encapsulated titania nanotube arrays nanocomposite. ....  | 184 |

|  |     |
|--|-----|
| Figure 5-5 Photocurrent of ferrite-encapsulated TNTAs nanocomposite at different ferrite nanoparticles loading. ....   | 186 |
| Figure 5-6 Effect of ferrite loading on photoconversion efficiency as a function of applied potential.....   | 187 |
| Figure 5-7 Effect of ferrite loading on 5-FU release profile of ferrite-encapsulated TNTAs fabricated by post-synthesis encapsulation technique. The release profile for the free drug is attached. .... | 189 |
| Figure 5-8 Effect of ferrite loading on 5-FU release profile of ferrite-encapsulated TNTAs fabricated by in-situ encapsulation technique. The release profile for the free drug is attached. ....        | 190 |
| Figure 5-9 Effect of ferrite-encapsulation technique into TNTAs on 5-FU release profile at constant ferrite NPs loading (50 mg ferrite). ....  | 191 |
| Figure 5-10 In-vitro cytotoxicity of 5-FU loaded ferrite-encapsulated TNTAs, 5-FU loaded ferrite NPs and stand-alone 5-FU as a function of 5-FU concentration .....                                      | 193 |

## List of Abbreviations and Symbols

|                              |  |
|------------------------------|--|
| $(\text{NH}_4)_2\text{SO}_4$ | Ammonium sulfate   |
| $\mu\text{m}$                | Micrometer, $10^{-6}$ m  |
| 5-FU                         | 5-fluorouracil   |
| Abs                          | Absorbance   |
| Ag                           | Silver   |
| AgCl                         | Silver chloride  |
| AM 1.5                       | Air mass solar spectrum ( $100 \text{ mW/m}^2$ )   |
| ATCC                         | American Type Culture Collection   |
| BE                           | Binding energy, eV   |
| BnMe <sub>3</sub> NF         | Bezyltrimethyl ammonium fluoride   |
| Bu <sub>4</sub> NF           | Tetrabutyl ammonium fluoride   |
| C                            | Drug concentration of the washing solution   |
| CB                           | Energy conduction band   |
| CBM                          | Conduction band minimum  |
| CdS                          | Cadmium sulfide  |
| Ci                           | Drug concentration in the original solution  |
| CMC                          | Carboxy methylcellulose  |
| CO                           | Carbon monoxide  |
| cP                           | Centipoise ( $=1 \text{ mPa}\cdot\text{s}^{-1} = 0.001 \text{ kg}\cdot\text{m}^{-1}\cdot\text{s}^{-1}$ ) |

|            |   |
|------------|---|
| CVD        | Chemical vapor deposition                                   |
| DC         | Direct current  |
| DMEM       | Dulbecco's modified eagle medium                            |
| DMSO       | Dimethyl sulfoxide  |
| DOSs       | Densities of states   |
| DSSCs      | Dye-sensitized solar cells                                  |
| $e^-$ (CB) | Electron charge at the conduction band                      |
| $E_{app}$  | External applied potential, V                               |
| EDX        | Energy dispersive X-ray                                     |
| $E_g$      | Band gap energy, eV   |
| EG         | Ethylene glycol   |
| $E_{meas}$ | The measured potential (vs Ag/AgCl ref. electrode), V       |
| $E_{oc}$   | Open circuit potential of working electrode (vs Ag/AgCl), V |
| eV         | Electron volt   |
| $F^-$      | Fluoride ion  |
| FA         | Formamide   |
| FBS        | Fetal bovine serum  |
| FESEM      | Field emission scanning electron microscopy                 |
| FF         | Fill factor   |
| GHGs       | Greenhouse gases  |

|                                 |  |
|---------------------------------|--|
| h                               | Planck constant ( $=6.62607004 \times 10^{-34} \text{ m}^2 \text{ kg / s}$ ) |
| $h^+$ (VB)                      | Positive charge (hole) at valence the band                                   |
| H <sub>2</sub> SO <sub>4</sub>  | Sulfuric acid  |
| H <sub>3</sub> PO <sub>4</sub>  | Phosphoric acid  |
| HF                              | Hydrofluoric acid  |
| hν                              | The energy of a single photon  |
| I <sub>ph</sub>                 | Photocurrent density (mA/cm <sup>2</sup> )                                   |
| M                               | Mole, molar  |
| MB                              | Methyl blue  |
| MTT                             | 3-(4,5-dimethylthiazolyl-2)-2,5-diphenyltetrazolium bromide assay            |
| NaF                             | Sodium fluoride  |
| NH <sub>4</sub> Cl              | Ammonium chloride  |
| NH <sub>4</sub> F               | Ammonium fluoride  |
| NH <sub>4</sub> NO <sub>3</sub> | Ammonium nitrates  |
| nm                              | Nanometer, 10 <sup>-9</sup> m  |
| NMF                             | N-methyl formamide   |
| NPs                             | Nanoparticles  |
| PBS                             | Phosphate buffer saline  |
| PCE                             | Photoconversion efficiency, %  |
| PE                              | Photoconversion efficiency, %  |

|                  |   |
|------------------|---|
| PEC              | Photoelectrochemical cell                             |
| PV               | Photovoltaic  |
| S-CBD            | Sequential chemical bath deposition                   |
| SEM              | Scanning electron microscopy                          |
| TEOS             | Tetraethylorthosilicate                               |
| TiO <sub>2</sub> | Titanium dioxide                                      |
| TNTAs            | Titania nanotube arrays                               |
| UV               | Ultraviolet   |
| UV-vis           | Ultraviolet-visible light                             |
| UV-vis. DRS      | Ultraviolet-visible light diffuse reflectance spectra |
| V                | Volt  |
| VB               | Energy valence band                                   |
| VBM              | Valence band maximum                                  |
| Vol.             | Volume  |
| wt. %            | Weight%   |
| XPS              | X-ray photoelectron spectroscopy                      |
| XRD              | X-ray diffraction                                     |
| $\epsilon$       | Drug loading efficiency                               |
| $\eta$           | Viscosity, cP   |
| $\nu$ (nu)       | Photon frequency, Hr (= s <sup>-1</sup> )             |

# Chapter 1 : Introduction



# 1 Introduction

## 1.1 Background

Low-dimensional nano-architectural materials have attracted considerable attention recently due to their physical properties and their potential applications [1]. Dimensionality is a crucial factor in determining the properties of nanomaterials. The ratio of surface atoms to interior atoms changes dramatically if one successfully divides a macroscopic object into smaller parts. For example, for a  $1 \text{ cm}^3$  iron cube, the percentage of surface atoms would be only  $10^{-5}\%$ , when the cube is divided into smaller cubes with an edge of 10 nm, the percentage of surface atoms would increase to 10%. In a  $1 \text{ nm}^3$  iron cube, every atom would be a surface atom [2]. So, the control of size and shape is of great interest. In contrast to size control, shape control of particulates is a more difficult and challenging topic. The tubes, flakes or wires in the nanoscale region possess novel properties. The discovery of carbon nanotubes by Iijima [3] with their variety of interesting properties has stimulated the quest for the synthesis of nanotubular structures of other substances and chemical compounds such as  $\text{V}_2\text{O}_5$ ,  $\text{SiO}_2$ ,  $\text{TiO}_2$ ,  $\text{ZrO}_2$  and  $\text{MoO}_3$ . Among these materials, titanium dioxide (also called titania) has attracted great interest since the discovery of its photosensitization effect by Honda and Fujishima in 1972 and due to its strong photo-oxidizing potential, high chemical stability, non-toxicity and low cost [4]. Titania nanotubes have improved properties compared to any other form of titania for application in photocatalysis, sensing, photoelectrolysis, photovoltaics, photoelectrochemical solar cells, water-splitting for hydrogen generation [5-12], electronics and optics [13],  $\text{CO}_2$  conversion into methanol [14]. The widespread technological use of titania is impaired by its wide band gap (3.2 eV), which requires

ultraviolet (UV) irradiation for photocatalytic activation. Because UV light accounts for only a small fraction (5%) of the sun energy compared to visible light (45%), any shift in the optical response of titania from the UV towards full spectrum light will have a positive impact on the photocatalytic and photoelectrochemical utility of the material. Historically, doping of the titania has been the approach taken for band-gap engineering of the material [15-20]. When employing dopants to change the optical response of a material, it is desirable to maintain the integrity of the host material crystal structure while changing its electronic structure. The crystal structure of the material is directly related to the ratio of cation and anion size in the crystal lattice. It appears to be relatively easier to replace  $\text{Ti}^{4+}$  in titania with any cation than to substitute  $\text{O}^{-2}$  with any other anion due to the difference in the charge states and ionic radii [5]. Titania nanotubes are known to be synthesized in two forms: random nanotubes and self-organized titania nanotube arrays (TNTAs) which are arrays of nanotubes supported and organized on a surface forming an integrated unit. Titania nanotubes, and nanotube arrays, have been produced by a variety of methods including deposition into a nanoporous alumina template [21, 22], sol-gel [23, 24], and hydrothermal processes [25, 26]. However, among these nanotubes fabrication routes, the electrochemical anodization method has recently attracted the most interest due to its ability to produce highly ordered nanotube arrays with precisely controllable dimensions [5, 27-30].

## 1.2 Motivation

The world is rapidly running out of fossil fuels. As a matter of considerable urgency, technologies for the generation of new types of energy must be developed. There is a

growing consensus that hydrogen has the potential to supplement and ultimately replace fossil fuels to produce energy [31, 32]. At the same time, there is a growing consensus that the emission of greenhouse gases must be reduced to address global warming which has become increasingly obvious and problematic [32, 33]. Therefore, there is an urgent need to develop both renewable and clean sources of energy, such as solar energy [32-34]. Hydrogen produced from the splitting of water using solar energy, termed solar-hydrogen, represents a sustainable fuel that is environmentally safe [33]. Solar-hydrogen has the capacity to provide global energy security and to reduce global warming [32-35]. Furthermore, the development of titania nanotube arrays, TNTAs, is not limited to fuel generation as an end-point. This material has many alternative applications of more immediately commercializable nature, including water purification, self-cleaning, sensing medicinal implants and controllable and specific-targeted drug delivery.

### 1.3 Why Titania Nanotube Arrays?

It is becoming increasingly clear that  $\text{TiO}_2$  is one of the most promising candidates for a commercial photoelectrode for a photoelectrochemical cell (PEC) to produce solar-hydrogen due to the following reasons: Unlike most other materials,  $\text{TiO}_2$  exhibits outstanding resistance to corrosion and photo-corrosion in aqueous environments [5, 32]. Consequently, the functional properties of  $\text{TiO}_2$  are known to remain unchanged with time. Moreover:

- $\text{TiO}_2$  is reactive with both light and water [33].

- $\text{TiO}_2$  is substantially less expensive than other photosensitive materials and so it may also be a candidate to replace silicon in photovoltaic (PV) cells if its photosensitivity can be increased sufficiently.
- $\text{TiO}_2$  with enhanced photosensitivity has many ancillary applications that are environmentally friendly [33].
- $\text{TiO}_2$  reserves are abundant [32].
- Nanotube arrays provide large electrode-electrolyte interface.
- The arrangement of the highly ordered titania nanotube array perpendicular to the surface permits facile charge transfer along the length of the nanotubes from the solution to the conductive substrate, thereby reducing the losses incurred by charge hopping across the nanoparticle grain boundaries.

## 1.4 Challenges

Relatively wide band gap ( $E_g$ ) of  $\text{TiO}_2$  limits the photoactivity to UV spectra. Surface electronic properties of  $\text{TiO}_2$  nanotube arrays need to be modified to narrow  $E_g$  to enhance the visible light absorption and consequently, increase photoconversion efficiency. When choosing any modification process, the following should be considered:

- The process should not cause damage to the unique nanotubular morphology.
- The process should not decrease the huge interfacial surface area.
- The process should not block the photons penetration paths to the inner surface area of the nanotubes

## 1.5 Objectives

The specific objectives of this research are:

1. Synthesis of titania nanotube arrays using anodization method and study the effect of different parameters on dimensionality, nanostructure and photoelectrochemical response of nanotube arrays.
2. Modification of the electronic properties to reduce band gap energy by introducing nitrogen and carbon to the surface of the nanotubes using a new, facile, low cost and environment-friendly method and characterization of photoelectrochemical performance of the modified nanotube arrays for solar applications.
3. Functionalizing titania nanotube arrays with magnetic ferrite nanoparticle to help narrowing the band gap energy and enhance the photoelectrochemical performance for solar applications.
4. Application of magnetic ferrite-encapsulated titania nanotube arrays for controlled and magnetically-targeted drug delivery of 5-FU anticancer drug as well as evaluation of their cytotoxicity.

## 1.6 Approach and Methodology

To achieve the above general and specific objectives, the following approaches were implemented in this thesis:

- An electrochemical anodization system was set up which consists of two electrodes electrochemical cell equipped with DC power supply provided with a data acquisition system and a state-of-the-art algorithm and interface for real time monitoring of electrical current and voltage.

- Titania nanotube arrays were fabricated in different electrolytes where fabrication parameters were studied to reach the optimum conditions at which a vertically-oriented, well-organized reproducible nanotube arrays were obtained.
- A new, facile, low-cost, environment-friendly method was proposed for the first time to synthesize N- and C-modified titania nanotube arrays with excellent visible light absorbance and enhanced photoelectrochemical performance.
- Morphology and nanoarchitecture were characterized using X-Ray diffractometer and FESEM imaging. Optical properties were characterized using UV-vis. diffuse reflectance spectra. Electrochemical performance was characterized by determining photocurrent densities in a 3 electrode photoelectrochemical cell with Ag/AgCl electrode as a reference electrode.
- Titania nanotube arrays were functionalized with magnetic ferrite nanoparticles which has an excellent band gap energy of 2.2 eV. The photoelectrochemical performance was characterized the ferrite-encapsulated titania nanotube arrays. The magnetic ferrite-encapsulated TNTAs were also tested in drug delivery application as an anticancer drug carrier.

## 1.7 Thesis Organization

The thesis is written in an integrated-article format as specified by the School of Postgraduate Studies at Western University. The thesis consists of four main chapters plus introduction and conclusions chapters:

- Chapter 1: Introduction: In this chapter, the author discussed the background behind the research topic, research motivations and advantages of TNTAs. Then he described the research challenges as well as approaches and methodologies in this thesis followed by thesis organization. Finally, the author highlighted the research novelty and major contributions.
- Chapter 2: In this chapter, a very comprehensive review on the latest developments in fabrication methods, modification and potential applications of TNTAs was conducted.
- Chapter 3: This chapter discussed the fabrication of TNTAs in different viscous electrolytes, namely; glycerol/water, ethylene glycol and, for the first time, the very cheap sodium carboxy methylcellulose (CMC) aqueous electrolyte. Fabrication parameters were extensively studied.
- Chapter 4: In this chapter, N- and C-modified TNTAs was fabricated using a new, facile, low-cost, environment-friendly and very safe-on-nanoarchitecture method. Modified TNTAs were characterized using FESEM, X-ray, UV-vis. diffuse reflectance spectra and photoelectrochemical performance. Effect of nanotube length on both photocurrent and photoconversion efficiency was studied for the first time for long nanotubes ranging from 18 to 55  $\mu\text{m}$ .
- Chapter 5: In this chapter, magnetic ferrite-encapsulated titania nanotube arrays was successfully synthesized using a new method. The ferrite nanoparticles were monodispersed on the inner and top surfaces of the  $\text{TiO}_2$  nanotube arrays. This magnetic nanocomposite showed excellent absorbance in the visible light spectra

as well as enhanced photoelectrochemical performance. Furthermore, the new magnetic nanocomposite was tested in drug delivery application using 5-FU anti-cancer drug as a drug model for excellent controlled drug release and magnetic-targeted local drug delivery.

- Chapter 6: in this chapter, research findings conclusions and future recommendations were discussed.

## 1.8 Novelty and major contributions

Chapter 2: Very comprehensive critical review study has introduced a strong platform for a wide diverse academic and industrial audience to understand the latest achievements in this field.

Chapter 3: The conducted study in this chapter provided a strong understanding of the effect of each synthesis parameter such as pH, water content, anodization time and electrolyte composition. TNTAs were successfully fabricated for the first time in a very cheap viscous electrolyte composed of 2 wt.% sodium carboxy methylcellulose (CMC). Double-sided TNTAs on both sides of Ti disc were successfully fabricated with total tube length of 9.5  $\mu\text{m}$  with a unique structure composed of conducting Ti metal sandwiched between two semiconducting layers of TNTAs on each side with a new potential electronic and photocatalytic applications.

Chapter 4: N- and C-modified TNTAs were successfully fabricated using a new, facile, low cost, environment-friendly method which was also very safe on the nanostructure. The modified TNTAs showed excellent absorbance in the visible light spectra as well as



enhanced photocurrent and photoconversion efficiency. Furthermore, photocurrent and photoconversion efficiency increased by increasing nanotube length in the range from 18 to 55  $\mu\text{m}$ . This implies an excellent light penetration up to 55  $\mu\text{m}$  depth into photoanode which is about 3.6 times higher than the maximum penetration depth in the nanoparticulate photoanode. This increasing pattern of photoconversion efficiency with increasing nanotubes length also implied a high charge separation rate and lower charge recombination rate.

Chapter 5: monodispersed ferrite NPs-encapsulated TNTAs were fabricated for the first time. The fabricated nanocomposite showed a high increase of photoconversion efficiency from 3% for pristine TNTAs to 5.18% for 20 mg ferrite loading ferrite-encapsulated TNTAs which represents a percentage increase of 72.6%. Magnetic ferrite-encapsulated TNTAs were tested in drug delivery and showed excellent drug release profile and cytotoxicity capacity.

## 1.9 References

1. Yuan, Z-Y., Su, B-L., Colloids and Surfaces A: Physicochemi. Eng. Aspects 241 (2004), pp. 173-183.
2. Guozhong, Cao, Nanostructures and Nanomaterials: Synthesis, Properties and Applications, 2004 by Imperial College Press p. 15.
3. Iijima, S., Nature 354 (1991) p. 56.
4. Wu, P, -G., Ma, C. -H., Shang, J. K., Applied Physics A 81 (2005), pp.1411-1417.
5. Mor, G. K., Varghese, O. K., Paulose, M., Shankar, K., Grimes, C. A., Solar Energy Materials & Solar cells 90 (2006) pp.2011-2075.
6. Shen, Q., Sato, T., Hashimoto, M., Chen, C., Toyoda, T., Thin Solid Films 499 (2006), pp. 299-305.
7. Macak. J.M., Tsuchiya, H., Berger, S., Bauer, S., Fujimoto, S., Schmuki, P., Chemical Physics Letters 428 (2006) pp. 421-425.
8. Banerjee, T. and Mukherjee, A., Energy Procedia 54, (2014), pp. 221-227.
9. Isimjan, T. T., Trifkovic, M., Abdullahi, I., Rohani, S. and Ray, A. K., Top Catal 58, (2015), pp. 114-122.
10. Zhou, Q., Fang, Z., Li, J. and Wang, M., Microporous and Mesoporous Materials 202, (2015), pp. 22-35.
11. Yoo, J., Zazpe, R., Cha, G., Prikryl, J., Hwang, I., Macak, J. M. and Schmuki, P., Electrochemistry Communications 86, (2018), pp. 6-11.
12. Yang, M., Zhang, L., Jin, B., Huang, L. and Gan, Y., Applied Surface Science 364, (2016), pp. 410-415.

13. Premchand, Y. D., Djenizian, T., Vacandio, F., Knauth, P., *Electrochemistry Communications* 8 (2006), pp. 1840-1844.
14. Kavil, Y. N., Shaban, Y. A., Al Farawati, R. K., Orif, M. I., Zobidi, M. and Khan, S. U. M., *Journal of Photochemistry and Photobiology A: Chemistry* 347, (2017), pp. 244-253.
15. Ghicov, A., Macak, J. M., Tsuchiya, H., Kunze, J., Haeublein, V., Frey, L., Schmuki, P., *Nano Lett.* Vol. 6 (5) (2006) pp. 1080-1082.
16. Madhusudan Reddy, K., Baruwati, B., Jayalakshmi, M., Mohan Rao, M., Manorama, S. V., *J. Solid State Chemistry* 178 (2005), pp. 3352-3358.
17. Wu, D., Chen, Y., Liu, J., Zhao, X., Li, A., Ming, N., *Appl. Phys. Lett.* 87 (2005) pp. 112501-112503.
18. Shankar, K., Paulose, M., Mor, G. K., Varghese, O. K., Grimes, C. A., *J. Physics D: Applied Physics* 38 (2005) pp. 3543-3549.
19. Shankar, K., Tep, K. C., Mor, G. K., Grimes, C. A., *J. Physics D: Applied Physics* 39 (2006) pp.2361-2366.
20. Park, J. H., Kim, S., Bard, A. J., *Nano Lett.* Vol. 6 (1) (2006) pp. 24-28.
21. Hoyer, P., *Langmuir* 12 (1996) pp.1411-1413.
22. lakshmi, B. B., Dorhout, P. K., Martin, C. R., *Chem. Mater.* Vol. 9 (3) (1997), pp. 857-862.
23. Kayabashi, S., Hamasaki, N., Suzuki, M., Kimura, M., Shirai, H., Hanabusa, K., *J. Am. Chem. Soc.* 124 (2002) pp. 6550-6551.
24. Zhang, M., Brando, Y., Wada, K., *J Mater. Sci. Lett.* 20 (2001), pp. 167-170.

25. Tian, R. Z., Voigt, J. A., Liu, J., Mckenzie, B., Xu, H., J. Am. Chem. Soc. 125 (2003) pp. 12384-12385.
26. Bavykin, D. V., Parmon, V. N., Lapkin, A. A., Walsh, F. C., J. Mater. Chem. 14 (2004), pp. 3370-3377.
27. Mor, G. K., Varghese, O. K., Paulose, M., Mukherjee, N., Grimes, C., A., J. Mater. Res. Vol. 18 (11), (2003) pp. 2588-2593.
28. Gong, D., Grimes, C., A., Hu, W., Singh, R. S., Chen, Z., Dickey, E. C., J. Mater. Res. Vol. 16 (12), (2001) pp. 3331-3334.
29. Zhao, J., Wang, X., Sun, T., Li, L., Nanotechnology 16 (2005), pp. 2450-2454
30. Cai, Q., Paulose, M., Varghese, O. K., Grimes, C. A., J. Mater. Res. Vol. 20 (1), (2005) pp. 230-236.
31. Thomas, C. E., James, J. B., Lomax, FD. Int. J. Hydrogen Energy Vol. 23 (1998), pp. 949-66.
32. Nowotny, J., Bak, T., Nowotny, M. K., Sheppard, L. R. Int. J. Hydrogen Energy (2006) doi: 10.1016/ijhydene.2006.09.004
33. Nowotny, J., Sorrell, C. C., Sheppard, L. R. Bak, T. Int. J. Hydrogen Energy 30 (2005) pp. 521-544.
34. Ni, M., Leung, M. K. H., Leung, D. Y. C., Sumathy. K. Renewable and sustainable Energy Reviews 11 (2007) pp. 401-425.
35. Murphy, A. B., Barnes, P. R. F., Randeniya, L. K., Plumb, I. C., Grey, I. E., Horne, M. D., Glasscock, J. A. Int. J. Hydrogen Energy 31 (2006) pp.1999-2017.

## Chapter 2 :

### **2 Modified TiO<sub>2</sub> Nanotube Arrays (TNTAs): Progressive Strategies Towards Visible Light Responsive Photoanode, A Review**

A version of this chapter was published as:

Ahmed El Ruby Mohamed and Sohrab Rohani, “Modified TiO<sub>2</sub> nanotube arrays (TNTAs): progressive strategies toward visible light responsive photoanode, a review”, *Energy Environ. Sci.* 4, (2011), pp. 1065-1086.

## 2.1 Abstract

Since first introduced by Zwillig and co-workers in 1999, titania nanotube arrays (TNTAs) fabricated by simple electrochemical anodization method have attracted great interest due to their outstanding photoelectrochemical properties which render them the most promising candidate for many solar energy harvesting applications. In this contribution, the fabrication, properties, and applications of TiO<sub>2</sub> nanotube arrays have been reviewed, with special focus on synthesis by anodization in fluoride-containing electrolytes. The effect of anodization process parameters such as electric potential, pH, anodization duration and electrolyte composition on the size, and morphology of TNTAs has been discussed in detail. Electronic property modification strategies of the wide band gap TNTAs to enhance the material responsiveness to visible light irradiation have also been reviewed. Modification strategies include nonmetal doping such as nitrogen, carbon, boron and sulfur; metal ion doping such as Fe, Zn, Zr and Cr; surface decoration with precious metal nanoparticles such as Pt, Ag, Au; and sensitization with CdS nanoparticles.

**Keywords:** Titania nanotube arrays, fabrications, aqueous electrolyte, organic electrolyte, anodization, doping, non-metal doping, metal ions doping, precious metal, CdS sensitization, photocatalysis, dye-sensitized solar cell

## 2.2 Introduction

Nanostructural materials of highly ordered one dimensional (1-D) architecture such as nanowires and nanotubes have attracted much interest in the last decade due to their high surface-to-volume ratio and other unique properties compared to their bulk similitudes. New chemical and physical properties appear when the size of the material decreases down

to the nanometer scale. Properties depend not only on the size of the nanomaterials but also on the shapes of the shrinking nanomaterials. Many excellent reviews and reports on the preparation and properties of nanomaterials have been published recently [1-4]. One of the most important and unique properties of nanomaterials is that the transfer of electrons and holes in semiconducting nanomaterials is mainly governed by the quantum confinement phenomenon, and the transport characteristics related to phonons and photons are largely affected by the size and geometrical building of the materials [2, 5-6]. The specific surface area and surface-to-volume ratio increase dramatically as the size of a material decreases. For example, for a  $1 \text{ cm}^3$  iron cube, the percentage of surface atoms would be only  $10^{-5}\%$ , when the cube is divided into small cubes with an edge of 10 nm, the percentage of surface atoms would increase to 10%. In a  $1 \text{ nm}^3$  iron cube, every atom would be a surface atom [7]. The high surface area brought about by size shrinking of nanomaterials is beneficial to many of applications such as heterogeneous catalysis, photocatalysis, sensing and electronic applications as it facilitates reaction/interaction between the devices and the interacting media, which primarily takes place on the surface or at the interface and strongly depends on the surface area of the material. Hence, the performance of nanomaterials-based devices is largely influenced by the sizes of the building units, obviously at the nanoscale [7].

The discovery of carbon nanotubes by Iijima [8] with their interesting properties has stimulated the quest for the synthesis of nanotubular structure of other inorganic materials such as  $\text{V}_2\text{O}_3$ ,  $\text{SiO}_2$ ,  $\text{TiO}_2$ ,  $\text{ZrO}_2$  and  $\text{MoO}_3$ . Nanotubes present a unique combination of shape, nanosize and functionality so that the properties can be directly influenced by the 1D-nanoscale feature of the geometrical morphology [9-12]. Among all nanotube

materials, titanium oxide nanotube arrays (we will refer to it as TNTAs hereinafter), is of particular interest because it is a highly functional material with many applications. These wide applications of TiO<sub>2</sub> nanotubes are based on their semiconducting and biocompatibility properties coupled with high surface area and excellent electrons/holes separation properties. Furthermore, the great oxidizing ability of photo-generated holes in titania associated with the high physical and chemical stability and low cost make it the preferred semiconductor material for many applications that utilize solar energy [13]. These properties make titania suitable for photocatalysis [14-16], water-splitting [17-18], self-cleaning [19], sensing [20], and dye-sensitized solar cells (DSSCs) [21]. In biological and medicinal applications, the biocompatibility is extremely important where the TiO<sub>2</sub> nanostructured layers on Ti are directly in contact with biological tissue in dental or hip implants [22]. Titania nanotubes can be synthesized in two forms: powdery form and self-organized nanotube arrays. The immobilized nanotubes are self-organized, vertically oriented and supported on a surface forming an integrated unit. Powdery titania nanotubes, and nanotube arrays, have been produced by a variety of methods including deposition into a nanoporous alumina template [23], sol-gel [24-25] and hydrothermal processes [26-27]. However, among these nanotubes fabrication routes, the electrochemical anodization method has attracted the most interest since first reported by Zwilling and co-workers [28] due to its ability to produce integrative, vertically-oriented highly ordered nanotube arrays with controllable dimensions [29-31]. The progressive increase in research interest in the TiO<sub>2</sub> nanotube arrays fabricated by anodization method is easily noticed from publication statistics (see Figure 2.1). Publication number increased several times from the first work by Zwilling and coworkers, 1999 [28] where only short nanotubes of a few hundred



nanometers in length and low degree of self-organization were obtained to the present state where highly-ordered, vertically-oriented, high-aspect ratio TiO<sub>2</sub> nanotube arrays with lengths of hundreds of micrometers can be obtained [32]. In contrast to random nanoparticle systems where slow electron diffusion typically limits their performance, the precisely oriented nature of the crystalline nanotube arrays makes them excellent electron percolation pathways for the vertical transfer of electrical charges across the length of nanotubes [33-35]. In addition, the nanotube array architecture is able to influence the absorption and propagation of light through the architecture by precisely designing and controlling the nanotube internal diameter, wall thickness, and length [36-38]. In this review, we focus on recent progress in synthesis, characterization and modification methods of titania nanotube arrays (TNTAs) as a most promising photoanode in solar energy conversion devices.

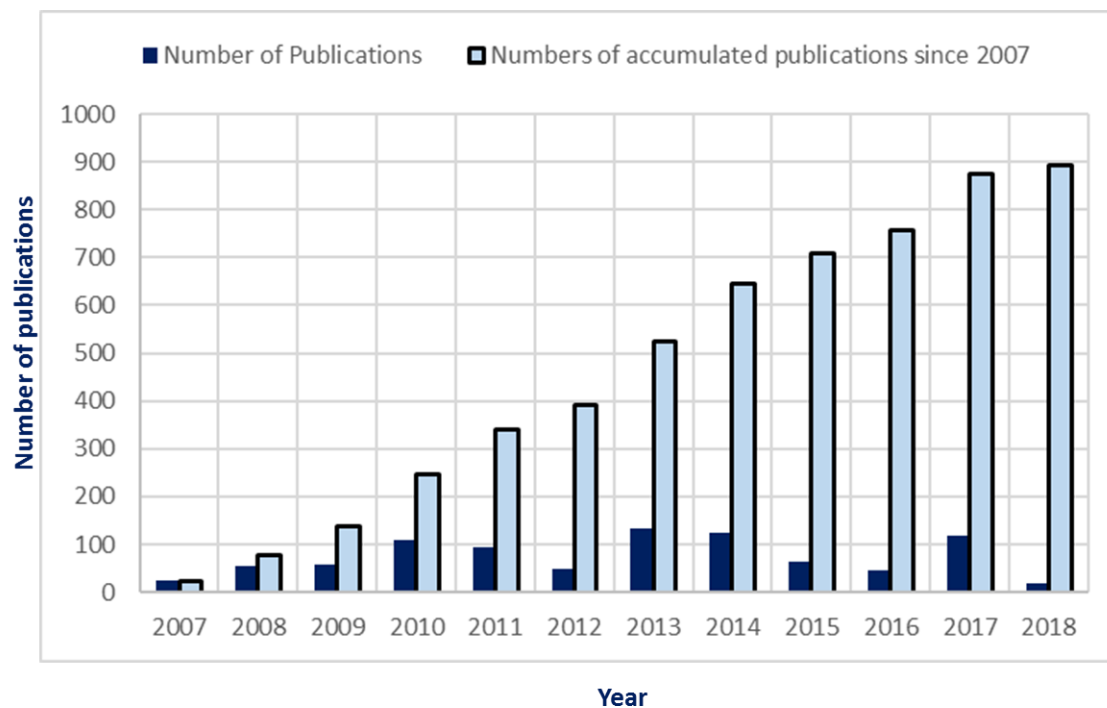


**Figure 2-1 The number of publications per year and accumulated publications on the topic of titania nanotube arrays in the last decade. (Statistics analysis was obtained from Scopus database on January 21<sup>st</sup>, 2018).**

### 2.3 TNTAs versus TiO<sub>2</sub> nanoparticles

A significant progress in the field of low cost photoelectrochemical energy conversion has been achieved using porous nanostructured semiconductor films. Up to now, the most effective photoelectrochemical cells (PEC) made of several micron-thick porous films consisted of 15-20 nm sized crystalline TiO<sub>2</sub> nanoparticles [39-40]. Nazeeruddin and co-workers have demonstrated liquid junction dye-sensitized solar cells with photoconversion efficiency higher than 10% [41]. In Si-based conventional solar cells, the photogenerated

electrons and holes are to be separated using built-in potential of the p-n junction. In the absence of such mechanism to separate the opposite charges, the photogenerated electrons and holes are lost due to recombination with each other. In nanoparticles-based solar cells, the nanoparticle size is too small to maintain significant electric potential therefore, other ways must be used to attain the holes/electrons separation. The photogenerated electron/hole charges are separated kinetically and because of the small size of nanoparticles, the hole may diffuse to the particle-electrolyte interface to react with a solution ion and hence a successful charge separation occurs, but it may also happen that the small size of nanoparticle facilitates the recombination process between the electron-hole pair before the hole successfully reacts with the solution ions. Furthermore, the movement of the electrons from the point where they were photogenerated to the electrons collector -- the conducting back contact of the photoanode -- is a limiting factor in the photoanode consisted of nanoparticles, obstructing the process to achieve a higher efficiency. The structure disorder at the boundary between two nanoparticles increases the scattering of the generated free electrons and, consequently, this reduces the electrons transport rate and collection property of the photoanode [42-43]. Although nanoparticles TiO<sub>2</sub> films have a highly effective photooxidation of a very wide variety of organic substances, they demonstrate, in contrast, very low photoconversion efficiency (PE) for the water photolysis to H<sub>2</sub> and O<sub>2</sub> in both acidic and alkaline solutions. This may be ascribed to the above mentioned poor electrons mobility as the water splitting primarily depends on the photogenerated free electrons rather than photogenerated holes [44-45]. In nanoparticulate films, the photogenerated electrons may also react with the intermediates of the photooxidation reactions between the photogenerated holes and electrolyte solution.

The poor performance of the nanoparticulate TiO<sub>2</sub> films may be ascribed to the possibility of back-charge reactions of intermediates of photooxidation of water [46]. The electrons' slow percolation through a random nanoparticles network and the low absorption capability of the low energy photons are both major factors hindering further enhancement in the photoconversion efficiency, PE, in nanoparticulate TiO<sub>2</sub>-based dye-sensitized solar cells (DSSCs). The increase of nanoparticulate film thickness (above 10 μm) to enhance the photons absorption is undermined by the slow electron transport through the nanoparticulate network. The haphazardness of the particles arrangement in the film almost duplicates the pathway length of the electrons [34, 47]. Highly ordered, vertically oriented TNTAs perpendicular to the photoanode surface allow the vertical charge transport from the photoanode/electrolyte interface to the conductive substrate in the back of the photoanode, thereby, minimizing the charge losses occurred due to the hopping of electrons through the boundaries of the nanoparticles. Therefore, electron transfer through TNTAs is superior to electron percolation through the random particulate films. This enhancement in electron charge transport in TNTAs is expected to increase the overall photoconversion efficiency [48-50]. The highly ordered vertically oriented nanotubular structure of TNTAs provides a better opportunity to harvest sunlight more efficiently than the randomly oriented nanoparticulate films or even nanotubes prepared by the sol-gel or hydrothermal processes [51]. Additionally, the nanotubular structure can improve the lifetime of the photogenerated charges by more than an order of magnitude [35, 52-54]. TNTAs exhibited a photoanodic response 10 times higher than that of a TiO<sub>2</sub> nanoparticulate film under the same irradiation condition [55]. It is expected that the performance of TNTAs could be

further significantly improved if their structure-property-relationship is established and the involved phenomena are fully understood.

## 2.4 Fabrication of TNTAs

Electrochemical anodization of metals and semiconductors is a relatively simple process for creating precisely engineered semiconductor nanostructures. Anodization is used to create highly ordered, self-oriented nanoporous materials such as alumina, silica, titania and zirconia. Anodization of titanium foils and thin films are conducted using a two-electrode electrochemical cell with a platinum foil as cathode at a constant potential -- a third electrode could be used as a standard reference electrode to eliminate noise effect when measuring the cell potential by potentiostat [56]. Figure 2.2 shows an illustrative drawing of a two-electrode electrochemical cell in which Ti foils are anodized when electrical potential is applied.

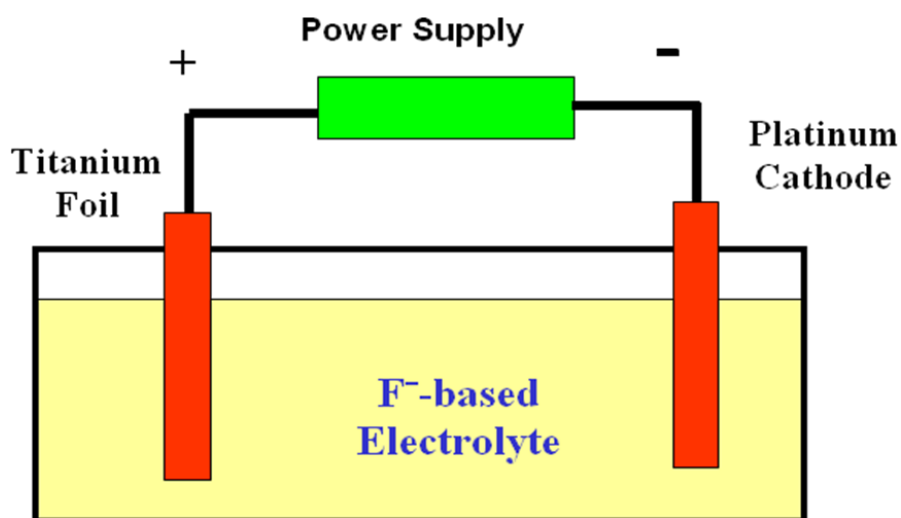


Figure 2-2 Illustrative drawing of a two-electrode electrochemical cell for anodization.

#### 2.4.1 Fabrication of TiO<sub>2</sub> Nanotube Arrays (TNTAs) in Aqueous Electrolytes

Titania nanotube arrays are grown on titanium surface by potentiostatic anodization of the parent Ti foil in aqueous electrolyte containing F<sup>-</sup> ions. HF acid was used as a source of F<sup>-</sup> and pH was adjusted by adding drops of diluted sulfuric acid or diluted sodium hydroxide [57-59]. Self-organized TNTAs were first fabricated by electrochemical anodization of Ti metal foils in aqueous hydrofluoric acid electrolyte by Gong and co-workers [57]. In this study, anodization voltage and HF concentration were investigated. Below 10 volts, no nanotubes were formed. Porous or particulate films were formed instead. Nanotubular structure was successfully fabricated in a voltage window from 10 to 40 V. Above 40 V, TNTAs structure disappeared and randomly porous layers began to appear again. HF concentrations from 0.5 to 3.5 wt.% were used and results showed that the appropriate voltage range required for the formation of TNTAs decreased by increasing HF concentration. [57]. By using HF aqueous electrolyte, TNTAs could be grown up to only

500 nm in length. This limited length of TNTAs was due to high chemical dissolution at the top of nanotubes because of the strong acidity of the electrolyte ( $\text{pH} < 2$ ). Later on, many studies focused on precise control and extension of the nanotubes architecture [58, 60-61].

Effect of anodization potential: Cai and co-workers studied the effect of potential in strong acidic ( $\text{pH} < 1$ ) aqueous electrolytes consisting of 1 M  $\text{H}_2\text{SO}_4$  and 0.1 M HF and found that nanotube arrays formed only in the range of 10 - 25 V. Also, they reported the inner diameter of nanotubes increased from 40 nm to 110 nm with potential increase from 10 to 25 V. Figure 2.3 shows the effect of anodization potential on the formation and morphology of titania nanotube arrays in 1 M  $\text{H}_2\text{SO}_4$  and 0.1 M HF aqueous electrolyte [62].

For specific electrolyte composition, there is an anodization potential window within which TNTAs can be fabricated. This window depends on chemical and physical properties of the electrolyte as well as its pH. Gong and coworkers [57] fabricated TNTAs over potential range from 10 to 40 V, while Cai and co-workers [62] found that TNTAs fabrication was possible only over potential range from 10 to 25 V. Tian and co-workers [63] obtained TNTAs at potential of 20 V in  $\text{NH}_4\text{F}/\text{H}_2\text{SO}_4$  aqueous electrolyte. Anodization potential has a key role in the formation of TNTAs as the formation of TNTAs is basically the result of equilibrium between electrochemical oxidation of Ti to  $\text{TiO}_2$  and the chemical dissolution of  $\text{TiO}_2$  in fluoride- containing electrolyte [63]. Very interestingly and in contrast to any electrolyte system for TNTAs formation, titania nanotube arrays were formed at potential as low as 1 V in 1 M  $\text{H}_3\text{PO}_4$  + 0.3 wt.% HF aqueous electrolyte in an electrochemical cell with three electrodes configuration employing Ag/AgCl as reference electrode [64]. The

nanotubes inner diameter and nanotube length were found to be dependent on anodization potential and when potential increased from 1 to 25 V, nanotubes diameter and length increased linearly from 15 nm and 20 nm to 120 nm and 1 $\mu$ m, respectively, as it can be seen from Figure 2.4. The high adjustability of the nanotubes geometry and long nanotubes, compared to the nanotubes fabricated in HF electrolyte, was ascribed on one hand to the fact that H<sub>3</sub>PO<sub>4</sub> acts as a buffer which regulates local acidity during the nanotubes growth. And, on the other hand: the phosphate ions were strongly adsorbed on TiO<sub>2</sub> surfaces, the fact that was verified by XPS characterization [64].



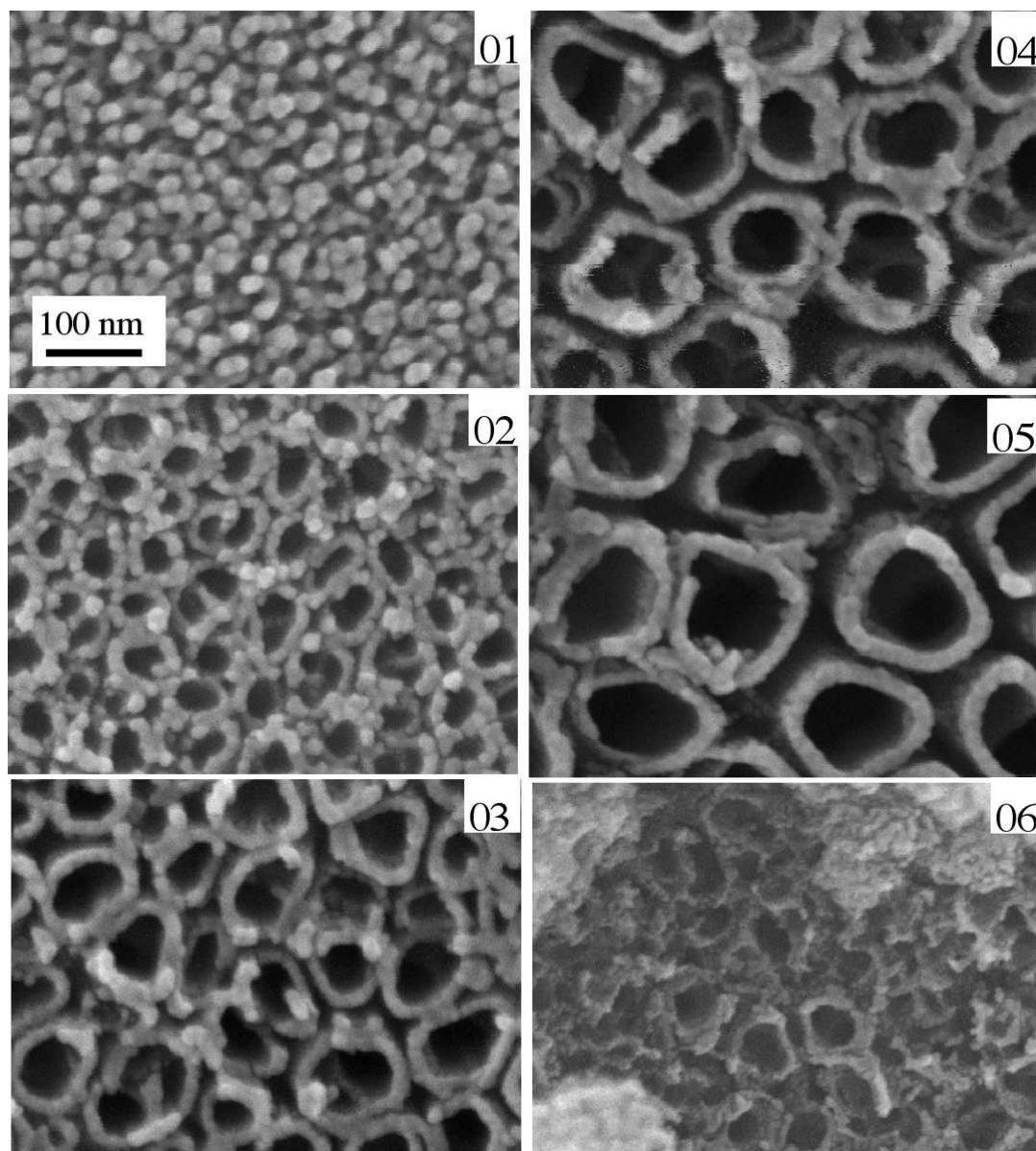


Figure 2-3 Effect of anodization potential on TNTAs formation and morphology in 1 M  $\text{H}_2\text{SO}_4$  and 0.1 M HF aqueous electrolyte at 01) 5 V, 02) 10 V, 03) 15 V, 04) 20 V, 05) 25 V and 06) 30 V (reprinted with permission from ref. [62] © 2005 Materials Research Society).

Although acidic electrolyte is essential for nanotube formation, lower pH electrolyte results in few hundred nanometers in nanotube length while higher pH buffered electrolytes give longer nanotubes up to 6  $\mu\text{m}$  at pH: 5-6. This was explained by the fact that the chemical dissolution rate of  $\text{TiO}_2$  nanotubes is increased by lowering pH of the electrolyte [35]. Cai and co-workers [62] synthesized titania nanotube arrays in aqueous electrolytes with pH range from 1 to 6.4 and their results showed that in strong acidic electrolytes, with pH between 1 and 2, titania nanotubes with few hundred nanometers in length were formed and by increasing pH to 5.6, the length increased to 4.4  $\mu\text{m}$  after anodization for 20 hrs. According to Cai and co-workers [62], there was no effect of pH on inner diameter. In contrast to the above study, Yin and co-workers found that the inner diameter of nanotubes decreased from 80 nm to 40 nm by decreasing pH from 5.6 to 4 [65]. Figure 2.5 indicates the effect of pH on nanotube length and nanostructure of the surface of nanotube samples.

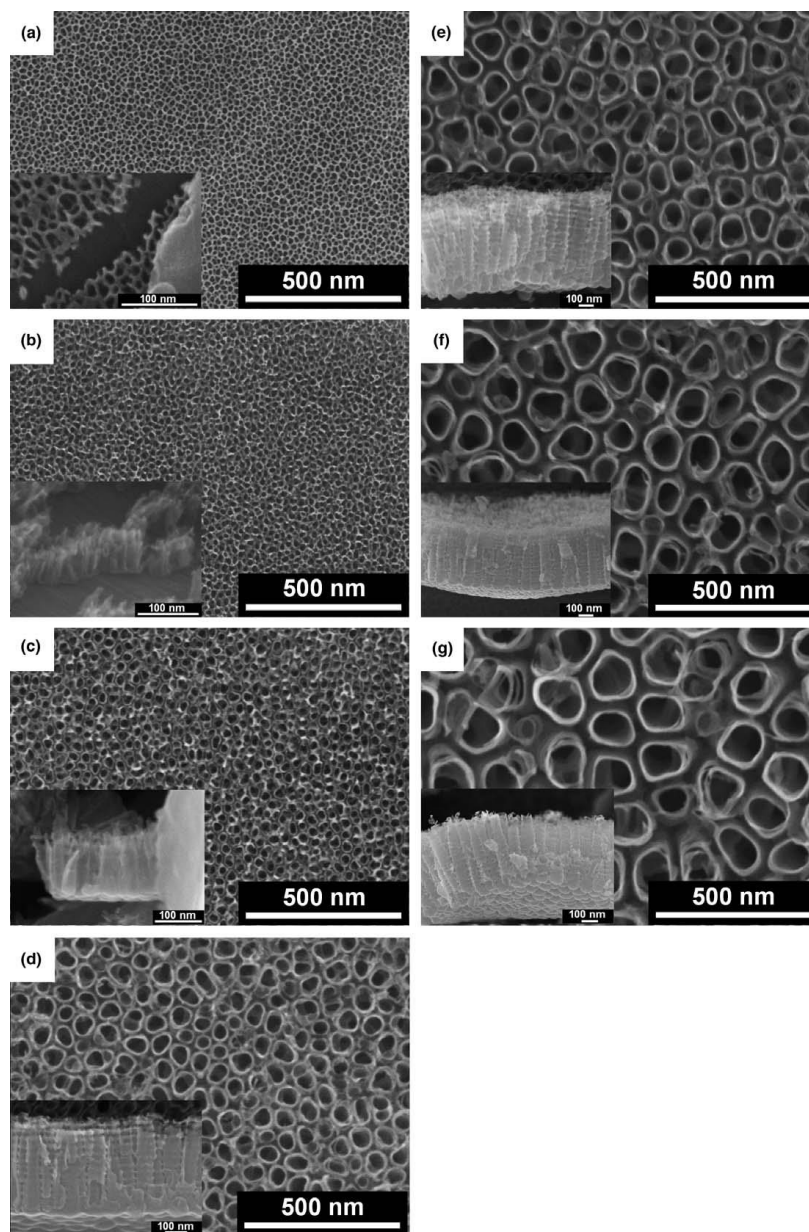


Figure 2-4 Effect of anodization potential on titania nanotube morphology (SEM top view and cross-section images) formed in 1 M  $\text{H}_3\text{PO}_4$  + 0.3 wt.% HF at: 1 V (a), 2.5 V (b), 5 V (c), 10 V (d), 15 V (e), 20 V (f) and 25 V (g) for 1 h. (Reprinted with permission from ref. [64] © 2006 Elsevier B.V.)

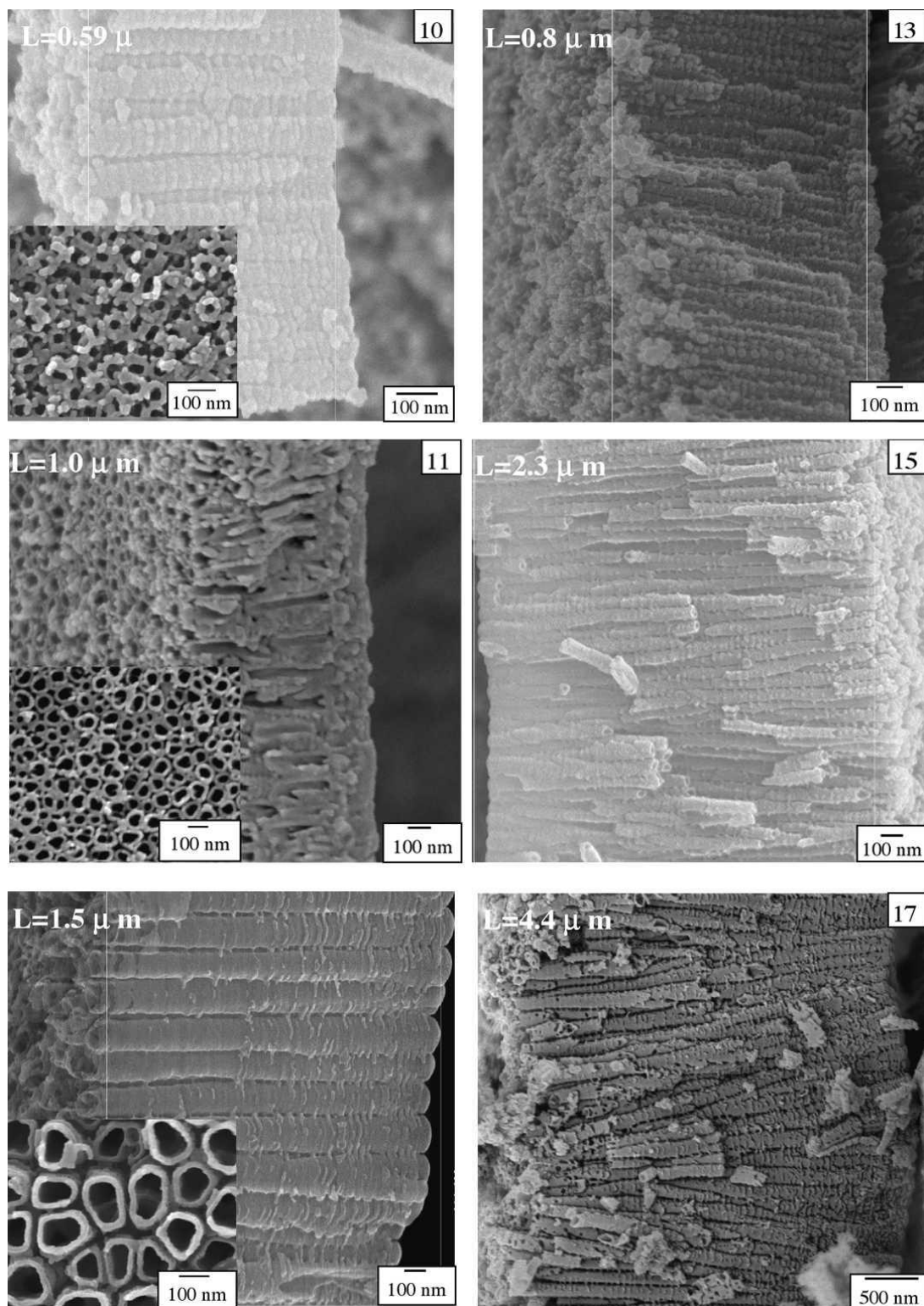


Figure 2-5 Lateral views of TNTAs formed in different pH solutions (preprinted with permission from ref. [62] © 2005 Materials Research Society)

Bai and co-workers [66] studied the morphology of anodized titanium foil after different anodization times, 10, 30, 60, 200, 800 and 1800 s in 0.5 wt.% HF in aqueous electrolyte. The FESEM images of the resulting anodized samples are shown in Figure 2.6. As can be seen from Figure 2.6, after 10 s, the surface was covered with titanium oxide film (Figure 2.6 a). At 30 s, the oxide layer was partially dissolved and randomly distributed grooves appeared in the oxide film (Figure 2.6 b). This was ascribed to localized dissolution of the oxide layer by HF [29]. After 60 s, (Figure 2.6 c), the original oxide layer was almost removed and replaced by another oxide layer consisted of small pores with 8 to 15 nm diameter. The inset in Figure 2.6 c shows the formation of larger pores by the integration of several small pores. After 200 s, larger tubes were formed with the integration of small tubes (Figure 2.6 d). At this time a tubular structure with uneven diameters ranging from 20 to 100 nm was observed. This means that the large pores, which previously formed from the integration of the small pores, are transformed into nanotubular structure. After 800 s, (Figure 2.6 e), the nanotube arrays with a diameter of about 100 nm were formed. After 1800 s, Figure 2.6 f, the development of highly ordered TNTAs was completed [66]. Based on this study and other similar work, a formation mechanism of TNTAs was proposed which will be discussed in a separate section in this review.

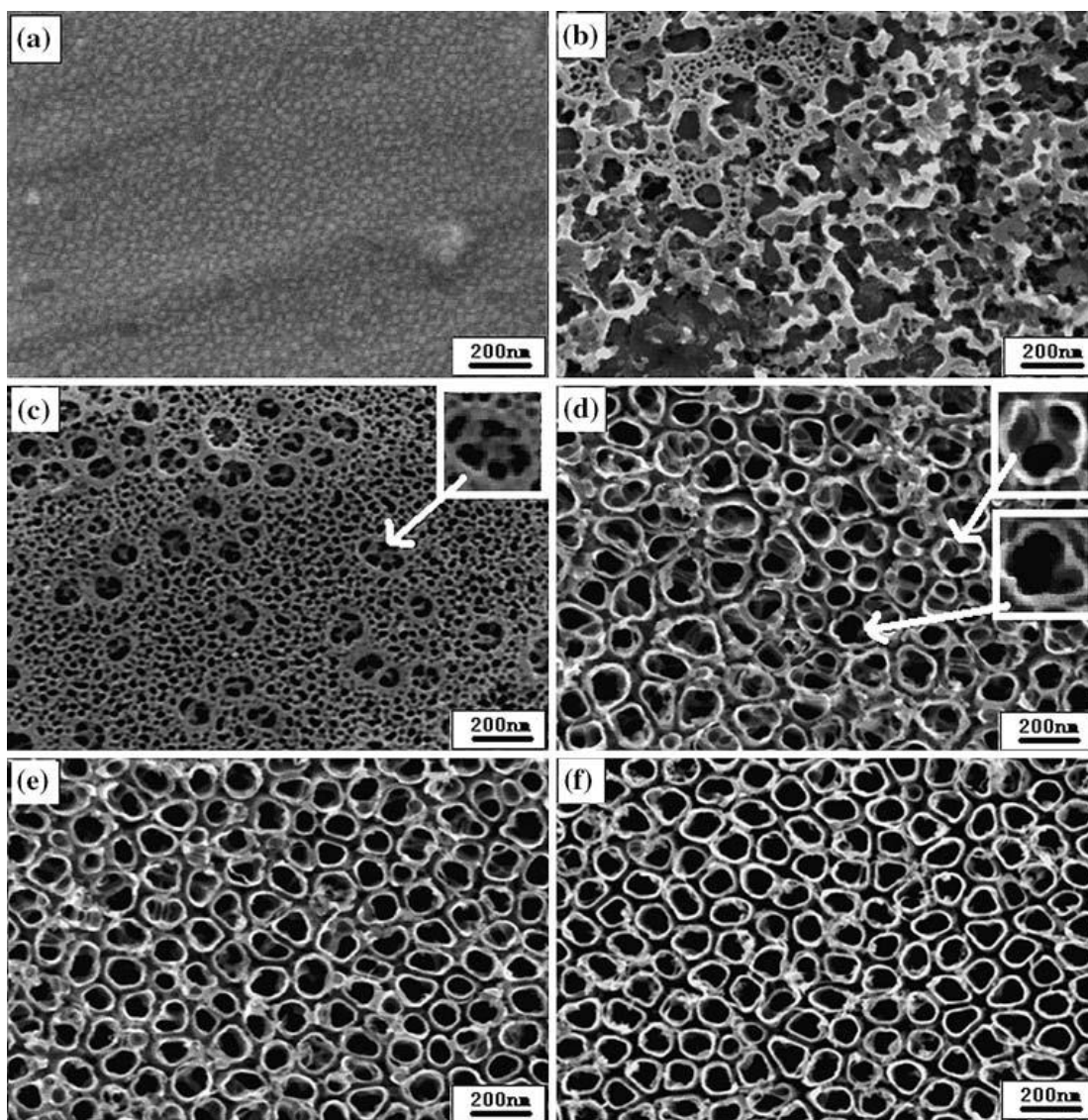


Figure 2-6 SEM top views of titania nanotube arrays anodized at 20 V in 0.5 wt.% HF aqueous electrolyte at different anodization times: (a) 10 s, (b) 30 s, (c) 60 s, (d) 200 s, (e) 800 s, and (f) 1,800 s (Reprinted with permission from ref. [66] © Springer Science + Business Media, LLC 2008).

## 2.4.2 Fabrication of TNTAs in organic electrolytes

Many organic solvents are known to be used in anodic fabrication of microporous silica and aluminum oxide [67-69]. It has been demonstrated that organic solvents crucially inhibit the electrochemical oxidation of Si compared to an aqueous electrolyte and that organic solvents behave as a mild oxidizing reactant for Si. Furthermore, it has been shown that the nanotubes growth benefits from the mildly reducing conditions in organic electrolytes compared to water due to the more difficult oxygen donation process. An organic electrolyte is a more reducing medium in comparison to an aqueous electrolyte [67, 70-71]. The TNTAs formation is strongly dependent on the chemical solubility, and chemical and physical properties of the electrolytes. In high acidic aqueous solutions ( $\text{pH} < 1$ ), the nanotube growth rate and dissolution rate are both high resulting in short nanotubes even after long anodization times. In comparison to aqueous electrolytes, much longer TNTAs can be formed in polar organic electrolytes due to low chemical dissolution rate resulting from low water content [52, 56]. Illustrative organic solvents for TNTAs formation include: glycerol, dimethyl sulfoxide (DMSO), formamide (FA), N-methyl formamide (NMF), acetic acid and ethylene glycol (EG).

### 2.4.2.1 Fabrication of TNTAs in glycerol-based electrolyte

Macak and Schmuki investigated the formation of TNTAs in glycerol electrolyte containing 0.5 wt. %  $\text{NH}_4\text{F}$  as well as in 1 M  $(\text{NH}_4)_2\text{SO}_4$  aqueous electrolyte containing 0.5 wt. %  $\text{NH}_4\text{F}$  at 20 V and 20 °C [72]. Although after 3 h anodization time, the tube length anodized in aqueous electrolyte was slightly more than 2  $\mu\text{m}$  while it was only 1.3  $\mu\text{m}$  in glycerol electrolyte, extending anodization time to 18 h resulted in increasing tube

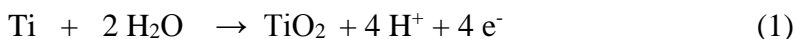
length up to 6.1  $\mu\text{m}$  in case of glycerol electrolyte while there was no noticeable increase in tube length in case of aqueous electrolyte as shown in Figure 2.7 a. The reason for the continuing growth of the nanotubes length over 18 h anodization time in glycerol-based electrolyte is the difference in pH value promoted by the high viscosity of the glycerol which resulted in high growth rate of nanotubes at the bottom of the nanotubes (low pH region) and lower dissolution rate of nanotubes at the top of nanotubes (high pH region). On the other hand, due to low viscosity of aqueous electrolyte, there is no gradient in pH value between the bottom and top regions of the nanotubes. This resulted in high dissolution rate of the nanotubes at the top and consequently, the net growth rate becomes 0 after 2.5 h. Figure 2.7 b shows the cross-section side view of TNTAs fabricated in glycerol electrolyte showing the extending tube length of 6.1  $\mu\text{m}$ . The inset image is the cross section of the same sample at high magnification to show the smooth walls of nanotubes which is another interesting feature of anodization in glycerol electrolyte where ripples structure that usually appears in aqueous electrolyte anodization disappeared. It is noteworthy that the smoothness of the nanotube walls could improve various properties of the self-organized TNTAs. For instance, ripples absence may influence the light reflection behavior and that may facilitate applications of TNTAs as photonic crystals [73-74] or waveguides [75]. Figures 2.7 c and d show the top and bottom views, respectively, of the nanotubes anodized in glycerol electrolyte at 20 V for 18 h [72].

Another interesting difference is that TNTAs anodized in glycerol electrolyte possessed a smaller pore diameter (approximately 50 nm) than TNTAs anodized in aqueous electrolyte (approximately 100 nm) [72, 76]. Changing anodization temperature influenced both the



length and diameter of nanotubes where both increased linearly with temperature in the range of 0 to 40°C. This explains the vital role of viscosity of glycerol electrolyte on the TNTAs morphology [72].

The low growth rate of nanotubes in glycerol electrolyte and the strong dependence of the results on the viscosity and temperature of the electrolyte show that the tubes growth rate is a diffusion-controlled process [77]. Viscous electrolytes such as glycerol are characterized by self-induced local acidification at the bottom of nanotube pores which is caused by electrochemical dissolution of Ti metal. This local acidification is mainly caused by Ti oxidation and hydrolysis as in the following reactions:



By using a buffered neutral solution as an electrolyte, one can create a pH profile gradient that is increased from the bottom to the mouth of the tube pore and consequently, increasing the chemical etching at the bottom of the tubes while reducing the chemical dissolution at the mouth of the tubes resulting in increasing growth rate of the tubes [58]. Anodization in glycerol electrolytes/ $\text{NH}_4\text{F}$  showed current efficiencies close to 100% compared to 30-40% current efficiency for anodization in 1 M  $(\text{NH}_4)_2\text{SO}_4$  +0.5 wt.% $\text{NH}_4\text{F}$  aqueous electrolyte, and only 5 – 15 % current efficiency for anodization in 1 M  $\text{H}_2\text{SO}_4$  + 0.15 wt. % HF. The current efficiency was defined as the ratio of the tube length values measured directly from SEM cross-sections to the tube length values calculated from Faraday's law assuming a four-electron process and an oxide density of  $3.84 \text{ g cm}^{-3}$  [72]. By returning to the above

three electrolytes, it will be easy to correlate the loss in current efficiency to the high chemical dissolution rate of each electrolyte.

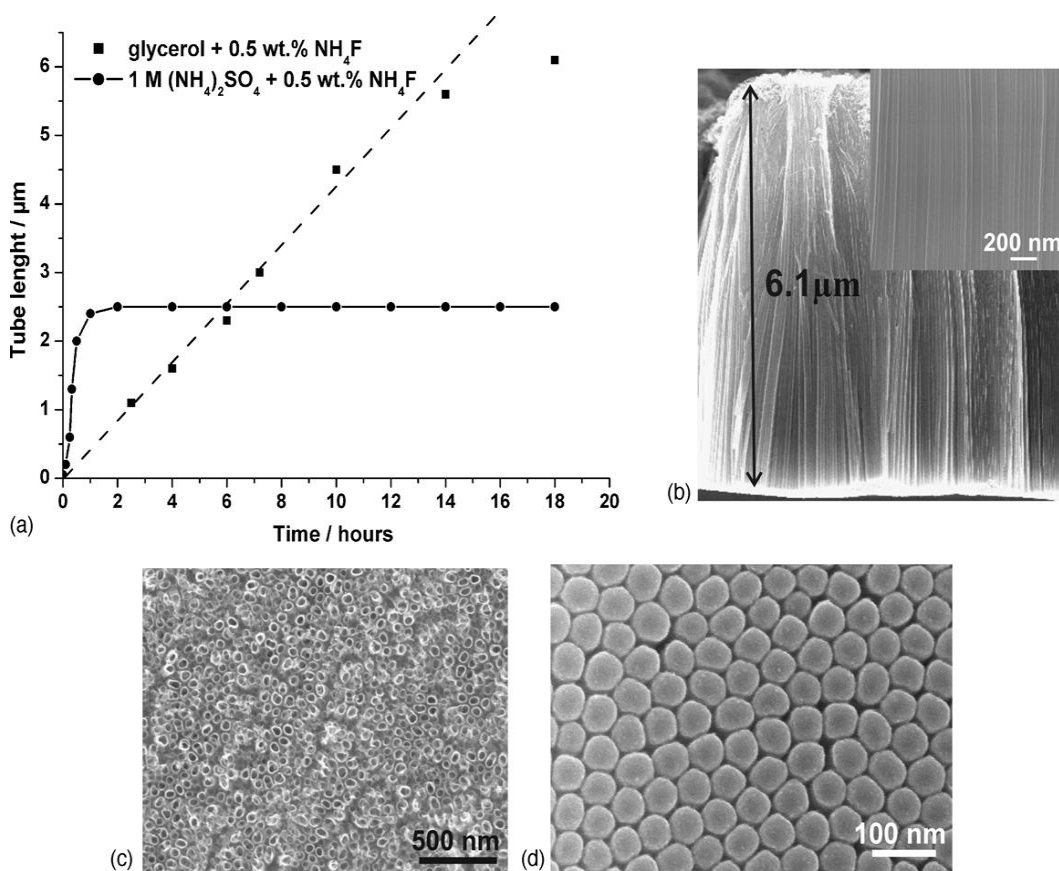


Figure 2-7 (a) The tube length as a function of anodization time of samples formed during different times in glycerol + 0.5 wt.% NH<sub>4</sub>F and 1 M (NH<sub>4</sub>)<sub>2</sub>SO<sub>4</sub> + 0.5 wt.% NH<sub>4</sub>F at 20 V at 20 °C. SEM images of (b) cross-section, (c) top view and (d) bottom view of self-organized TiO<sub>2</sub> nanotubes of length of 6.1 μm formed after 18 hrs anodization in glycerol electrolyte. (Reprinted with permission from ref. [72] ©2006 Elsevier Ltd.)

A key parameter in TNTAs formation is fluoride ion concentration. With no  $F^-$  ions in the electrolyte, no nanotubes are formed, instead a compact layer of oxide is formed. By increasing fluoride concentration from 0.135 M to 0.54 M, the anodization current density and the nanotubes length were increased. The anodization potential window widened from 10-25 V in aqueous electrolytes to 2-40 V in glycerol electrolyte. Glycerol/water/ $NH_4F$  mixture electrolyte provided a platform for fabrication TNTAs with a very high level of flexibility towards the tubes dimensions and morphology. TNTAs with diameters ranges from 20 to 300 nm were fabricated by tuning the potential from 2 to 40 V as shown in Figure 2-8 [78]. It can be seen in SEM images in this figure that mixing glycerol with water results in the appearance of ripples on the walls of nanotubes. Increasing water content in glycerol electrolyte results in increasing tube diameter and appearance of ripples on the tube walls and decreases the tube length [72, 78].

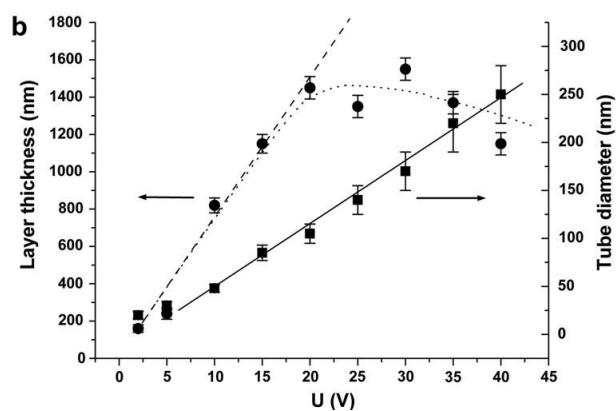
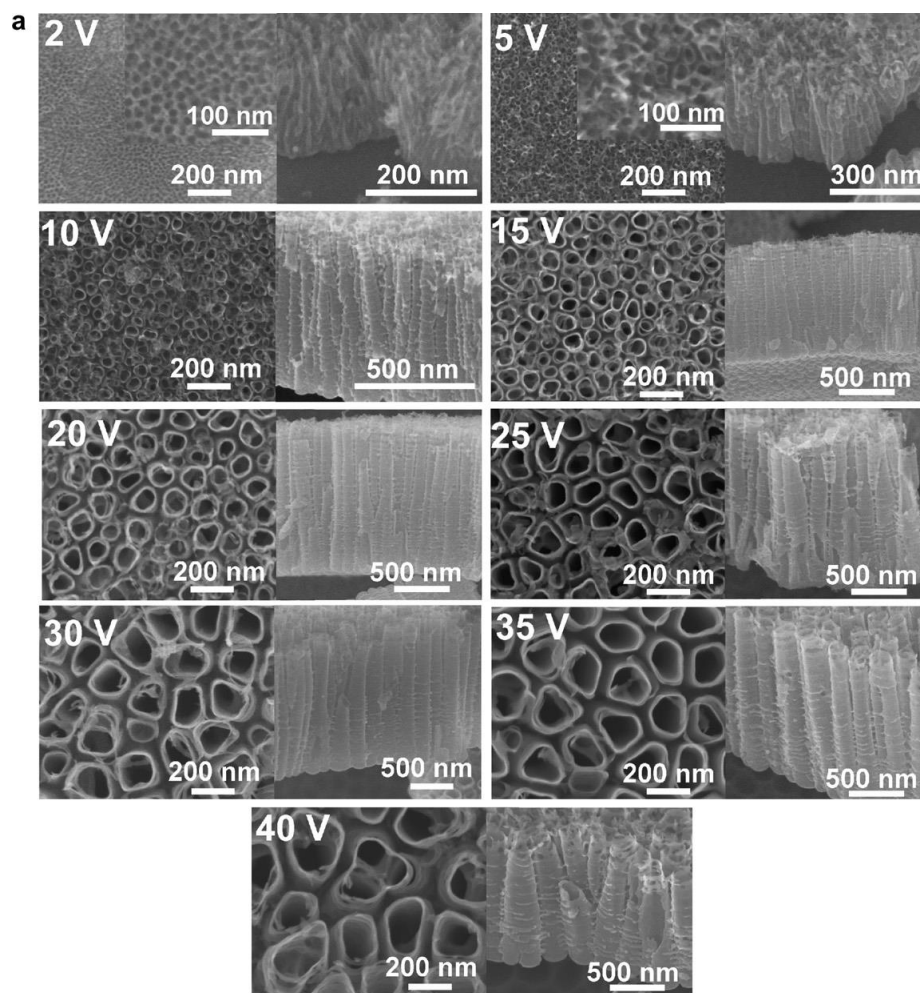


Figure 2-8 SEM top and cross sectional of the TNTAs grown in water/glycerol (1:1 v/v)/0.27 M  $\text{NH}_4\text{F}$  for 3 h anodization time at different potentials. (Reprinted with permission from ref. [78] ©2008 Elsevier B. V. All rights reserved)

#### 2.4.2.2 Fabrication of TNTAs in DMSO electrolyte

Dimethyl sulfoxide (DMSO) is the organosulfur compound with a chemical formula of  $(\text{CH}_3)_2\text{SO}$ . DMSO is a dipolar aprotic solvent. Unlike protic solvents, aprotic solvents do not have a hydrogen atom directly bonded to an electronegative atom such as oxygen or nitrogen. The hydrogen atoms in such solvents are only bonded to carbon atoms. DMSO has a very weak ability to donate protons (hydrogen bond donation) and is more basic than water, and therefore, it has a protophilic nature. DMSO has a dielectric constant of 47 which is lower than the dielectric constant of water at  $80^\circ\text{C}$ . The viscosity of DMSO (1.99 cP) is very close to that of water (0.89 cP) and much lower than the viscosity of glycerol (945 cP at  $25^\circ\text{C}$ ) [79]. Ruan and co-workers [80] conducted the first study of TNTAs formation by anodization in DMSO electrolyte. They obtained  $2.5\ \mu\text{m}$  long TNTAs using an electrolyte composed of DMSO:ethanol (1:1 volume ratio) and 4% HF after anodization time of 72 h at 20 V. It is worth to mention that nanotubes were only observed after 48 h of anodization while in aqueous electrolytes nanotubes were observed in the first hour of anodization. The anodized samples showed an inhomogeneous cracked surface with  $\text{TiO}_2$  nanotubes bundled together. To see the effect of anodization electrolyte on the photoelectrochemical properties of TNTAs, photocurrent and photoconversion efficiency of TNTAs sample anodized in DMSO: ethanol (1:1 volume ratio) and 4% HF at 20 V and TNTAs sample anodized in aqueous 1% HF electrolyte were measured. The photocurrent of DMSO sample was 6 times higher than that of aqueous HF electrolyte sample and the photoconversion efficiency of DMSO sample was 10.7%, 14 times greater than the photoconversion efficiency of aqueous HF electrolyte sample [80]. Paulose and co-workers [81] increased the length of DMSO anodized TNTAs up to  $93\ \mu\text{m}$ . The HF concentration

was varied from 1 to 6 wt.%, the anodization potential was studied in the range of 10 to 70 V and anodization time was varied from 20 to 90 hrs. As DMSO is a protophilic solvent, it accepts the hydrogen proton from HF reducing its effect in chemical dissolution of nanotubes at the tube mouth leading to an increase in nanotube growth rate. Figure 2.9 is representative FESEM images of TNTAs grown at 40 V in DMSO containing 2% HF a) cross-section view, b) lateral view and c) view of top surface. The nanotubes have a length of 45  $\mu\text{m}$ , an inner tube diameter of 120 nm and a wall thickness of 15 nm. The roughness factor, (total surface area of the nanotubes per the flat surface area of the sample), for this sample was 1800 [81]. Increasing anodization potential from 20 to 60 V resulted in an increase in TNTAs length from 10 to 93  $\mu\text{m}$ . The inner diameters of nanotubes were 50, 120 and 150 nm for 20, 40 and 60 V, respectively [81-82]. The increase in the diameter with increase in potential is in line with the trend that previously observed in aqueous HF electrolyte anodization [83-84]. When HF concentration increased from 1 to 4 wt. % at anodization potential 20 V, the nanotube length increased from 4.4 to 29  $\mu\text{m}$ . Also, when Ti foil pre-anodized in 0.5 % HF aqueous electrolyte before anodization in 2 % HF DMSO electrolyte at 40 V, nanotube length of 82  $\mu\text{m}$  was obtained, almost a 100% increase in nanotube length, from that obtained without pre-anodization of Ti foil in aqueous HF electrolyte [81]. Figure 2.10 shows the effect of anodization parameters on the length of nanotubes. Figure 2.10 a) shows that TNTAs length increased with increasing anodization potential as mentioned above but it reached its maximum at 60 V and then decreased rapidly at 70 V. The figure shows also how the pre-anodization of Ti foil in HF aqueous electrolyte enhanced the growth rate of the nanotubes where the pre-anodization worked as tinplating the surface for rapid nanotube growth rate.

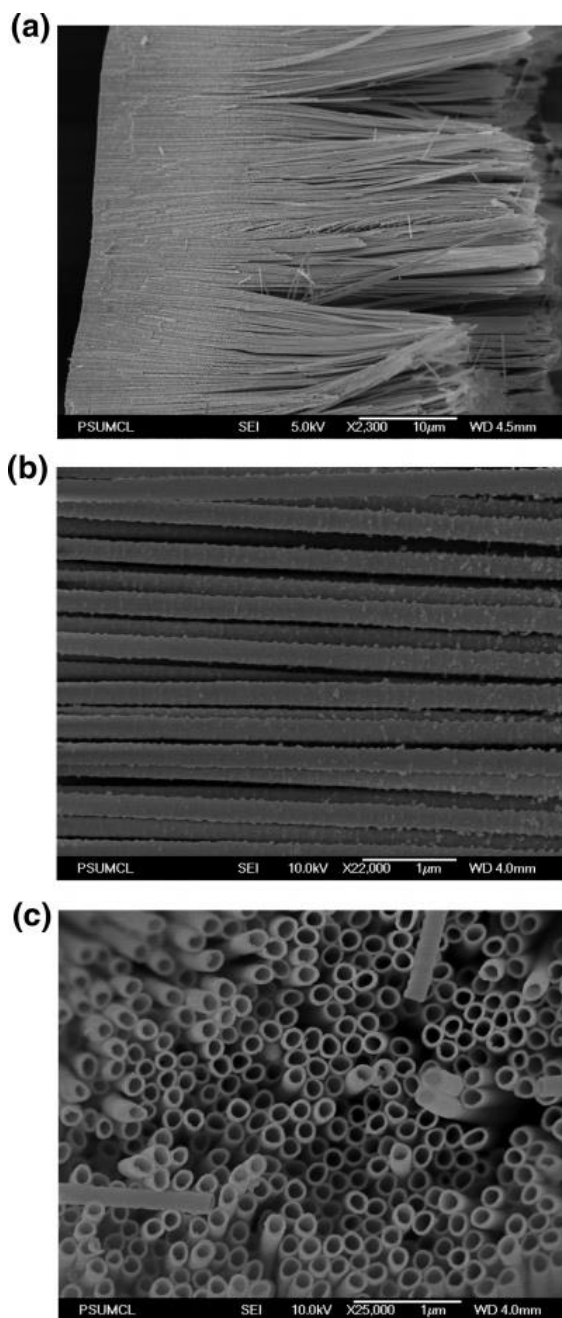


Figure 2-9 SEM images of TNTAs fabricated in DMSO containing 2% HF at 40 V for 69 h: a) cross sectional view, b) lateral view and c) top view (reprinted with permission from ref. [81], ©2006 American Chemical Society.)

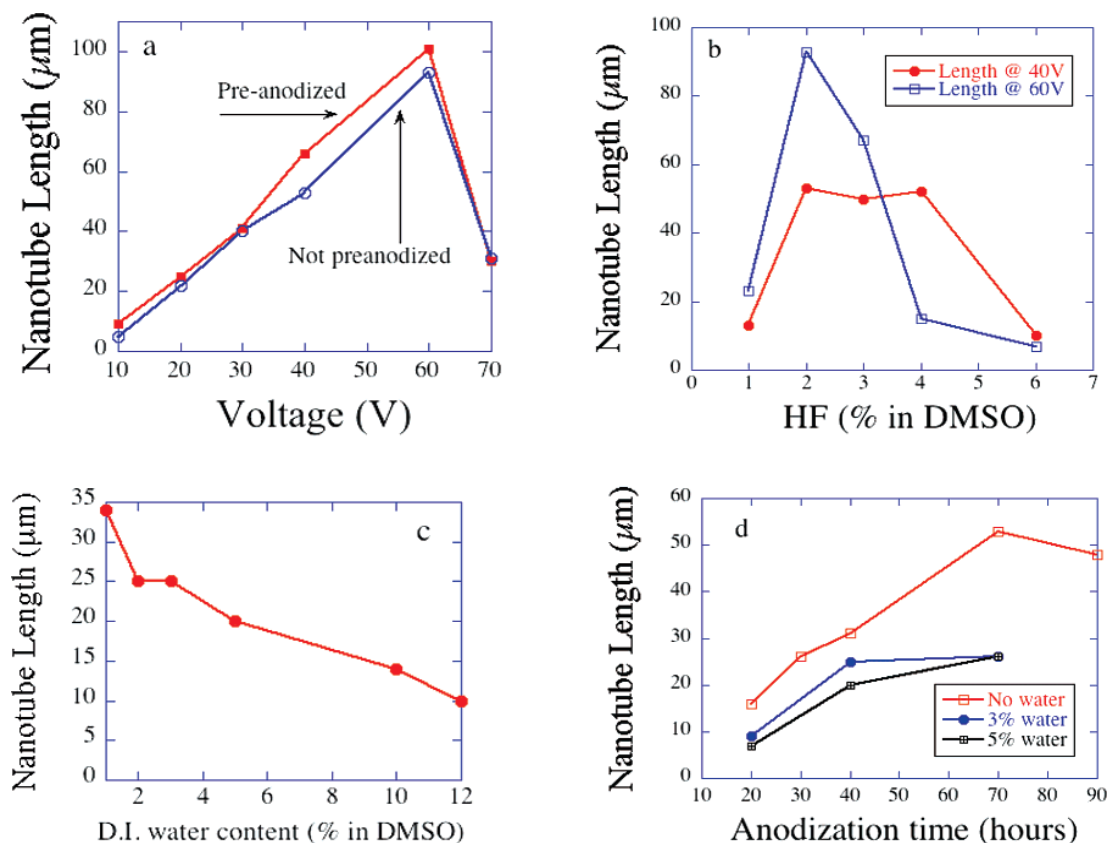


Figure 2-10 TNTAs length as a function of (a) anodization potential for 70 h anodization in 2% HF-DMSO with and without a pre-anodization step, (b) HF concentration in DMSO for 40V and 60 V for 70 h, (c) H<sub>2</sub>O concentration in 2% HF DMSO (at 40 V and 40 h), and (d) anodization duration time for 40 V in 2% HF-DMSO electrolytes with 0%, 3%, and 5% deionized water content (reprinted with permission from ref. [82], ©2006 American Chemical Society).

Figure 2.10 b) indicates that 2% HF concentration was the optimum concentration at which longest nanotubes were obtained at both 40 and 60 V. HF concentration higher than 2% increased the chemical dissolution rate of the tubes resulting in reducing the final nanotube length while low concentration of HF below 2% resulted in very slow growth rate of



nanotubes extending the anodization time required to obtain the same length of TNTAs. The addition of water to the 2% HF–DMSO electrolyte increased the chemical dissolution of TiO<sub>2</sub> and decreased the nanotube length as shown in Figure 2.10 c and d. Figure 2.10 d), also, shows that nanotube length increased with extended anodization time up to 70 h and decreased after 70 h. The reason behind the reduction in length by increasing the time after 70 h is that the nanotube growth rate at the bottom of the tubes becomes slower due to the increased diffusion resistance of both F<sup>-</sup> ions and the reaction products at the tube bottom by increasing the tube length while the dissolution rate of the tubes at the tube mouth may be increased with increasing the conductivity of the electrolyte due to the dissolved Ti ions. This results in the dominance of the dissolution rate and decreasing the nanotube length with time [85]. Anodization in previously used DMSO electrolytes influences the pore size and length of the formed TNTAs and improved the adhesion between the nanotubes and the underlying oxide barrier. The important difference between fresh and used electrolytes is that the used electrolytes have very high conductivity compared to fresh electrolytes, for example, the conductivity of 2 % HF DMSO electrolyte used for anodization of Ti foil at 40 V for 70 h is 100.6 μS/cm compared with 8.76 μS/cm for the fresh electrolyte. Previously used DMSO electrolytes usually produce TNTAs of shorter length if compared with fresh electrolytes. For example, using a fresh 2% HF DMSO electrolyte, 53 μm length TNTAs were obtained after 24 h at 40 V and then, by using the same electrolyte again with other Ti foil for 70 h at 40 V, only 50 μm length TNTAs were obtained. It is worth mentioning that the higher conductivity of used electrolytes was found to be useful in increasing initial nanotube growth rate. In addition,

nanotubes fabricated in used electrolytes do not have debris and have unclogged tubes [82, 85-86].

#### 2.4.2.3 Fabrication of TNTAs in Formamide (FA) and N-Methyl formamide (NMF).

Formamide (FA) and N-methyl formamide (NMF) are both protophilic like DMSO, meaning their acidity nature is weaker than water. Therefore, they provide a more reducing environment than that of water. In addition, they have a high dissolving power for both  $H^+$  and  $F^-$  ions. Furthermore, FA and NMF are highly polar and their dielectric constants are 111 and 182.4, respectively which are much higher than dielectric constant of water, 80. Also, their viscosities are comparable to that of water (3.3 and 1.65 cP for FA and NMF, respectively). The higher polarity of the electrolyte facilitates the dissolving of HF and makes it chemically available in the reaction sites at  $TiO_2$ -electrolyte interface [79]. Few reports were published on fabrication of TNTAs in FA and NMF electrolytes [86-88]). Paulose and co-workers [81] fabricated TNTAs of 70  $\mu m$  long anodized in a FA based electrolyte for 48 h at constant voltage of 35 V. The nanotubes had an average outer diameter of 180 nm and an aspect ratio of 390. The average wall-thickness was about 24 nm. Keeping water content in the anodization organic electrolyte below 5% is crucial to successfully grow long TNTAs [81]. By reducing water content in organic electrolytes, the availability of oxygen for oxide formation is reduced resulting in thinner oxide barrier beneath the nanotube arrays [68]. Furthermore, reducing water content inhibits chemical dissolution of  $TiO_2$  at the mouth of nanotubes in  $F^-$ -containing electrolytes hence assisting growth of longer TNTAs [85]. FA electrolytes used in Ti anodization usually included FA and/or NMF solutions containing 1–5 wt.% of deionized water and 0.3–0.6 wt.%  $NH_4F$

[81, 87, 89]. The potential window in which TNTAs can be grown in FA/NMF electrolytes is from 10 to 50 V which is wider than potential window for both aqueous (10-30 V) and glycerol electrolytes (5-40 V). Increasing anodization potential generally increases both diameter and length of nanotubes -- the same phenomenon which was found in aqueous, DMSO and glycerol electrolytes. The increase in nanotube length with anodization potential is ascribed to the increased driving force for ionic transport through the oxide layer barrier beneath the nanotubes, consequently, resulting in faster movement of the Ti/TiO<sub>2</sub> interface towards the Ti metal. Nanotube length was found to increase with anodization time up to a maximum length. Increasing anodization time after reaching the maximum length decreases the length of nanotubes which may be attributed to the nanotubes cleavage due to chemical dissolution [85]. The effect of the presence of different cations in the water-FA mixture electrolyte was studied by Shankar and co-workers [87]. Five different fluoride compounds, namely; HF, NH<sub>4</sub>F, sodium fluoride (NaF), tetrabutyl ammonium fluoride (Bu<sub>4</sub>NF) and benzyltrimethyl ammonium fluoride (BnMe<sub>3</sub>NF) were the fluoride ion bearing species used to study the effect of the corresponding cations, H<sup>+</sup>, NH<sub>4</sub><sup>+</sup>, Na<sup>+</sup>, Bu<sub>4</sub>N<sup>+</sup> and BnMe<sub>3</sub>N<sup>+</sup>, respectively. Under similar conditions, the nanotube length and aspect ratio increased with increasing the cation size. The longest nanotube arrays (94 μm) were obtained from the electrolyte containing Bu<sub>4</sub>N<sup>+</sup>, while the shortest nanotubes were grown in the electrolyte containing only H<sup>+</sup> cations. The significant difference in nanotubes length was ascribed to the repressive effect of the quaternary ammonium ions which confined the thickness of the barrier oxide layer beneath the nanotube arrays. The thinner the barrier oxide layer the faster the ionic transport through this barrier which increases the nanotube growth rate [87].

#### 2.4.2.4 Fabrication of TNTAs in ethylene glycol (EG)

As mentioned earlier, viscosity of the electrolyte has a direct impact on diffusion of reactants and products to and from the titania nanotubes surface. It is necessary to control diffusion for synthesis of well-organized titania nanotubes; however, there is a certain range out of which the viscosity has negative impact on synthesis and growth rate of titania nanotubes. The growth rate was low in glycerol-based ( $\eta = 945$  cP at 25°C) electrolytes and addition of water improved the growth rate due to the reduction in the viscosity of electrolyte solution. Ethylene glycol (EG) is less viscous ( $\eta = 16$  cP at 25 ° C) compared to glycerol and results in lower diffusion resistance. Therefore, the growth rate would be higher in EG-based electrolytes. The anodization process of titanium to fabricate TNTAs in EG-based electrolytes has two distinctive characteristics [81, 86, 90-91]. First distinctive characteristic is the highly rapid TNTAs growth rate of up to 15  $\mu\text{m}$  per hour which is five times the maximum growth rate of TNTAs formed in FA- or DMSO-based electrolytes and an order of magnitude greater than the growth rate of TNTAs formed in aqueous [78, 92-93] or glycerol based electrolytes [94-95]. In EG-based electrolytes, TNTAs were fabricated within anodization window from 20 to 65 V with water content varying from 1 to 4 vol. % and ammonium fluorides ranging from 0.1 to 0.5 wt.%. At constant voltage of 60 V, 2 vol.% water content and anodization time of 17 h, it was found that the length of TNTAs increased by increasing  $\text{NH}_4\text{F}$  concentration from 0.1 to 0.3 wt.% from 85 to 165  $\mu\text{m}$ . While, when keeping  $\text{NH}_4\text{F}$  concentration at 0.3 wt.% and other parameters unchanged, TNTAs increased from 67  $\mu\text{m}$  to 165  $\mu\text{m}$  by increasing water content from 1 vol.% to 2 vol.% but further increase of water content to 3 vol. % reduced the TNTAs to 136  $\mu\text{m}$  which implies that the optimum condition for production of longest TNTAs is 2

vol. % water content and 0.3 wt.%  $\text{NH}_4\text{F}$  in ethylene glycol. Inner and outer diameters and TNTAs length were found to increase by increasing anodization potential from 20 to 60 V, where inner diameter increased from 45 to 105 nm, outer diameter increased from 65 to 155 nm and tube length increased from 5 to 165  $\mu\text{m}$ , respectively. Further increase of anodization potential to 65 V, resulted in a further increase in both inner and outer diameters to 135 and 185 nm, respectively, but it resulted in a decrease in tube length to 105  $\mu\text{m}$ . This implies that at these conditions, the optimum anodization potential at which longest TNTAs can be obtained is 60 V. The resulting TNTAs lengths showed a power low dependence on the applied potential in the potential range from 30 to 60 V. At 80 V and a variety of electrolyte compositions, Ti foil was merely corroded and no nanotubes were formed [90]. The effect of time on nanotube length was studied at 0.3 wt. %  $\text{NH}_4\text{F}$  and 2 vol. % water content at 60 V anodization potential. Samples were anodized for different intervals, namely, 4, 17, 21, 48 and 96 h. Figure 2.11 shows cross-sectional views of TNTAs obtained at these intervals. The TNTAs lengths were 58, 160, 188, 289 and 360  $\mu\text{m}$  for 4, 17, 21, 48 and 96 h, respectively. The TNTAs lengths fabricated at various anodization times up to 21 h were proportional to the charge passed during those anodization times indicating that the current efficiency was constant and very close to 100%. This implies that there are almost no side reactions during the anodization and the bulk chemical dissolution of formed TNTAs is negligible. The proportionality between the total charge passed and the length of formed TNTAs was also held for anodization potentials lower than 60 V while above anodization potential of 60 V, the current efficiency decreased [90].

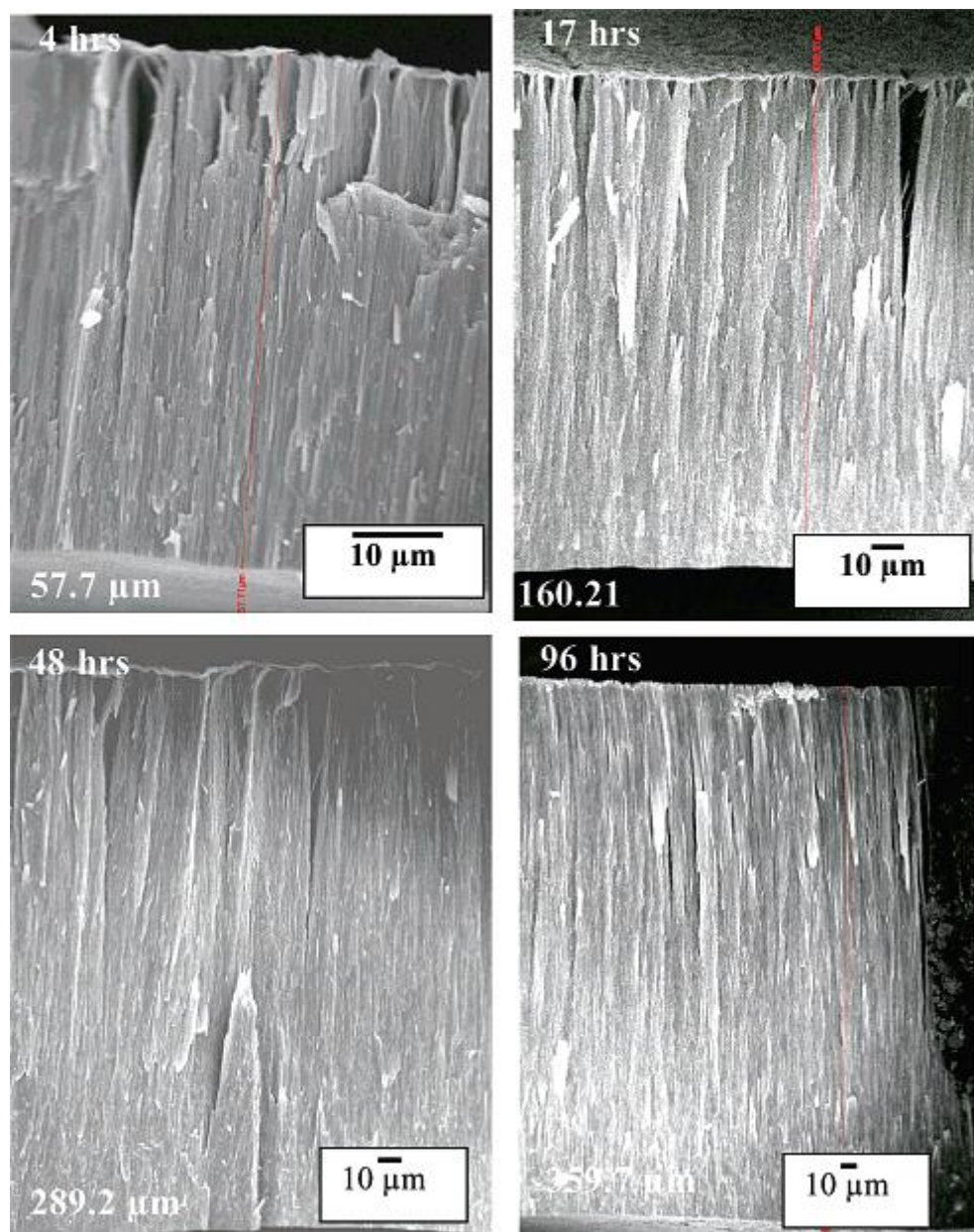


Figure 2-11 FESEM images of cross sectional views indicating the lengths of TNTAs as a function of time at 60 V in ethylene glycol, 0.3 wt. %  $\text{NH}_4\text{F}$  and 2 vol. %  $\text{H}_2\text{O}$ .

(Reprinted with permission from ref. [90], © 2007 American Chemical Society)

## 2.5 TNTAs formation mechanism

The fundamental processes responsible for anodic oxidative formation of nanoporous alumina and titania are the same, and are principal to the formation of straight titania nanotubes [96-97]. These processes are [56, 66, 85, 98]:

- (1) Formation of oxide layer at the surface of the Ti metal takes place due to interaction of the metal with  $O^{2-}$  or  $OH^-$  ions. After the development of an initial oxide layer, these anions move through the oxide layer towards the metal/oxide interface where they react with the Ti metal.
- (2) Metal ion ( $Ti^{4+}$ ) transfer from the Ti metal at the metal/oxide interface by ejection under application of an electric field and migration towards the oxide/electrolyte interface.
- (3) Field-assisted dissolution of Titanium oxide at the oxide/electrolyte interface. Under applied electric potential, the Ti–O bond is polarized and tends to be weak facilitating dissolution of the metal cations.  $Ti^{4+}$  cations dissolve into the electrolyte, and the free  $O^{2-}$  anions transfer towards the metal/oxide interface to interact with the Ti metal.
- (4) Chemical dissolution of the Ti metal, or oxide also occurs due to the acidic electrolyte. Chemical dissolution of titania plays a key role in the formation of TNTAs rather than a nanoporous structure. As mentioned before, the chemical dissolution rate depends on the pH value, which then causes more etching at the pore-bottom than at the opening and at the walls (as illustrated in Figure 2.12).

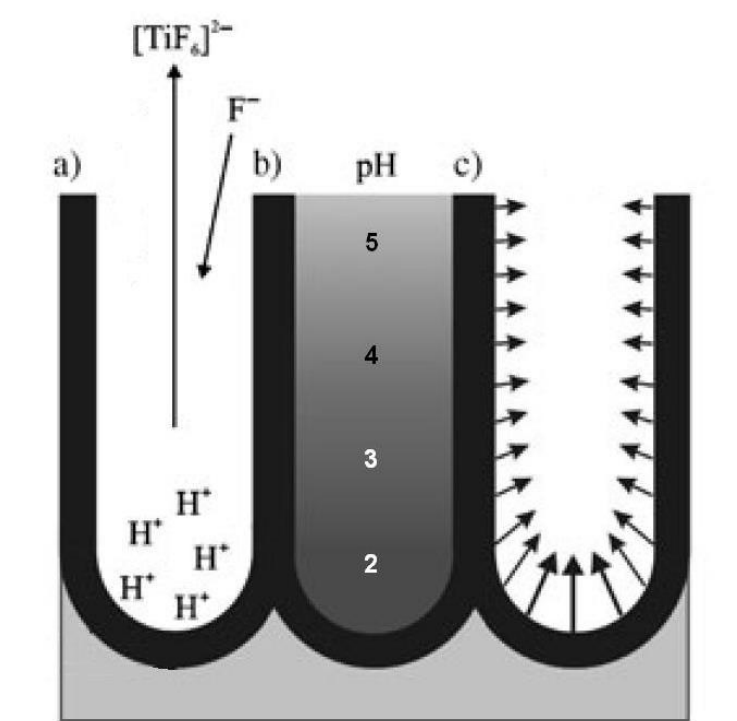
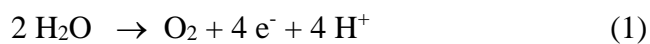


Figure 2-12 The chemical dissolution rate in c), depends on the pH-value as in b), caused by the reaction illustrated in a). (Reprinted with permission from ref. [58], ©2005 Wiley-VCH Verlag GmbH & Co. KGaA, Weinheim).

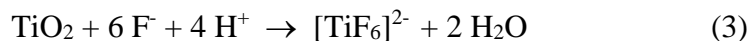
The overall reactions for the anodization process of titanium can be represented as:



In the early stages of the anodization process, field-assisted dissolution dominates chemical dissolution which can be attributed to the relatively large electric field across the thin oxide layer (the resistance to the current is minimum). Small pits form due to the



localized dissolution of the Ti oxide and act as nuclei for pore formation. The formation of these small pits is represented by the following reaction:



Then, these pits convert into larger pores. Subsequently, the pores spread uniformly over the surface. The pore depth increases due to the inward movement of the pore bottom (barrier layer). This occurs due to processes (1) to (3) mentioned above (see Figure 2.13).

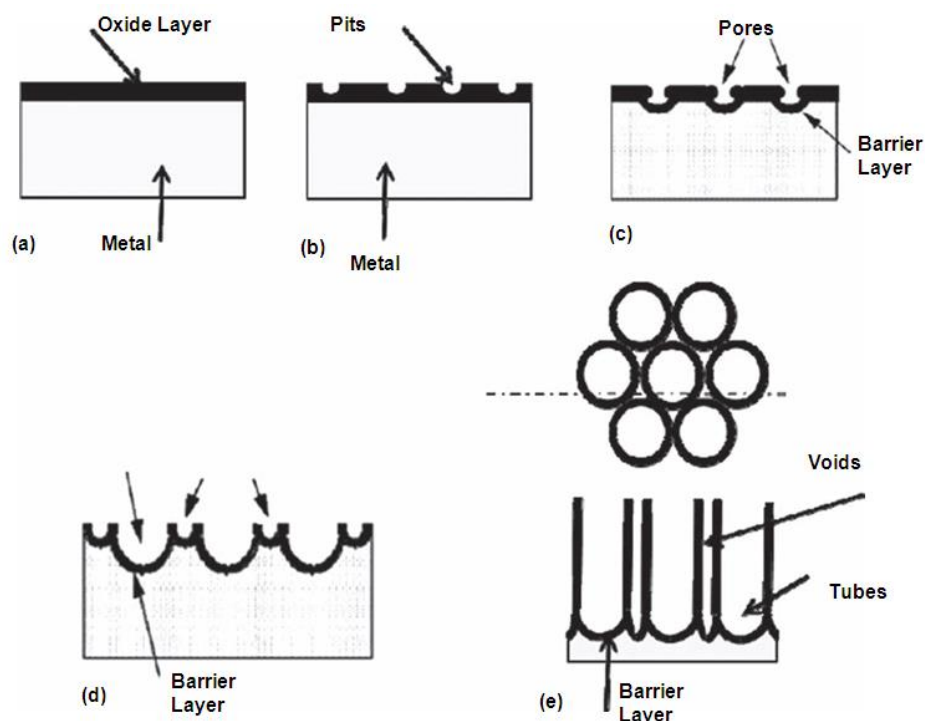


Figure 2-13 Illustrative diagram of the evolution of a nanotube array at constant anodization voltage: (a) oxide layer formation, (b) pit formation on the oxide layer, (c) growth of the pit into scallop shaped pores, (d) metallic part between the pores undergoes oxidation and field assisted dissolution, and (e) fully developed nanotube array with a corresponding top view. Redrawn with permission from ref. [56], © 2006 Elsevier B. V.

All rights reserved.

Although the formation mechanism was originally proposed for the generation TNTAs fabricated in low pH HF aqueous electrolytes, it still holds for all organic electrolytes discussed above in Section 3.2 considering the following differences:

1. Using organic electrolytes with low water content, the inhibiting organic medium and low oxygen availability hinder the growth of oxide layer barrier thickness beneath the nanotube arrays which help increase the transfer rate of different ionic species across this oxide layer barrier and consequently, increase the nanotube growth rate.
2. The corrosion-inhibiting organic medium at low water content minimizes the chemical dissolution rate of  $\text{TiO}_2$  at the nanotubes mouths which increases the nanotube growth rate and enhances the electrical current efficiency.
3. Replacing the strong acidic HF aqueous electrolytes with near-neutral fluoride salts electrolytes such as  $\text{NH}_4\text{F}$  and  $\text{KF}$ , minimizes the chemical dissolution rate of  $\text{TiO}_2$  nanotubes.
4. Although high viscous glycerol electrolyte helps widen the pH gradient across the nanotube length (see Figure 2.12) which increases the nanotube growth at the bottom and decreases the chemical dissolution rate at the nanotubes mouths, the low transfer rate of different ionic species through the electrolyte due to high viscosity results in a relatively low growth rate of nanotubes if compared with other organic electrolytes such as DMSO and ethylene glycol [78].
5. The anodization potential window within which TNTAs can be fabricated is a characteristic of the electrolyte and depends on its chemical and physical properties. For aqueous electrolytes, the potential window for TNTAs fabrication was found

to be within 10-30 V with an optimum potential of 20-25 V [62], whereas for organic electrolytes, the potential window tends to be wider: for glycerol electrolyte (1-40 V) [78], for DMSO (10-70 V) [82] and for ethylene glycol from 20 to 65 V with a maximum growth rate at 60 V [90].

## 2.6 Modification of TNTAs Electronic and Photoelectrochemical Properties

### 2.6.1 Non-metal doping

The electronic structure of a semiconductor (e.g. band gap value as well as the level of valence and conduction bands) plays a key factor in semiconductor photoactivity. A semiconductor comprises of energy valence band (VB) and energy conduction band (CB). The energy difference between these two bands is known as band gap energy or band gap ( $E_g$ ). Electrons in VB are excited to CB when absorb photons with energy equal or higher than  $E_g$ . The valence band maximum edge of titania mainly comes from the oxygen 2p orbitals and the conduction band minimum edge comes from the 3d orbitals of titanium. The electrons transitions from the dopants 2p or 3p orbitals to the 3d orbitals of titanium generally results in optical properties modifications [99]. Highly-ordered, vertically-oriented, high surface area titania nanotube arrays are ideal for water photolysis and photocatalytic degradation of wide range organic substances due to high catalyst/electrolyte interface area, electrolyte percolation and highly efficient charge transfer [56].  $\text{TiO}_2$  nanotube arrays demonstrate quantum efficiency exceeding 80% under UV illumination for water photolysis [100]. However, the widespread application of  $\text{TiO}_2$  is limited by its wide band gap ( $\sim 3.2$  eV) which is photoresponsive only under UV illumination. Because UV portion accounts for only about 5% of the solar spectra while

visible light accounts for about 45%, any shift in photoactivity of TiO<sub>2</sub> from UV toward visible light region increases the photoconversion efficiency and therefore has a positive impact on photocatalytic and photoelectrochemical applications of the materials [56, 98]. In order to resolve the above problem and modify the electronic structure of TiO<sub>2</sub> to narrow its band gap, non-metals such as carbon [101], nitrogen [102-103], phosphorous-fluorine [104] and nitrogen-fluorine-iodine [105] have recently been doped into TiO<sub>2</sub> and proved significant enhancements in visible light photoactivity of the material.

Asahi and co-workers [106] calculated densities of states (DOSs) of the substitutional doping of N, C, F, P and S for O in anatase TiO<sub>2</sub> and found that when mixing p states of N with 2p of O in the substitutional doping of N, valence band (VB) edge shifted upwards leading to narrower band gap of TiO<sub>2</sub>. Although doping of S resulted in a similar band gap narrowing, the ionic radius of S was found to be too large to be introduced into TiO<sub>2</sub> lattice as proved by larger formation energy needed for the substitution of S than that needed for the substitution of N. N-doped TiO<sub>2</sub> films were prepared by sputtering TiO<sub>2</sub> in N<sub>2</sub> (40%)/Ar gas for 4 h and the films were a mixture of anatase and rutile crystal phases. It is worth mentioning that authors of this study [106] set the following requirements to introduce visible-light photoactivity by doping: 1) doping should introduce states in the band gap of TiO<sub>2</sub> that absorb visible light photons; 2) The conduction band minimum (CBM), after doping, should be as high as that of TiO<sub>2</sub> or higher than the potential level of H<sub>2</sub>/H<sub>2</sub>O to secure the photoreduction activity; and 3) the introduced states in the gap should overlap adequately with the band states of TiO<sub>2</sub> to carry over the photoinduced electrons to reactive

sites at the surface within their lifetime. Requirements 2 and 3 are most likely achieved when using non-metal doping rather than metal doping [106, 107].

The densities of states (DOS) calculations conducted by Asahi and co-workers [106] proved that the substitutional doping of N for O site was expected to be the most effective among other non-metal dopants considered because the nitrogen p states placed just above the valence bands maximum (VBM) of TiO<sub>2</sub> may contribute to the band gap narrowing without noticeable increase of the carrier recombination. Experimental investigation of nitrogen doped TiO<sub>2</sub> conducted by Chen and co-workers using X-ray photoelectron spectroscopy confirmed the findings of Asahi study [108].

A huge number of publications have been reported on the photocatalytic properties of N-doped TiO<sub>2</sub> under visible-light [107, 1089-115]. N-modified TNTAs were synthesized by annealing the as-prepared amorphous TNTAs at 400 °C in the presence of urea pyrolysis gaseous products [116]. In contrast to the pure TNTAs, modified TNTAs demonstrated photocurrent under visible light illuminated. For the pure TNTAs, the photocurrent disappeared at wavelengths > 400 nm, which corresponds to anatase band gap, E<sub>g</sub>, of 3.2 eV. While N-modified TNTAs demonstrated photocurrent down to wave length of 750 nm showing strong response in visible light region. N1s X-ray photoelectron spectroscopy (XPS) spectra of modified TNTAs showed two sub-peaks at 400.1 eV and 398.2 eV which can ascribed to C-N=C and C-NH<sub>2</sub> species [116-117]. Vetiello and co-workers [102] synthesized TNTAs in HF/H<sub>2</sub>SO<sub>4</sub> aqueous electrolyte under anodization potential of 20 V for 2 h. The produced TNTAs were of an average inner diameter of 100 nm, wall thickness

of 15 nm and tube length of 500 nm. To induce nitrogen doped TNTAs, some samples were annealed in pure ammonia atmosphere at temperature 600°C, where other samples were annealed in air at 450°C and 600°C for comparison. The ammonia-treated TNTAs exhibited photocurrent in the visible light range up to 525 nm while the other two samples annealed in air at 450 and 600°C did not demonstrate photocurrent in wave length range above 400 nm. The photocurrent of NH<sub>3</sub>-treated TNTAs is attributed to the introducing of nitrogen doping of TNTAs which was confirmed by XPS spectra peak at 395.8 eV which corresponds to atomic nitrogen in form of mixed titanium oxide-nitride [102, 118]. N-doped TNTAs were also synthesized by annealing the as-anodized TNTAs in ammonia gas atmosphere at 500°C [119]. In this study, the nanotubular structure was found to remain unchanged after annealing. X-ray diffraction and Raman spectra demonstrated the presence of both anatase and rutile phases in the N-doped TNTAs as well as the non-doped TNTAs but the XRD spectra of the nitrogen-doped TNTAs showed increased peak intensity in the rutile (110) peak and an emerging (210) rutile peak implying that nitrogen doping could have enhanced the phase transition from anatase to rutile at lower annealing temperature [119-120]. The photocatalytic degradation of methyl orange using nitrogen doped TNTAs was shown to be evidently higher than that of undoped TNTAs which may be ascribed to the role of nitrogen doping in band gap,  $E_g$ , narrowing [121]. During anodization process, Ti metal foil is positively biased against Pt cathode. Under the effect of this positive bias, negative ions will move toward the anode surface and get oxidized and some of these atoms may be incorporated into the growing TiO<sub>2</sub> layer. Nitrogen atoms may be incorporated into growing TNTAs by adjusting the electrolyte composition so that only nitrogen and fluoride containing species are added into anodization electrolyte. Shankar and co-workers prepared

nitrogen-doped TNTAs in one anodization step in 0.07 M HF aqueous electrolyte containing varying concentrations of  $\text{NH}_4\text{NO}_3$  from 0.2 to 2.5 M for various anodization times ranging from 17 s to 6 h. XPS spectra showed formation of  $\text{TiO}_{2-x}\text{N}_x$  with maximum value of  $x=0.23$  in sample anodized for only 17 s with decreasing until reaching  $x=0.02$  for sample anodized for 6 h. Unfortunately, at very short anodization times such as 17 s, there are no nanotubes formed. Only thin oxide layer with small pits and pores appearing on it was formed. With a complete formed TNTAs after 6 h and  $x=0.02$ , the absorption edge was slightly shifted from around 400 nm to 423 nm whereas for sample anodized for 17 s (no nanotubes were formed), and  $x=0.23$ , the absorbance shift was from 400 nm to 510 nm. The nitrogen doping and TNTAs formation were found to be competing process [122].

In 2010, Xu and co-workers [123] reported a new approach for N-doped TNTAs. They immersed short amorphous TNTAs, previously prepared by anodization in 0.1 M HF and 1 M  $\text{H}_2\text{SO}_4$  aqueous electrolyte for 60 min. at 20 V, in hydrazine hydrate (80 %) for 6 h and then dried in air at 110°C. The dried TNTAs were annealed at 450°C for 3 h to crystallize amorphous TNTAs to anatase phase. Nitrogen content of hydrazine-treated crystalline TNTAs was determined using EDX characterization. The atomic ratio of N/Ti was 8/25. Photocurrent of hydrazine-treated nitrogen-doped TNTAs was found to be double that of untreated TNTAs (samples annealed in air at 450°C for 3h without immersing in hydrazine hydrate). The photocurrent of N-doped TNTAs was 182  $\mu\text{A}$  while it was only 92  $\mu\text{A}$  for undoped TNTAs. The UV-Vis diffuse reflectance spectra of nitrogen doped and un-doped TNTAs showed a clear red-shift in the absorption edge for doped TNTAs and a band gap value for nitrogen-doped TNTAs of 3.04 eV (corresponding to wavelength of 408 nm) compared to 3.26 eV (corresponding to wavelength of 380 nm) for

un-doped TNTAs. In addition, n-doped TNTAs exhibited a higher visible light absorbance (from 400-450 nm). The photocatalytic activity of N-doped and un-doped TNTAs was investigated by the degradation of reactive brilliant X-3B dye. The degradation percent of X-3B was 59 % using un-doped TNTAs in photocatalysis, while it was 99 % when N-doped TNTAs was used. The apparent first order rate constant ( $k_{app}$ ) of photodegradation of the X-3B dye was  $0.04 \text{ min}^{-1}$  for N-doped TNTAs whereas it was only  $0.009 \text{ min}^{-1}$  for un-doped TNTAs [123]. Although the EDX spectra did not show doped nitrogen atoms inside the  $\text{TiO}_2$  lattice, the UV-Vis diffuse reflectance spectra, photocurrent enhancement and the increase in photodegradation efficiency of hydrazine-treated TNTAs all proved the effectiveness of this approach to enhance the visible light activity of TNTAs.

Aqueous electrolyte containing 1/12 M oxalic acid and 0.5 wt. %  $\text{NH}_4\text{F}$  was employed to prepare N- and F- co-doped TNTAs by Su and co-workers [124]. The prepared TNTAs were annealed at  $400 \text{ }^\circ\text{C}$  to induce anatase crystalline phase. The incorporation of N and F atoms into TNTAs crystal lattice was verified by XPS spectra peaks of 401.9 eV and 396.25 eV for N1s and 686.4 eV and 688.5 eV for F1s, respectively. The large peak of 401.9 eV was ascribed to adventitious  $\text{N}_2$  and  $\text{NH}_3$  adsorbed on  $\text{TiO}_2$  surface whereas the peak of 396.25 eV was attributed to the presence of Ti-N bonds formed by replacing O atoms in  $\text{TiO}_2$  lattice. The F1s peak at 686.4 eV was ascribed to  $\text{TiOF}_2$  while the peak at 688.5 eV may belong to Ti-F bonds [124-125]. Preparation of N- and F-co-doped TNTAs in one anodization step followed by annealing in either  $\text{N}_2$  or air atmosphere was also reported by [126]. They used electrolyte consisted of glycerin:water (9:1 volume ration) containing 0.36 M  $\text{NH}_4\text{F}$  and 0.25 M  $\text{NH}_4\text{Cl}$  for TNTAs formation at anodization potential of 20 V



and then annealed as-prepared TNTAs at 500°C in a flow of nitrogen. XPS spectra confirmed both nitrogen and fluorine doping by the presence of peaks at 397 and 687.7 eV which attributed to Ti-N and Ti-F bonds, respectively. N- and F- co-doped TNTAs both annealed in air and nitrogen flow showed an enhanced absorbance in the whole visible light region but the one that annealed in nitrogen flow showed higher absorbance than that annealed in air. This may be attributed to the resubstitution of dopants by oxygen when annealed in air resulting in lower dopants concentration. The N-, F-co-doped TNTAs exhibited a high degradation rate of methyl blue (MB) under visible light illumination leaving only 19% of the initial concentration of MB after 2 h irradiation, compared to 60% of the initial concentration left in case of un-doped TNTAs [126]. Ghicov and co-workers reported the preparation of N-doped TNTAs using ion implantation [127]. The approach was to first anneal as-prepared TNTAs at 450°C for 3 h in air to induce the crystalline phase then implant nitrogen ions into the crystallized TNTAs using a multipurpose implanter at 60 keV accelerating energy and a nominal dose of  $1 \times 10^{16}$  ions.cm<sup>-2</sup>. Finally, the N-implanted TNTAs were reannealed again at 450°C for 3 h in air to reform the structure damage that might have happened during ion implantation process. Photocurrent measured for samples after first annealing without ion implantation was only below 400 nm wavelength. The photocurrent measured after ion implantation was also below 400 nm, but its value was very small compared to the photocurrent measured before N-implantation process. The loss in photocurrent after ion implantation process was ascribed to the huge damage to the crystal structure caused by ion implantation process. After reannealing at 450°C for 3 h in air, the damage was reformed and photocurrent spectra exhibited an

increase in the value in the range below 400 nm and an extension up to 550 nm which corresponds to a sub band gap of 2.2 eV [127].

Since the very publicized report by Khan and co-workers in 2002, many attempts have been made to decrease the band gap energy of TiO<sub>2</sub> by carbon doping [55, 101,128-131]. The most common approach for synthesis of a carbon-doped TiO<sub>2</sub> film is by direct oxidation in a burning flame [101, 132]. Although flame annealing method exhibited enhanced absorbance in visible light region as well as enhanced photocurrents, a substantial damage occurred in the TNTAs resulting in a subsequent decrease in the overall performance. C-doped TNTAs were prepared by reannealing the crystalline anatase phase TNTAs in CO gas flow at temperatures ranging from 500 to 800 °C. Although the carbon content ranged between 8 and 42 atoms% according to XPS results, no appreciable peak was found at 281.5 eV meaning that there was no Ti-C bonding [55].

Very interestingly, fabrication of TNTAs in organic electrolyte such as ethylene glycol-based electrolyte and then annealing in a reducing atmosphere (H<sub>2</sub> gas flow) helped introducing carbon dopant from the reduced ethylene glycol to give a C-doped TNTAs with a modified band gap of 2.2 eV [51]. Carbon-modified TNTAs were also obtained by annealing as-anodized TNTAs at 550 °C under an argon and acetylene gas mixture (9:1) flow for 1 h. XPS spectra of carbon modified TNTAs exhibited a peak at 288.9 eV which can be ascribed to the carbon existing in the form of interstitial atoms which come from the diffusion of carbon atoms into the TNTAs lattice during carbon modification process [133]. Figure 2.14 shows that the absorbance edge of carbon-modified TNTAs was shifted towards the visible light region compared to the un-modified TNTAs. Photoactivity of carbon-modified TNTAs was evaluated by photodegradation of methyl blue under the sun

light irradiation. Figure 2.15 shows the change in MB concentration with irradiation time using un-modified TNTAs, carbon-modified TNTAs and without any TNTAs (just photofading under sun light irradiation). The large enhancement of photoactivity after carbon-modification is very clear from Figure 2.15. The MB is almost completely removed by photodegradation after 300 min. using carbon-modified TNTAs whereas only 18 % and 9 % were removed after 300 min using un-modified TNTAs and without any catalyst, respectively [133].

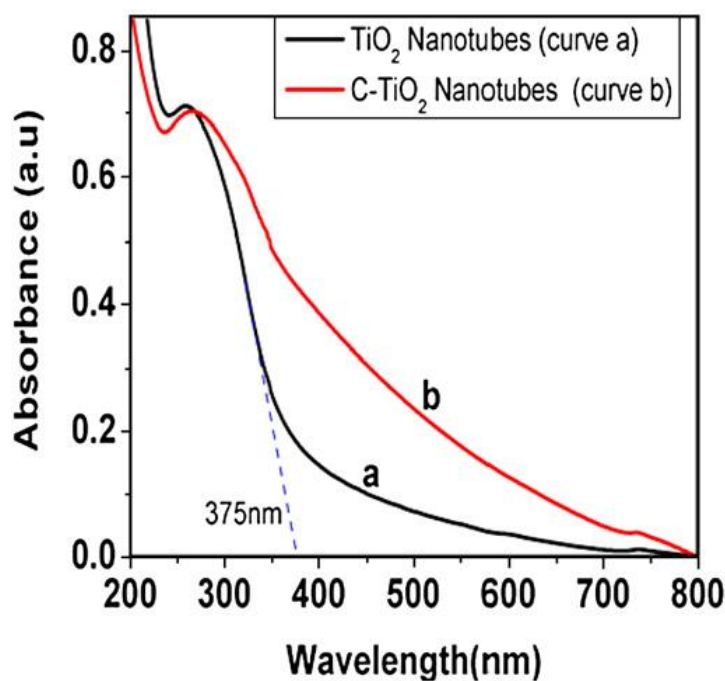


Figure 2-14 UV-vis absorption spectra of TNTAs and carbon –modified TNTAs reprinted from [133] © 2008 Elsevier B. V. all rights reserved

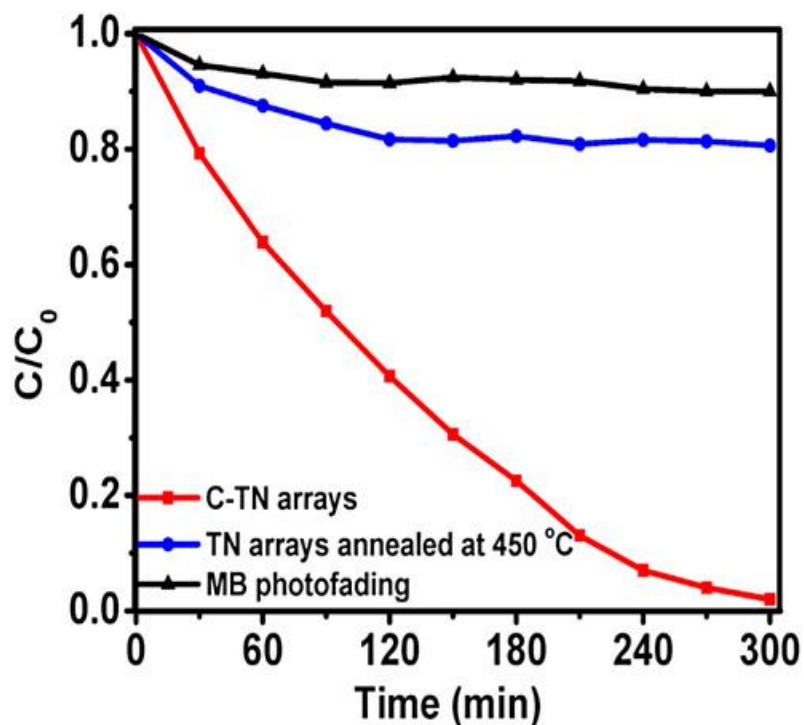


Figure 2-15 Change of MB concentration with irradiation time under different photocatalysts (reprinted from [133] © 2008 Elsevier B. V. all rights reserved)

Boron doping was found to enhance the performance of TNTAs. Lu and co-workers [134] prepared B-doped TNTAs by chemical vapor deposition. The as-anodized TNTAs was first annealed at 450°C in oxygen for 3 h to be converted to anatase phase, then Boron doping process was carried out using chemical vapor deposition (CVD). The boron source was trimethyl borate and N<sub>2</sub> was used as a carrier gas. Chemical vapor deposition (CVD) process was carried out at 600°C for 40 min. The XPS spectra for B-doped TNTAs exhibited a binding energy peak at 192 eV which lies between the standard binding energy for Ti-B in TiB<sub>2</sub> (187.5 eV) and the binding energy for B-O in B<sub>2</sub>O<sub>3</sub> (193.1 eV); implying that the boron atoms could be probably incorporated into TNTAs crystal lattice and boron might exist as Ti-B-O [59, 134]. Although UV-vis spectra for B-doped TNTAs revealed

small absorption edge shift toward visible light region (from 385 nm to 405 nm), compared with the large shift occurred in N-doping and C-doping, there is enhancement in the light absorbance in UV region implying an enhancement in the photocurrent and photoconversion efficiency under UV irradiation. B-doped TNTAs exhibited photocurrent density 60% higher than un-doped TNTAs and maximum 31.5% photo-conversion efficiency compared to only 16% for un-doped TNTAs under UV irradiation [134-136]. Although introducing sulfur into  $\text{TiO}_2$  lattice as dopant narrows band gap similar to nitrogen doping, the large ionic radius of sulfur would make it more difficult to incorporate it into the  $\text{TiO}_2$  crystal which is proved by the much higher formation energy necessary for the sulfur substitution than that required for nitrogen substitution [106]. Tang and Li [137] prepared sulfur-doped TNTAs by annealing as-anodized TNTAs at  $380^\circ\text{C}$  for 14 h under  $\text{H}_2\text{S}$  flow at 10 mL/min. XPS studies of sulfur-doped TNTAs showed the presence of two distinctive peaks of S2p at 167.70 and 163.88 eV. The higher peak was ascribed to surface adsorbed  $\text{SO}_2$  according to Umebayashi and co-workers [138] and Sayago and co-workers [139], while the lower peak at 163.88 eV was attributed to mixed state such as S-Ti-O according to [135]. Figure 2.16 shows the UV-vis spectra of sulfur-doped TNTAs and undoped annealed TNTAs. As shown, sulfur-doped TNTAs demonstrate a strong responsiveness over the whole visible light region which is reflected on the large enhancement in photocurrent compared to the un-doped TNTAs [137].

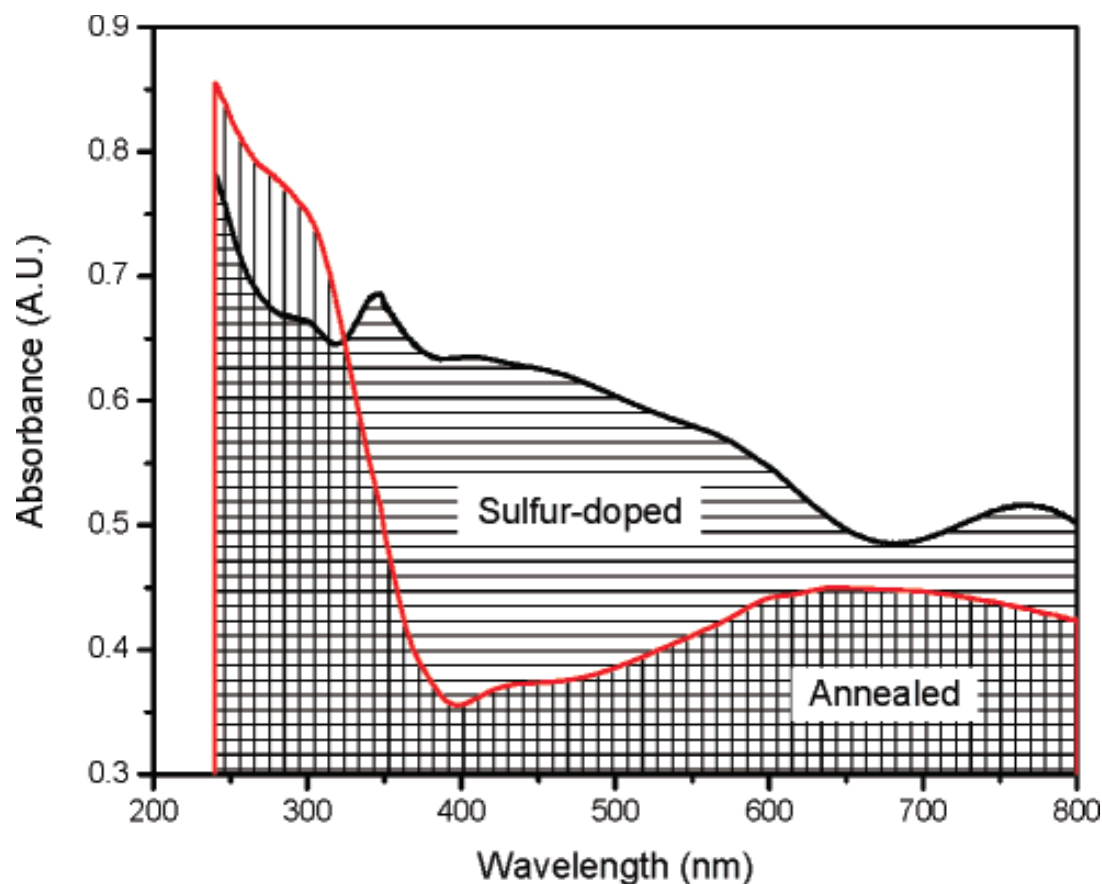


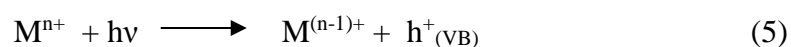
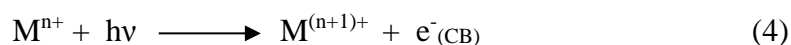
Figure 2-16 UV-vis DR spectra of sulfur-doped TNTAs and un-doped annealed TNTAs  
(reprinted from ref. [137], © 2008 American Chemical Society)

Silicon-dopant was successfully incorporated to TNTAs using chemical vapor deposition method by Su and co-workers [140]. The as-anodized TNTAs were first annealed at 450°C for 3 h to convert the amorphous phase to anatase crystalline phase. Then the crystalline TNTAs were subjected to CVD treatment. Tetraethylorthosilicate, (TEOS), carried by Ar gas was admitted to the tube furnace as a silicon source at 500°C for 15 min. the silicon concentration in the carrier gas was about 156 mg L<sup>-1</sup>. After CVD process, the TNTAs were reannealed at 650°C for 30 min. XRD patterns for Si-doped TNTAs and un-doped TNTAs which were treated at the same conditions except CVD process, indicated that Si-

doping was inhibiting the crystallite growth and the anatase-to-rutile phase transformation at high annealing temperatures. The reason behind these phenomena is attributed to the presence of the amorphous silica phase. The UV-vis DRS showed a blue shift in band gap due to Si-doping where the band gap absorption edge for Si-doped TNTAs was 375 nm (corresponding to 3.62 eV) and for un-doped TNTAs was 388 nm (corresponding to 3.32 eV). The blue shift in band gap absorption edge of Si-doped TNTAs showed photocurrent spectra 1.5 times higher than the un-doped TNTAs under UV irradiation. The enhancement of photoresponse of Si-doped TNTAs was also confirmed by the increase in photoelectrochemical degradation of PCP under UV irradiation with a degradation kinetic constant of  $1.22 \text{ h}^{-1}$  which was 84.8 % higher than that of un-doped TNTAs [140].

### 2.6.2 Metal Ions Doping

Doping of  $\text{TiO}_2$  nanoparticles with transitional metal ions and rare earth metal ions to improve the  $\text{TiO}_2$  photocatalytic performance have been extensively investigated [115, 141-143]. Metal ions doping can expand the photo-responsiveness of  $\text{TiO}_2$  into visible light spectrum. Due to metal ions incorporation into the  $\text{TiO}_2$  lattice, extrinsic energy levels in the band gap of  $\text{TiO}_2$  are formed, according to the following equations [115]:



where  $M$  and  $M^{n+}$  represent metal and metal ion dopant, respectively,  $h\nu$  is the energy of a single photon where  $h$  is the Planck constant ( $= 6.626 \times 10^{-34}$  kg.m<sup>2</sup>/s) and  $\nu$  is the frequency in Hz or s<sup>-1</sup>,  $e^-_{(CB)}$  electron charge at conducting band and  $h^+_{(VB)}$  positive charge (hole) at valence band. It is very important to understand that the electron (hole) transfer between metal dopant and TiO<sub>2</sub> may also increase the rate of electron/hole recombination. The energy level of metal ion reduction should be less negative than the conduction band edge of TiO<sub>2</sub> while the energy level of metal oxidation should be less positive than the valence band edge of TiO<sub>2</sub>. Metal ions dopants should exist near titania surface to facilitate charge transferring. Deep metal ions dopants act as recombination centers. Additionally, there is an optimum concentration for each metal dopant above this concentration the photocatalytic performance decreases because of the increase in electron/hole recombination process [115, 141, 144-145]. It should be recognized that in contrast to metal doping of TiO<sub>2</sub> nanoparticles, metal ions doping of TNTAs is more difficult as one should choose carefully the doping method that introduces the metal ions efficiently into TNTAs crystal lattice and at the same time not damage the highly organized nanotubular structure. Yang and co-workers [146] prepared Zn-doped TNTAs by immersing TNTAs in Zn-containing solution for hours then annealing samples at 400 °C for 3 h. The incorporation of Zn<sup>+</sup> was concluded only from FESEM images and HRTEM observations of Zn-doped TNTAs. The powerful XPS investigation did not clarify the chemical state of zinc ions [146]. Liu and co-workers [147] employed an electrochemical strategy to fabricate Zr-doped TNTAs. After short TNTAs were formed by anodization in aqueous electrolyte containing 0.14 M NaF and 0.5 M H<sub>3</sub>PO<sub>4</sub>, the formed TNTAs and platinum electrode were used as a cathode and anode, respectively, in an electrolyte of 0.1 M Zr



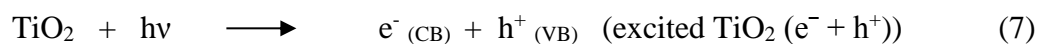
(NO<sub>3</sub>)<sub>4</sub> for preparation of Zr-doped TNTAs at varying electric potentials ranging from 3 to 15 V and post annealing temperatures ranging from 400 to 700°C. Zr and Ti have similar atomic radii (Ti, 2 Å, Zr, 2.16 Å) and they are both IV B elements and tetravalent (+4) elements. Thus, it is possible to introduce Zr atoms into TiO<sub>2</sub> lattice. XPS spectra demonstrated a peak at 182 eV which is ascribed to the presence of Zr in the TiO<sub>2</sub> lattice but the UV-vis DRS did not show any difference between Zr-doped TNTAs and pure TNTAs. Photocatalytic degradation of rhodamine B using Zr-doped and un-doped TNTAs exhibited an enhancement due to Zr-doping [147]. W-doped TNTAs was prepared by a one anodization step of 3% tungsten titanium alloy foil in 0.5 % HF containing ethylene glycol at 60V. The UV-Vis DRS of the produced W-doped TNTAs showed a red shift in the absorbance edge and a reduction in band gap about 0.14 eV which resulted in an increase of photocurrent density compared to the un-doped TNTAs [148]. Cr-doped TNTAs prepared by ion implantation method exhibited a significant enhancement in photocurrent response in both UV and visible light regions [149].

Many studies have focused on iron ion doping to TiO<sub>2</sub> nanoparticles or nanoparticulate films including preparation methods, characterization, charge transport and recombination dynamics, and photocatalytic performance [150-156]. Adan and co-workers [153] reported that the presence of iron shifts the absorption edge of TiO<sub>2</sub> towards the visible region and this red shift increases with increasing the iron content, consistent with the changes in the samples color from white to yellow or light brown. The enhanced absorbance of Fe-doped TiO<sub>2</sub> in visible light region could be ascribed to the excitation of 3d electrons of Fe<sup>3+</sup> to the conduction band of TiO<sub>2</sub> resulting in a band centered at ca. 400 nm [151, 157]. The wide red shift of absorbance edge to ca. 500 nm which particularly appeared at high Fe content

(5.1 %) was attributed to the d-d transitions of  $\text{Fe}^{3+}$  or the charge transfer between the Fe ions due to the following reaction [151, 158].



To explain how the reaction in eq. (6) can occur in Fe-doped TNTAs electrode under UV-visible light irradiation, the following reactions were proposed by Sun and co-workers [159]:



Where,  $h\nu$  is the energy of a single photon,  $h$  is the Planck constant ( $= 6.626 \times 10^{-34}$ ) and  $\nu$  (nu) is the frequency in Hz or  $\text{s}^{-1}$ ,  $e^-_{(\text{CB})}$  electron charge at conducting band and  $h^+_{(\text{VB})}$  positive charge (hole) at valence band. Equations 8 and 9 explain that  $\text{Fe}^{3+}$  may behave either as an electron or a hole trap, depending on the favorable energy levels (see Figure 2.17); consequently, photogenerated charges are separated more effectively. Furthermore,

the electrons trapped in  $\text{Fe}^{3+}$  sites may transfer to the molecular oxygen more rapidly [160-161].

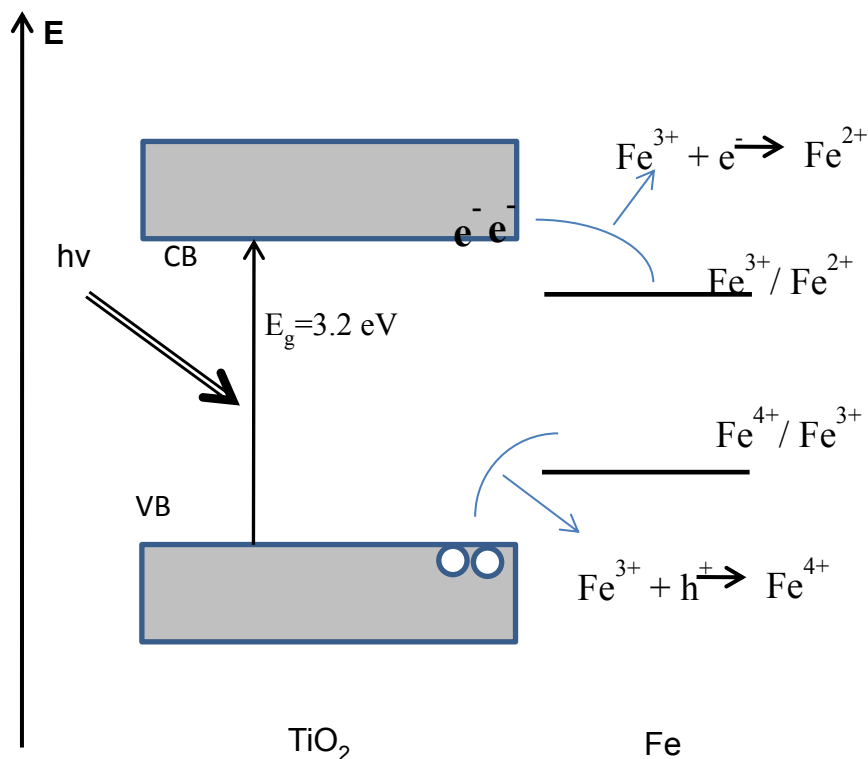


Figure 2-17 Illustrative diagram for the charges transfer in Fe-doped  $\text{TiO}_2$

There are very few reports about Fe-doped TNTAs. Sun and co-workers [159] prepared  $\text{Fe}^{3+}$ -doped TNTAs by anodization of Ti foil in HF-aqueous electrolyte containing ferric nitrate. The TNTAs were very short (only 220 nm length), with an average inner diameter of 50 nm and wall thickness of 10 nm. The concentration of ferric nitrate was found to affect the TNTAs formation which means that an appropriate concentration of ferric nitrate must be chosen to obtain regular uniform nanotubes. XPS spectra coupling with Raman spectra confirmed that the presence of  $\text{Fe}_2\text{O}_3$  dispersed uniformly in the bulk of TNTAs. The Fe-doped TNTAs prepared in electrolyte containing 0.1 M ferric nitrate exhibited the

highest photocatalytic activity with apparent first order rate constant of  $0.972 \text{ h}^{-1}$  for MB photodegradation under a 365 nm UV light irradiation which was 80% higher than undoped TNTAs [159]. Li and co-workers [162] prepared Fe-doped TNTAs by anodization of Ti foil in  $\text{F}^-$  containing aqueous electrolytes containing ferrous sulfate. The prepared Fe-doped TNTAs were about 500 nm in length, a tube diameter of 90 nm and a wall thickness of 13 nm. The as-anodized TNTAs were annealed at  $450^\circ\text{C}$ . The photocurrent spectra and UV-vis DR spectra confirmed the extension of photoresponse of Fe-doped TNTAs to visible light region with a calculated band gap of 2.9 eV [162]. Although, there was an enhancement in photocurrent due to the introducing of Fe dopant into TNTAs by Sun and co-workers [159] and Li and co-workers [162], the photocurrent densities were very low about several  $\mu\text{A}$  which can be attributed to the low surface area of the short TNTAs produced in aqueous electrolyte compared to the high surface area of long TNTAs of the third and fourth generations which are prepared in organic electrolytes. Another synthesis route for preparing  $\text{Fe}_2\text{O}_3$ -modified TNTAs was reported by Kuang and co-workers [163]. First, TNTAs of a 340 nm length and inner diameter of 90 nm was fabricated by anodizing Ti foil in an aqueous electrolyte containing 0.1 M NaF and 0.5 M  $\text{NaHSO}_4$  for 3 h at a potential of 15 V. Then TNTAs electrode was immersed in turn in  $\text{FeCl}_3$ , NaOH and  $\text{H}_2\text{O}$  for 5 min each time and this immersion cycle was repeated four times. The as-anodized amorphous TNTAs have positive charges on their surface, so that  $\text{OH}^-$  groups can be easily absorbed on the surface by electrostatic forces during the immersion process in NaOH solution. Then the rich  $\text{OH}^-$  TNTAs were immersed in  $\text{FeCl}_3$  aqueous solution in which the  $\text{OH}^-$  groups on TNTAs surface can easily combine with  $\text{Fe}^{3+}$  to form  $\text{Fe}(\text{OH})_3$ . After the four immersion cycles completed,  $\text{Fe}(\text{OH})_3$ -TNTAs were annealed at  $550^\circ\text{C}$ . The

amount of  $\text{Fe}_2\text{O}_3$  loaded on TNTAs can be tuned by varying  $\text{FeCl}_3$  concentration in the immersion solution. The existence of  $\text{Fe}_2\text{O}_3$  on TNTAs was verified by both SEM scan and EDX spectra.  $\text{Fe}_2\text{O}_3$ -modified TNTAs exhibited enhanced absorption in the visible light region which increased by increasing Fe content from 0.01 M to 0.2 M. The absorption edge shift of  $\text{Fe}_2\text{O}_3$ -modified TNTAs towards visible light region is attributed to the low band gap  $\text{Fe}_2\text{O}_3$  (2.2 eV). The photocurrent response of  $\text{Fe}_2\text{O}_3$ -modified TNTAs was also enhanced significantly and increased with increasing  $\text{Fe}_2\text{O}_3$  loading [163].

### 2.6.3 CdS Nanoparticle Sensitization

Another method to modify the wide band gap of  $\text{TiO}_2$  is to couple  $\text{TiO}_2$  with a small band gap semiconductor thin film or nanoparticles. Coupling a wide band gap semiconductor with a small band gap semiconductor with a more negative conduction band level will facilitate the injection of electrons from the conduction band of the small band gap semiconductor to the CB of the wide band gap semiconductor. CdS has a small band gap of 2.4 eV which allows the absorption of low energy photons from the visible light region up to 520 nm and its conduction band, CB, is 0.5 eV more negative than that of  $\text{TiO}_2$  which should be beneficial in enhancing the charge separation as illustrated in Figure 2.18. Therefore, sensitization of  $\text{TiO}_2$  with CdS nanoparticles or thin film could make the performance more efficient in solar energy conversion applications by increasing the ability to harvest the visible light as well as improving charge separation process [164-169]. Previous studies about combination of CdS and  $\text{TiO}_2$  showed outstanding photoelectrochemical properties under visible light spectrum [170-171]. Chen and co-workers [165] first reported the preparation of CdS-sensitized TNTAs by electrodeposition method. CdS was deposited into TNTAs surface by cathodic reduction from benzene

saturated with elemental sulfur and 0.6 M CdCl<sub>2</sub> mixed with DMSO. The counter electrode was a rod of Cd and the cathodic potential was -0.5 V. The existence of CdS was verified from XPS spectra peaks for sulfide at 161.9 eV and for Cd 3d<sub>3/2</sub> at 411.9 eV and for Cd 3d<sub>5/2</sub> at 405.3 eV. The CdS sensitization has red-shifted the absorption edge of TNTAs towards the visible light spectra up to wave length of 500 nm. The CdS-modified TNTAs annealed at 400 °C exhibited a photocurrent of 2.51 mA.cm<sup>-2</sup> under illumination intensity of 1 sun (AM 1.5, 100 mW/cm<sup>2</sup>). This high photocurrent value is about 16 times higher than that obtained from bare unmodified TNTAs [165].

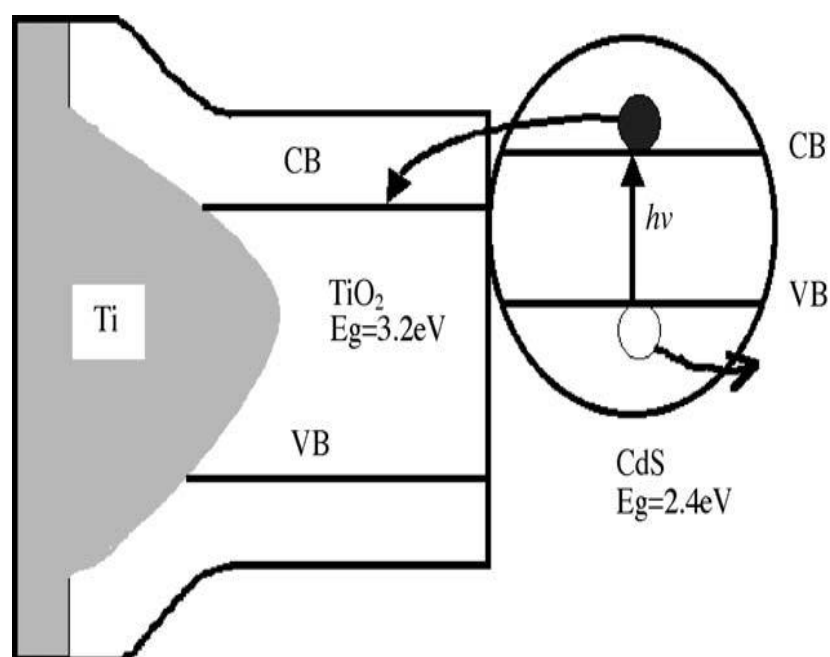


Figure 2-18 Illustrative diagram for the charge injection from excited CdS into TiO<sub>2</sub>. CB and VB refer to the energy levels of conduction and valence bands respectively.

(Reprinted with permission from ref. [165] © 2005 Elsevier B. V. All rights reserved).

Furthermore, Yin and co-workers demonstrated that the cathodic deposition parameters such as cathodic potential and deposition time, would affect the photoelectrochemical performance of CdS-modified TNTAs. The maximum photocurrent of about  $3.8 \text{ mA/cm}^2$  was obtained when the cathodic potential was 5 V and deposition time 30 min [65]. Bai and co-workers [168] prepared CdS-modified TNTAs on a conducting glass by depositing CdS nanoparticles into the crystallized TNTAs by S-CBD (sequential chemical bath deposition) method [168, 172-173]. The crystallized TNTAs were successively immersed in  $\text{CdSO}_4$  solution and  $\text{Na}_2\text{S}$  solution as one cycle for several times. CdS-modified TNTAs fabricated by this method demonstrated very high photocurrent of 4.8 mA under AM 1.5 illumination which was more than 6 times higher than photocurrent obtained from unmodified TNTAs ( $0.75 \text{ mA/cm}^2$ ) under the same conditions [168]. Despite the outstanding photoelectron-chemical properties of CdS-modified TNTAs, the instability of CdS nanoparticles in aqueous solutions [165, 168] may hinder industrial and commercial applications of CdS-modified TNTAs.

#### 2.6.4 Loading of Precious Metals Nanoparticles

Attaching noble metal nanoparticles to TNTAs provides nanotubes/nanoparticles composite materials with enhanced photocatalytic and photoelectrochemical properties which increase the overall performance of TNTAs [174].  $\text{TiO}_2$  has been loaded with various noble metal particles such as Pt [1745-178], Au [179-180], Pd [181], Ag [182-183] and Co-Ag-Pt [1]. Noble metal nanoparticles loading on TNTAs is beneficial to depress the recombination of photogenerated electron/hole charges and consequently, increase the overall photocatalytic process efficiency. For example, for Ag-loaded TNTAs, the flat CB

potential of  $\text{TiO}_2$  is lower (more negative) than that of metallic Ag and this allows the photogenerated electrons to follow towards Ag and accumulate there forming a Schottky barrier between the TNTAs and Ag nanoparticles [182, 185-187]. The photogenerated electrons accumulated on Ag nanoparticles surface have a good fluidity and could be easily transferred to the absorbed oxygen on Ag surface forming  $\text{O}_2^-$  active species. The  $\text{O}_2^-$  species favors the photocatalytic process. Furthermore, the accumulated hole charges at the VB of TNTAs react with water to produce hydroxyl radical  $\text{OH}^\bullet$  which is very active oxidant for many organic compounds in water [188].

## 2.7 Advantages of $\text{TiO}_2$ Nanotube Arrays (TNTAs) Over Nanowires and Nanorods

Although nanowires and nanorods are one dimensional nanomaterials like nanotube arrays with unique properties which make them promising candidates for many diverse applications, the hollow structure gains the nanotube arrays further advantages as explained below:

- 1- For the same outer diameter and length, nanotubes have larger surface area than nanowires and nanorods due to internal surface area of the hollow tubes which results in enhanced photoanode performance [189].
- 2- Nanotubes can be easily functionalized by filling their hollows with either organic or inorganic nanomaterials to produce wide range of nanocomposites for vast number of applications; for instance, synthesis of CdS-sensitized  $\text{TiO}_2$  nanotube arrays as visible light responsive photoanode [165]. And, filling nanotubular hollows with iron oxide [190] or nickel oxide nanoparticles or nanorods [191]



produces nanocomposites with excellent semiconducting and magnetic properties for photocatalytic and electronic applications.

- 3- The TiO<sub>2</sub> nanotube arrays produced by anodization are vertically-oriented, well-organized and top-opened nanotubes and attached to a conducting Ti-metal support which plays as an electron collector to facilitate rapid separation of photogenerated charges before recombination.
- 4- The above feature in point number 3 also facilitates the propagation of the incident and scattered photons over the internal and external surfaces through the entire length of nanotubes which increases the light absorptivity [192].
- 5- TiO<sub>2</sub> nanotubes produced by anodization are integrated and immobilized arrays over large surfaces which help their incorporation in a photoreactor or a photoelectroreactor either continuously or in batch fashion without the need for an expensive solid liquid separation step that is necessary in case of nanoparticles, nanowires or nanorods.
- 6- The unique hollow structure of nanotube arrays along with the excellent TiO<sub>2</sub> biocompatibility makes nanotube arrays a promising candidate for drug delivery applications by using nanotubes as a drug carrier to control the drug release in the body [52, 189].
- 7- The anodization process is inexpensive (compared with other nanomaterials synthesis methods such as sol-gel) and already is a well-established industrial process and has been used in metal industries for about 100 years which means that large scale production and commercialization of TiO<sub>2</sub> nanotube arrays is more reliable and cost-efficient.

## 2.8 Applications of TiO<sub>2</sub> Nanotube Arrays (TNTAs) Photoanodes

The positive environmental and economic impact of TNTAs photoanodes is extremely high due to the versatile applications of this new nanomaterial. One major application is in photoelectrochemical cells to produce ultimately clean and renewable H<sub>2</sub> fuel from photolysis of water using the abundant and renewable solar energy. This technology will help reduce the world consumption of fossil fuels and consequently reduce the greenhouse gases (GHGs) emissions [193-195]. Secondly, using TNTAs as a photoanode in photochemical reactions for photodegradation of a wide range of organic contaminants in both water and air streams will result in a cleaner and healthier environment [188].

Since the year 1972, when Fujishima and Honda reported photoelectrochemical generation of hydrogen by water splitting using TiO<sub>2</sub> nanoparticles [17], significant research interest has been raised and many subsequent efforts have been devoted to improving the photoconversion efficiency using different semiconducting materials or different material structures. Generally, any applications where titania in a compact or powder form is presently used is a potential application for TNTAs, for example, photocatalytic degradation of organic contaminants in both aqueous and air streams, low cost dye-sensitized solar cells (DSSCs), water splitting by light for generation of clean H<sub>2</sub> fuel, self-cleaning, anti-fogging and many other applications. The highly ordered vertically oriented

well-defined structure of TNTAs strongly attached to Ti- metal support can bring specific advantages and help enhancing the performance in such applications [12, 196-198]. Dye-sensitized solar cells, DSSCs, also known as Gratzel cells, schematically represented in Figure 2.19-(a), represent one of the widest and most important applications of TiO<sub>2</sub>. DSSCs efficiencies have reached over 11% using nanocrystalline TiO<sub>2</sub> films [199]. As mentioned in Section 2, these nanocrystalline particulate-based DSSCs are characterized by slow percolation of electrons through the random polycrystalline network and the poor absorption of low energy photons by the available dyes which are both two of the major factors hindering further improvement in photoconversion efficiencies. Detailed kinetic and dynamic studies of DSSCs made of nanoparticulate TiO<sub>2</sub> films revealed that the limiting factors are random path processes of charges and trapping /detrapping of electrons through the porous network. When using crystallized highly ordered vertically oriented TiO<sub>2</sub> nanotube arrays as photoanodes they offer large surface areas with vectorial charge transport along the length of the nanotubes as schematically represented in Figure 2.19 b [12, 34, 200]. TNTAs length and diameter are proved to be crucial parameters in photoconversion efficiency optimization as it can be seen from Figure 2.19 (c) [12]. A DSSC fabricated from 3.6 μm thick nanotube array as a photoanode sensitized with N719 dye exhibited a short-circuit current density ( $J_{SC}$ ) of 10.3 mA cm<sup>-2</sup>, an open-circuit potential ( $V_{oc}$ ) of 0.84 V and a fill factor (FF) of 0.54, for an overall conversion efficiency of 4.7% under AM1.5 solar simulator illumination [200-201]. A maximum photoconversion efficiency of 6.89% was obtained from 20 μm length TNTAs photoanode DSSC sensitized with N719 dye under AM 1.5 solar simulator illumination with an open circuit voltage of 0.817 V, short circuit current density of 12.72 mA.cm<sup>-2</sup> and a fill factor

(FF) of 0.663 [86]). Although these results are very promising in terms of the overall photoconversion efficiency under whole solar spectrum illumination (AM 1.5 solar simulator), effects of parameters such as anodization conditions, nanotube length, diameter, wall thickness, and nanostructure disorder still need further investigations from researchers to optimize the TNTAs photoanode-based dye sensitized solar cells for further increase in photoconversion efficiency [54, 202].

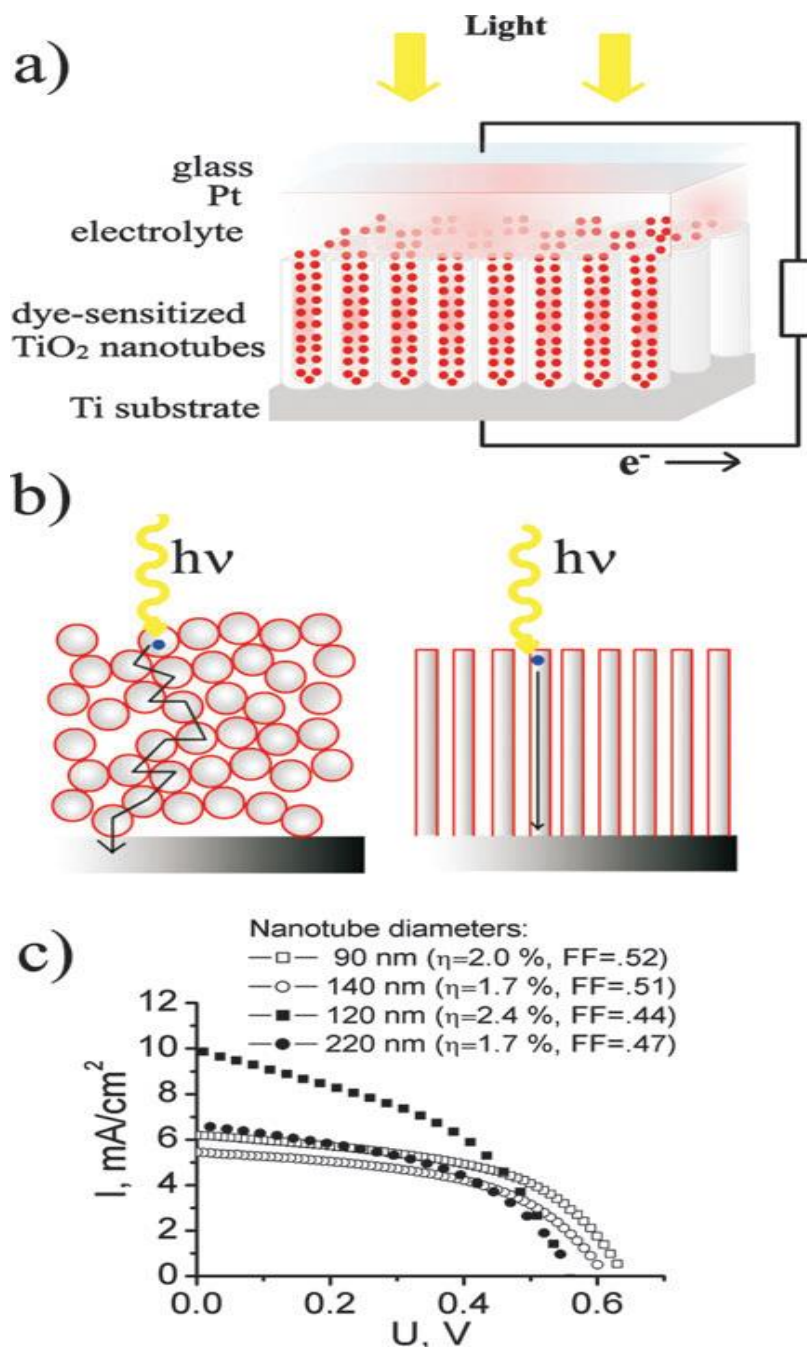


Figure 2-19 (a) Schematic representation of dye-sensitized solar cells based on TNTAs (a), electron path through a percolated nanoparticulate and oriented TNTAs structures (b) and I–V characteristic of DSSCs based on different diameter nanotubes (empty symbols correspond to 8  $\mu\text{m}$  and filled symbols to 16  $\mu\text{m}$  nanotubes length) (c). (Reprinted with permission from ref. [12] © The Royal Society of Chemistry 2009).

Photoelectrolysis of water to generate renewable and clean H<sub>2</sub> fuel is another very promising application of TNTAs photoanode. Mor and coworkers [203] reported hydrogen generation by water splitting using first generation short TNTAs as photoanode at a power-time normalized rate of 960  $\mu\text{mol/h.W}$  (24 ml/h.W) at an overall conversion efficiency of 6.8% under 320-400 nm light illumination of 100  $\text{mW.cm}^{-2}$  intensity. Mohapatra and coworkers [51] designed a photoelectrochemical cell consisting of carbon-modified TNTAs arrays as a photoanode and Pt-nanoparticles decorated TNTAs as a cathode for H<sub>2</sub> generation from water splitting under both UV and visible light illumination. They achieved photoconversion efficiencies of 13.3% and 8.5% for UV and visible illumination, respectively, which were very encouraging [51].

Furthermore, TNTAs photoanode exhibited enhanced photocatalytic activity compared with traditional powder counterpart for degradation of wide range of organic pollutants in both water and air streams such as phenol [90], 2,3-dichlorophenol [204, 205], pentachlorophenol [134], tetracycline [130], methylene blue (MB) [159], methyl orange [206], p-nitrophenol and methyl red [207]. For instance, 80% degradation of bisphenol A (BPA) was achieved using 4  $\mu\text{m}$  length TNTAs after 180 min photocatalysis which was much higher than 51% for micro-structured TiO<sub>2</sub> photoanode under the same UV illumination [208].

## 2.9 Concluding Remarks

Photocatalytic reactions of  $\text{TiO}_2$  have gained much interest during the past decades due to their vast applications based on solar energy conversion. More recently, during the last decade,  $\text{TiO}_2$  nanotube arrays which were produced by electrochemical anodization of Ti metal in  $\text{F}^-$  ions containing electrolytes have attracted more research interest due to their outstanding properties rendering them the most promising photoanode in many solar energy conversion applications including both environmental and energy production applications. The big challenge is to increase the light energy to electrical or chemical energy efficiency. There are three key factors for increasing the efficiency of solar energy applications using  $\text{TiO}_2$  photoanodes. The first key factor is to increase the surface area. The second key factor is to minimize the recombination of photogenerated electron/hole charges by facilitating rapid charge separation. The third factor is to extend the photoresponsiveness of  $\text{TiO}_2$  to the visible light region by modifying the band gap energy of the material. Although the high surface area could be achieved by reducing material size to nanoscale, minimizing the photogenerated electron/hole charges recombination could only be achieved through the unique architecture of highly ordered, vertically oriented titania nanotube arrays produced by electrochemical anodization of parent Ti metal foil in  $\text{F}^-$  ions containing electrolytes. The nano-architecture and high surface area can be easily tuned by controlling the anodization process parameters, especially, anodization potential, anodization duration, pH and chemistry of the anodization electrolyte. For example, titania nanotube length can be easily produced in the range from few hundred nanometers in HF aqueous electrolytes to up to several hundreds of microns in ethylene glycol-based electrolytes. Inner diameter and wall thickness can also be tuned by controlling anodization

potential and other anodization conditions. In this contribution, fabrication of titania nanotube arrays in different anodization electrolytes such as HF-aqueous electrolyte, glycerol-based electrolytes, DMSO electrolyte, formamide electrolyte and ethylene glycol electrolyte was extensively reviewed. Process parameters and results were discussed in detail. Ethylene glycol was proven to be the best anodization electrolyte in terms of rapid growth rate of nanotubes and the smoothness of produced nanotube arrays. The third key factor to enhance the performance of  $\text{TiO}_2$  is to modify electronic bands structure to be able to harvest low energy visible light photons. Many different strategies have been proposed to achieve this target, including non-metal doping such as nitrogen, carbon and boron, metal doping such iron, CdS sensitization and noble metal nanoparticles loading. In each strategy, basic principles and selected results have been discussed in this review.



## 2.10 References

1. Fujishima, A., Rao, T. N. and Tryk, D. A., *J. Photochem. Photobiol. C* 1, (2000), pp. 1-21.
2. Adams, D. M., Brus, L., Chidsey, C. E. D., Creager, S., Creutz, C., Kagan, C. R., Kamat, P. V., Lieberman, M., Lindsay, S., Marcus, R. A., Metzger, R. M., Michel-Beyerle, M. E., Miller, J. R., Newton, M. D., Rolison, D. R., Sankey, O., Schanze, K. S., Yardley, J. and Zhu, X., *J. Phys. Chem. B* 107, (2003), pp. 6668-6697.
3. Burda, C., Chen, X., Narayanan, R. and El-Sayed, M. A., *Chem. Rev.* 105, (2005), pp. 1025-1102.
4. Chen, X. and Mao, S. S., *Chem. Rev.* 107, (2007), pp. 2891-2959.
5. Alivisatos, A. P., *J. Phys. Chem.* 100, (1996), pp. 13226-13239.
6. Alivisatos, A. P., *Science* 271, (1996), pp. 933-937.
7. Guozhong, Cao, *Nanostructures and Nanomaterials: Synthesis, Properties and Applications*, (2004), Imperial College Press, P. 15.
8. Iijima, S., *Nature* 354, (1991), pp. 56-58.
9. Xia, Y., Yang, P., Sun, Y., Wu, Y., Mayers, B., Gates, B., Yin, Y., Kim, F. and Yan, H., *Adv. Mater.* 15, (2003), pp. 353-389.
10. Kuchibhatla, S. V. N. T., Karakoti, A. S., Bera, D. and Seal, S., *Progress in Materials Science* 52, (2007), pp. 699-913.

11. Rao, C. N. R., Muller, A. And Cheetham, A. K., *The Chemistry of Nanomaterials: Synthesis, Properties and Applications*, Wiley-VCH, Weinheim, Germany, (2006).
12. Ghicov, A. and Schmuki, P., *Chem. Commun.*, (2009), pp. 2791-2808.
13. Shankar, K., Basham, J. I., Allam, N. K., Varghese, O. K., Mor, G. K., Feng, X., Paulose, M., Seabold, J. A., Choi, K-S. and Grimes, C. A., *J. Phys. Chem. C* 113, (2009), pp. 6327-6359.
14. Linsebigler, A. L., Lu, G. and Yates, J. T., *Chem. Rev.* 95, (1995), p. 735.
15. Nakamura, R., Ohashi, N., Imanishi, A., Osawa, T., Matsumoto, Y., Koinuma, H. and Nakato, Y., *J. Phys. Chem. B* 109, (2005), pp. 1648-1651.
16. Neumann, B., Bogdanoff, P., Tributsch, H., Sakthivel, S. and Kisch, H., *J. Phys. Chem. B* 109, (2005), pp. 16579-16586.
17. Fujishima, A. and Honda, K., *Nature* 238, (1972) pp. 37-38.
18. Paulose, M., Mor, G. K., Varghese, O. K., Shankar, K. and Grimes, C. A., *J. Photochem. Photobiol. A* 178, (2006), pp. 8-15.
19. Wang, R., Hashimoto, K., Chikuni, M., Kojima, E. and Kitamura, A., *Nature* 388, (1997), p. 431.
20. Yoriya, S., Prakasam, H. E., Varghese, O. K., Shankar, K., Paulose, M., Mor, G. K., Latempa, T. J. and Grimes, C. A., *Sensors Letters* 4, (2006), pp. 334-339.
21. Ngamsinlapasathian, S., Sakulphaemaruehai, S., Pavasupree, S., Kitiyanan, A., Sreethawong, T., Suzuki, Y. and Yoshikawa, S., *J. Photochem. Photobiol. A* 164, (2004), pp.145-151.

22. Brunette, D. M., Tengvall, P., Textor, M. and Thomsen, P., "Titanium in Medicine", Springer, Berlin, (2001).
23. Hoyer, P., *Langmuir* 12, (1996), pp. 1411-1413.
24. Lakshmi, B. B., Dorhout, P. K. and Martin, C. R., *Chem. Mater.* 9, (1997), pp. 857-862.
25. Zhang, M., Brando, Y. and Wada, K., *J. Mater. Sci. Lett.* 20, (2001), pp. 167-170.
26. Bavykin, D. V., Parmon, V. N., Lapkin, A. A. and Walsh, F. C., *J. Mater. Chem.* 14, (2004), pp. 3370-3377.
27. Ou, H-H. and Lo, S-L., *Separation and Purification Technology* 58, (2007), pp. 179-191.
28. Zwilling, V., Darque-Ceretti, E., Boutry-Forveille, A., David, D., Perrin, M. Y. and Aucouturier, M., *Surf. Interface Anal.* 27, (1999), pp. 629-637.
29. Mor, G. K., Varghese, O. K., Paulose, M., Niloy, M. and Grimes, C. A., *J. Mater. Res.* 18, (2003) p.2588.
30. Zhao, J., Wang, X., Chen, R. and Li, L., *Solid State Communications* 134, (2005), pp. 705-710.
31. Zhao, J., Wang, X., Sun, T. and Li, L., *Nanotechnol.* 16, (2005), pp. 2450-2454.
32. Albu, S. P., Ghicov, A., Macak, J. M. and Schmuki, P., *Phys. Status Solidi RRL* 1, (2007), pp. R65-R67.
33. Frank, A. J., Kopidakis, N. and de Lagemaat, J. V., *Coordination chemistry Reviews* 248, (2004), pp. 1165-1179.
34. Law, M., Greene, L., Johnson, J. C., Saykally, R. and Yang, P., *Nature Materials* 4, (2005), pp. 455-459.

35. Mor, G. K., Shankar, K., Paulose, M., Varghese, O. K. and Grimes, C. A., *Nano Lett.* 6, (2006), pp. 215-218.
36. Paulose, M., Prakasam, H. E., Varghese, O. K., Peng, L., Popat, K. C., Mor, G. K., Desai, T. A. and Grimes, C. A., *J. Phys. Chem. C* 111, (2007), pp. 14992-14997.
37. Wan, J., Yan, X., Ding, J., Wang, M. and Hu, K., *Materials Characterization* 60, (2009), pp. 1534-1540.
38. Yang, H. and Pan, C., *J. Alloys and Compounds* 492, (2010), pp. 133-135.
39. Gratzel, M., *Nature* 414, (2001) pp.338-344.
40. Gratzel, M., *J. Photochem. Photobiol. C* 4, (2003), pp. 145-153.
41. Nazeeruddin, M. K., Pechy, P., Renouard, T., Zakeeruddin, S. M., Humphry-Baker, R., Comte, P., Liska, P., Cevey, L., Costa, E., Shklover, V., Spiccia, L., Deacon, G. B., Bignozzi, C. A. and Gratzel, M., *J. Am. Chem. Soc.* 123, (2001), 1613-1624.
42. Cao, F., Oskam, G., Meyer, G. J. and Searson, P. C., *J. Phys. Chem.* 100, (1996), pp. 17021-17027.
43. De Jongh, P. E. and Vanmaekelbergh, D., *Phys. Rev. Lett.* 77, (1996), pp.3427-3430.
44. Wahl, A., Ulmann, M., Carroy, A. and Augustynski, J., *J. Chem. Soc. Chem. Comm.* (1994), pp. 2277-2278.
45. Santato, C., Ulmann, M. and Augustynski, J., *J. Phys. Chem. B* 105, (2001), pp. 936-940.

46. Wahl, A., Ulmann, M., Carroy, A., Jerman, B., Dolata, M., Kedzierzawski, P., Chatelain, C., Monnier, A. and Augustynski, J., *J. Electroanalytical Chem.* 396, (1995), pp.41-51.
47. Comte, P., Nazeeruddin, M. K., Ruzinger, F. P., Frank, E. J. and Gratzel, M., *J. Mol. Catal.* 52, (1989), pp. 63-84.
48. Adachi, M., Murata, Y., Okada, I. and Yoshikawa, S., *J. Electrochem. Soc.* 150, (2003). Pp. G488-G493.
49. Rao. C. N. R. and Govindaraj, A., *Nanotubes and Nanowires*, The Royal Society of Chemistry, Cambridge, UK, (2005).
50. Paulose M., Shankar, K., Varghese, O. K., Mor, G. K. and Grimes, C. A., *J. Phys. D* 39, (2006), pp. 2498-2503.
51. Mohapatra, S. K., Misra, M., Mahajan, V. K. and Raja, K. S., *J. Phys. Chem. C* 111, (2007), pp. 8677-8685.
52. Grimes, C. A., *J. Materials Chemistry* 17, (2007), pp. 1451-14457.
53. Zhu, K, Neale, N. R., Miedaner, A. and Frank, A. J., *Nano Lett.* 7, (2007), pp. 69-74.
54. Zhu, K., Vinzant, T. B., Neale, N. R. and Frank, A. J., *Nano Lett.* 7, (2007), pp.3739-3746.
55. Park, J. H., Kim, S. and Bard, A. J., *Nano Lett.* 6, (2006), pp. 24-28.
56. Mor, G. K., Varghese, O. K., Paulose, M., Shankar, K. and Grimes, C. A., *Solar Energy Mater. Solar Cells* 90, (2006), pp. 2011-2075.

57. Gong, D., Grimes, C. A., Varghese, O. K., Hu, W., Singh, R. S., Chen, Z. and Dickey, E., *J. Mater. Res.* 16, (2001), pp. 3331-3334.
58. Macák, J. M., Tsuchiya, H. and Schmuki, P., *Angew. Chem. Int. Ed.* 44, (2005), pp.2100-2102.
59. Zhao, W., Ma, W., H., Chen, C. C., Zhao, J. C. and Shuai, Z. G., *J. Am. Chem. Soc.* 126, (2004), pp. 4782-4783.
60. Cai, Q., Yang, L. and Yu, Y., *Thin Solid Films* 515, (2006), pp. 1802-1806.
61. Wang, H., Yip, C. T., Cheung, K. Y., Djurisic, A. B., Xie, M. H., Leung, Y. H. and Chen, W. K., *Appl. Phys. Lett.* 89, (2006), pp. 023508, 1-3.
62. Cai, Q., Paulose, M., Varghese, O. K. and Grimes, C. A., *J. Mater. Res.* 20, (2005), pp. 230-236.
63. Tian, T., Xiao, X.-F., Liu, R.-F., She, H.-D. and Hu, X.-F., *J. Mater. Sci.* 42, (2007), pp. 5539-5543.
64. Bauer, S., Kleber, S. and Schmuki, P., *Electrochemistry Communications* 8, (2006), pp.1321-1325.
65. Yin, Y.; Jin, Z., Hou, F. and Wang, X., *J. Am. Ceram. Soc.* 90, (2007), pp. 2384-2389.
66. Bai, J., Zhou, B., Li, L., Liu, Y., Zheng, Q., Shao, J., Zhu, X., Cai, W., Liao, J. and Zou, L., *J. Mater. Sci.* 43, (2008), pp. 1880-1884.
67. Propst, E. K. and Kohl, P. A., *J. Electrochem. Soc.* 141, (1994), pp. 1006-1013.

68. Christophersen, M., Carstensen, J., Voigt, K. and Föll, H., *Phys. Status Solidi A* 197, (2003), pp. 34-38.
69. Ponomarev, E. A. And Levy-Clement, C., *Electrochem. Solid-state Lett.* 1, (1998), pp. 42-45.
70. Föll, H., Christophersen, M., Carstensen, J. and Hasse, G., *Mater. Sci. Eng. R* 39, (2002) pp. 93-141.
71. Föll, H., Langa, S., Carstensen, J., Christophersen, M. and Tiginyanu, I. M., *Adv. Mater.* 15, (2003), p. 183.
72. Macak, J. M. and Schmuki, P., *Electrochimica Acta* 52, (2006), pp. 1258-1264.
73. Birner, A., Wehrspohn, R. B., Gösele, U. M. and Busch, K., *Adv. Mater.* 13, (2001), p. 378.
74. Petukhov, D. I., Eliseev, A. A., Kolesnik, I. V., Napolskii, K. S., Lukashin, A. V., Tretyakov, Y. D., Grigoriev, S. V., Grigorieva, N. A. and Eckerlebe, H., *Microporous and Mesoporous Materials* 114, (2008), pp.440-447.
75. Haginoya, C., Ishibashi, M. and Koike, K., *Appl. Phys. Lett.* 71, (1997), p. 2934.
76. Tsuchiya, H., Macak, J. M., Ghicov, A., Taveira, L. and Schmuki, P., *Corrosion Science* 47, (2005), pp.3324-3335.
77. Macak, J. M., Tsuchiya, H., Taveira, L., Aldabergerova, S. and Schmuki, P., *Angew. Chem. Int. Ed.* 44, (2005), pp. 7463-7465.
78. Macak, J. M., Hildebrand, H., Marten-Jahns, U. and Schmuki, P., *J. Electroanalytical Chemistry* 621, (2008), pp. 254-266.
79. Izutsu, K., "Electrochemistry in Nonaqueous Solutions", 2<sup>nd</sup> Ed., (2009), Wiley-VCH Verlag GmbH & Co.KGaA, Weinheim.

80. Ruan, C., Paulose, M., Varghese, O. K., Mor, G. K. and Grimes, C. A., *J. Phys. Chem. B* 109, (2005), pp. 15754-15759.
81. Paulose, M., Shankar, K., Yoriya, S., Prakasam, H. E., Varghese, O. K., Mor, G. K., Latempa, T. A., Fitzgerald, A. and Grimes, C. A., *J. Phys. Chem. B* 110, (2006), pp. 16179-16184.
82. Yoriya, S., Paulose, M., Varghese, O. K., Mor, G. K. and Grimes, C. A., *J. Phys. Chem. C* 111, (2007), pp.13770-13776.
83. Bestetti, M, Franz, S., Cuzzolin, M., Arosio, P. and Cavallotti, P. L., *Thin Solid Films* 515, (2007), pp. 5253-5258.
84. Yang, D-J., Kim, H-G., Cho, S-J. and Choi, W-Y., *IEEE Transactions on Nanotechnology* 7, 2, March (2008), pp. 131-134.
85. Grimes, C. A. and Mor, G. K., "Titanium Nanotube Arrays: Synthesis, Properties, and Applications", Springer Science + Business Media, LLC (2009), New York, NY, USA. DOI 10.1007/978-1-4419-0068-5
86. Shankar, K., Mor, G. K., Prakasam, H. E., Yoriya, S., Paulose, M., Varghese, O. K. and Grimes, C. A., *Nanotechnology* 18, (2007), pp 1-11.
87. Shankar, K., Mor, G. K., Fitzgerald, A. and Grimes, C. A., *J. Phys. Chem. C* 111, (2007), pp. 21-26.
88. Fabregat-Santiago, F., Barea, E. M., Bisquert, J., Mor, G. K., Shankar, K. and Grimes, C. A., *J. Am. Chem. Soc.* 130, (2008), pp. 11312-11316.



89. Liu, Z., Zhang, X., Nishimoto, S., Jin, M., Tryk, D. A., Murakami, T. and Fujishima, A., *J. Phys. Chem. C* 112, (2008), pp. 253-259.
90. Prakasam, H. E., Shankar, K., Paulose, M., Varghese, O. K. and Grimes C. A., *J. Phys. Chem. C* 111, (2007), pp. 7235-7241.
91. Yang, L. X., Luo, S. L., Cai, Q. Y. and Yao, S. Z., *Chinese Sci. Bull.* 55, (2010), pp. 331-338.
92. Mohapatra, S. K., Misra, M., Mahajan, V. K. and Raja, K. S., *J. Catalysis* 246, (2007), pp.362-369.
93. Ruan, C., Paulose, M., Varghese, O. K. and Grimes, C. A., *Solar Energy Materials and Solar Cells* 90, (2006), pp. 1283-1295.
94. Watcharenwong, A., Chanmanee, W., de Tacconi, N. R., Chenthamarakshan, C. R., Kajitvichyanukul, P. and Rajeshwar, K., *J. Mater. Res.* 22, (2007), pp. 3186-3195.
95. Chanmanee, W., Watcharenwong, A., Chenthamarakshan, C. R., Kajitvichyanukul, P., de Tacconi, N. R. and Rajeshwar, K., *Electrochemistry Communications* 9, (2007), pp. 2145-2149.
96. Thompson, G. E., *Thin Solid Films* 297, 192 (1997)
97. Sul, Y-T., Johansson, C. B., Jeong, Y. and Albrektsson, T., *Medical Engineering and Physics* 23, (2001), pp.329-346.
98. Mohamed, A. E., Kasemphaibulsuk, N., Rohani, S. and Barghi, S., *J. Nanosci. Nanotechnol.* 10, (2010), pp. 1998-2008.

99. Chen, X. and Burda, C., *J. Am. Chem. Soc.* 130, (2008), pp. 5018-5019.
100. Varghese O. K., Paulose, M., Shankar, K., Mor, G. K. and Grimes C. A., *J. Nanosci. Nanotechnol.* 5, (2005), pp. 1158-1165.
101. Xu, C., Shaban, Y. A., Ingler, W. B. and Khan, S. U. M., *Solar Energy Mater. Solar Cells* 91, (2007), pp. 938-943.
102. Vitiello, R. P., Macak, J. M., Ghicov, A., Tsuchiya, H., Dick, L. F. P. and Schmuki, P., *Electrochemistry Communications* 8, (2006), pp. 544-548.
103. Geng, J., Yang, D., Zhu, J., Chen, D. and Jiang Z., *Mater. Res. Bulletin* 44, (2009), pp.146-150.
104. Chen, X., Zhang, X., Su, Y., and Lei, L., *Applied Surface Science* 254, (2008), pp. 6693-6696.
105. Lei, L., Su, Y., Zhou, M., Zhang, X. and Chen, X., *Mater. Res. Bulletin* 42, (2007), pp. 2230-2236.
106. Asahi, R., Morikawa, T., Ohwaki, T., Aoki, K. and Taga, Y., *Science* 293, (2001), pp. 269-271.
107. Devi, L. G. and Kavitha, R., *Applied Catalysis B: Environmental* 140-141, (2013), pp. 559-587.
108. Chen, X., Glans, P. -A., Qiu, X., Dayal, S., Jennings, W. D., Smith, K. E., Burda, C. and Guo. J., *J. Electron Spectroscopy and Related Phenomena* 162, (2008), pp. 67-73.
109. Kosowska, B., Mozia, S., Morawski, A. W., Grzmil, B., Janus, M. and Kalucki, K., *Solar Energy Materials Solar Cells* 88, (2005), pp.269-280.

110. Yates, H. M., Nolan, M. G., Sheel, D. W. and Pemble, M. E., *J. Photochem. Photobiol. A* 179, (2006), pp. 213-223.
111. Wu, P. -G., Ma, C. -H. and Shang, J. K., *Appl. Phys. A* 81, (2005), pp. 1411-1417.
112. Horikawa, T., Katoh, M. and Tomida, T., *Microporous and Mesoporous Materials* 110, (2008), pp. 397-404.
113. Sano, T., Puzenat, E., Guillard, C., Geantet, C. and Matsuzawa, S., *J. Molecular Catalysis A* 284, (2008), pp. 127-133.
114. Yuan, J., Chen, M., Shi, J. and Shangguan, W., *Int. J. Hydrogen Energy* 31, (2006), pp.1326-1331.
115. Ni, M., Leung, M. K. H., Leung, D. Y. C. and Sumathy, K., *Renewable and Sustainable Energy Reviews* 11, (2007), pp. 401-425.
116. Beranek, R., Macak, J. M., Gartner, M., Meyer, K. and Schmuki, P., *Electrochimica Acta* 54, (2009), pp. 2640-2646.
117. Beranek, R. and Kisch, H., *Electrochemistry Communications* 9, (2007), pp. 761-766.
118. Saha, N. C. and Tompkins, H. G., *J. Appl. Phys.* 72, (1992), p.3072.
119. Dong, L., Cao, G. -X., Ma, Y., Jia, X. -L., Ye, G. -T. and Guan, S. -K., *Tras. Nonferrous Met. Soc. China* 19, (2009), pp. 11583-1587.
120. Dong, L., Ma, Y., Wang, Y., Tian, Y., Ye, G., Jia, X. and Cao, G., *J. Materials Letters* 64, (2009), pp. 1598-1600.
121. Dong, F., Zhao, W., Wu, Z. and Guo, S., *J. Hazardous Materials* 162, (2009), pp. 763-770.

122. Shankar, K., Tep, K. C., Mor, G. K. and Grimes, C. A., *J. Phys. D* 39, (2006), pp. 2361-2366.
123. Xu, J., Ao, Y., Chen, M. and Fu, D., *Appl. Surf. Sci.* 256, (2010), pp. 4397-4401.
124. Su, J., Zhang, X., Zhou, M., Han, S. and Lei, L., *J. Photochem. Photobiol. A* 194, (2008), pp. 152-160.
125. Menero, C., Mariella, G., Maurino, V., Vione, D. and Pelizzetti, E., *Langmuir* 16, (2000), pp. 8964-8972.
126. Li, Q. and Shang, J. K., *Environ. Sci. Technol.* 43, (2009), pp.8923-8929.
127. Ghicov, A., Macak, J. M., Tsuchiya, H., Kunze, J., Haeublein, V., Frey, L. and Schmuki, P., *Nano Lett.* 6, (2006), pp. 1080-1082.
128. Xu, C., Killmeyer, R., Gray, M. L. and Khan, S. U. M., *Appl. Catal. B* 64, (2006), pp. 312-317.
129. Shaban, Y. A. and Khan, S. U. M., *Chemical Physics* 339, (2007), pp.73-85.
130. Liu, H., Liu, G. and Zhou, Q., *J. Solid State Chem.* 182, (2009), pp. 3238-3242.
131. Yun, H. J., Lee, H., Joo, J. B., Kim, N. D. and Yi, J., *Electrochem. Commun.* 12, (2010), pp. 769-772.
132. Shankar, K., Paulose, M., Mor, G. K., Varghese, O. K. and Grimes, C. A., *J. Phys. D* 38, (2005), pp. 3543-3549.
133. Hu, X., Zhang, T., Jin, Z., Zhang, J., Xu, W., Yan, J., Zhang, J., Zhang, L. Wu, Y., *Mater. Lett.* 62, (2008), pp. 1579-1581.
134. Lu, N., Quan, X., Li, J. Y., Chen, S., Yu, H. T. and Chen, G. H., *J. Phys. Chem.* 111, (2007), pp.11836-11842.

135. Lu, N., Zhao, H., Li, J., Quan, X. and Chen, S., *Separation and Purification Technol.* 62, (2008), pp. 668-673.
136. Su, Y., Han, S., Zhang, X., Chen, X. and Lei, L., *Mater. Chem. Phys.* 110, (2008), pp. 239-246.
137. Tang, Z. and Li, D., *J. Phys. Chem. C* 112, (2008), pp. 5405-5409.
138. Umebayashi, T., Yamaki, T., Itoh, H. and Asai, K., *Appl. Phys. Lett.* 81, (2002), pp. 454-456.
139. Sayago, D. I., Serrano, P., Bohme, O., Goldoni, A., Paolocci, G., Roman, E. and Martin-Gago, J. A., *Phys. Rev. B* 64, (2001), 205402(1-7).
140. Su, Y., Chen, S., Quan, X., Zhao, H. and Zhang, Y., *Appl. Surf. Sci.* 255, (2008), pp. 2167-2172.
141. Choi, W., Termin, A. and Hoffmann, M. R., *J. Phys. Chem.* 84, (1994), pp. 13669-13679.
142. Dvoranova, D., Brezova, V., Mazur, M. and Malati, M. A., *Appl. Catal. B* 37, (2002), pp. 91-105.
143. Xu, A. -W., Gao, Y. and Liu, H. -Q., *J. Catal.* 207, (2002), pp. 151-157.
144. Tu, Y. -F., Huang, S. -Y., Sang, J. -P. and Zou, X. -W., *J. Alloys and Compounds* 482, (2009), pp. 382-387.
145. Tu, Y. -F., Huang, S. -Y., Sang, J. -P. and Zou, X. -W., *Mater. Res. Bullet.* 45, (2010), pp. 224-229.
146. Yang, Y., Wang, X. and Li, L., *Key Engineering Materials* vols. 434-435, (2010), pp. 446-447.

147. Liu, S., Yang, L., Xu, S., Luo, S. and Qai, Q., *Electrochem. Commun.* 11, (2009), pp. 1748-1751.
148. Zhao, J., Wang, X., Kang, Y., Xu, X. and Li, Y., *IEEE Photonics Technol. Lett.* 20, (2008), pp. 1213-1215.
149. Ghicov, A., Schmidt, B., Kunze, J. and Schmuki, P., *Chem. Phys. Lett.* 433, (2007), pp. 323-326.
150. Zhu, J. F., Zheng, W., He, B., Zhang, J. L. and Anpo, M., *J. Mol. Catal. A* 216, (2004), pp. 35-43.
151. Zhu, J. F., Chen, F., Zhang, J. L., Chen, H. J. and Anpo, M., *J. Photochem. Photobiol. A* 180, (2006), pp. 196-204.
152. Carneiro, J. O., Teixeira, V., Portinha, A., Magalhaes, A. and Coutinho, P., *Mater. Sci. Enging. B* 138, (2007), pp. 144-150.
153. Adan, C., Bahamonde, A., Fernandez-Garca, M. and Martunez-Arias, A., *Appl. Catal. B* 72, (2007), pp. 11-17.
154. Xin, B. F., Ren, Z. Y., Wang, P., Liu, J., Jing, L. Q., and Fu, H. G., *Appl. Surf. Sci.* 253, (2007), pp.4390-4395.
155. Asong, N., Dukes, F., Wang, C. and Shultz, M. J., *Chem. Phys.* 339, (2007), pp. 86-93.
156. Wang, J., Sun, W., Zhang, Z., Jiang, Z., Wang, X., Xu, R., Li, R. and Zhang, X., *J. Colloids Interface Sci.* 320, (2008), pp. 202-209.
157. Umebayashi, T., Yamaki, T., Itoh, H. and Asai, K., *J. Phys. Chem. Solids*, 63, (2002), pp. 1909-1920.
158. Li, X., Yue, P. -L. and Kutal, C., *New J. Chem.* 27, (2003), pp.1264-1269.

159. Sun, L., Li, J., Wang, C. L., Li, S. F., Chen, H. B. and Lin, C. J., *Sol. Energy Mater. Sol. Cells* 93, (2009), pp. 1875-1880.
160. Wang, C., Bottcher, C., Bahnemann, D. W. and Dohrmann, J. K. *J. Mater. Chem.* 13, (2003), pp.2322-2329.
161. Tryba, B., *Int. J. photoenergy* vol. 2008, (2008), Article ID 721824, pp. 1-15.
162. Li, J., Yun, H., and Lin, C. –J., *ECS Transactions* 3 (43), (2008), pp. 1-9.
163. Kuang, S., Yang, L., Luo, S. and Cai, Q., *Appl. Surf. Sci.* 255, (2009), pp. 7385-7388.
164. Yin, Y., Jin, Z. and Hou, F., *Nanotechnol.* 18, (2007), 495608, pp. 1-6.
165. Chen, S., Paulose, M., Ruan, C., Mor, G. K., Varghese, O. K., Kouzoudis, D. and Grimes, C. A., *J. Photochem. Photobiol. A* 177, (2006), pp. 177-184.
166. Sun, W. –T., Yu, Y., Pan, H. –Y., Gao, X. –F., Chen, Q. and Peng, L. –M., *J. Am. Chem. Soc.* 130, (2008), pp. 1124-1125.
167. Li, X., Cheng, Y., Liu, L. and Mu, J., *Colloids and Surfaces A* 353, (2010), pp.226-231.
168. Bai, J., Li, J., Liu, Y., Zhou, B. and Cai, W., *Appl. Catal. B* 95, (2010), pp. 408-413.
169. Zhang, J., Tang, C. and Bang, J. H., *Electrochem. Commun.* 12, (2010), pp. 1124-1128.
170. Vogel, R., Pohl, K. and Weller, H., *Chem. Phys. Lett.* 174, (1990), pp. 241-246.
171. Kohtani, S., Kudo, A. and Sakata, T., *Chem. Phys. Lett.* 206, (1993), pp.166-170.
172. Lin, C. J., Yu, Y. H. and Liou, Y. H., *Appl. Catal. B* 93, (2009), pp.119-125.

173. Larramona, G., Chone, C., Jacob, A., Sakakura, D., Delatouche, B., Pere, D., Cieren, X., Nagino, M. and Bayon, R., *Chem. Mater.* 18, (2006), pp. 1688-1696.
174. Zhu, B. L., Guo, Q., Huang, X. L., Wang, S. R., Zhang, S. M., Wu, S. H. and Huang, W. P., *J. Mol. Catal. A* 249, (2006), p. 211.
175. Mussy, J.P. G., Macpherson, J. V. and Delplancke, J. L., *Electrochimica Acta* 48, (2003), p. 1131.
176. Lei, B., Xue, J., Jin, D., Ni, S. and Sun, H., *Rare Metals* 27, (2008), pp.445-450.
177. Ikuma, Y. and Bessho, H., *Int. J. Hydrogen Energy* 32, (2007), pp. 2689-2692.
178. Yang, L., Xiao, Y., Zeng, G., Luo, S., Kuang, S. and Cai, Q., *Energy and Fuels* 23, (2009), pp.3134-3138.
179. Furube, A., Du, L., Hara, K., Katoh, R. and Tachiya, M., *J. Am. Chem. Soc.* 129, (2007), pp. 14852-14853.
180. Milsom, E. V., Novak, J., Oyama, M. and Marken, F., *Electrochem. Commun.* 9, (2007), p. 436.
181. Lee, J. -H., Choi, H. -S., Lee, J. -H., Kim, Y. -J., Suh, S. -J., Chi, C. S. and Oh, H. -J., *J. Crystal Growth* 311, (2009), pp. 638-641.
182. Sun, L., Li, J., Wang, C., Li, S., Lai, Y., Chen, H. and Lin, C., *J. Hazardous Materials* 171, (2009), pp. 1045-1050. (b).
183. He, B. L., Dong, B. and Li, H. L., *Electrochem. Commun.* 9, (2007), p. 425.
184. Yang, L., He, D., Cai, Q. and Grimes, C. A., *J. Phys. Chem.* 111, (2007), pp. 8214-8217.
185. Yu, J., Xiong, J., Cheng, B. and Liu, S., *Appl. Catal. B* 60, (2005), pp. 211-221.



186. Subramanian, V., Wolf, E. and Kamat, P. V., *J. Phys. Chem. B* 105, (2001), pp. 114-39-11446.
187. Anandan, S., Sathish Kumar, P., Pugazhenthiran, N., Madhavan, J. and Maruthamuthu, P., *Sol. Energy Mater. Sol. Cells* 92, (2008), pp. 929-937.
188. Hyung, M. S., Hea, R. C., Hoe, J. H., Sang, M. K. and Young, C. B., *J. Photochem. Photobiol. A* 163, (2004), pp. 37-44.
189. Bavykin, D. V. and Walsh, F. C., "Titanate and Titania Nanotubes: Synthesis, Properties and Applications", (2010), Published by Royal Society of Chemistry, Cambridge, UK.
190. Haehnel, V., Fähler, S., Schaaf, P., Miglierini, M., Mickel, C., Schultz, L. and Schlörb, *Acta Materialia* 58, (2010), pp. 2330-2337.
191. Xie, Y., Zhou, L., Huang, C., Huang, H. and Lu, J., *Electrochimica Acta* 53, (2008), pp. 3643-3649.
192. Ong, K. G., Varghese, O. K., Mor, G. K., Shankar, K. and Grimes, C. A., *Solar Energy Materials and Solar Cells* 91, (2007), pp. 250-257.
193. Raja, K. S., Misra, M., Mahajan, V. K., Gandhi, T., Pillai, P. And Mohapatra, S. K., *J. Power Sources* 161, (2006), pp. 1450-1457.
194. Ratnawati, Gunlazuardi, J., Dewi, E. L. and Slamet, *International Journal of Hydrogen Energy* 39, (2014), pp. 16927-16935.
195. Isimjan, T. T., Trifkovic, M., Abdullahi, I., Rohani, S. and Ray, A. K., *Top catal.* 58, (2015), pp. 114-122.
196. Yoo, J., Zazpe, R., Cha, G., Prikryl, J., Hwang, I., Macak, J. M. and Schmuki, P., *Electrochemistry Communications* 86, (2018), pp. 6-11.

197. Yang, M., Zhang, L., Jin, B., Huang, L. and Gan, Y., *Applied Surface Science* 364, (2016), pp. 410-415.
198. Kavil, Y. N., Shaban, Y. A., Al Farawati, R. K., Orif, M. I., Zobidi, M. and Khan, S. U. M., *Journal of Photochemistry and Photobiology A: Chemistry* 347, (2017), pp. 244-253.
199. Kroon, J. M., Bakker, N. J., Smit, H. J. P., Liska, P., Thampi, K. R., Wang, P., Zakeeruddin, S. M., Gratzel, M., Hinsch, A., Hore, S., Wuerfel, U., Sastrawan, R., Durrant, J. R., Palomares, E., Pettersson, H., Gruszecki, T., Walter, J., Skupien, K. and Tulloch, G. E., *Prog. Photovoltaics* 15, 2007, pp. 1–18.
200. Rani, S., Roy, S. C., Paulose, M., Varghese, O. K., Mor, G. K., Kim, S., Yooriya, S., LaTempa, T. J. and Grimes, C. A., *Phys. Chem. Chem. Phys.* 12, (2010), pp. 22780-2800.
201. Paulose M., Shankar, K., Varghese, O. K., Mor, G. K., Mor, G., Hardin, B. and Grimes, C. A., *Nanotechnology* 17, (2006) pp. 1446-1448.
202. Xie, Z. B., Adams, S., Blackwood, D. J. and Wang, J., *Nanotechnology* 19, (2008), 405701, pp. 1-6.
203. Mor, G. K., Shankar, K., Paulose, M., Varghese, O. K. and Grimes, C. A., *Nano Lett.* 5, (2005), pp. 191-195.
204. Liang, H. –C. and Li, X. –Z., *J. Hazardous Materials* 162, (2009), pp. 1415-1422.
205. Liang, H-C and Li, X-Z, *Applied Catalysis B: Environmental* 86, (2009), pp. 8-17.

206. Zhao, Q., Li, X., Wang, N., Hou, Y., Quan, X. and Chen, G., *J. Nanopart. Res.* 11, (2009), pp. 2153-2162.
207. Quiroz, M. A., Martinez-Huitle, C. A., Meas-Vong, Y., Bustos, E. and Cerro-Lopez, M., *Journal of Electrochemical Chemistry* 807, (2017), pp. 261-267.
208. Xie, Y., *Electrochimica Acta* 51, (2006), pp.3399-3406.

## Chapter 3

### 3 Fabrication of Titania Nanotube Arrays in Viscous Electrolytes

\*A version of this chapter was published as:

Ahmed El Ruby Mohamed, Nualjarose Kasemphaibulsuk, Sohrab Rohani and Shahzad Barghi, "Fabrication of titania nanotube arrays in viscous electrolytes", *J. Nanosci. Nanotechnol.* 10, (3), (2010), pp.1998-2008.

\*\*Another version of this chapter was published as:

Ahmed El Ruby Mohamed and Sohrab Rohani, "Synthesis of Titania Nanotube Arrays by Anodization", *AIDIC Series Vol. 9*, (2009) pp. 121-130. DOI:10.3303/ACOS090915.

### 3.1 Abstract

This study probes the dependence of titania nanotube arrays nanoarchitecture on different synthesis parameters in viscous electrolytes. Titania nanotube arrays were synthesized in glycerol, ethylene glycol and carboxymethylcellulose as base materials. The effects of anodization voltage and time, as well as chemical composition and pH of the electrolyte bath were studied. Nanotube arrays with an inner diameter ranging from 16 to 91 nm, and wall thickness ranging from 7 to 29 nm were fabricated in a glycerol–water electrolyte. Water content of 5 wt.% or higher was found to be essential for nanotubes fabrication in glycerol electrolyte. Diameter and length were influenced by varying water content above 5 wt.%. Nanotube length was found to be time dependent at high pH values. A pH value of 6 was favorable for fabrication of highly ordered and continuous nanotube arrays with length up to 900 nm. Using modified ethylene glycol (containing 2 wt.% and 0.5 wt.%  $\text{NH}_4\text{F}$ ) instead of glycerol, resulted in nanotube length up to 430 nm after 1.5 h anodization time. With a minor modification of electrochemical anodization cell, double-sided titania nanotube arrays layers with a total thickness of 9.5  $\mu\text{m}$  were successfully fabricated for the first time. Nanotube arrays were successfully fabricated in 2 wt.% sodium carboxy methylcellulose aqueous electrolyte (CMC electrolyte). These nanotube arrays had an inner diameter of 42 nm similar to those fabricated in 2 wt.% urea–ethylene glycol electrolyte but their length was 450 nm.

**Keywords:** Titania Nanotube Arrays, Anodization, Anodization parameters, Viscous electrolytes, Nanotubular structure.

## 3.2 Introduction

In the last decade, low-dimensional nanostructural materials have attracted increasing scientific and technological attention due to their physical properties and their potential applications [1]. Dimensionality has a crucial role in determining the properties and performance of nanomaterials [2, 3]. Therefore, the control of size and shape of nanomaterials is of immense importance. In contrast to size control, shape control of nanostructural materials is more difficult and challenging. The tubes, flakes or wires in the nanoscale region possess novel properties. The discovery of carbon nanotubes by Iijima [4] with their diverse interesting properties has motivated the quest for the synthesis of nanotubular structures of other substances and chemical compounds such as  $V_2O_5$ ,  $SiO_2$ ,  $TiO_2$ ,  $Fe_2O_3$ ,  $ZrO_2$  and  $MoO_3$ . Among these materials, titanium dioxide (titania) has attracted great interest since the discovery of its photosensitivity by Honda and Fujishima [5] in 1972 and due to its strong photo-oxidizing potential, high chemical stability, non-toxicity and low cost [6]. Titania nanotubes have improved properties compared to any other form of titania for applications in water and air purification photocatalysis, sensing, water photoelectrolysis for hydrogen generation, photovoltaics, photoelectrochemical solar cells [7-9], electronics, optics [10], tissue engineering and molecular filtration [11, 12]. The widespread technological use of titania is impaired by its wide band-gap (3 eV for anatase phase and 3.2 eV for rutile phase), which requires ultraviolet (UV) irradiation for photocatalytic activation. Because UV spectrum accounts for only a small fraction (8%) of the solar spectrum compared to visible light (45%), any shift in the light absorbance of titania from the UV towards visible spectrum region will improve the photocatalytic and photoelectrochemical utility of the material. Titania band gap can be narrowed by doping

with different nonmetal ions such as N [13, 14], C and S [15-17] and different metal ions such as Fe, Mo, Ru, Os and V [18]. When employing dopants to change the photo-response of a material, it is desirable to maintain the integrity of the host material crystal structure while changing its electronic structure. The crystalline structure of the material is directly related to the ratio of cation and anion size in the crystal lattice. It appears to be relatively easier to replace  $\text{Ti}^{4+}$  in titania with any cation than to substitute  $\text{O}^{-2}$  with any other anion due to the difference in the charge states and ionic radii [7]. Titania nanotubes are known to be synthesized in two forms: powdery form and self-organized titania nanotube arrays form. Nanotubes in the latter form are self-organized, vertically oriented and supported on a surface forming an integrated unit. Powdery titania nanotubes, and nanotube arrays, have been produced by a variety of methods including deposition into a nanoporous alumina template [19], sol-gel [20], and hydrothermal processes [21]. However, among these nanotubes fabrication routes, the electrochemical anodization method has attracted the most interest due to its ability to produce integrative, vertically-oriented highly ordered nanotube arrays with controllable dimensions [7, 22-25].

In contrast to random nanoparticle systems where slow electron diffusion typically limits their performance [11, 26], the precisely oriented nature of the crystalline nanotube arrays makes them excellent electron percolation pathways for the vertical transfer of electrical charges across the length of nanotubes [26, 27]. In addition, the nanotube-array architecture is able to influence the absorption and propagation of light through the architecture by precisely designing and controlling the nanotube internal diameter, wall thickness, and length [28]. These advantages have manifested themselves in an extraordinary enhancement of the extant  $\text{TiO}_2$  properties. For example, titania nanotube arrays of single-

micron length exhibited a remarkably high sensitivity when used in H<sub>2</sub> sensing with unprecedented 50 billion% change in electrical resistivity upon exposure to 1000 ppm of hydrogen gas at room temperature [28, 29]. In their use as hydrogen sensors, the TiO<sub>2</sub> nanotube arrays possess such excellent photocatalytic properties that they are able to self-clean from environmental contamination with exposure to ambient light [7]. Among one-dimensional architectures, nanotube arrays have a higher surface area than nanowires due to the additional surface area enclosed inside the hollow structure. For a given pore diameter and wall thickness, the internal surface area increases almost linearly with nanotube length [28].

The world is rapidly running out of fossil fuels. As a matter of considerable urgency, technologies for the generation of new types of energy must be developed. There is a growing consensus that hydrogen has the potential to supplement and ultimately replace fossil fuels to produce energy [30, 31]. At the same time there is a growing consensus that the emission of greenhouse gases has to be reduced in order to address global warming which has become increasingly obvious and problematic [31, 32]. Therefore, there is an urgent need to develop renewable and clean sources of energy, such as solar energy [31-33]. Hydrogen produced from the splitting of water using solar energy, termed solar-hydrogen, represents a sustainable fuel that is environmentally safe. Solar-hydrogen has the capacity to assure global energy sustenance and to reduce global warming [34]. The bottle-neck in the development of solar-hydrogen is the development of new photosensitive materials for efficient and clean conversion of solar energy [35, 36]. The development of these materials, which must exhibit sophisticated functional properties, requires the application of the most recent progress of the science of material interfaces and the solid-



state science as well as nanotechnology. There is a growing awareness that titania nanotube arrays developed by anodization method are the most promising candidates for the development of photoelectrodes for solar hydrogen production [25]. Furthermore, the development of titania nanotube arrays is not limited to fuel generation as an end-point. This material has many alternative applications including water purification, self-cleaning building and paving forms, sensing and electronic applications [37, 38]. Electrochemical anodization of metals and semiconductors is a relatively simple process for creating precisely engineered semiconductor nanostructures. Anodization is used to create highly ordered, self-oriented nanoporous materials such as alumina, silica, titania and zirconia. Anodization of titanium foils and thin films have been conducted using a two-electrode electrochemical cell with a platinum foil as cathode at a constant potential. A third electrode could be used as a standard reference electrode to eliminate noise effect when measuring the cell potential by a potentiostat [39, 40].

The key processes responsible for anodic formation of nanoporous alumina and titania nanotubes appear to be the same, and are fundamental to the formation of straight titania nanotubes [41]. The key processes are:

1. Oxide growth at the surface of the Ti metal due to interaction of the metal with  $O^{2-}$  or  $OH^-$  ions.
2. Metal ion ( $Ti^{4+}$ ) migration from the metal at the metal/oxide interface.  $Ti^{4+}$  cations will be ejected from the metal/oxide interface under application of an electric field and move towards the oxide/electrolyte interface.

3. Field-assisted dissolution of the oxide at the oxide/electrolyte interface. Due to the applied electric field the Ti–O bond undergoes polarization and tends to be weak promoting dissolution of the metal cations.  $\text{Ti}^{4+}$  cations dissolve into the electrolyte, and the free  $\text{O}^{2-}$  anions migrate towards the metal/oxide interface to interact with the metal.
4. Chemical dissolution of the metal or oxide, by the acidic electrolyte during anodization [7, 41, 42]. The chemical dissolution rate depends on the pH-value, which then causes more etching at the pore-bottom than at the opening and at the walls of the nanotubes.

In the initial stages of the anodization process, field-assisted dissolution dominates chemical dissolution due to the relatively large electric field across the thin oxide layer (the resistance to the current is minimum). Small pits form due to the localized dissolution of the oxide. The pits convert into bigger pores and the pore density increases. Subsequently, the pores spread uniformly over the surface. The pore growth occurs due to the inward movement of the oxide layer at the pore bottom (barrier layer). This occurs due to the above-mentioned processes (1) to (3) [42]. Figure 3-1 shows a systematic illustration of the development of titania nanotube arrays by anodization [7].

The maximum length of titania nanotube arrays fabricated in low pH, HF-aqueous electrolytes was found to be limited to about 500 nm [43]. Some other works showed that longer nanotube arrays can be achieved by adjusting the pH-profile inside the tubes. For example, to use near-neutral pH values at the nanotube top and more acidic local pH values at the bottom of the nanotubes, increases the nanotube length. This pH gradient across the

length of nanotubes can be achieved by using viscous electrolytes because the diffusion of  $H^+$  ions produced from the dissolution reactions at the nanotube bottom becomes much slower in viscous electrolytes than in aqueous electrolytes resulting in more acidity at the nanotubes bottom than at the nanotubes top [43, 44]. In addition to positively affecting the length of the nanotube arrays, viscous organic electrolytes have proved to be instrumental in doping of nanotubes with nonmetal ions such as C, N and S [45]. In contrast to anodization in aqueous based electrolytes, the investigation of effect of anodization parameters in viscous organic electrolytes has not been widely reported. This study aims at investigation of the effect of different anodization parameters on titania nanotubes morphology fabricated in aqueous glycerol and ethylene glycol based electrolytes.

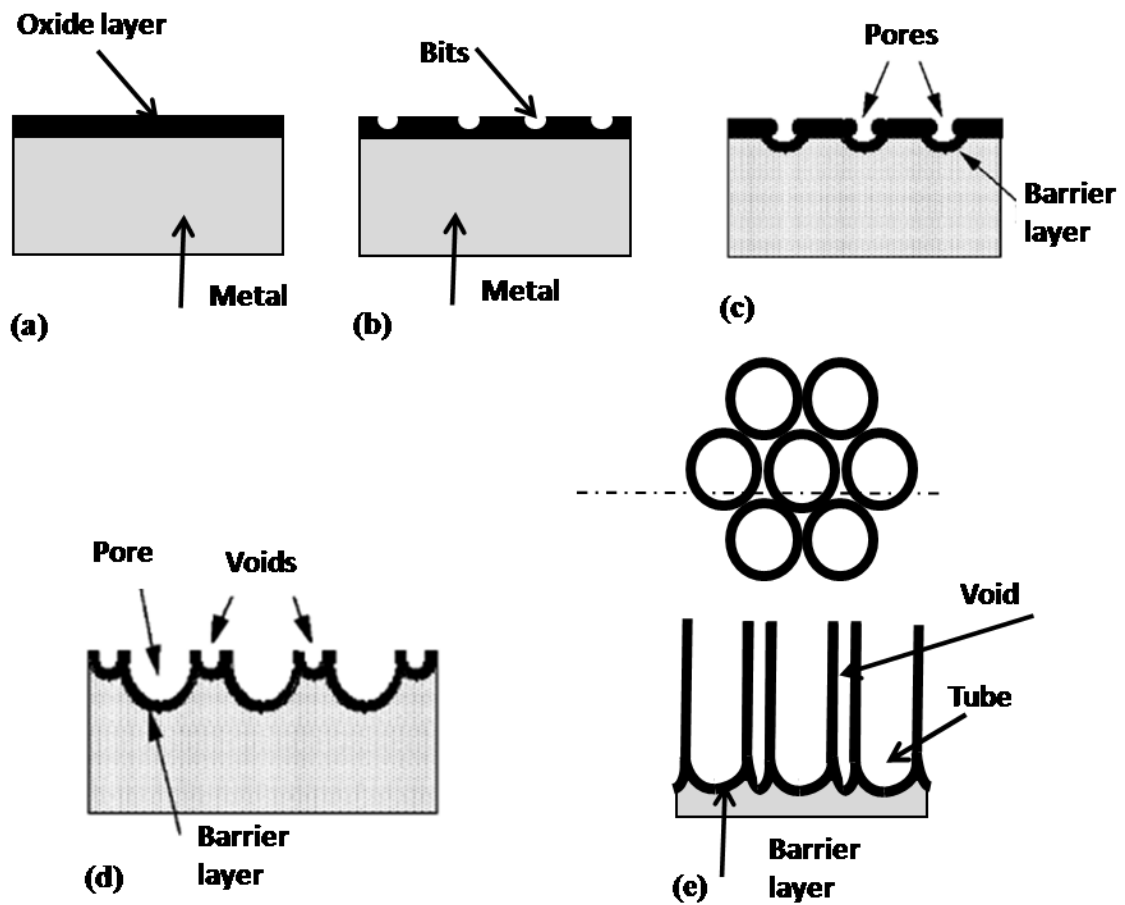


Figure 3-1 Figure 3-1 Schematic diagram of the evolution of a nanotube array at constant anodization voltage: (a) oxide layer formation, (b) pit formation on the oxide layer, (c) growth of the pit into scallop shaped pores, (d) metallic part between the pores undergoes oxidation and field assisted dissolution, and (e) fully developed nanotube array with a corresponding top view. (Redrawn with permission from Ref. [7]).

### 3.3 Experimental setup and methods

The experiments were carried out in a two-electrode electrochemical cell where the two electrodes were placed 4 cm apart. Titanium foil, over which titania nanotubes were grown, was used as anode while platinum foil was the counter electrode. A direct current power supply (Bio-Rad Laboratories, model 400, Irvine, CA) was employed as a source of constant potential. The DC power supply was equipped with a data acquisition system and a state-of-the-art algorithm and interface for real time monitoring of electrical current and voltage during the experiments. An ultrasonic bath was used for degreasing of titanium foil and final cleaning of fabricated nanotubes. The ultrasonic waves were also used for agitation of the electrolyte during the anodization process to improve the quality of nanotubes by mixing at microscopic level which led to detachment of bubbles from the surface of the electrode. The pH of the electrolyte was measured using an Orion 5-star plus Benchtop multimeter (Thermoelectron Corp., Waltham, MA). All experiments were carried out at room temperature around 25°C. The morphology of titania nanotube arrays was studied using Hitachi S 4500 field emission SEM. The cross-sectional images were taken on mechanically bent samples where titania nanotube layers were liberated from the supporting Ti foil. All experiments were carried out under a fume hood. Titanium foils (0.89 mm thick, 99.7% purity, Alfa Aesar, Ward Hill, MA) cut into 1.4 cm diameter discs. The Ti disc was mounted in a Teflon holder so that only one face of it was exposed to the electrolyte. Glycerol (A. R., 99.5%, Caledon Laboratory Ltd., Georgetown, ON), ethylene glycol 99.5 % with water residual ~ 0.4%. (Caledon Laboratory Ltd., Georgetown, ON),  $\text{NH}_4\text{F}$ ,  $\text{NH}_4\text{NO}_3$ , urea (All three chemicals were A. R. 98 %, J. T. Baker purchased from Mallinckrodt Baker Inc., Phillipsburg, NJ) and deionized water were used in the experiments

without any further treatment. Titanium foil discs were degreased by sonication in methanol followed by rinsing with deionized water. Then, they were chemically polished in nitric and hydrofluoric acids solution (5.6 M and 3.3 M, respectively) for 10 sec. The solution was agitated gently to avoid uneven corrosion resulting in non-homogeneous surface of the discs. The discs were then kept in deionized water in an ultrasonic bath for about 5 min and dried in clean oil free air. The pretreated discs were kept in a closed vessel to prevent the deposition of dust and any effect of surrounding air or other gases on the discs surface. Anodization of Ti foils was carried out at room temperature using a two-electrode electrochemical cell (4 cm apart) with a direct current power supply as illustrated in Figure 3-2. Titania nanotube arrays were grown from Ti foils by potentiostatic anodization in glycerol/water electrolyte or ethylene glycol electrolyte, containing 0.5 wt.%  $\text{NH}_4\text{F}$ . In glycerol/water electrolyte, the water content was changed from 0 to 99.5 wt.% and the corresponding electrolyte composition are summarized in Table 3-1. After anodization, the samples were sonicated in ultrasonic bath in methanol and then in deionized water for 5 min each.

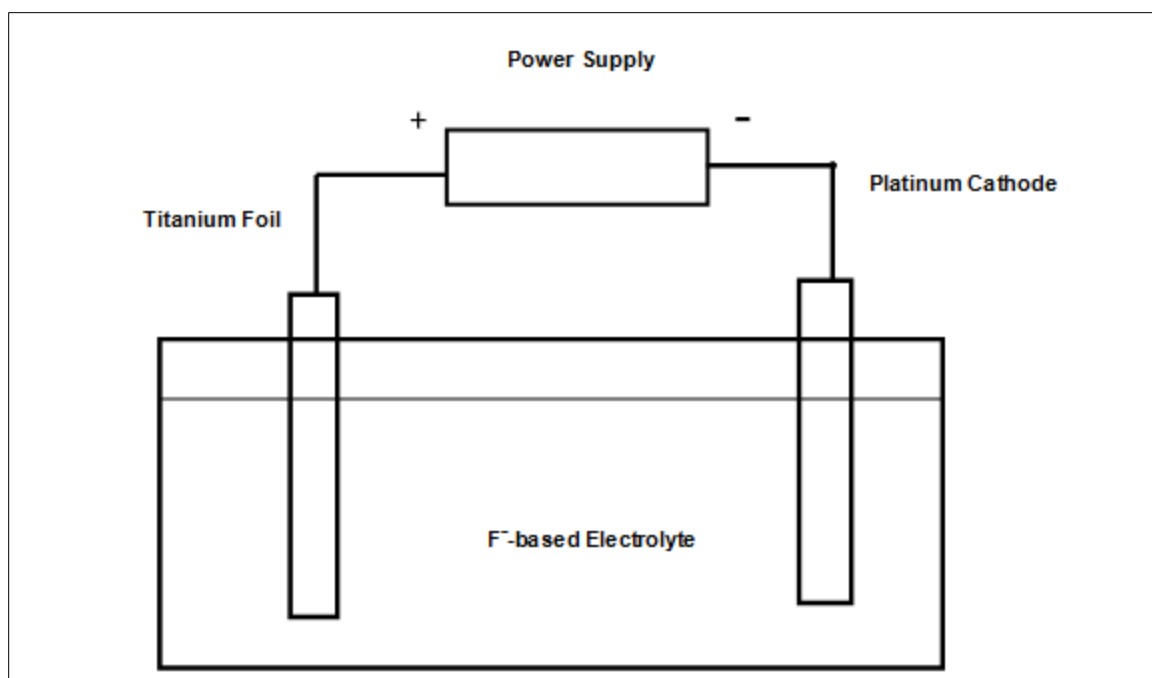


Figure 3-2 Schematic drawing of an electrochemical cell in which the Ti electrode is anodized. Titania nanotube arrays are grown on the Ti metal electrode surface which is in contact with the electrolyte.

**Table 3- 1 Electrolyte compositions at different water content**

| Electrolyte batch name<br>(Water content, %) | 0    | 5    | 16   | 30   | 50   | 70   | 90  | 99.5 |
|--|------|------|------|------|------|------|-----|------|
| Glycerol, wt. %                              | 99.5 | 94.5 | 83.5 | 69.5 | 49.5 | 29.5 | 9.5 | 0    |
| Water, wt. %                                 | 0*   | 5    | 16   | 30   | 50   | 70   | 90  | 99.5 |
| NH <sub>4</sub> F, wt. %                     | 0.5  | 0.5  | 0.5  | 0.5  | 0.5  | 0.5  |     | 0.5  |

\* ( $\approx 0.4\%$  residual water exists in glycerol).

## 3.4 Results and Discussion

Titania nanotubes were fabricated at different conditions and the effects of voltage, pH, water content and anodization time were investigated.

### 3.4.1 Effect of Anodization Voltage

Formation and architecture of titania nanotubes depend on a number of parameters. Due to electrochemical nature of the process, applied voltage during the anodization is crucial in the quality of the nanotubes and their dimensions. It is essential to keep the voltage fixed where the current density will change due to the changes in resistance between the two electrodes. The majority of published results on the synthesis of titania nanotube by anodization have been carried out in the voltage range of 10- 20 volts. Some researchers reported that no nanotubes were formed at voltages higher than 25 volts [39], while others were able to grow nanotubes at voltages above 30 volts [46]. Watcharenwong and co-workers synthesized titania nanotubes at 40 volts and observed coalescence of nanotubes tip at this voltage. The synthesized nanotubes at 60 volts were much shorter due to collapse of nanotube tips [47]. Albu and coworkers synthesized long titania nanotubes at higher voltages (up to 250 volts) by decreasing fluoride ion concentration in the electrolyte. Therefore, depending on the chemical composition of electrolyte and operating conditions, titania nanotubes with different geometries can be synthesized. However, in any fixed electrolyte composition, there is a voltage above which the nanotubes become shorter and may not be even formed [48]. For example, in aqueous electrolytes containing a large concentration of ions, the TiO<sub>2</sub> barrier layer (the bottom of nanotubes) exhibits dielectric breakdown at certain voltage value. Beyond dielectric breakdown, electronic conduction rather than the desirable ionic conduction contributes to all the anodization current. In other



words, as the dielectric constant of anodization electrolyte increases, the optimum voltage for nanotube formation increases. The higher breakdown potential of titanium oxide in organic electrolytes allows a larger potential window for nanotube formation [49]. For any specific electrolyte composition there is an optimum range of anodization voltage wherein specific nanotubular structures are obtained. It must be mentioned that fluoride concentration and anodization potential are the two main factors affecting the nanotubes formation and geometry [50]. Several anodization experiments were conducted to study the effect of voltage on synthesis and nanoarchitecture at the following conditions: pH: 6, water content: 16 wt.%, anodization time: 1.5 h. Results are shown in Figure 3-3. Titania nanotube diameter increased with increasing voltage. Similar trends have been reported by Mor and co-workers [7] (max 25 volts) and Petukhov and co-workers (max 30 volts) [46] as shown in Figure 3-4. In spite of similarities in the electrolyte composition, Petukhov obtained at 0°C, which was much lower than the temperature in this study, smaller diameter nanotubes. It is challenging to compare the results between different studies due to the sensitivity of the anodization process to minor changes in the experimental conditions. In this study, experiments at 40 volts revealed that the nanotubes were formed at the edge of the sample while at the center, only shallow pores appeared (see Figure 3-3: e and f). The discontinuity could be attributed to the field-assisted high dissolution rate at high voltages. Titania nanotubes wall thickness also increased with increasing anodization voltage as shown in Figure 3-5. The length of nanotubes also increased by increasing voltage up to a critical level above which, increasing rate of dissolution reduced the length of nanotubes.

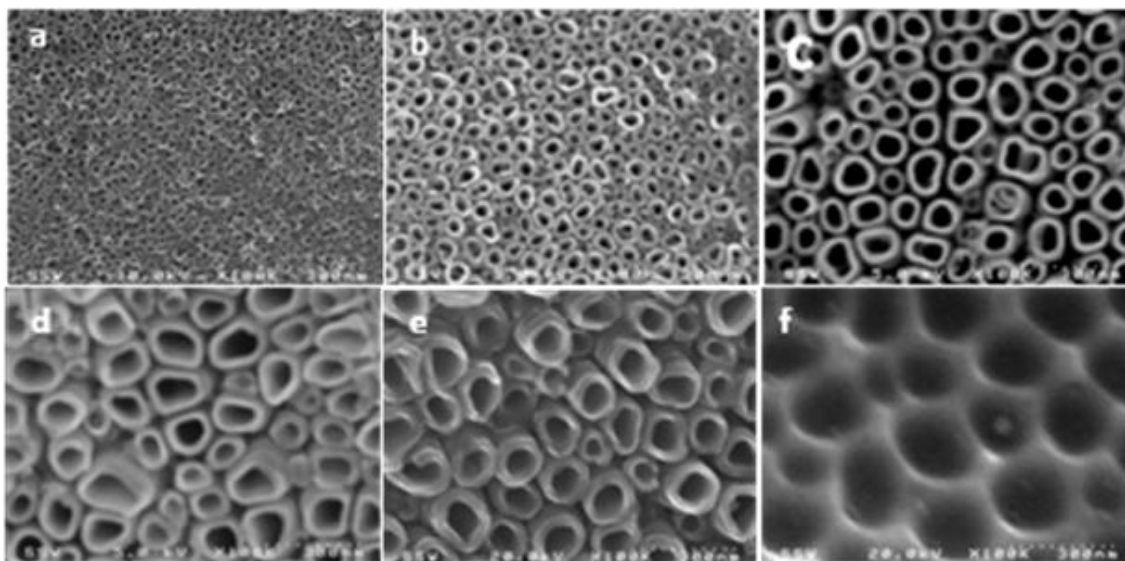


Figure 3-3 FESEM images for samples anodized at different voltage: a) 5V, b) 10V, c) 20V, d) 30V, e) 40V at sample edge, and f) 40V at sample center.

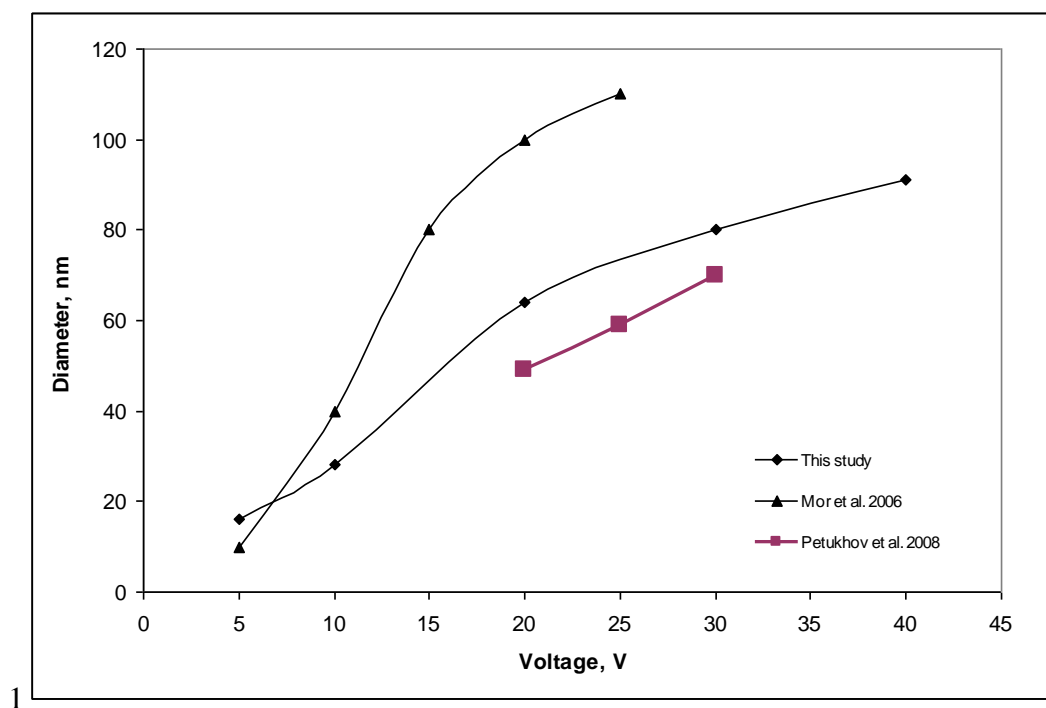
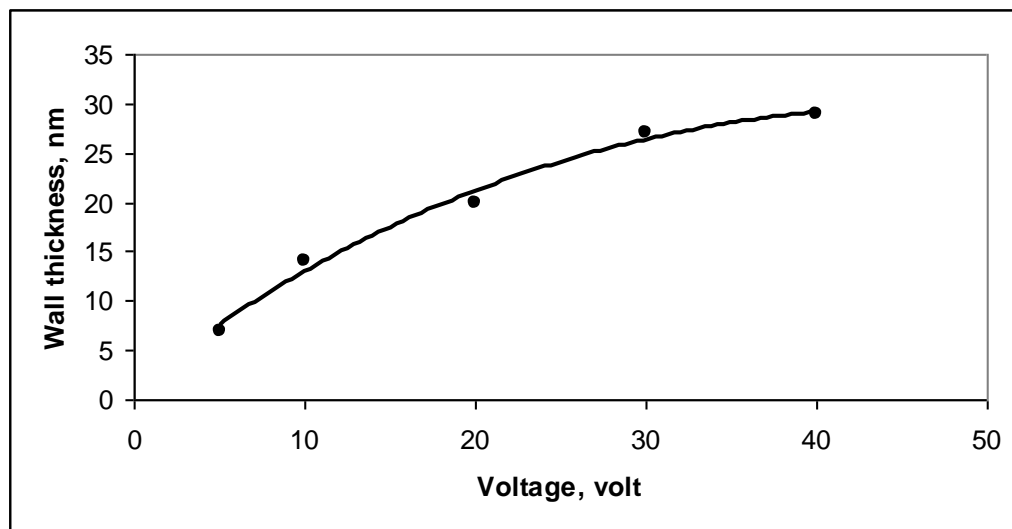


Figure 3-4 Effect of voltage on titania nanotubes diameter: a comparison between results in this study and previous studies.

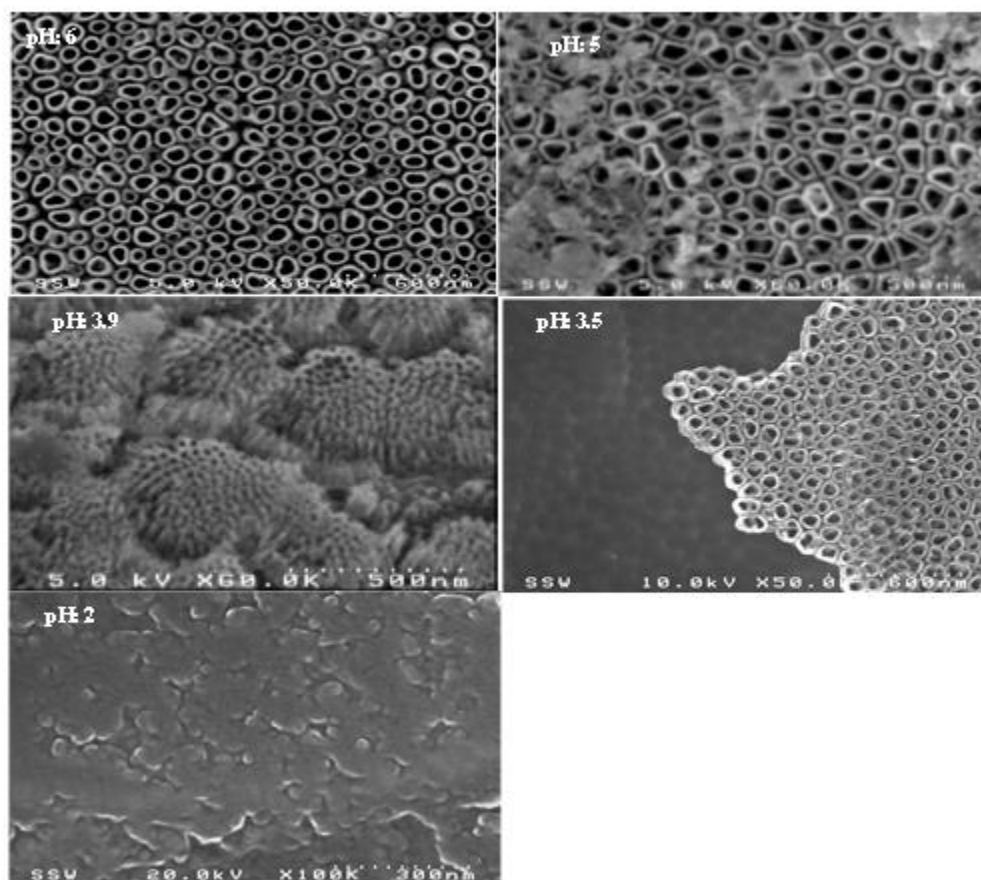


**Figure 3-5 Effect of voltage on wall thickness of nanotubes**

### 3.4.2 Effect of Electrolyte pH

Acidity of electrolyte solution plays an important role in synthesis of titania nanotubes. Etching and corrosion processes are directly related to pH of the electrolytes containing fluoride ions. Interestingly, apart from the pH of electrolyte solution, the formation of anodization reaction products can induce local changes of pH in the vicinity of nanotubes which has more profound effect on anodization process compared to electrolyte acidity. The role of pH in the formation mechanism of titania nanotube arrays was explained in Section 2.5. in Chapter 2. In fact, the electrochemical reactions in an acidic electrolyte can be carried out at different voltages and the level of applied voltage affects the local pH, which in turn leads to the electrochemical dissolution of titanium foil. A series of experiments were conducted at different pH values. The electrolyte pH was controlled by adding drops of diluted sulfuric acid. Figure 3-6 shows the effect of pH on the formation and quality of nanotube arrays. Well-organized, vertically oriented nanotube arrays were

formed at pH: 5-6. A decrease of pH to 3.9 resulted in segregated bundles of nanotubes. As pH decreased to 3.5, nanotube arrays formed only in some parts of the sample surface. Further decrease of pH to 2, resulted in no nanotube arrays. According to the nanotube formation mechanism, as the pH decreased, the rate of chemical dissolution of  $\text{TiO}_2$  at electrode/electrolyte interface became larger than the rate of  $\text{TiO}_2$  formation at  $\text{Ti}-\text{TiO}_2$  interface, resulting in no nanotube formation. Direct comparison with the published data cannot be made due to the large variations in the chemical composition of the electrolyte and other operating conditions.



**3-6 FESEM top view images taken for samples anodized at different pH values.**

Figure 3-7: FESEM top view images taken for samples anodized at different pH values.

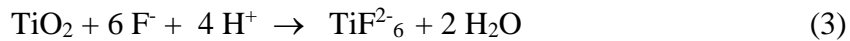
### 3.4.3 Effect of Water Content

In general, in the absence of water in electrolytes, the anodization process will suffer from lack of  $H^+$  ions and also high viscosity of the solution which leads to the formation of titanium dioxide layers only.

The overall reaction for anodic oxidation of titanium can be represented as:



In the initial stages of the anodization process, field-assisted dissolution dominates chemical dissolution due to the relatively large electric field across the thin oxide layer (the resistance to the current is minimum). Small pits formed due to the localized dissolution of the oxide, represented by the following reaction, act as pore forming centers:



The pits convert into bigger pores and the pore density increases. Subsequently, the pores spread uniformly over the surface. The pore growth occurs due to the inward movement of the oxide layer at the pore bottom (barrier layer).

Figure 3-7 shows SEM top view images of samples anodized at different water contents at 20 volts, pH: 6 and anodization time 1.5 h. Table 3-2 shows the effect of water content at the same operating conditions. Raja and coworkers [49] observed that a minimum amount

of 0.18% of water in ethylene glycol was required to form a well ordered titania nanotube arrays. In this study, no nanotube arrays were formed at 0 or 2 wt.% water.

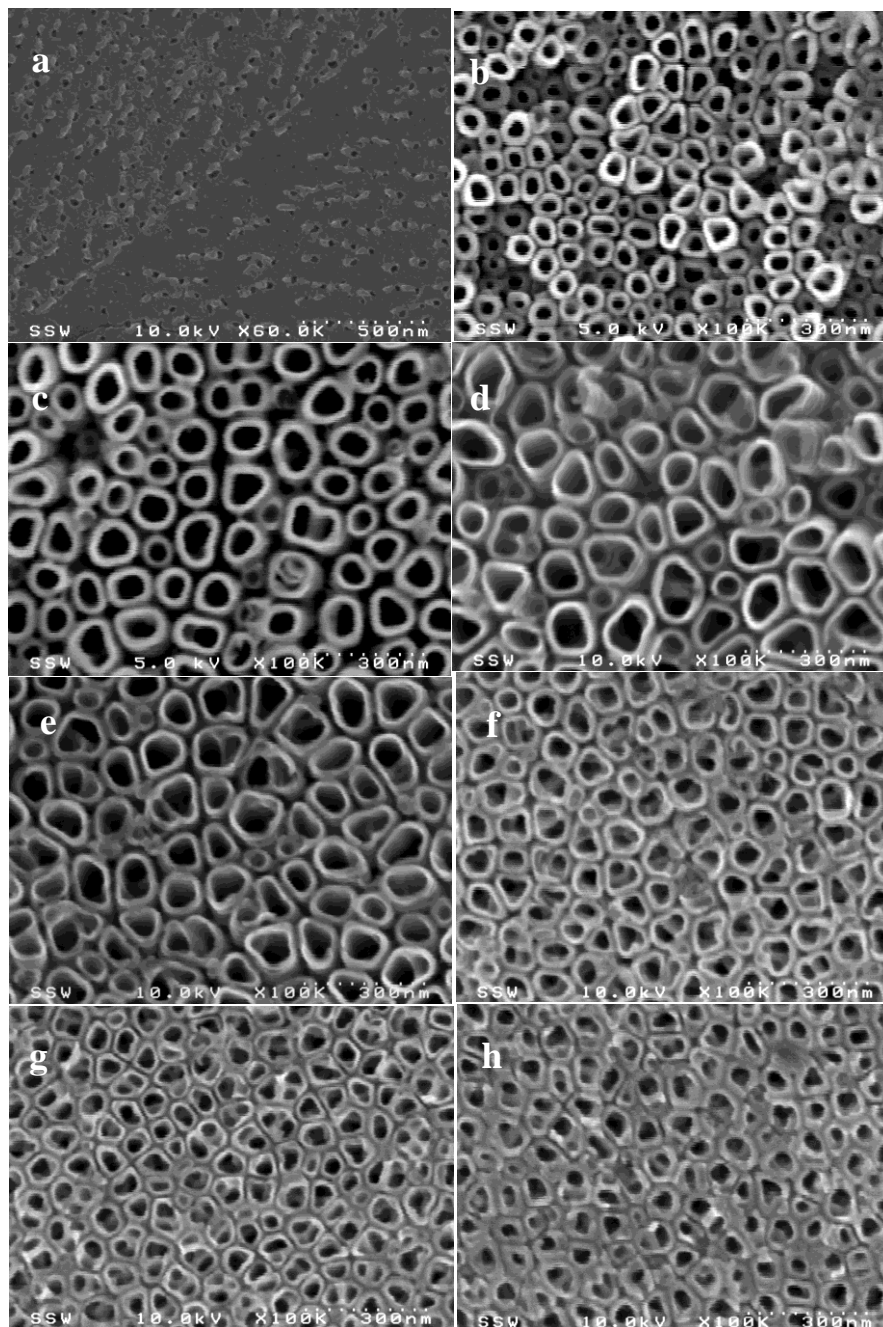


**Figure 3-8 SEM topview images for samples anodized at 20 V, pH: 6 and anodization time 1.5 h and H<sub>2</sub>O wt.%: a) 0, b) 5, c)16, d) 30, e) 50, f) 70, and g) 90, h) 99.5**

Table 3-2 Effect of water content in glycerol electrolyte on nanotube arrays formation and their nanoarchitecture

(20 volts, pH: 6, 0.5 wt.% NH<sub>4</sub>F and 1.5 h anodization time)

| H <sub>2</sub> O wt. % | 0    | 2    | 5  | 16  | 30  | 50  | 70  | 90  | 99.5 |
|------------------------|------|------|----|-----|-----|-----|-----|-----|------|
| Diameter, nm           | n/a* | n/a* | 38 | 64  | 76  | 72  | 48  | 43  | 40   |
| Wall Thickness, nm     | n/a* | n/a* | 18 | 20  | 20  | 18  | 13  | 12  | 14   |
| Length, nm             | n/a* | n/a* | -  | 250 | 512 | 900 | 533 | 460 | 424  |

\* (n/a): Not applicable because no nanotubes were formed at these conditions.

Well-ordered nanotube arrays began to form at 5 wt.% H<sub>2</sub>O and increasing water content from 5 wt.% to 50 wt.% affected the nanoarchitecture of nanotube arrays by increasing the inner diameter from 38 to 76 nm and nanotube length from 250 to 900 nm. Further increase of water content to 99.5 wt.% (0 % glycerol) led to a decrease in nanotube diameter and length to 40 nm and 424 nm, respectively. The increase of diameter and length with water content in the range from 5 to 50 wt.% can be explained due to the electrolyte viscosity. There are two competing rate processes: the growth rate at the bottom of the tube and the rate of chemical dissolution of the tubes at the top of nanotubes. Both processes are affected by the viscosity of the electrolyte and the rate of diffusion of different ions through it. At low water contents, the viscosity is very high, and this results in high H<sup>+</sup> ion concentration gradients between the bottom and top of the nanotubes. At the same time, the overall low

diffusion rate of other ions in the electrolyte, constraints the reaction rate. It was found that 50% water content was the optimum condition at which maximum nanotube growth rate was obtained as shown in Table 3-2. Figure 3-8 shows the effect of water content on the inner diameter of the nanotubes.

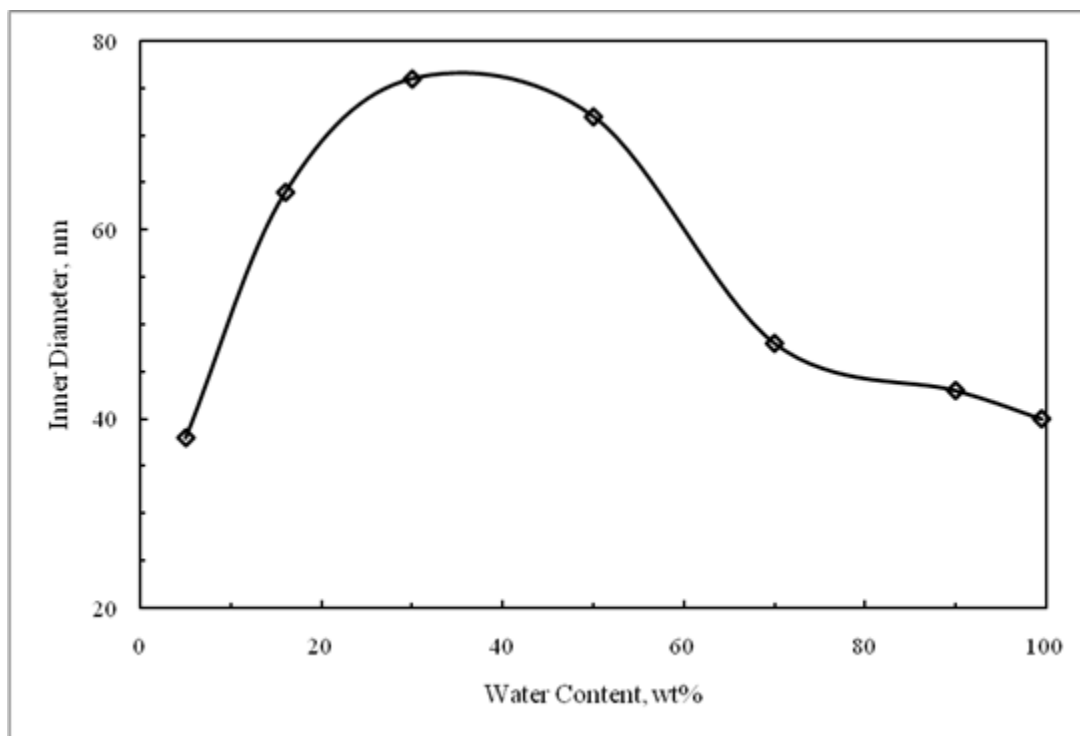


**Figure 3-9 Effect of water content on inner diameter of nanotubes.**

#### 3.4.4 Effect of Anodization Time

A few minutes are needed in aqueous electrolytes [39] for the preliminary development of the nanotubular structures. This is followed by an increase of the length of nanotubes. The growth of nanotube length is time dependent and the time dependence differs according to the composition of electrolyte bath. For the strong acidic HF – water based electrolytes, the nanotube length is time independent after the first hour because the rate



of chemical dissolution at the top of nanotubes equals the rate of nanotubes formation at the bottom of the tubes. Under these conditions, the length is limited to about 500 nm and further increase in anodization time does not increase the nanotube length. For aqueous electrolytes with near-neutral pH, the maximum nanotube length reported was 4.4  $\mu\text{m}$  after 20 h [25]. Macak and Schmuki [43] studied the effect of time on nanotube length in two electrolyte baths: (1) glycerol + 0.5 wt.%  $\text{NH}_4\text{F}$  and (2) 1 M  $(\text{NH}_4)_2\text{SO}_4$  + 0.5 wt.%  $\text{NH}_4\text{F}$  in water. For the first electrolyte they found that the length increased almost linearly with time until it reached 6  $\mu\text{m}$  after 18 h (nanotube length was time-dependent), while in the second electrolyte, the length reached its maximum value of about 2.5  $\mu\text{m}$  after 2 h and after that the nanotube length was time-independent for the rest of the 18 h. They also found that the rate of growth of nanotube length in water-based electrolyte was higher than in glycerol-based electrolyte in the first 2 h which could be attributed to the high viscosity of the glycerol electrolyte.

In the present study, several anodization experiments were conducted at pH: 10 V and 16 wt.% water content and different anodization times and the results are shown in Figures 3-9 and 3-10. SEM top view images in Figures 3-9 and the graph in Figure 3-10 indicate that increasing the anodization time affected neither nanotube diameter nor wall thickness and they remained approximately constant at 30 and 13 nm, respectively. But the nanotubes length increased from 200 nm to 470 nm when anodization time increased from 0.5 h to 10 h. It is worth-mentioning that by increasing the voltage from 10 to 20 volts and water content from 16 to 50 wt. %, nanotube arrays with length of 900 nm were obtained after only 1.5 h. This implies that longer nanotubes can be formed by increasing anodization time. It is desirable to have longer continuous nanotubes as the photocurrent

intensity increases with increasing the tube length. The results of this study agree with other research works which showed that the diameter and wall thickness of nanotube arrays are independent of anodization time when other anodization conditions are kept constant [7]. The results show that the length of nanotubes is time-dependent at high pH values (pH around 6). This is because at high pH, the growth rate of nanotubular oxide layer at metal/oxide interface is much higher than the dissolution rate of TiO<sub>2</sub> nanotubes at the oxide/electrolyte interface [25].

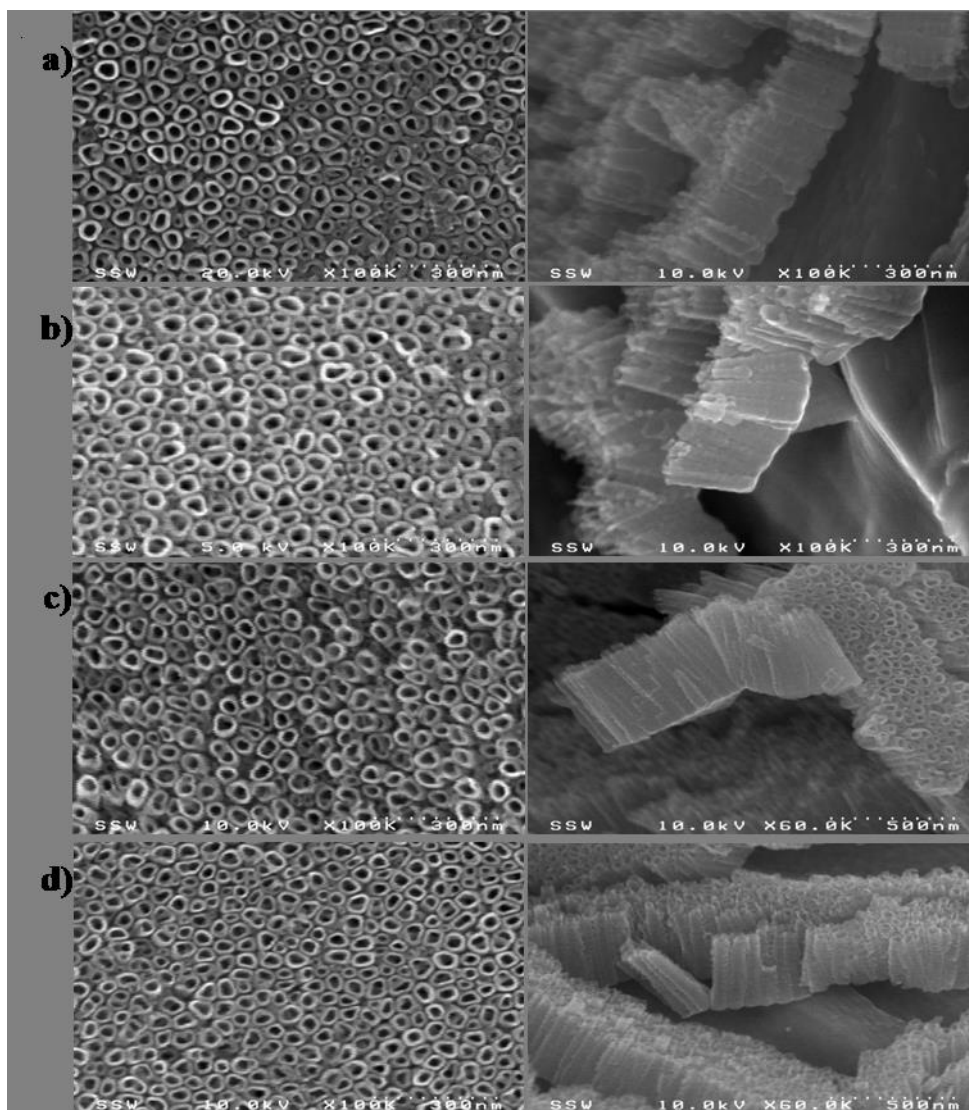
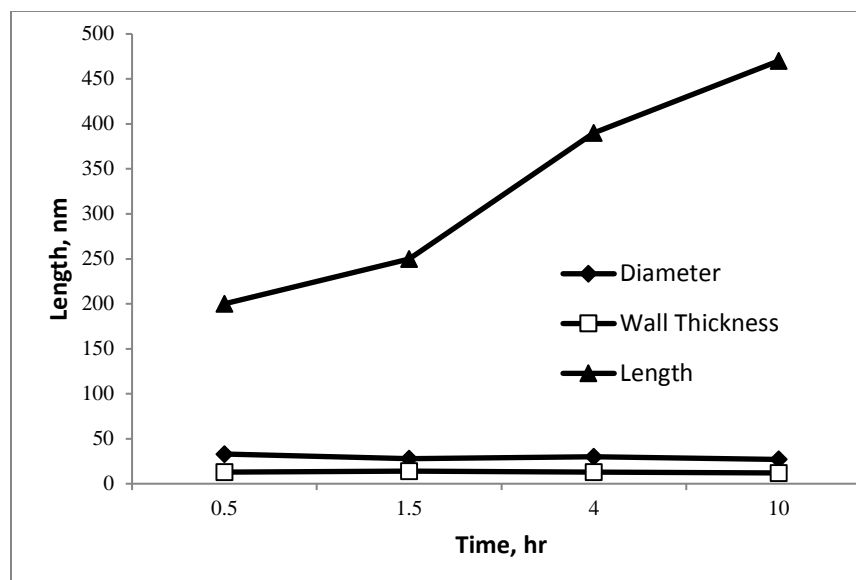


Figure 3-10 SEM images of top view and lateral view of TNTAs, fabricated in glycerol-based electrolyte at 10 V, pH: 6, H<sub>2</sub>O : 16 wt.% and various time intervals: a) 0.5 h, b) 1.5 h, c) 4 h and d) 10 h.



**Figure 3-11 Effect of anodization time on length, diameter and wall thickness of TNTAs fabricated in glycerol-based electrolyte at 10 V, 16 wt.% H<sub>2</sub>O, pH: 6 and 0.5 wt.% NH<sub>4</sub>F**

### 3.4.5 Anodization in Ethylene Glycol Electrolyte

As mentioned earlier, viscosity of the electrolyte has a direct impact on diffusion of reactants and products to and from the titania nanotubes surface. It is necessary to control diffusion for synthesis of well-organized titania nanotubes, however, there is a certain range out of which the viscosity has negative impact on synthesis and growth rate of titania nanotubes. The growth rate was low in glycerol-based ( $\eta = 945$  cP at 25°C) electrolytes and addition of water improved the growth rate due to the reduction in the viscosity of electrolyte solution. Ethylene glycol is less viscous ( $\eta = 16$  cP at 25°C) compared to glycerol and results in lower diffusion resistance. Therefore, the growth rate would be higher in ethylene glycol electrolytes. Parameters that were previously studied in glycerol experiments were fixed at 20 V, 1.5 h, pH: 6 and water content was kept at only the residual

amount (~ 0.4 wt.%). Urea and  $\text{NH}_4\text{NO}_3$  were added to study their effect on nanotubes morphology and as additional sources for nitrogen doping into the nanotubes. Results in Table 3-3 show that adding 1 wt.% urea increased nanotube length from 286 nm to 397 nm (more than 27%) and adding 2 wt.% urea increased the nanotube length to 430 nm (50 % increase). Adding 1-2 wt.% urea increased the nanotube diameter from 30 nm to around 40 nm and thickness from 11 nm to 18 nm. Urea is likely to have an inhibitory effect on acid corrosion of metals in the presence of halide ions. Adding 1 wt.% ammonium nitrate increased the nanotube length from 286 to 365 nm (21 % increase) while adding 2 wt.% ammonium nitrates to the electrolyte increased the length to 320 nm. This increase in nanotubes length in the presence of ammonium nitrate was attributed to the increase of electrolyte conductivity by addition of this ionic compound

**Table 3-3 Anodization in Ethylene Glycol: Fabrication conditions and nanotubes dimensions**

| Experiment # | Urea % | $\text{NH}_4\text{NO}_3$ % | TNTAs*<br>Length, nm | TNTAs*<br>Diameter, nm | Wall<br>thickness, nm |
|--------------|--------|----------------------------|----------------------|------------------------|-----------------------|
| 1            | 0      | 0                          | 286                  | 30                     | 11                    |
| 2            | 0      | 1                          | 365                  | 28                     | 11                    |
| 3            | 0      | 2                          | 320                  | 33                     | 9                     |
| 4            | 1      | 0                          | 397                  | 40                     | 18                    |
| 5            | 2      | 0                          | 430                  | 43                     | 16                    |

\*TNTAs: Titania nanotube arrays

### 3.4.6 Double-sided Nanotube Arrays Fabrication

The electrochemical anodization setup used in the above experiments was designed to allow only one side of the titanium foil to be in contact with the electrolyte. With some modifications of the setup, both sides of a one cm<sup>2</sup> disc were anodized by placing two platinum foils on both sides of the Ti foil at the same distance. Both platinum foils were connected to the negative terminal of the power supply. Figure 3-11 shows the SEM images of double-sided nanotube arrays fabricated in 0.5 wt.% NH<sub>4</sub>F and 1 wt. % urea in ethylene glycol for 12 h at 20°C. It is clear from Figure 3-11-a that the nanotube arrays exhibit a hexagonal close-packing order with an average inner diameter of 50 nm and wall thickness of 11 nm. Figure 3-11.b shows cross sectional view of the nanotube arrays with a length of 4.73 μm. Nanotube arrays were fabricated on both sides of Ti foil and with almost the same length and diameter. Hence, double-sided titania nanotube arrays layers of a total length of ~ 9.5 μm were fabricated. These double-sided grown TNTAs have a very interesting layers arrangement where Ti conducting metal layer sandwiched between two semiconducting TNTAs could have a promising electronic and photocatalytic applications. Furthermore, this setup modification can be used for fabrication of larger areas of Ti foils for higher rates of hydrogen production and more effective photocatalytic systems.

### 3.4.7 Anodization in CMC Aqueous Electrolyte

Due to the high cost of glycerol and ethylene glycerol as viscous electrolytes for Ti anodization, preliminary investigation of nanotube arrays fabrication in sodium carboxy methylcellulose (CMC) aqueous solutions was conducted.

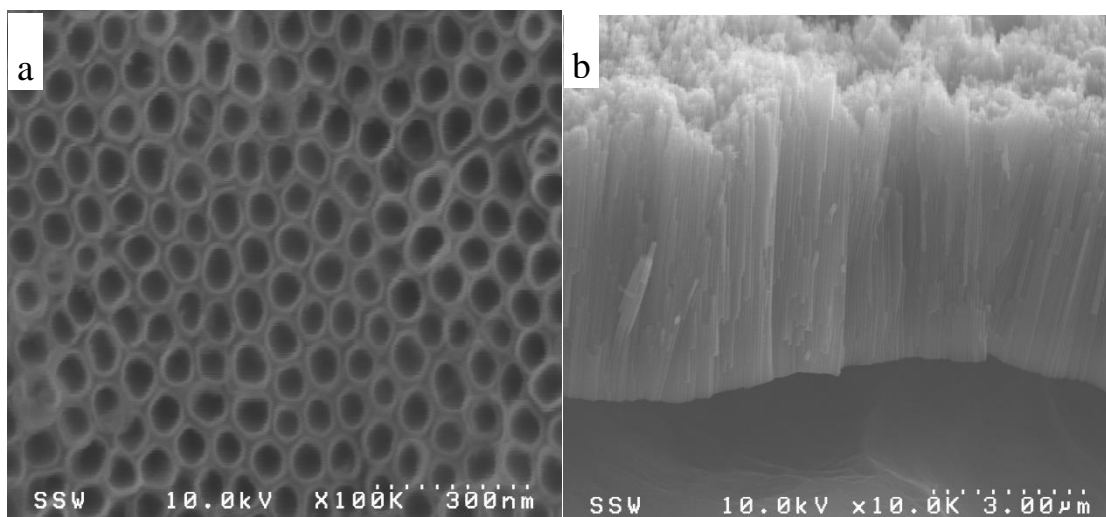


Figure 3-12 FESEM top and cross-sectional views of double-sided titania nanotube arrays anodized in 0.5 wt.%  $\text{NH}_4\text{F}$  + 1 wt. % urea in ethylene glycol

The use of CMC-based electrolyte for the anodization of titania is not reported in the literature. We were able to fabricate nanotube arrays by Ti anodization in CMC aqueous electrolyte. Figure 3-12 shows the SEM images of titania nanotube arrays fabricated at 20 volts, 2 wt.% CMC aqueous electrolyte, 0.5 wt.%  $\text{NH}_4\text{F}$ , pH: 6 and anodization time 1.5 hr. As it is shown in Table 3-4, the nanotubes length was 450 nm and the average diameter was 42 nm at 20 volts and 28 nm at 10 volts, which assures the trend of diameter increase with increasing voltage. Figure 3-13 shows a comparison between 7 different electrolyte compositions in terms of length and diameter of the nanotube arrays anodized at 20 V, pH: 6, 0.5 wt.%  $\text{NH}_4\text{F}$  and anodization time: 1.5 h. The electrolyte composition are as follows:

1: Water: 0.5 wt.%  $\text{NH}_4\text{F}$  in water, 2: Gl (16%  $\text{H}_2\text{O}$ ): 16 wt.% water in Glycerol, 3: Gl (Glycerol) :  $\text{H}_2\text{O}$ : 1:1 (wt./wt.), 4: Ethylene glycol (EG), 5: 2 wt.% Ammonium Nitrate in EG, 6: 2 wt.% urea in EG and 7: 2 wt.% CMC aqueous solution. As it can be easily seen from the histogram in Figure 3-13, maximum nanotube length and diameter were obtained from 50 wt.% water in glycerol. Nanotubes anodized in CMC electrolyte have almost the same diameter as those anodized in ethylene glycol (2 wt. % urea) electrolyte and those anodized in aqueous electrolyte (0 % glycerol) but the length of CMC –nanotubes was slightly higher than the nanotube length obtained from those both electrolytes. Also, CMC-nanotubes length was 80 % longer than the nanotube length obtained from 16 wt. % water in glycerol.

**Table 3-4 Diameter, wall thickness and length of titania nanotube arrays synthesized in CMC aqueous electrolyte.**

|             | CMC, wt.<br>% | Voltage,<br>V | Length,<br>nm | Diameter,<br>nm | Wall thickness,<br>nm |
|-------------|---------------|---------------|---------------|-----------------|-----------------------|
| Expr.<br>#1 | 2             | 20            | 450           | 42              | 13                    |
| Expr.<br>#2 | 2             | 10            | -             | 28              | 11                    |



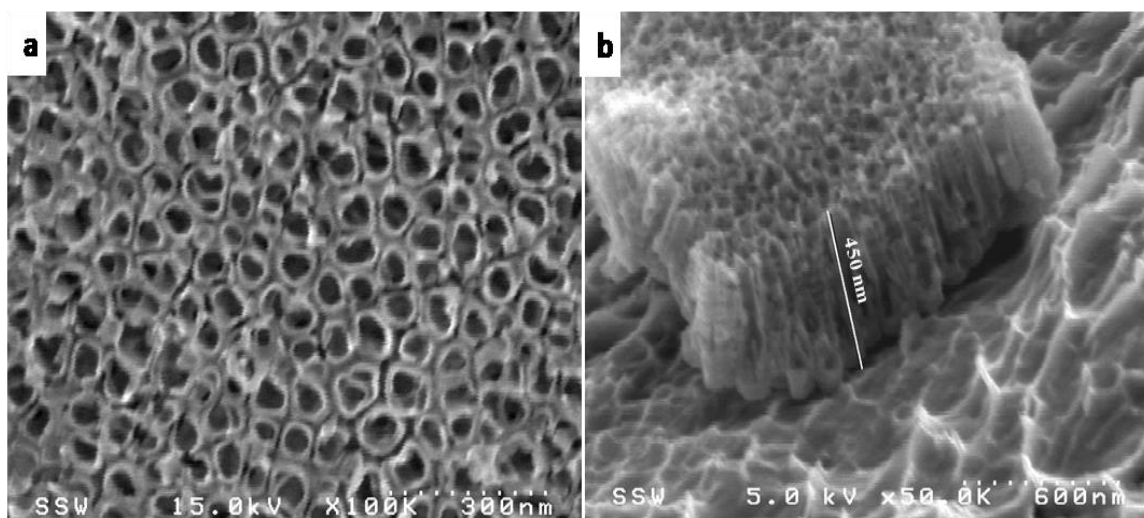


Figure 3-13 SEM image of titania nanotube arrays fabricated in 2 wt. % CMC aqueous solution at 20 V, pH: 6, 0.5 wt.%  $\text{NH}_4\text{F}$ , and 1.5 h: a) top view and b) lateral

view

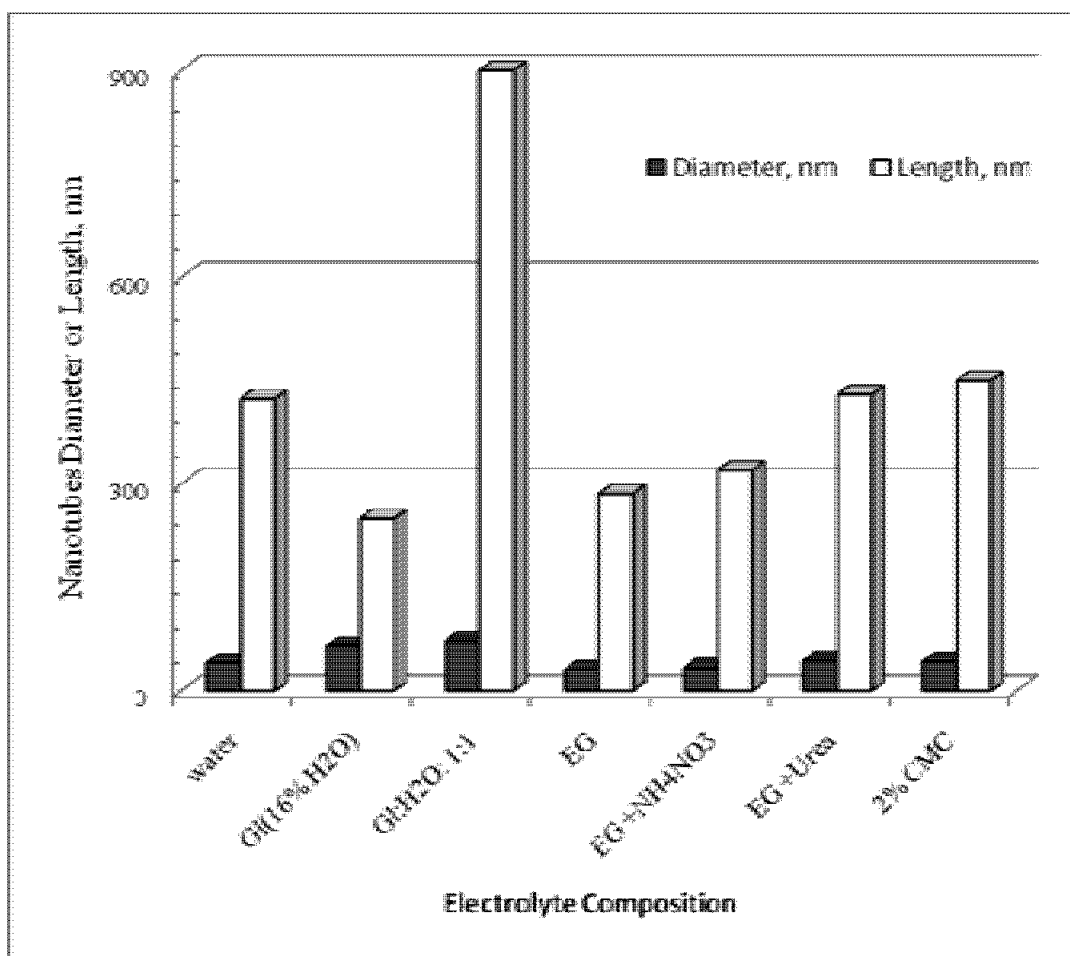


Figure 3-14 Comparison among different electrolyte compositions in terms of diameter and length of nanotubes (see electrolyte composition details in text).

### 3.5 Conclusions

Highly ordered Titania nanotube arrays were successfully fabricated in glycerol, ethylene glycol and CMC-based electrolytes. Our results showed that synthesis parameters play a

crucial role in both nanotube arrays formation and tailoring of their nanoarchitecture. Nanotube arrays with an inner diameter ranging from 16 to 91 nm, and wall thickness ranging from 7 to 29 nm were fabricated in a glycerol-water electrolyte. Water content of at least 5 wt.%, was found to be essential for nanotubes fabrication in glycerol electrolyte. Diameter and length were influenced by varying water content above 5 wt.%. Maximum length of 900 nm was achieved at 50 wt.% H<sub>2</sub>O in glycerol. Nanotube length was found to be time dependent at high pH values and a pH value of 6 was favorable for fabrication of highly ordered, long and continuous nanotube arrays. Using modified ethylene glycol solution instead of glycerol resulted in nanotubes length up to 430 nm after 1.5 h anodization time in ethylene glycol containing 2 wt. % urea and 0.5 wt.% NH<sub>4</sub>F. Double-sided titania nanotube arrays layers with a total thickness of 9.5 μm were fabricated for the first time with a minor modification in the anodization cell. These double-sided grown TNTAs have a very interesting layers arrangement where Ti conducting metal layer sandwiched between two semiconducting TNTAs could have a promising electronic and photocatalytic applications. Nanotube arrays were successfully fabricated in 2 wt. % sodium carboxy methylcellulose aqueous electrolyte.

### 3.6 References

1. Yuan, Y-Z. and Su, B-L., Colloids and Surfaces A: Physicochem. Eng. Aspects 241, (2004), p. 173.
2. Rao, C. N. R., Müller, A. and Cheetham, A. K., The Chemistry of Nanomaterials: Synthesis, Properties and Applications, Edited Rao, C. N. R., Müller, A. and Cheetham, A. K., Wiley-VCH Verlag GmbH & Co. KgaA, Weinheim, Vol. 1, (2004), p. 1.
3. Guozhong, C., Nanostructures and Nanomaterials: Synthesis, Properties and Applications, Imperial College Press, London, (2004), p. 15.
4. Iijima, S, Nature 354, (1991), pp. 56-58.
5. Fujishima, A. and Honda, K., Nature 238, (1, 72), pp. 37-38.
6. Wu, P. -G., Ma, C. -H. and Shang, J. K., Applied Physics A: Material Science & Processing 81, (2005), p. 1411.
7. Mor, G. K., O. K. Varghese, O. K., Paulose, M., Shankar, K and Grimes, C. A., Solar Energy Materials & Solar cells 90, (2006), p. 20,11.
8. Shen, Q., Sato, T., Hashimoto, M., Chen, C. and Toyoda, T., Thin Solid Films 499, (2006), p. 299.
9. J. M. Macak, J. M., Tsuchiya, H. Berger, S., Bauer, S., Fujimoto, S. and Schmuki, P., Chemical Physics Letters 428, (2006), p. 421.
10. Y. D. Premchand, Y., D., Djenizian, T., Vacandio, F. and Knauth, P., Electrochemistry Communications 8, (2006), p. 1840.

11. Hueso, L. and Mathur, N., *Nature* 427, (2004), p. 301.
12. Law, M., Greene, L. E., Johnson, J. C., Saykally, R. and Yang, P. D., *Nature Materials* 4, (2005), p. 455.
13. Ghicov, A., Macak, J. M., Tsuchiya, H., Kunze, J., Haeublein, V., Frey, L. and Schmuki, P., *Nano Lett.* 6, (2006), p. 1080.
14. Shankar, K., Tep, K. C., Mor, G. K. and Grimes, C. A., *J. Physics D: Applied Physics* 39, (2006), p. 2361
15. Shankar, K., Paulose, M., Mor, G. K., Varghese, O. and Grimes, C. A., *J. Physics D: Applied Physics* 38, (2005), p. 3543.
16. Madhusudan Reddy, K., Baruwati, B., Jayalakshmi, M., Mohan Rao, M. and Manorama, S. V., *J. Solid State Chemistry* 178, (2005), p. 3352.
17. Park, J. H., Kim, S. and Bard, A. J., *Nano Lett.* 6, (2006), p. 24.
18. Choi, W., Termin, A. and Hoffmann, M. R., *J. Phys. Chem.* 98, (1994), p. 13669.
19. Hoyer, P., *Langmuir* 12, (1996), p. 1411.
20. Zhang, M., Brando, Y. and Wada, K., *J. Mater. Sci. Lett.* 20, (2001), p. 167.
21. Bavykin, D. V., Parmon, V. N., Lapkin, A. A. and Walsh, F. C., *J. Mater. Chem.* 14, (2004), p. 3370.
22. Mor, G. K., Varghese, O. K., Paulose, M., Mukherjee, N. and Grimes, C. A., *J. Mater. Res.* 18, (2003), p. 2588.
23. Gong, D., Grimes, C. A., Hu, W., Singh, R. S., Chen, Z. and Dickey, E. C., *J. Mater. Res.* 16, (2001), p. 3331.
24. Zhao, J., Wang, X., Sun, T. and Li, L., *Nanotechnology* 16, (2005), p. 2450.

25. Cai, Q., Paulose, M., Varghese, O. K. and Grimes, C. A., *J. Mater. Res.* 20, (2005), p. 230.
26. Frank, A. J., Kopidakis, N. and Van de Lagemaat, J., *Coord. Chem. Rev.* 248, (2004), p. 1165.
27. Mor, G. K., Shankar, K., Paulose, M., Varghese, O. K. and Grimes, C. A., *Nano Lett.* 6, (2006), p. 215.
28. Paulose, M., Shankar, K., Yoriya, S., Prakasam, H. E., Varghese, O. K., Mor, G. K., Latempa, T. A., Fitzgerald, A. and Grimes, C. A., *J. Physical Chemistry B: Letters* 110, (2006), p. 16179.
29. Mor, G. K., Varghese, O. K., Paulose, M., Ong, K. G. and Grimes, C. A., *Thin Solid Films* 496, (2006), p. 42.
30. Thomas, C. E., James, J. B. and Lomax, F. D., *Int. J. Hydrogen Energy* 23, (1998), p. 949.
31. Nowotny, J., Bak, T., Nowotny, M. K. and Sheppard, L. R., *Int. J. Hydrogen Energy* 32, (2007), p. 2609.
32. Nowotny, J., Sorrell, C. C., Sheppard, L. R. and Bak, T., *Int. J. Hydrogen Energy* 30, (2005), p. 521.
33. Ni, M., Leung, M. K. H., Leung, D. Y. C. and Sumathy, K., *Renewable and sustainable Energy Reviews* 11, (2007), p. 401.
34. Murphy, A. B., Barnes, P. R. F., Randeniya, L. K., Plumb, L. C., Grey, I. E., Horne, M. D. and Glasscock, J. A., *Int. J. Hydrogen Energy* 31, (2006), p. 1999.

35. Nowotny, J., Sorrell, C. C., Bak, T. and Sheppard, L. R., *Solar Energy* 78, (2005), p. 593.
36. Ruan, C., Paulose, M., Varghese, O. K. and Grimes, C. A., *Solar Energy Materials & Solar Cells* 90, (2006), p. 1283.
37. Liu, Z., Zhang, X., Nishimoto, S., Jin, M., Tryk, D. A., Murakami, T. and Fujishima, A., *J. Phys. Chem. C* 112, (2008), p. 253.
38. Quiroz, M. A., Martinez-Huitle, C. A., Meas-Vong, Y., Bustos, E. and Cerro-Lopez, M., *Journal of Electrochemical Chemistry* 807, (2017), pp. 261-267.
39. Cai, Q., Yang, L. and Yu, Y., *Thin Solid Films* 515, (2006), p. 1802.
40. Ratnawati, Gunlazuardi, J., Dewi, E. L. and Slamet, *International Journal of Hydrogen Energy* 39, (2014), pp. 16927-16935
41. Thompson, G. E., *Thin Solid Films* 297, (1997), p. 192.
42. Pletnev, M. A., Shirobokov, I. B., Ovechkina, O. E. and Reshetnikov, S. M., *Protection of Metals* 31, (1995), p. 317.
43. Macak, J. M. and Schmuki, P., *Electrochimica Acta* 52, (2006), p. 1258.
44. Yin, Y., Jin, Z., Hou, F. and Wang, X., *J. Am. Ceram. Soc.* 90, (2007), p. 2384.
45. Mohapatra, S. K., Misra, M., Mahajan, V. K. and Raja, K. S., *J. Phys. Chem. C* 111, (2007), p. 8677.
46. Petukhov, I., Eliseev, A. A., Kolesnik, I. V., Napolskii, K. S., Lukashin, A. V., Tretyakov, Y. D., Grigoriev, S. V., Grigorieva, N. A. and Eckerlebe, H., *Microporous and Mesoporous Materials* 14, (2008), p. 440.

47. Watcharenwong, A., Chanmanee, W., De Tacconi, N. R., Chenthamarakshan, C. R., Kajitvichyanukul, P. and Rjeshwar, K., *J. Mater. Res.* 22, (2007), p. 3186.
48. Albu, S. P., Ghicov, A., Macack, J. M. and Schmuki, P., *Phys. Stat. Sol. (RRL)* 1, R65 (2007).
49. Shankar, K., Effect of Architecture and doping on the Photoelectrochemical Properties of Titania nanotubes, Ph. D. Thesis, Electrical Engineering Department, The Pennsylvania State University, (2007), p. 39.
50. Raja, K. S., Ganndhi, T. and Misra, M., *Electrochemistry Communications* 9, (2007), p. 1069.



## Chapter 4

### **4 N and C Modified TiO<sub>2</sub> Nanotube Arrays: Enhanced Photoelectrochemical Properties and Effect of Nanotubes length on Photoconversion Efficiency**

\* A paper based on this chapter is under final revision as: Ahmed El Ruby Mohamed and Sohrab Rohani, "N and C Modified TiO<sub>2</sub> Nanotube Arrays: Enhanced Photoelectrochemical Properties and Effect of Nanotubes length on Photoconversion Efficiency" to be submitted for possible publication.

## 4.1 Abstract

In this investigation, a new, facile, low cost and environmental-friendly method was introduced to fabricate N- and C-modified TiO<sub>2</sub> nanotube arrays by immersing the as-anodized TiO<sub>2</sub> nanotube arrays in a urea aqueous solution with mechanical agitation for a short time. and keeping the TNTAs immersed in the solution for 6 h at room temperature. Then, the TNTAs were annealed at different temperatures. The produced N-, C-modified TNTAs were characterized using FESEM, EDX, XRD, XPS, UV-Vis diffuse reflectance spectra. Modified optical properties with narrow band gap energy, E<sub>g</sub>, of 2.65 eV was obtained after annealing the modified TNTAs at 550°C. Modified TNTAs showed enhanced photoelectrochemical performance. Photoconversion efficiency (PCE) was increased from 4.35% for pristine (unmodified) TNTAs to 5.18% for modified TNTAs, an increase of 19%. Effect of nanotubes length of modified TNTAs on photoelectrochemical performance was also studied. Photocurrent density and PCE were increased by increasing nanotube length with a maximum PCE of 6.38% for nanotube length of 55 μm. This high PCE value was attributed to: band gap reduction due to C- and N modification of TNTAs surface, increased surface area of long TNTAs compared with short TNTAs, investigated in previous studies.

**Keywords:** TiO<sub>2</sub> nanotube arrays, N- and C- modification, band gap, recombination rate, photocurrent, photoconversion efficiency.

## 4.2 Introduction

Since first introduced by Zwillling and co-workers in 1999 [1], titania nanotube arrays (TNTAs) fabricated by electrochemical anodization method have attracted great interest due to their outstanding properties such as high specific surface area [2], high charge transport and separation rates [3], light absorption and propagation properties [4-6], biocompatibility and chemical stability [7]. Furthermore, the integrated, vertically oriented, highly ordered nanotubular structure strongly adhered to Ti parent metal substrate imparts a very important practical advantage by eliminating the costly solid/liquid separation step which is necessary when using the nanoparticles counterpart. Due to these properties, TNTAs have proved to be a promising candidate in many advanced applications including dye-sensitized solar cells [8-12], sensors development [13-14], hydrogen generation from water by photoelectrolysis [15-19], photocatalysis [20-23], self-cleaning [24], bone and medicinal implants [25], drug delivery and biomaterials applications [26], and molecular filtration [27]. On the other hand, in spite of the above mentioned outstanding properties of TNTAs, the widespread solar applications of TNTAs are hindered by the relatively wide energy band gap ( $E_g$ ) of  $\text{TiO}_2$  (3.2 eV for anatase and 3.0 for rutile) which is photoresponsive only to UV illumination. Because UV portion of the solar radiation accounts for only about 5% compared to the visible light which accounts for about 45%, any shift in photoactivity of TNTAs from UV toward visible light region increases the photoconversion efficiency and therefore has a positive impact on photocatalytic and photoelectrochemical applications of TNTAs [28-31]. In order to resolve the above problem and modify the electronic structure of  $\text{TiO}_2$  to narrow its band gap and enhance the visible light responsiveness, metal ions such as Fe [32-33], Zr [34],

Cr [35], and Zn [36] have been doped to TiO<sub>2</sub> nanotube arrays using different doping techniques. Recently, non-metals such as carbon [37], nitrogen [38-40], phosphorous-fluorine [41] and nitrogen-fluorine-iodine [42, 43] have been doped into TiO<sub>2</sub> nanotube arrays and proved significant enhancements in the visible light photoactivity. It is worth mentioning that in contrast to doping of TiO<sub>2</sub> nanoparticles, doping of TNTAs is more difficult and presents a challenge as one should carefully choose the doping method that introduces the dopant ions efficiently into TNTAs crystal lattice and at the same time not damage the highly organized nanotubular structure. Particularly, carbon dopant has been introduced to TNTAs either by flame annealing [44], annealing under carbonaceous gas stream at elevated temperature [19] or hydrothermal treatment of TNTAs in an aqueous solution of glucose followed by annealing in Ar gas at 450 °C [45]. But these techniques either result in huge damage to the nanoarchitecture and crystal structure of the nanotube arrays [44] or involve complicated elevated temperature multistage processes [45-47].

Ordinary phases of the titania include amorphous, anatase and rutile. The crystal phase and nano-architecture of titania manipulate its properties and potential applications. For example, the anatase phase of titania is favored in catalysis and dye-sensitized solar cells applications, whereas rutile is preferred in the area of dielectrics and high-temperature oxygen gas sensors due to its excellent elevated temperature stability [24]. Moreover, the performance of TNTAs in different applications is highly dependent on the nanostructure parameters such as nanotube length, diameter and wall thickness. These parameters are mostly determined by adjusting the anodization conditions such as anodization potential, pH, anodization time and anodization electrolyte composition. Although a remarkable success has recently been achieved in fabrication of high-aspect-ratio TNTAs with

nanotube length up to hundreds of micrometers, very little attention has been paid to study the effect of nanotube length on TNTAs performance, in particular, in the third generation of TNTAs with nanotube length longer than 10  $\mu\text{m}$  [48].

In this study, we investigated a new facile and low-cost method to fabricate N- and C-modified TNTAs of length up to 55  $\mu\text{m}$  by treating the as-anodized TNTAs in urea aqueous solution at room temperature for several hours. This method is also safe on the morphology and nanoarchitecture of TNTAs. The modified TNTAs were characterized by FESEM, X-ray diffraction, XPS, EDX and UV-vis. diffuse reflectance spectra. Photoelectrochemical performance of modified and non-modified TNTAs was investigated. Moreover, we studied the effect of nanotube length on the photoelectrochemical performance.

## 4.3 Experimental setup and methods

### 4.3.1 Preparation of Modified $\text{TiO}_2$ Nanotube Arrays (TNTAs)

The Ti foil (0.89 mm thickness, 99.6% purity) and all chemicals were purchased from Alfa-Aesar (Ward Hill, MA, USA). Prior to anodization, the titanium foil was cleaned by using distilled water, acetone and distilled water, respectively, in ultrasonic bath for five minutes each. It was then dried off in air, etched in (3.3 M HF and 5.6 M  $\text{HNO}_3$ ) solution for 10 s and immediately rinsed with deionized water, dried with air and used immediately. To prepare TNTAs, we used the same setup as in our previous work [49] and a modified procedure proposed by Prakasam and co-workers [3]. Ti foil was first anodized in ethylene glycol solution containing  $\text{NH}_4\text{F}$  (0.4 wt. %) and  $\text{H}_2\text{O}$  (1 wt. %) for 2 h at 60 V at room temperature using Keithley Source Meter Unit Model SMU 2602 (Keithley Instruments

Inc., Cleveland, Ohio, USA). The Ti foil was cut into 1.5 cm diameter discs and mounted into a Teflon electrode holder which allowed only 1 cm<sup>2</sup> of one side of the disc to be exposed to the electrolyte while the whole backside area was isolated. Ti foil was used as anode and a platinum foil was used as a cathode.

The produced nanotubes were removed by sonication in ethanol for 30 min to obtain textured fresh Ti surface. Subsequently, the second anodization was performed in the same electrolyte. The second anodization time was changed to obtain different nanotube lengths. The anodization current was monitored with a computer. After the second anodization step, the samples were washed with distilled water and sonicated in water for 5 min to clean the surface and remove debris, then dried with air. The TNTAs samples were immersed in a 10 wt.% urea solution and mechanically mixed for 30 min and kept immersed in urea solution for 6 h at room temperature to allow urea molecules to be adsorbed on TNTAs inner surface. Then annealed at temperature ranging from 350-650°C for 3h in air with a heating and cooling rate of 5 °C/min to promote crystallinity.

#### 4.3.2 Characterization of Modified TNTAs

The morphology of TNTAs was examined with a field emission scanning electron microscope (FESEM, Hitachi S-5000, Tokyo, Japan) equipped with an energy dispersive X-ray analyzer unit (EDXA). The elemental compositions of the samples were determined by EDX analysis. The crystalline phases were recorded by X-ray diffraction using a powder X-ray diffractometer (Rigaku RINT 2500, Tokyo, Japan) with Cu K $\alpha$  radiation ( $\lambda = 1.54$  Å) at 40 kV and 50 mA with a scan rate of 0.02° per s over a  $2\theta$  range from 15° to 80°. The results of the elemental compositions were determined by X-ray photoelectron spectroscopy (XPS, Perkin Elmer, Waltham, MA, USA). The XPS analyses were carried

out with a Kratos Axis Ultra spectrometer using a monochromatic Al K $\alpha$  source (15 mA, 14 kV). The instrument work function was calibrated to give a binding energy (BE) of 83.96 eV for the Au 4f $_{7/2}$  line for metallic gold and the spectrometer dispersion was adjusted to give a BE of 932.62 eV for the Cu 2p $_{3/2}$  line of metallic copper. The Kratos charge neutralizer system was used on all specimens. Survey scan analyses were carried out with an analysis area of 300  $\mu\text{m} \times 700 \mu\text{m}$  and a pass energy of 160 eV. High-resolution analyses were carried out with an analysis area of 300  $\mu\text{m} \times 700 \mu\text{m}$  and a pass energy of 20 eV. Spectra charge was corrected to the main line of the carbon 1s spectrum (adventitious carbon) set to 284.8 eV. Spectra were analyzed using CasaXPS software (version 2.3.14). UV–Vis diffuse reflectance absorption spectra were measured using a Cary 100 UV–Vis–NIR spectrophotometer.

### 4.3.3 Photoelectrochemical Properties

The photocurrent spectra were recorded by a home-made photoelectrochemical measurement system using an LPX150 Xe lamp solar simulator with a light intensity of 100 mW/cm $^2$ . The TNTAs sample served as the working electrode and a Pt sheet was used as the counter electrode. The testing electrolyte was 1 M KOH solution with 0.05 vol. % ethylene glycol. A computer-controlled power supply (Keithley SMU 2602, Keithley Instruments Inc., Cleveland, Ohio, USA) was employed to control the potential and record the photocurrent generated. The intensity of the light was measured by a radiation power and energy meter. The incident light intensity on the sample was measured as 100 mW cm $^{-2}$ . The external potential was applied to the anode at a scan rate of 20 mV s $^{-1}$  under illumination and the photocurrent was recorded. The potential of the open circuit was measured by a digital multimeter during the illumination.

## 4.4 Results and Discussion

### 4.4.1 FESEM and XRD Studies

Figure 4-1 shows the FESEM images of TNTAs fabricated in ethylene glycol electrolyte containing 1 vol. % H<sub>2</sub>O and 0.4 wt. % NH<sub>4</sub>F at 60V. Figures 4-1-a and b show top view and cross-sectional view of TNTAs anodized at room temperature for 6 h at room temperature, while Figures 4-1-c and d represent top and lateral views of TNTAs anodized in the same conditions for 10 h. The as-anodized TNTAs were sonicated in water for 5 min to clean surface and remove debris Figure 4-1-e shows high magnification of top view and Figure 4-1-f represents high magnification of cross sectional view near the TNTAs bottom showing the test-tube-like closed round bottom of the nanotubes. Clearly the smoothness of nanotube walls and the absence of ripples associated with the aqueous electrolytes anodization as in our previous work [49] are discernible. From the FESEM images, we conclude that TNTAs fabricated with this process are of high quality, well-organized, vertically oriented and homogeneous. The TNTAs are also reproducible as it can be seen by comparing the nano-architectures in the two samples shown in Figures 4-1-a and 4-1-c. The only difference is TNTAs length which increases by increasing the anodization time. The average inner diameter and wall thickness for TNTAs fabricated at 60 V in ethylene glycol are 173±16 nm and 13±1, respectively. The length of nanotube depends on the anodization time and is found to be 36 and 55 μm for 6 and 10 h anodization times, respectively (Figures 4-1-b and 4-1-d).



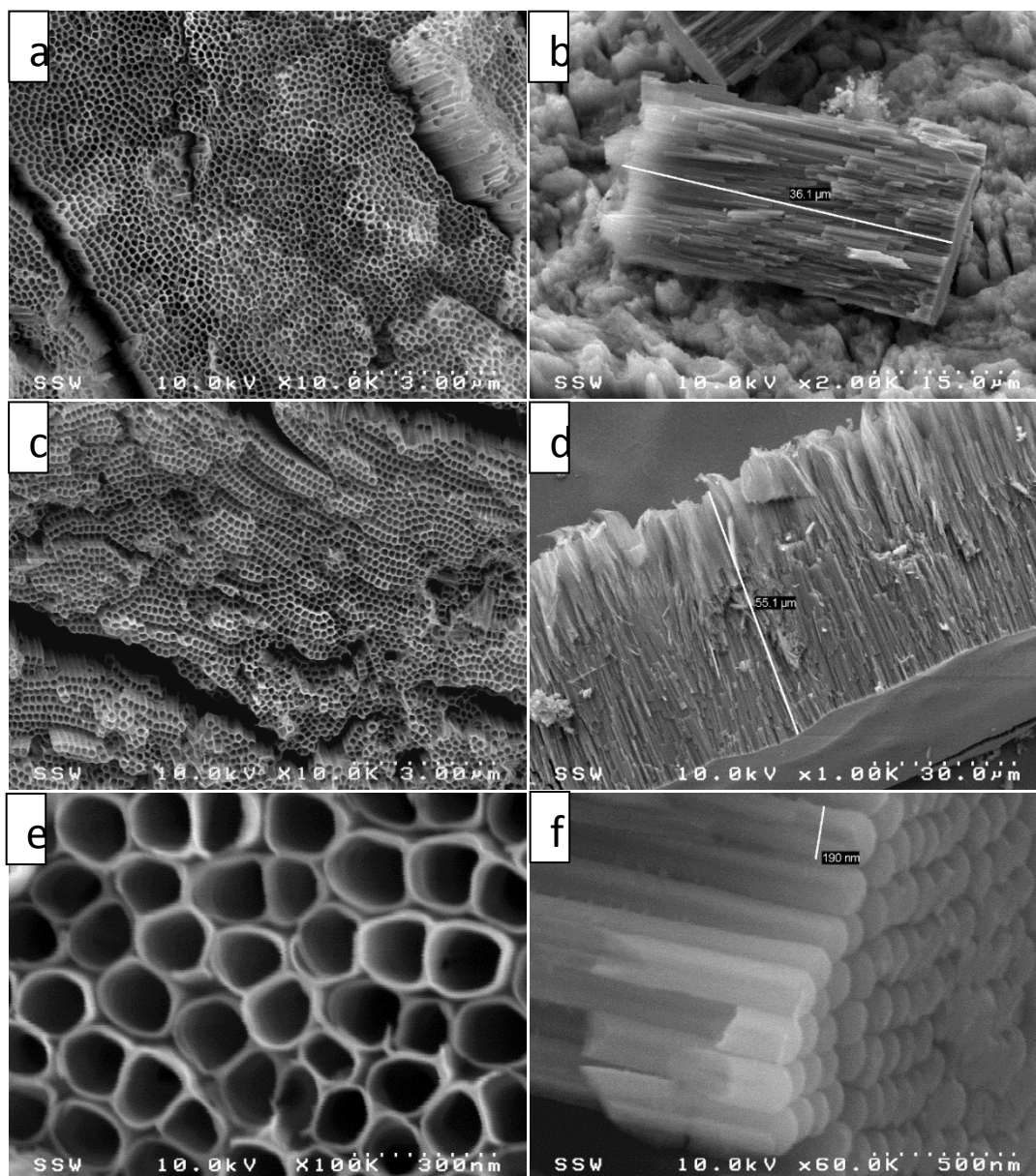


**Figure 4-1** FESEM images for TNTAs synthesized in ethylene glycol electrolyte containing 1wt% H<sub>2</sub>O and 0.4 wt.% NH<sub>4</sub>F at constant potential of 60V; a) and b) Top view and cross sectional view of TNTAs anodized for 6 h and then sonicated in water for 5 min to clean surface and remove debris, c) and d) are top and cross sectional views of TNTAs anodized at the same conditions for 10 h, and e) and f) are high magnification of top and lateral views of TNTAs in (a), respectively.

Ethylene glycol electrolyte helps not only in getting longer nanotubes in relatively short anodization time, but also in yielding smooth nanotube walls. One more difference between glycerol-water electrolyte and ethylene glycol electrolyte is the optimum anodization potential at which maximum nanotube growth rate can be achieved. The optimum anodization voltage for glycerol - water electrolyte was found to be 20 V [49], while it was 60 V for the ethylene glycol electrolyte [3]. Figure 4-2 shows the FESEM images of pristine TNTAs, Figures 4-2-a and c (without modification), and Figures 4-2-b and d the modified TNTAs. Both samples were annealed at 550°C for 3 h. As we can see from the FESEM images of pristine and modified TNTAs, the modification process did not cause any damage to the well-organized vertically oriented nanotubular architecture of TNTAs which is an important advantage of this modification method. In addition, the method is simple, low cost and environment-friendly.

As-anodized TNTAs were amorphous and annealing at elevated temperature was required to promote crystallinity which increased the stability of the material and enhanced the charge transport and photoelectrochemical properties. By varying the annealing temperature, the phase structure of TNTAs can be controlled as anatase or rutile or a combination of both phases. As mentioned above, each crystal phase has its preferred application. Figure 4-3 shows the XRD patterns of TNTAs annealed at different temperatures from 350 to 650°C for 3 h, as well as Ti-metal foil and as-anodized TNTAs for comparison. As it can be seen from Figure 4-3, both Ti-metal foil and as-anodized TNTAs (curves a and b, respectively) show only Ti metal peaks which implies that the as-anodized TNTAs layer was amorphous. Anatase phase began to appear at 350°C (curve c) and increased and became dominant at 450°C (curve d). At 450°C, one can see traces of

rutile phase. At 550°C (curve e), the crystal structure of TNTAs was a conjugate of both anatase and rutile phases while the rutile phase became prominent when annealing at 650°C (curve f). These X-ray results are consistent with other studies [16, 50-52].

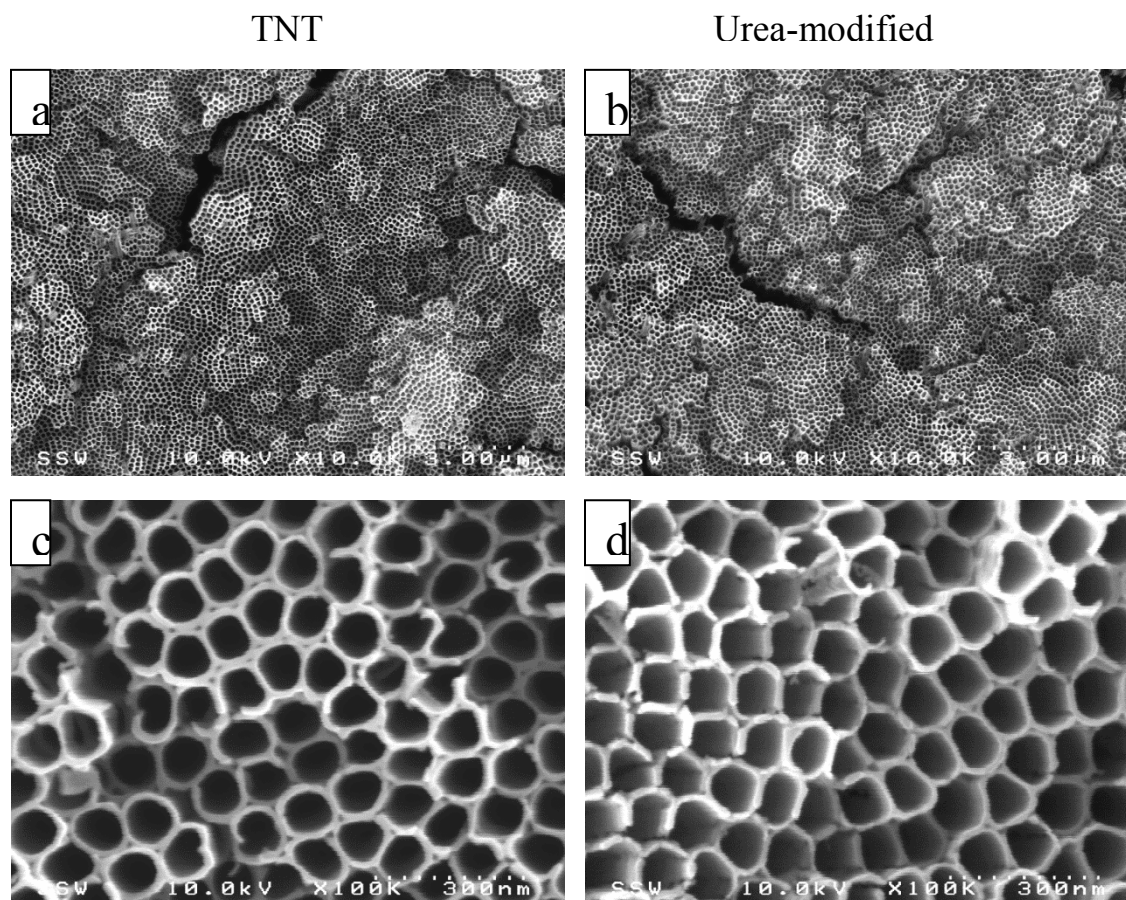


**Figure 4-2 FESEM images of pristine (unmodified) and modified TNTAs: a) and c) top view and high magnified top view of pristine TNTAs, b) and d) top view and high magnified top view of modified TNTAs.**

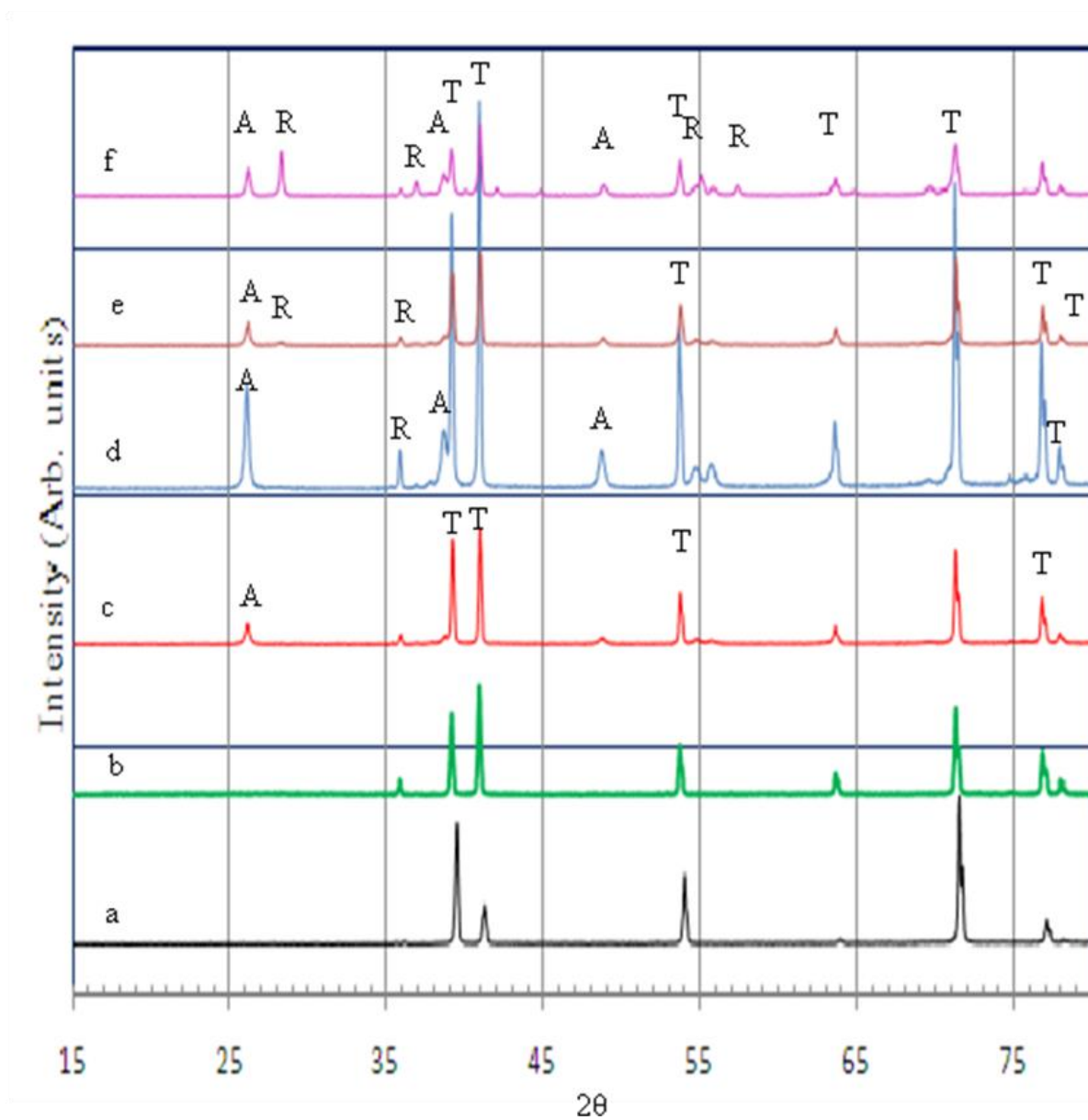
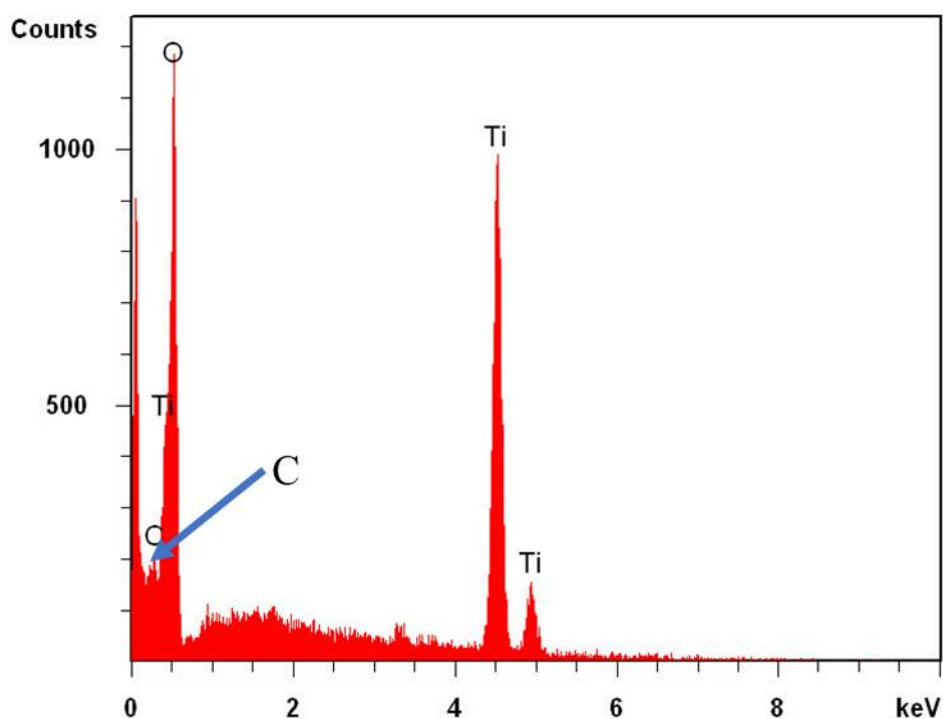


Figure 4-3 X-ray diffraction patterns for a) Ti-metal foil, b) as-anodized TNTAs, c) TNTAs annealed at: 350°C, d) 450°C, e) 550°C and f) 650°C, all for 3 h in air.

#### 4.4.2 EDX and XPS Results

Elemental composition of TNTAs and determining whether foreign elements are introduced into  $\text{TiO}_2$  lattice can be investigated using both EDX and XPS spectra techniques. Figure 4-4 shows the EDX spectra of  $\text{TiO}_2$  nanotube arrays fabricated in ethylene glycol electrolyte and annealed at  $550^\circ\text{C}$  for 3 h. The EDX spectra indicate the presence of Ti, O and C in the nanotubular sample and that the ratio of Ti:O is approximately 1:2 indicating that the structure of the nanotubes is  $\text{TiO}_2$  with the presence of carbon which comes from the organic electrolyte and urea after pyrolysis during annealing at elevated temperature. EDX analysis technique did not show nitrogen as it exists in low concentration that cannot be detected by EDX spectra.



**Figure 4-4** The EDX spectra of modified TNTAs indicating the elemental composition Ti and O with a ratio of Ti:O = 1:2 and the presence of carbon in TNTAs.

Figure 4-5 shows the XPS spectra for the TNTAs sample annealed at 550°C for 3 h in air. As it can be seen from Figure 5-a, TNTAs contained Ti, O, C and N. The binding energies of Ti 2p, O 1s, C 1s and N 1s were 459.7, 531.1, 285.4 and 399.75 eV, respectively. The atomic ratio of Ti:O was very close to 1:2 implying that the chemical composition of nanotubes was TiO<sub>2</sub>. Figure 4-5-b shows high resolution of N 1s peak at binding energy of 399.75 eV. This binding energy exists between two binding energies at 400.1 and 398.2 eV which correspond to C-N=C and C-NH<sub>2</sub>, respectively [53]. This suggests that the existing nitrogen is mainly bonded to carbon atoms. The high resolution of C 1s peak region (Figure 4-5-c) exhibits the following peaks; the peak at 284.8 eV is assigned to adventitious carbon, and the peak at 286.3 eV is ascribed to C=O bonds due to pyrolysis of urea during annealing [54], and the peak at 288.28 eV is attributed to the carbon existing in the form of interstitial atoms which takes place due to the diffusion of carbon atoms during the annealing process at elevated temperature [19].

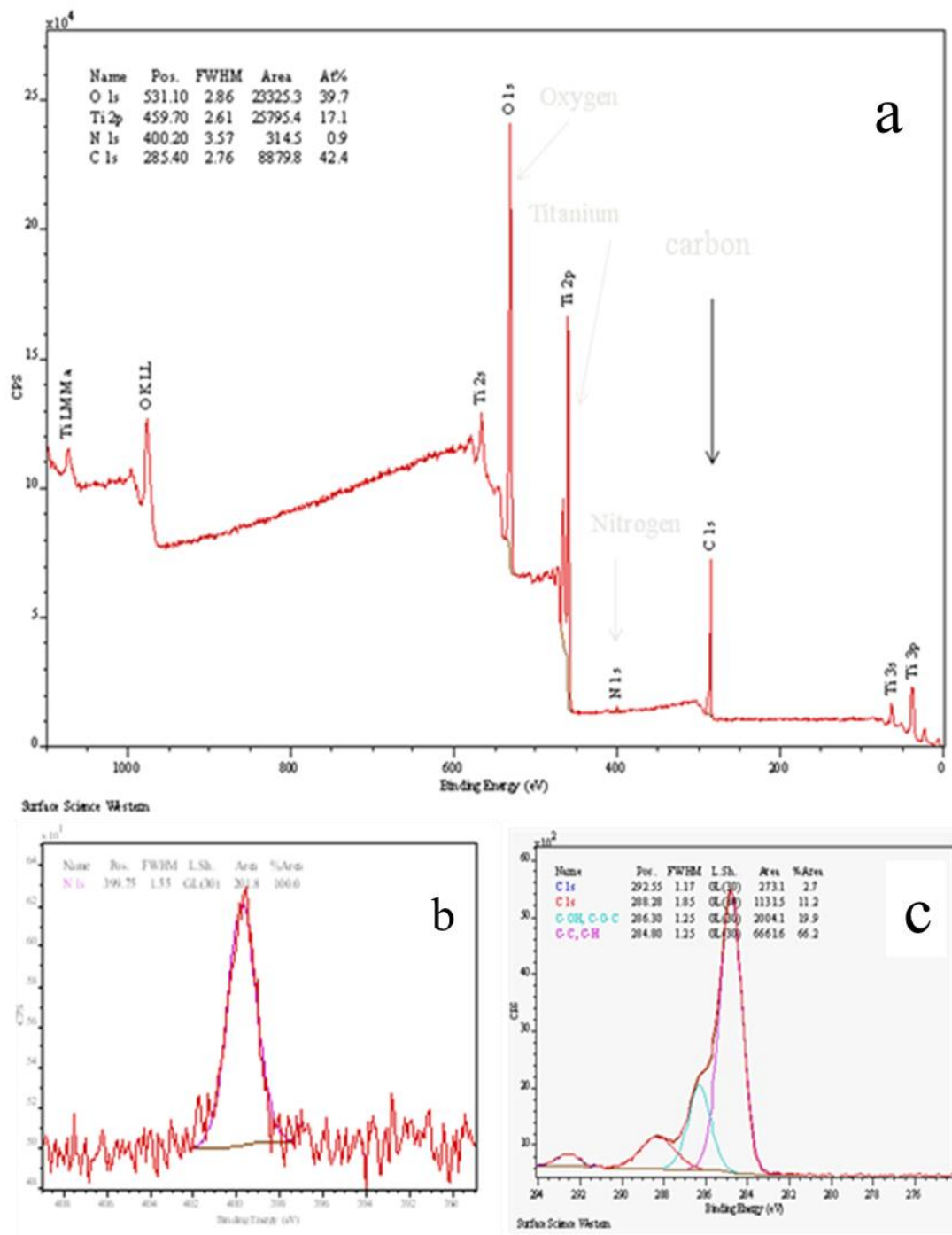


Figure 4-5 The XPS spectra of TiO<sub>2</sub> nanotube arrays: a) Wide range survey spectra, b) High resolution XPS spectra over N 1s peak at 399.75 eV, and c) High resolution XPS spectra over C 1s peak

### 4.4.3 Optical Properties

The UV-Vis diffuse reflectance absorption spectra of modified TNTAs as a function of annealing temperature are shown in Figure 4-6. As it can be seen easily from Figure 4-6, annealing temperature has a large effect on the light absorbance of the nanotube arrays because annealing temperature not only affects on the crystallization process but also the incorporation of foreign elements such as carbon and nitrogen into  $\text{TiO}_2$  crystal lattice. Figure sh4-6 indicates that all samples have strong absorbance in the visible region with the best absorbance for the sample annealed at  $650^\circ\text{C}$ . In Figure 4-7, absorbance data from Figure 4-6 were manipulated using Kubelka-Munk equation to calculate the modified band gap energies for each sample [55].

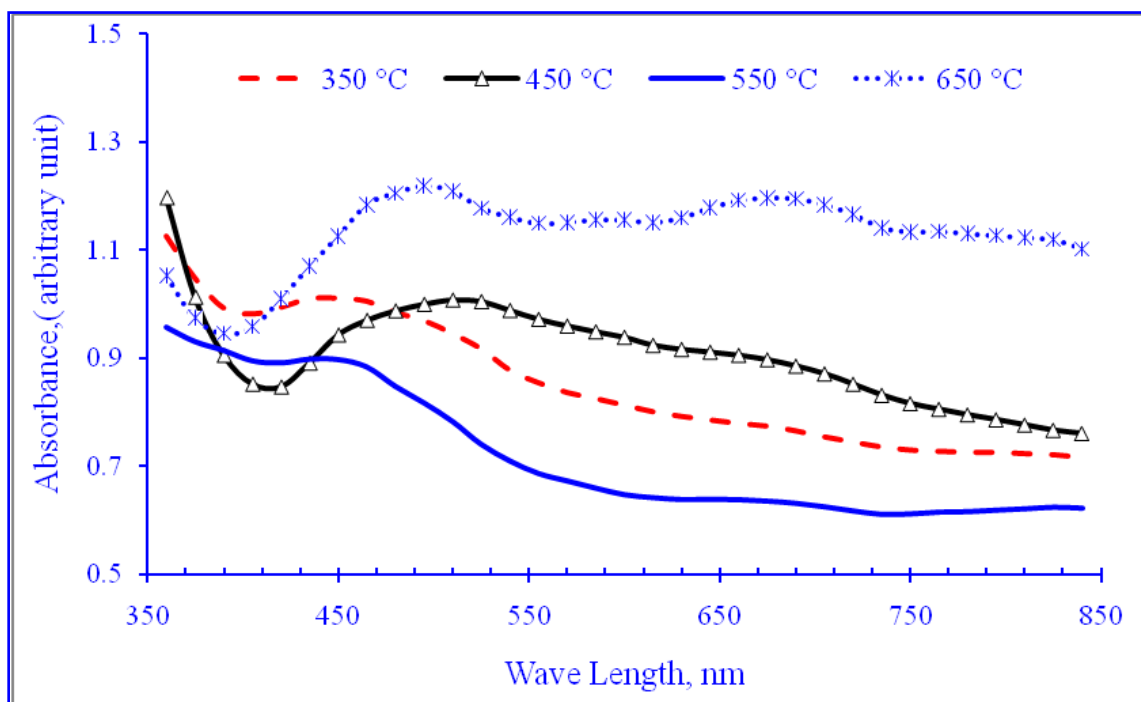
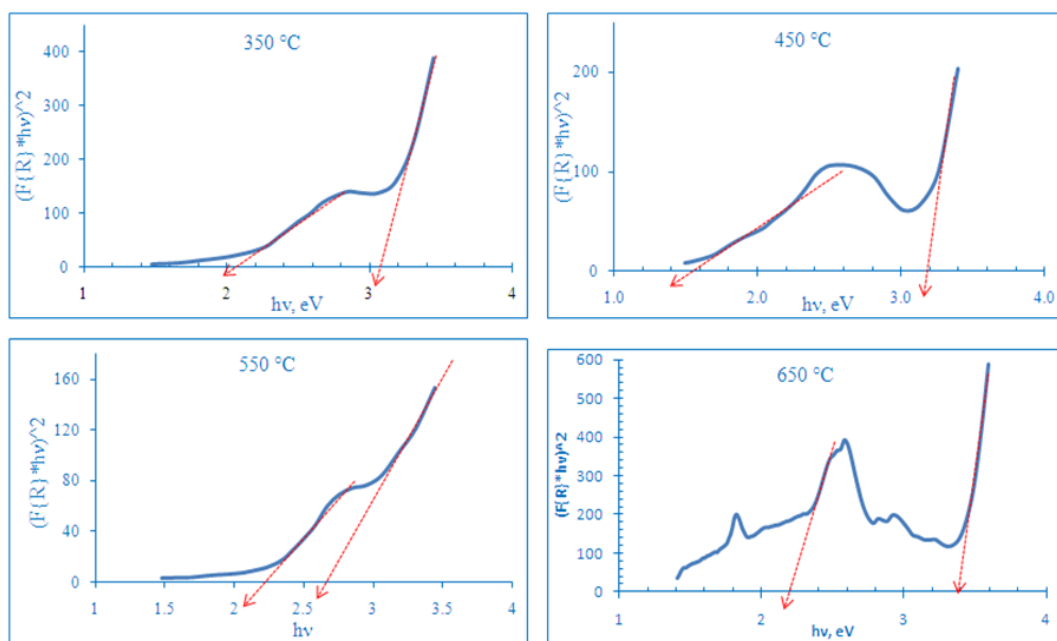


Figure 4-6 UV-Vis diffuse reflectance absorbance of  $\text{TiO}_2$  annealed at different temperatures.



From Figure 4-7 and Table 1, each sample has two band gap energies, a primary one and a secondary one due to the effect of the electronic levels of the foreign dopants. The primary one has the larger effect on photoelectrochemical properties of TNTAs. As seen in Figure 4-7 and in Table 4-1, the sample annealed at 550°C has the smallest primary band gap energy,  $E_g$ , (2.65 eV) which corresponds to the absorbance edge wavelength of 468 nm while sample annealed at 450°C has the smallest secondary band gap energy,  $E_g$ , (1.6 eV) which corresponds to absorbance edge wave length of 775 nm.



**Figure 4-7 Kubelka-Munk transferred diffuse reflectance spectra of samples annealed at 350, 450, 550 and 650°C. The intersections of red rows with X-axis represent the values of band gap energy.**

**Table 4-1 The band gap energies ( $E_g$ ) and corresponding absorbance edges of  $\text{TiO}_2$  nanotube arrays annealed at different temperatures**

| Anneal. Temperature | Main $E_g$ , eV | Secondary $E_g$ , eV | Main Abs. Edge, nm | Secondary Abs. Edge, nm |
|---------------------|-----------------|----------------------|--------------------|-------------------------|
| 350 °C              | 3.1             | 2.1                  | 400                | 590                     |
| 450 °C              | 3.2             | <u>1.6</u>           | 387                | <u>775</u>              |
| 550 °C              | <u>2.65</u>     | 2.2                  | <u>468</u>         | 564                     |
| 650 °C              | 3.38            | 2.2                  | 367                | 564                     |

#### 4.4.4 Photoelectrochemical Properties

Figure 4-8 shows photocurrent density,  $I_{ph}$ , of modified TNTAs compared with that of (unmodified) TNTAs. Both samples were anodized and treated at the same conditions to obtain identical nanoarchitectures. Unmodified (pristine) sample was annealed directly at 550° C for 3h while the other sample was first treated with urea solution as described in experimental part, then annealed at 550° C for 3 h. Both samples have nanotube length of 25  $\mu\text{m}$ , an inner diameter and a wall thickness of  $173\pm 16$  and  $13\pm 1$  nm, respectively. As we can see from Figure 4-8, the modified TNTAs shows a considerable increase in  $I_{ph}$  compared with the pristine (unmodified) TNTAs.  $I_{ph}$  increased from 7.1  $\text{mA}/\text{cm}^2$  for pristine (unmodified) TNTAs to 9.9  $\text{mA}/\text{cm}^2$  for modified TNTAs with a maximum % increase of 39 % at 1 V applied potential.

Figure 4-9 shows the % photoconversion efficiency, PCE, for modified and unmodified TNTAs as a function of applied potential. The percent PCE was calculated using the following equation [18, 56]:

$$\text{PCE (\%)} = [I_{\text{ph}} \times (1.23 - E_{\text{app}}) \times 100] / I_0 \quad (1)$$

$$E_{\text{app}} = E_{\text{meas}} - E_{\text{oc}} \quad (2)$$

Where:  $I_{\text{ph}}$  is the photocurrent density in  $\text{mA}/\text{cm}^2$ ,  $E_{\text{app}}$  is the external applied potential in V given in eq. (2),  $E_{\text{meas}}$  is the measured bias potential in V (vs Ag/AgCl reference electrode), and  $E_{\text{oc}}$  is the electrode potential (vs Ag/AgCl) of the same working electrode at open circuit conditions under the same illumination and in the same electrolyte. As we can see from Figure 4-9, the photoconversion efficiency, was increased from 4.35% for pristine (pure) TNTAs to 5.18% for modified TNTAs with an increase of 19%. The high value of photocurrent density and photoconversion efficiency of both pristine and modified TNTAs measured in this work was attributed to the high surface area of long nanotubes (25  $\mu\text{m}$ ) and the presence of 0.05 % ethylene glycol as electron donor to decrease the charges recombination rate.

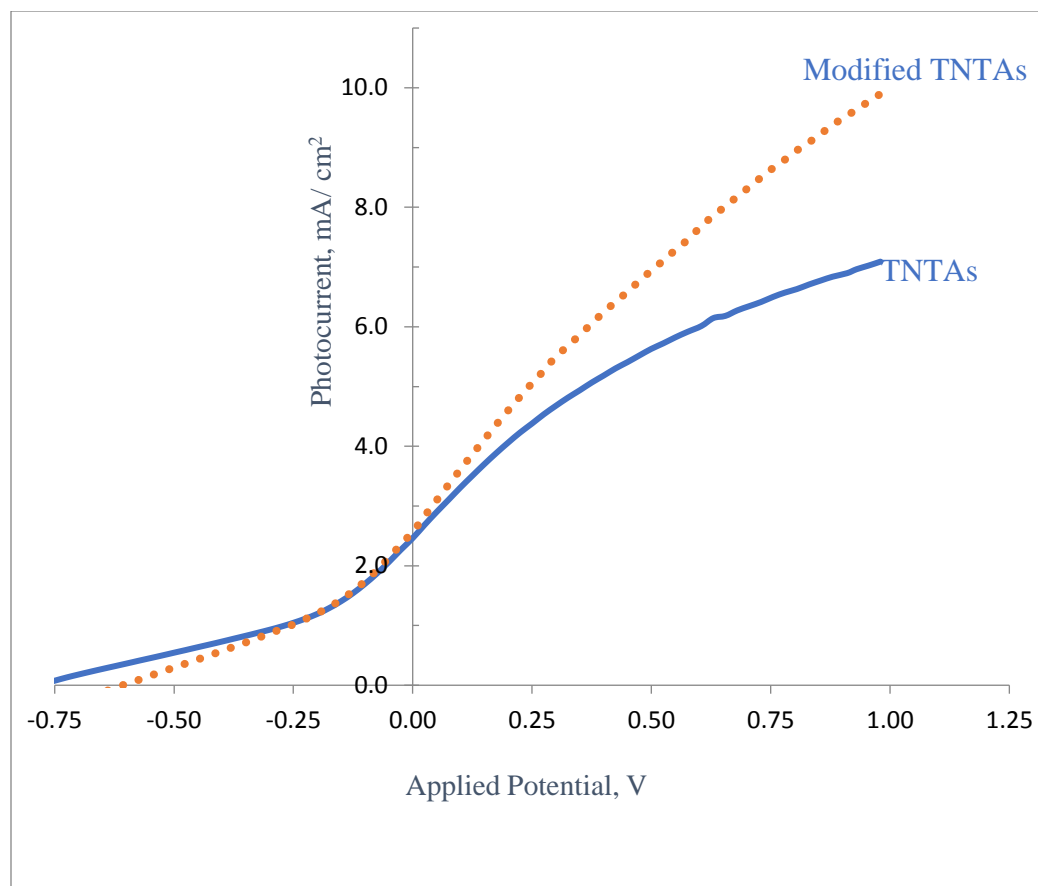
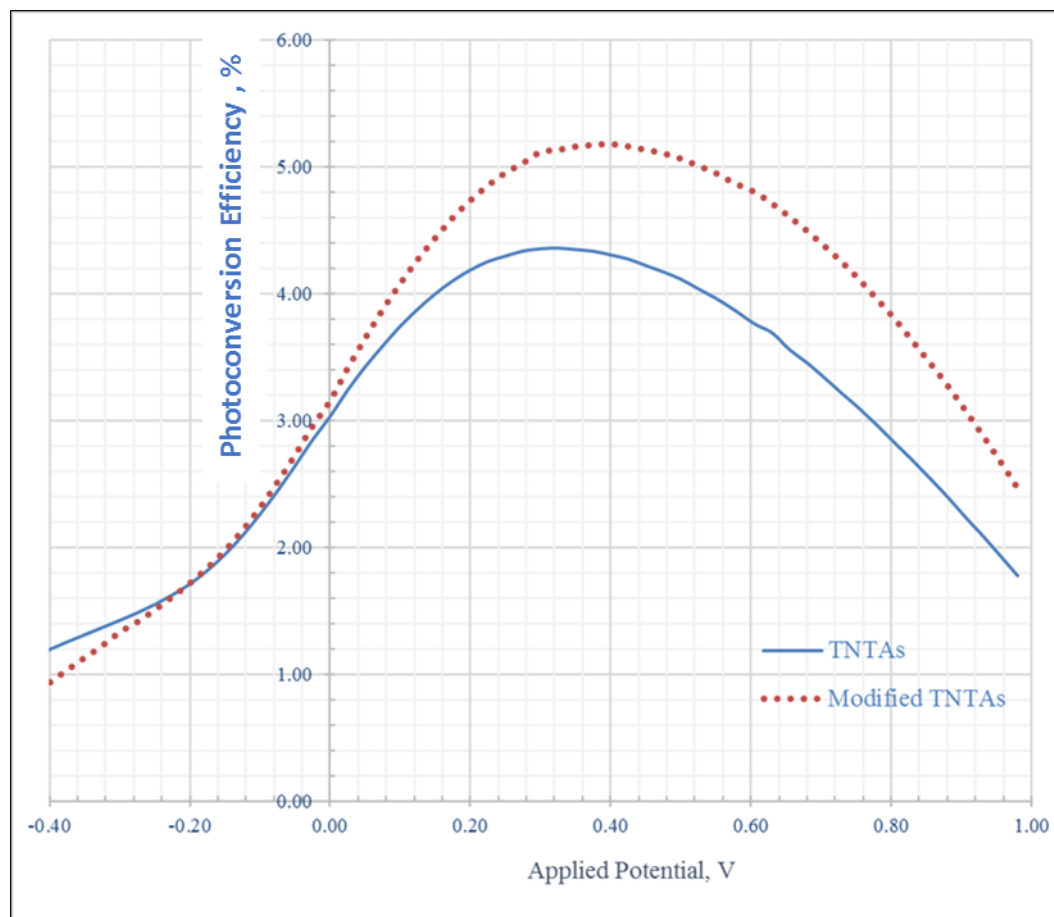


Figure 4-8 Photocurrent density of modified TNTAs compared with that of pristine (unmodified) TNTAs. Both samples were anodized in the same conditions with identical nanoarchitectures.



**Figure 4-9 Photoconversion efficiency of modified TNTAs and pristine (unmodified) TNTAs**

Although vast number of studies have been conducted in the last decade on fabrication of long TNTAs of up to hundreds of micrometers [57, 58], there is a shortage of studies of photoelectrochemical performance of long nanotubes. The increase in the surface area by increasing nanotubes length enhances the capacity to harvest light photons. But on the other hand, diffusion path of the electrons to reach the conducting layer in the back of the

photoanode increases with increasing the nanotubes length which results in increasing the charge recombination rate. A series of TNTAs samples were fabricated at the same anodization conditions mentioned above. Only anodization time was changed from 3 h to 10 h to produce TNTAs with the same inner diameter and wall thickness but with different nanotube lengths as shown in table 4-2. All TNTAs samples were treated with urea solution as described in experimental part to produce C- and N-modified TNTAs then annealed for 3 h at 550°C.

**Table 4-2 Nanotubes lengths anodized for different anodization times**

|                                 |    |    |      |    |    |
|---------------------------------|----|----|------|----|----|
| Anodization Time, h             | 3  | 4  | 6    | 7  | 10 |
| Nanotubes Length, $\mu\text{m}$ | 18 | 23 | 30.5 | 36 | 55 |

Figure 4-10 shows the photocurrent density of modified TNTAs with different lengths as a function of applied potential. As we can see, photocurrent increases with increasing nanotubes length. this implies that due to the one dimensional vertically oriented nanotubular architecture of the photoanode, the light photons successfully penetrated the entire length of the nanotube arrays up to 55  $\mu\text{m}$  and the huge surface area increased the light harvesting capacity of TNTAs. Furthermore, the presence of ethylene glycol as electrons donor, although in very small concentration (0.05 vol.%), reduced the charge recombination rate in very long nanotubes photoanode.

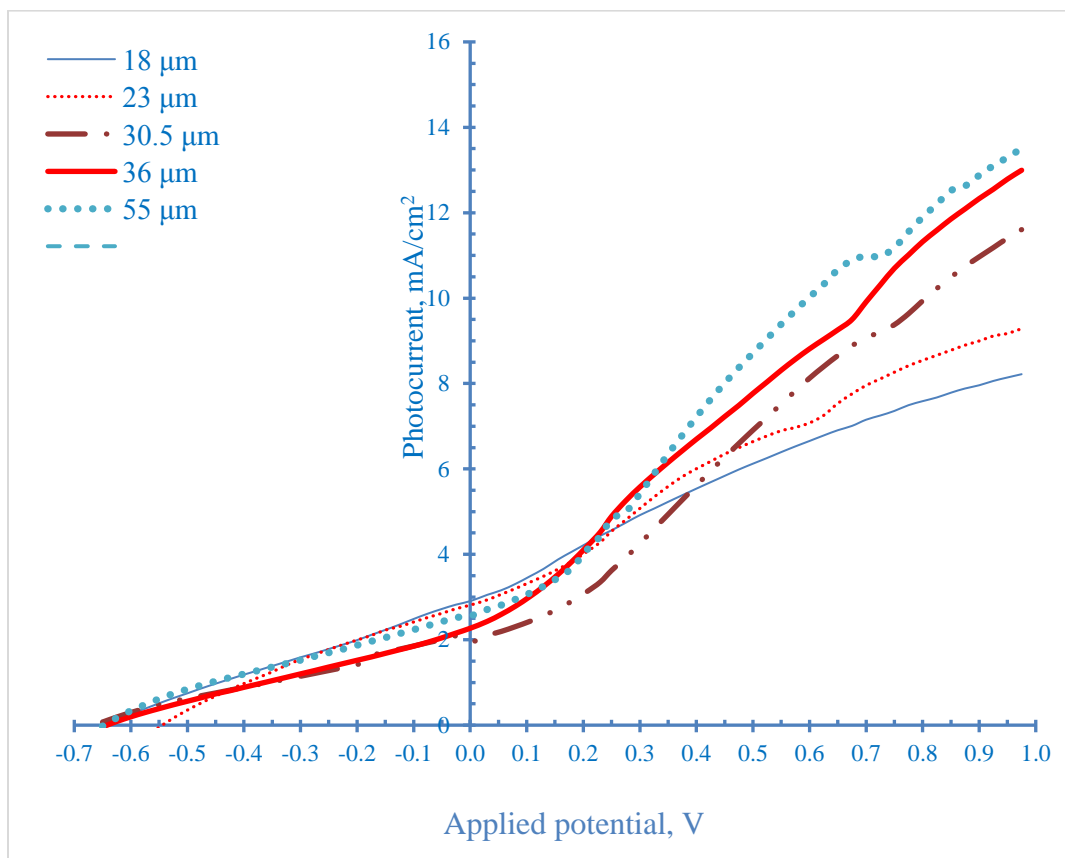


Figure 4-10 Effect of nanotubes length on photocurrent as a function of applied potential.

Effect of nanotube length on photoconversion efficiency, PCE, is shown in Figure 4-11. Photoconversion efficiency increases with increasing nanotube length, too, with a maximum PCE of 6.38 % at 55  $\mu\text{m}$  nanotubes length. Figure 4-12 shows a linear relation between PCE and nanotube length in the range from 18 to 55  $\mu\text{m}$ . The increase of PCE with increasing nanotube length and the linear dependence of PCE on nanotube length up to 55  $\mu\text{m}$  imply that the light successfully penetrates the long TNTAs photoanode up to 55  $\mu\text{m}$  which is more than 3.6 times longer than the maximum layer of nanoparticulate photoanode that light can penetrate.

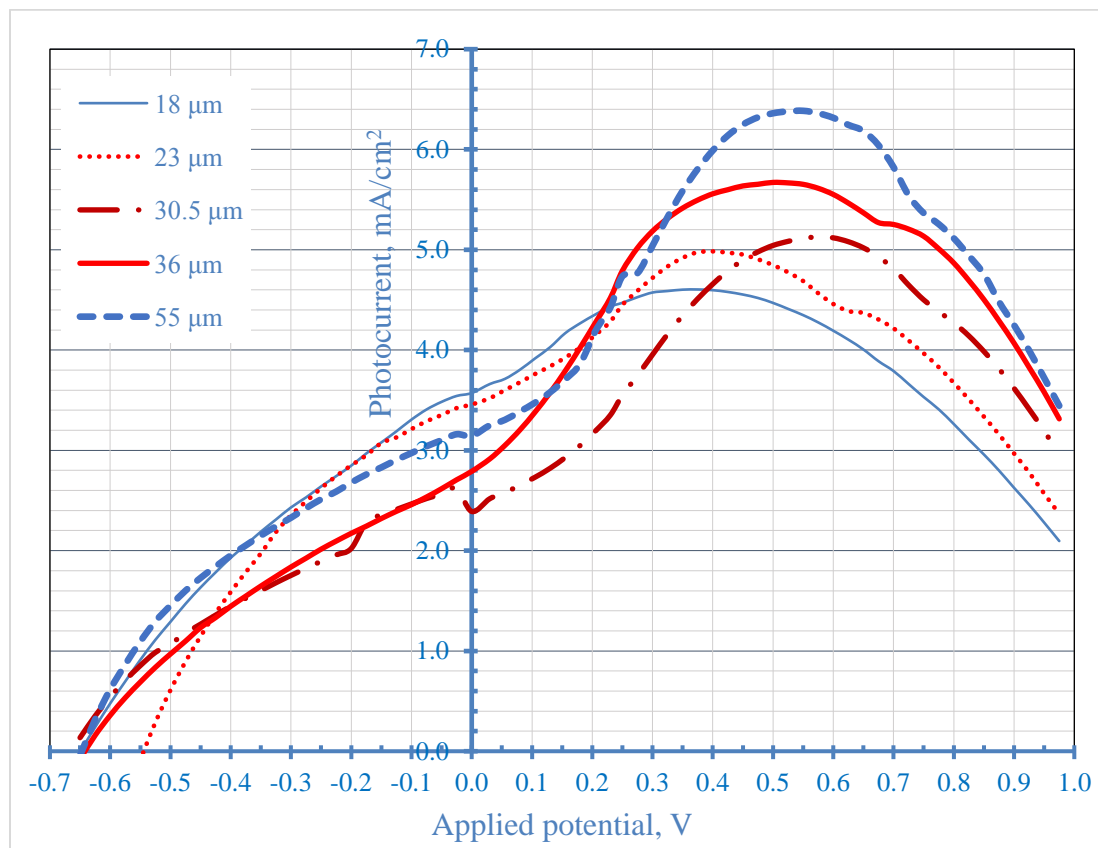
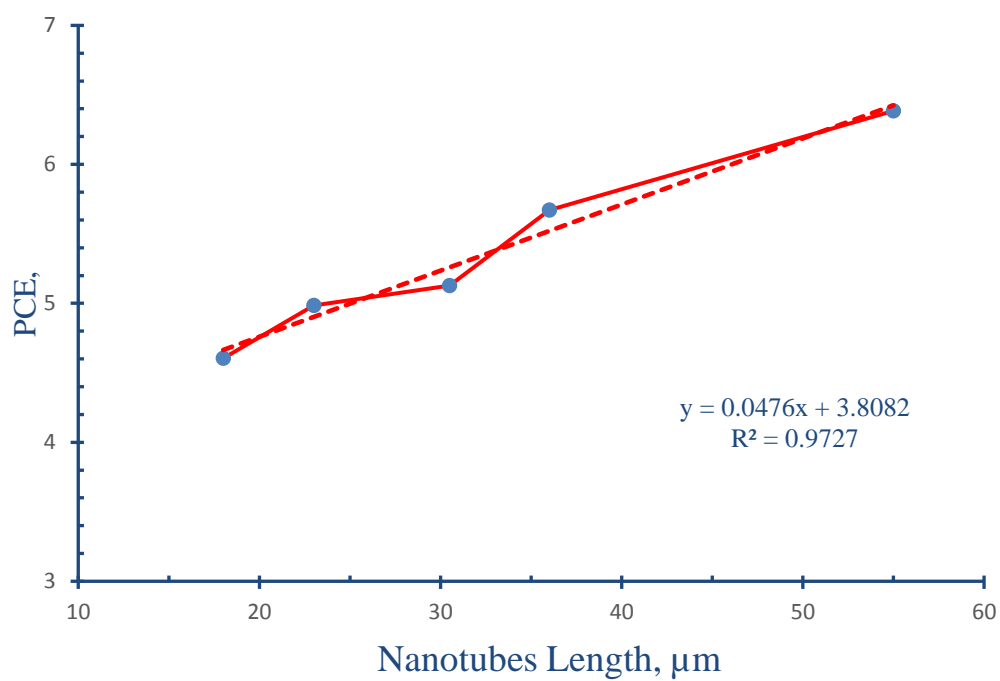


Figure 4-11 Effect of nanotube length on photoconversion Efficiency, PCE, as a function of applied potential





**Figure 4-12 Linear dependence of photoconversion efficiency on nanotube length of modified TNTAs in the range from 18 to 55  $\mu\text{m}$ .**

## 4.5 Conclusions

In this investigation, a new, facile, low cost and environmental-friendly method for the fabrication of N- and C-modified TiO<sub>2</sub> nanotube arrays was reported. The titania nanotube arrays were immersed in a 10 wt. % urea solution with mechanical agitation for 30 min. The TNTAs were immersed in the solution for 6 h at room temperature. Then, TNTAs were annealed at different temperatures. Modified TiO<sub>2</sub> nanotube arrays with different lengths from 18 μm to 55 μm were synthesized in this study. The produced N- and C-modified TNTAs were characterized by FESEM, EDX, XRD, XPS, UV-Vis diffuse reflectance. Modified optical properties with narrow band gap energy, E<sub>g</sub>, of 2.65 eV was obtained after annealing the modified TNTAs at 550°C. Modified TNTAs showed enhanced photocurrent density and photoconversion efficiency. Photoconversion efficiency, PCE, was increased from 4.35% for pristine (unmodified) TNTAs to 5.18% for modified TNTAs, an increase of 19%. Effect of nanotubes length of modified TNTAs on photoelectrochemical performance was studied. Photoconversion efficiency PCE was increased by increasing nanotube length with maximum PCE of 6.38% at nanotube length of 55 μm. The PCE increase pattern was linear with nanotubes length. This implies excellent light penetration up to 55 μm depth into photoanode which is about 3.6 times higher than the maximum penetration depth (15 μm) in the nanoparticulate photoanode. This increasing pattern of photoconversion efficiency with increasing nanotubes length also implied a high charge separation rate and lower charge recombination rate. The high PCE was attributed to band gap reduction due to C- and N-modification of TNTAs and the increased surface area of

long TNTAs compared to short TNTAs resulted in excellent light penetration and harvesting properties.

## 4.6 References

1. Zwilling, V., Darque-Ceretti, E., Boutry-Forveille, A., David, D., Perrin, M. Y. and Aucouturier, M., *Surf. Interface Anal.* 27, (1999), pp. 629-637.
2. Lu, N., Zhao, H., Li, J., Quan, X. and Chen, S., *Separation and Purification Technol.* 62, (2008), pp. 668-673.
3. Prakasam, H. E., Shankar, K., Paulose, M., Varghese, O. K. and Grimes C. A., J. *Phys. Chem. C* 111, (2007), pp. 7235-7241.
4. Ong, K. G., Varghese, O. K., Mor, G. K. and Grimes, C. A., *J. Nanosci. Nanotechnol.* 5, (2005), pp. 1801-1808.
5. Ong, K. G., Varghese, O. K., Mor, G. K., Shankar, K. and Grimes, C. A., *Solar Energy Materials and Solar Cells* 91, (2007), pp. 250-257.
6. Grimes, C. A. and Mor, G. K., "Titania Nanotube Arrays: Synthesis, Properties, and Applications", Springer Science + Business Media, LLC (2009), New York, NY, USA. DOI 10.1007/978-1-4419-0068-5.
7. Zhao, J., Wang, X., Chen, R. and Li, L., *Solid State Communications* 134, (2005), pp. 705-710.

8. Wang, H., Yip, C. T., Cheung, K. Y., Djuricic, A. B., Xie, M. H., Leung, Y. H. and Chen, W. K., *Appl. Phys. Lett.* 89, (2006), pp. 023508, 1-3.
9. Paulose, M., Shankar, K., Varghese, O. K., Mor, G. K. and Grimes, C. A., *J. Phys. D* 39, (2006), pp. 2498-2503.
10. Chen, P., Brillet, J., Bala, H., Wang, P., Zakeeruddin, S. M. and Gratzel, M., *J. Mater. Chem.* 19, (2009), pp.5325-5328.
11. Jennings, J. R., Ghicov, A., Peter, L. M., Schmuki, P. and Walker, A. B., *J. Am. Chem. Soc.* 130, (2008), pp. 13364-13372.
12. Wen, X., Tao, J., Sun, Y., Sun, Y. and Dai, N., *Int. Symposium on Photoelectronic Detection and Imaging (2009): Proc. Of SPIE Vol. 7381*, (2009), 7381Z, pp. 1-9.
13. Yoriya, S., Prakasam, H. E., Varghese, O. K., Shankar, K., Paulose, M., Mor, G. K., Latempa, T. J. and Grimes, C. A., *Sensors Letters* 4, (2006), pp. 334-339.
14. Xiao, P., Garcia, B. B., Guo, Q., Liu, D. and Cao, G., *Electrochemistry Communications* 9, (2007), pp. 2441-2447.
15. Fujishima, A. and Honda, K., *Nature* 238, (1972) pp. 37-38.
16. Paulose, M., Mor, G. K., Varghese, O. K., Shankar, K. and Grimes, C. A., *J. Photochem. Photobiol. A* 178, (2006), pp. 8-15.
17. Paulose, M., Shankar, K., Yoriya, S., Prakasam, H. E., Varghese, O. K., Mor, G. K., Latempa, T. A., Fitzgerald, A. and Grimes, C. A., *J. Phys. Chem. B* 110, (2006), pp. 16179-16184.

18. Mohapatra, S. K., Misra, M., Mahajan, V. K. and Raja, K. S., *J. Phys. Chem. C* 111, (2007). Pp. 8677-8685.
19. Hu, X., Zhang, T., Jin, Z., Zhang, J., Xu, W., Yan, J., Zhang, J., Zhang, L. Wu, Y., *Mater. Lett.* 62, (2008), pp. 4579-4581.
20. Linsebigler, A. L., Lu, G. and Yates, J. T., *Chem. Rev.* 95, (1995), p. 735.
21. Nakamura, R., Ohashi, N., Imanishi, A., Osawa, T., Matsumoto, Y., Koinuma, H. and Nakato, Y., *I. Phys. Chem. B* 109, (2005), pp. 1648-1651.
22. Neumann, B., Bogdanoff, P., Tributsch, H., Sakthivel, S. and Kisch, H., *J. Phys. Chem. B* 109, (2005), pp. 16579-16586.
23. Zhao, Q., Li, X., Wang, N., Hou, Y., Quan, X. and Chen, G., *J. Nanopart. Res.* 11, (2009), pp. 22153-2162.
24. Tian, T., Xiao, X.-F., Liu, R.-F., She, H.-D. and Hu, X.-F., *J. Mater. Sci.* 42, (2007), pp. 5539-5543.
25. Brunette, D. M., Tengvall, P., Textor, M. and Thomsen, P., "Titanium in Medicine", Springer, Berlin, (2001).
26. Vasilev, K., Poh, Z., Kant, K., Chan, J., Michelmore, A. and Losic, D., *Biomaterials* 31, (2010), pp. 532-540.
27. Grimes, C. A., *J. Materials Chemistry* 17, (2007), pp. 1451-14457.
28. Mor, G. K., Varghese, O. K., Paulose, M., Shankar, K. and Grimes, C. A., *Solar Energy Mater. Solar Cells* 90, (2006), pp. 2011-2075.

29. Quiroz, M. A., Martinez-Huitle, C. A., Meas-Vong, Y., Bustos, E. and Cerro-Lopez, M., *Journal of Electrochemical Chemistry* 807, (2017), pp. 261-267.
30. Ratnawati, Gunlazuardi, J., Dewi, E. L. and Slamet, *International Journal of Hydrogen Energy* 39, (2014), pp. 16927-16935.
31. Isimjan, T. T., Trifkovic, M., Abdullahi, I., Rohani, S. and Ray, A. K., *Top catal.* 58, (2015), pp. 114-122.
32. Sun, L., Li, J., Wang, C. L., Li, S. F., Chen, H. B. and Lin, C. J., *Sol. Energy Mater. Sol. Cells* 93, (2009), pp. 1875-1880.
33. Tu, Y. -F., Huang, S. -Y., Sang, J. -P. and Zou, X. -W., *Mater. Res. Bullet.* 45, (2010), pp. 224-229.
34. Liu, H., Liu, G. and Zhou, Q., *J. Solid State Chem.* 182, (2009), pp. 3238-3242.
35. Ghicov, A., Schmidt, B., Kunze, J. and Schmuki, P., *Chem. Phys. Lett.* 433, (2007), pp. 323-326.
36. Yang, L. X., Luo, S. L., Cai, Q. Y. and Yao, S. Z., *Chinese Sci. Bull.* 55, (2010), pp. 331-338.
37. Xu, C., Shaban, Y. A., Ingler, W. B. and Khan, S. U. M., *Solar Energy Mater. Solar Cells* 91, (2007), pp. 938-943.
38. Asahi, R., Morikawa, T., Ohwaki, T., Aoki, K. and Taga, Y., *Science* 293, (2001), pp. 269-271.
39. Vitiello, R. P., Macak, J. M., Ghicov, A., Tsuchiya, H., Dick, L. F. P. and Schmuki, P., *Electrochemistry Communications* 8, (2006), pp. 544-548.

40. Geng, J., Yang, D., Zhu, J., Chen, D. and Jiang Z., *Mater. Res. Bulletin* 44, (2009), pp.146-150.
41. Chen, X., Zhang, X., Su, Y., and Lei, L., *Applied Surface Science* 254, (2008), pp. 6693-6696.
42. Lei, L., Su, Y., Zhou, M., Zhang, X. and Chen, X., *Mater. Res. Bulletin* 42, (2007), pp. 2230-2236.
43. Devi, L. G. and Kavitha, R., *Applied Catalysis B: Environmental* 140-141, (2013), pp. 559-587.
44. Shankar, K., Paulose, M., Mor, G. K., Varghese, O. K. and Grimes, C. A., *J. Phys. D: Appl. Phys.* 38, (2005), pp. 3543–3549.
45. Yang, H. and Pan, C., *J. Alloys and Compounds* 501, (2010), pp. L8-L11.
46. Yoo, J., Zazpe, R., Cha, G., Prikryl, J., Hwang, I., Macak, J. M. and Schmuki, P., *Electrochemistry Communications* 86, (2018), pp. 6-11.
47. Yang, M., Zhang, L., Jin, B., Huang, L. and Gan, Y., *Applied Surface Science* 364, (2016), pp. 410-415.
48. Loget, G. and Schumki, P., *Langmuir* 30, (2014), pp. 15365-15363.
49. Mohamed, A. E., Kasemphaibulsuk, N., Rohani, S. and Barghi, S., *J. Nanosci. Nanotechnol.* 10, (2010), pp. 1998-2008.
50. Zhang, Y., Fan, X. and Xiao, P., *Materials Science Forum* Vols. 610-613, (2009), pp. 1143-1149.
51. Sennik, E., Colak, Z., Kilinc, N. and Öztürk, Z. Z., *Int. J. Hydrogen Energy* 35, (2010), pp. 4420-4427.

52. Yu, J. and Wang, B., *Applied Catalysis B: Environmental* 94, (2010), pp.295-302.
53. Beranek, R., Macak, J. M., Gartner, M., Meyer, K. and Schmuki, P.,  
*Electrochimica Acta* 54, (2009), pp. 2640-2646.
54. Liu, S., Yang, L., Xu, S., Luo, S. and Cai, Q., *Electrochemistry Communications*  
11, (2009), pp. 1748-1751.
55. Escobedo Morales, A., Sanchez Mora, E. and Pal, U., *Revista Mexicana De Fisica*  
S 53 (5), (2007), pp. 18-23.
56. Zhang, Y., Nie, J., Wang, Q., Zhang, X., Wang, Q. and Cong, Y., *Applied Surface*  
*Science* 427, (2018), pp. 1009-1018.
57. Mohamed, A. E. R. and Rohani, S., *Energy Environ. Sci.* 4, (2011), pp. 1065-  
1086.
58. Matsuda, A., Sreekantan, S. and Krengvirat, W, *Journal of Asian Ceramic*  
*Societies* 1, (2013), pp. 203-219.



## Chapter 5

### **5 Multifunctional Magnetic Ferrite-encapsulated Self-organized TiO<sub>2</sub> Nanotubes Nanocomposite: Fabrication, Properties and Drug Release Control**

\* A paper based on this chapter is under final revision as: Ahmed El Ruby Mohamed and Sohrab Rohani, “Multifunctional Magnetic Ferrite-encapsulated Self-organized TiO<sub>2</sub> Nanotubes Nanocomposite: Fabrication, Properties and Drug Release Control” to be submitted for possible publication.

## 5.1 Abstract

A new class of multifunctional nanocomposites has been fabricated by encapsulating ferrite nanoparticles into self-organized, vertically oriented TNTAs using a facile and efficient method. The fabricated nanocomposite was characterized using SEM, EDX, XRD, UV-Vis diffuse reflectance, photocurrent and vibrating sample magnetometer (VSM). Ferrite nanoparticles of  $13 \pm 3$  nm diameters were successfully distributed all over the top and inner surface of the nanotubes. UV-Vis reflectance spectra showed excellent visible light absorbance up to wave length of 660 nm ( $E_g = 1.88$  eV). The prepared magnetic nanocomposite showed their potential capability to controlling the drug release of an anti-cancer drug (5-fluorouracil). The drug release of 5-fluorouracil by diffusion was sustained with controlled initial burst effect. The suitability of magnetic nanocomposite for cancer drug delivery was confirmed by in vitro cytotoxicity study.

**Keywords:** Ferrite nanoparticles, titania nanotube arrays, photoconversion efficiency, magnetic nanocomposite, drug delivery, band gap energy.

## 5.2 Introduction

Titanium dioxide (TiO<sub>2</sub>) nanotube arrays (TNTAs) fabricated by anodization have attracted an outstanding interest in the recent years because of their unique photo-induced reactivity, well-organized vertically-oriented tubular nano-architecture, high surface area, and biocompatibility. This nanomaterial was extensively-explored for a wide range of applications such as environmental photocatalysis [1, 2], water-splitting [3,4], self-cleaning [5], sensing [6], dye-sensitized solar cells (DSSCs), photovoltaic hydrogen generation by water-splitting [7, 8], light-induced amphiphilicity involving the control of its surface wettability by UV radiation [9]. Due to relatively wide band gap,  $E_g$ , of TNTAs, they are photoactive only in the UV spectra. Different routes have been applied to modify optical properties of TNTAs to increase the photoactivity in the visible light spectra. Among these routes, decorating TNTAs surface with metal oxide nanoparticles improved the photoelectrochemical performance by enhancing the photoactivity in the visible light spectra [10]. Introducing magnetic iron oxide nanoparticles such as ferrite nanoparticles, Fe<sub>3</sub>O<sub>4</sub> NPs, not only enhances the visible light absorbance and photoelectrochemical performance of TNTAs, but also results in obtaining magnetic ferrite-TNTAs nanocomposite which has very important potential applications as medicinal implants and long-acting targeted drug delivery [11, 12]. In medicinal applications, it is very important to control the drug release rate inside the body. By slowing the drug release rate, drug quantities and doses can be minimized which results in avoiding the side effects and increasing the drug effectiveness. Drug loading into ferrite nanoparticles and encapsulating them into the pores of TNTAs would slow down and control the drug release rate. Furthermore, the magnetic properties of ferrite-encapsulated TNTAs provides an excellent

functionality for application in magnetic targeted drug delivery in which drugs can be magnetically-targeted only to the local affected organ or tissue rather than the whole body [13, 14]. The objectives of this research work are to fabricate magnetic Fe<sub>3</sub>O<sub>4</sub>-TNTAs nanocomposite and investigate its optical and enhanced photoelectrochemical performance and applications in drug delivery of 5 fluorouracil (5FU) for cancer treatment.

## 5.3 Materials and Methods

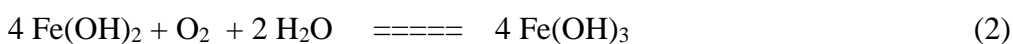
### 5.3.1 Fabrication of TiO<sub>2</sub> nanotube arrays

The Ti foil (0.89 mm thickness, 99.6% purity) and all chemicals were purchased from Alfa-Aesar (Ward Hill, MA, USA). Prior to anodization, the titanium foil was cleaned by using distilled water, acetone and distilled water, in an ultrasonic bath for five min each step. It was then dried off in air, etched in (3.3 M HF and 5.6 M HNO<sub>3</sub>) solution for 10 s, rinsed with deionized water, dried with air and used immediately. To prepare TNTAs, the same setup used in our previous work [15] was used here with a modified procedure proposed by Prakasam and co-workers [16]. Ti foil was first anodized in ethylene glycol solution containing NH<sub>4</sub>F (0.3 wt. %) and H<sub>2</sub>O (2 wt. %) for 2h at 60 V at room temperature using Keithley Source Meter Unit Model SMU 2602 (Keithley Instruments Inc., Cleveland, Ohio, USA). The Ti foil was cut into 1.5 cm diameter discs and mounted on a Teflon electrode holder which allowed only 1 cm<sup>2</sup> of one side of the disc to be exposed to the electrolyte while the whole backside area was isolated. Ti foil was used as anode and a platinum foil of 2 cm by 4 cm area was used as a cathode.

The samples were washed with distilled water and sonicated in water for 5 min to clean the surface and remove debris, and dried with air. Then annealed at 550°C for 3 h in air with a heating and cooling rate of 5°C/min to promote crystallinity.

### 5.3.2 Synthesis of Ferrite nanoparticles

Pluronic F-68 was dissolved in 50 mL of distilled water under mechanical stirring to prepare 0.6% block co-polymer solution. A specified amount of ferrous sulfate heptahydrate ( $\text{FeSO}_4 \cdot 7\text{H}_2\text{O}$ , 1.39 g) was added drop wise to the block copolymer solution with continuous stirring. The final concentration of block co-polymer in the medium was 0.3 % w/v. After stirring for 30 min, the above mixture was transferred into a preheated water bath (80°C) for 10 min. NaOH solution (3.0 M) was quickly added to the mixture to adjust the pH value to about 13 and the reaction mixture was subsequently stirred at 80°C for 90 min. The obtained solid magnetite nanoparticles were washed with distilled water several times and then freeze dried for overnight [17]. The proposed ferrite synthesis reactions can be shown as the following reaction equations [18]:



### 5.3.3 Ferrite drug loading

5-Fluorouracil (5-FU) was loaded into magnetic nanoparticles as a post-synthesis step. In this method, 10 mg of 5-FU was mixed with 20 mg of magnetite nanoparticles in distilled water. The mixture was then stirred mechanically overnight at room temperature. Thereafter, 5-FU loaded magnetite particles were collected with a permanent magnet and rinsed 3 times with ethanol and freeze dried overnight. The loaded magnetite nanoparticles were then encapsulated into titania nanotubes using different techniques.

### 5.3.4 Encapsulation of Ferrite nanoparticles into titania nanotube arrays

#### 5.3.4.1 In-situ encapsulation

The in-situ encapsulation technique was performed according to the method mentioned in section 5.2.2 with the immersion of titania nanotubes in the ferrite-synthesis reaction medium. Briefly, titania nanotubes were immersed in iron precursor/block co-polymer solution and continuously stirred for 30 min. Thereafter, the reaction temperature was raised to 80°C with subsequent adjustment of the reaction medium pH to 13. After 90 min, titania nanotubes were washed for several times with PBS (phosphate buffer saline) to remove the un-encapsulated magnetite. The washing solution was kept for further analysis. For preparation of 5-FU loaded in-situ magnetite encapsulated titania nanotubes, 50 mg of 5-FU was mixed with the iron precursor and the reaction was completed following the same sequence as mentioned previously. Then, the ferrite-encapsulated titania nanotube arrays and 5-FU pre-loaded ferrite-encapsulated titania nanotube arrays samples were freeze dried overnight.

#### 5.3.4.2 Post-synthesis encapsulation

In this method, titania nanotubes were mixed with 5-FU pre-loaded magnetite nanoparticles dispersed in distilled water. The mixing process was performed mechanically for 3 h on the top of permanent magnet to help pulling the magnetic nanoparticles downward inside the nanotubes holes and then the top surface of TNTAs samples was rinsed with phosphate buffered saline (PBS) to remove the excess un-encapsulated nanoparticles. The ferrite-titania nanotubes samples were then freeze dried overnight to obtain the ferrite-loaded titania nanotubes. The rinsed solutions were collected and stored for further analysis.

#### 5.3.5 Characterization

The morphology of all the samples was examined with a field emission scanning electron microscope (FESEM, Hitachi S-5000, Tokyo, Japan) equipped with an energy dispersive X-ray analyzer unit (EDXA). X-ray diffractometer (Rigaku Miniflex XRD, USA) was utilized for examination of the crystal profile of loaded and unloaded samples. The samples were exposed to x-ray radiation (CuK $\alpha$ , 40 KV, 20 mA) at a wavelength of 1.54 Å. The samples were scanned over a 2-theta range between 15° to 80° and at a step size of 0.02 °. The magnetic properties were measured using vibrating sample magnetometer (VSM, Model 74035, LakeShore Cryotronics, Inc., USA) at 300°K. The magnetic properties of ferrite-encapsulated TNTAs samples were studied at field range of  $\pm$  10,000 Gauss. UV–Vis diffuse reflectance absorption spectra were measured using a Cary 100 UV–Vis–NIR spectrophotometer.

The photocurrent spectra were recorded by a home-made photoelectrochemical measurement system using an LPX150 Xe lamp solar simulator with a light intensity of  $100 \text{ mW/cm}^2$ . The TNTAs sample served as the working electrode and a Pt sheet was used as the counter electrode. The testing electrolyte was 1 M KOH solution with 0.05 vol. % ethylene glycol. A computer-controlled power supply (Keithley SMU 2602, Keithley Instruments Inc., Cleveland, Ohio, USA) was employed to control the potential and record the photocurrent generated. The intensity of the light was measured by a radiation power and energy meter. The incident light intensity on the sample was measured as  $100 \text{ mW/cm}^2$ . The external potential was applied to the anode at a scan rate of  $20 \text{ mV s}^{-1}$  under illumination and the photocurrent was recorded. The potential of the open circuit was measured by a digital multimeter during the illumination.

### 5.3.6 Drug release

#### 5.3.6.1 Drug loading efficiency

Before investigation of the drug release profiles, it is important to estimate the drug loading efficiency of magnetite loaded nanotubes. The concentration of 5-FU in the original and the rinse solution were measured using UV-Vis spectrophotometer at 265 nm and the rinse solution from the drug free samples was used as a reference. It should be noted that the rinse solution (5-FU loaded magnetite) must be first rinsed with 1 M HCl before evaluation of drug content. The drug loading efficiency was expressed mathematically as follows:



$$\varepsilon = \frac{C_i - C}{C_i} \dots\dots\dots (6)$$

where  $\varepsilon$  is loading efficiency,  $C_i$  drug concentration in the original solution and  $C$  drug concentration in the washing solution.

### 5.3.6.2 In-vitro release study

The in-vitro release of 5-FU magnetite loaded titania nanotubes was investigated by immersing them in 5 mL of phosphate buffered saline (PBS). The samples were withdrawn at predetermined time intervals and then analyzed spectrophotometrically for evaluation of the amount of drug released as a function of time.

### 5.3.6.3 In-vitro cytotoxicity study

The cell culture experiments were carried out on human breast adenocarcinoma MCF-7 cell line purchased from American Type Culture Collection (ATCC, USA). Cells were maintained in Dulbecco's modified eagle medium (DMEM) containing 10% fetal bovine serum (FBS) in a CO<sub>2</sub> incubator (5% CO<sub>2</sub> at 37°C). Cells were seeded at a density of 5 × 10<sup>3</sup>/well in a 96-well plate containing 100 µl of DMEM medium and left overnight to reach 80% confluence. The cytotoxicity of the free drug (5-FU), drug-loaded Ferrite nanoparticles and the drug-loaded ferrite-encapsulated TNTAs nanocomposites on MCF-7 human breast cancer cell line was assessed by 3-(4,5-dimethylthiazolyl-2)-2,5-diphenyltetrazolium bromide (MTT) assay. The medium was replaced by fresh medium containing different concentrations of the drug either as a free solution, loaded into ferrite

nanoparticles or loaded into the ferrite-encapsulated TNTAs nanocomposites and incubated for another 24 h. The culture medium was then replaced with 100  $\mu$ l of MTT solution (0.5 mg/ml in DMEM) then incubated for 4 h at 37°C under light protection. After removal of MTT solution by centrifugation at 2000 rpm for 10 min, 100  $\mu$ l of dimethyl sulfoxide (DMSO) were added to the wells to dissolve MTT-formazan crystals formed after internalization of MTT by live cells and maintained in agitation for 15 min. Absorbance of the converted dye was measured at a wavelength of 570 nm with background subtraction at 690 nm using a microplate reader (Model 550, Bio-Rad, USA). The relative cell viability was expressed as a percentage of the untreated control wells[19].

## 5.4 Results and Discussion

### 5.4.1 Structure and Morphology

Figure 5-1-a and b show FESEM images of top view and lateral view, respectively, of titania nanotube arrays TNTAs anodized in ethylene glycol electrolyte containing 0.3 wt. %  $\text{NH}_4\text{F}$  and 2 wt. %  $\text{H}_2\text{O}$  at 60 V anodization potential for 3 h. Figure 5-1 -c shows FESEM image for top view of ferrite-encapsulated TNTAs. Figure 5-1-d shows a high magnification of Figure 5-1-c. TNTAs have an inner diameter of  $100 \pm 11$  nm, wall thickness of  $15 \pm 3$  nm and nanotubes length of  $20 \pm 2.5$   $\mu\text{m}$ , with a length to diameter aspect ratio of 200. The average particle size diameter of ferrite nanoparticles was  $13 \pm 3$  nm. As it can be clearly seen from Figure 5-1, the ferrite nanoparticles are monodispersed and there was no particles agglomeration inside the nanotube pores or on the top surface

of TNTAs which was an advantage of using freeze-drying rather than conventional heat drying. Figure 5-2 shows the x-ray spectra of both ferrite NPs (above chart) and ferrite-encapsulated TNTAs (below chart). All assigned ferrite x-ray peaks in ferrite NPs sample existed in ferrite-encapsulated TNTAs sample which implies that the crystal structure of ferrite remained unchanged after the encapsulation process.

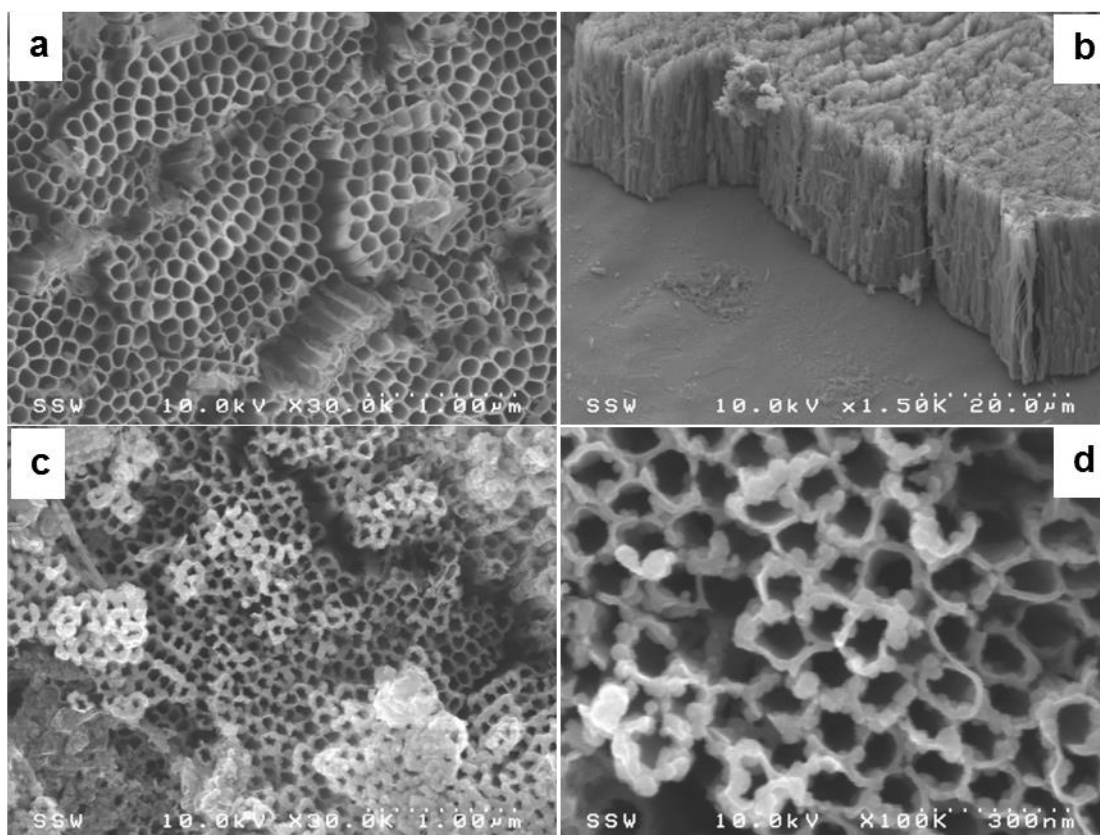


Figure 5-1 FESEM images of pristine TNTAs and ferrite-encapsulated TNTAs fabricated using in-situ encapsulation method; a) and b) top view and lateral view, of pristine TNTAs, c) top view of in-situ ferrite-encapsulated TNTAs and d) high magnification of image c.

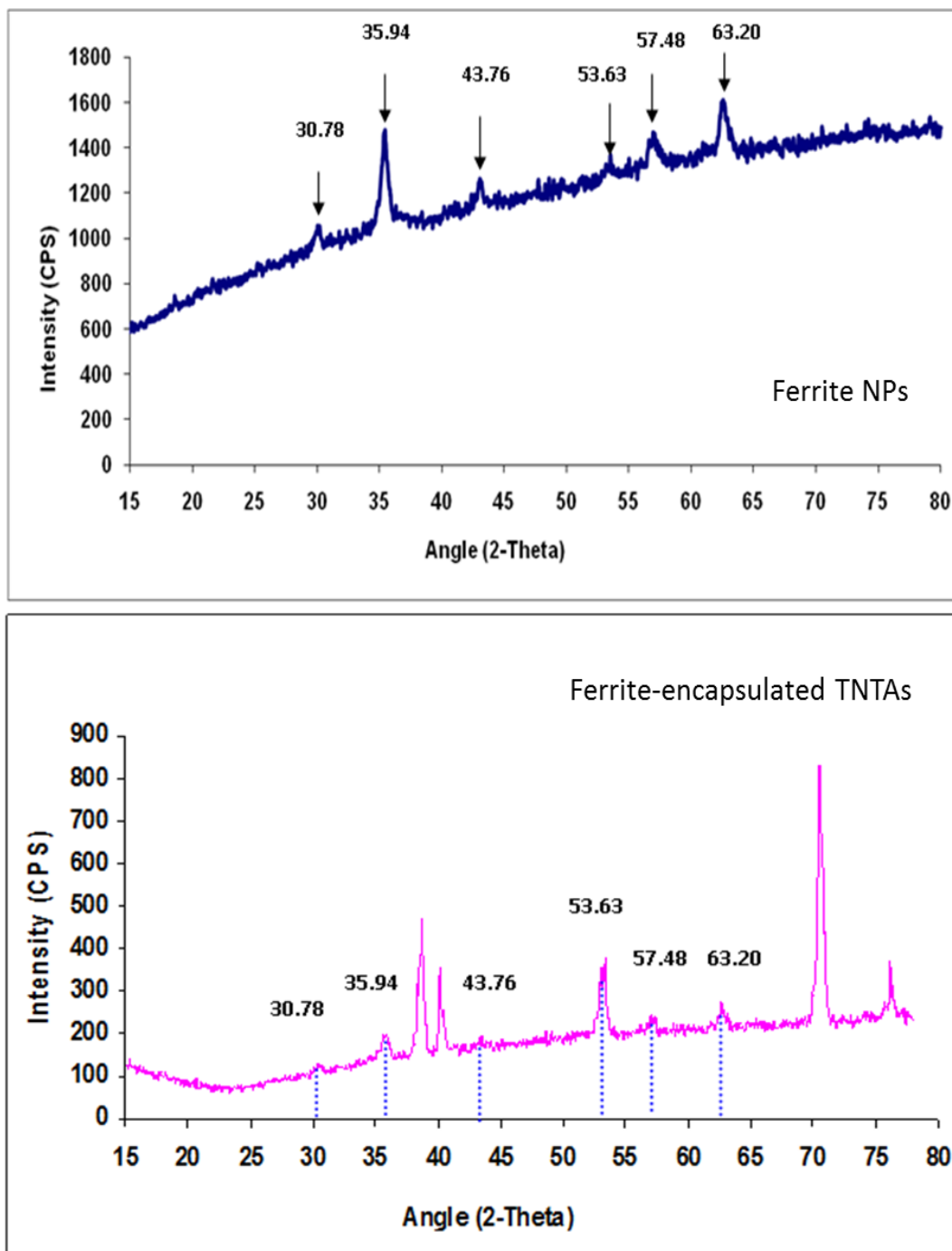
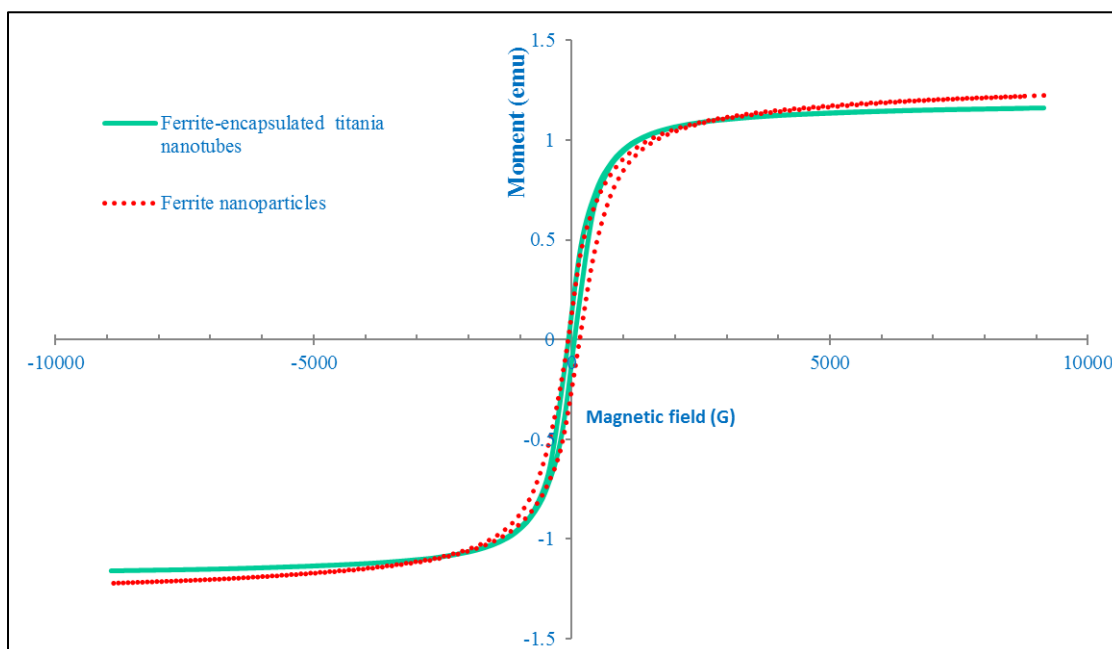


Figure 5-2 X-Ray spectra of: ferrite nanoparticles (above chart) and ferrite-encapsulated TNTAs (below). All assigned peaks of ferrite nanoparticles in the above chart existed in ferrite-encapsulated TNTAs x-ray spectra (below chart).

### 5.4.2 Magnetic and Optical Properties

Figure 5-3. shows the hysteresis loop of ferrite-encapsulated TNTAs fabricated by in-situ encapsulation method and that of ferrite NPs. Results show slight decrease of magnetic moment of ferrite-encapsulated TNTAs compared to that of ferrite NPs.



**Figure 5-3 Hysteresis loops of ferrite-encapsulated TNTAs (solid green lines) compared to ferrite nanoparticles (dotted red line).**

Several samples of ferrite-encapsulated TNTAs were prepared with different ferrite loading to study the effect of ferrite loading on optical properties as well as photoelectrochemical performance. Figure 5-4 shows UV-Vis. diffuse reflectance spectra for ferrite-encapsulated TNTAs with different ferrite loading as well as for pristine (pure)

TNTAs. Results showed that loading of ferrite NPs resulted in excellent absorbance over the whole visible light spectra shifting the absorbance threshold from about 420 nm wave length ( $E_g = 2.95$  eV) for pristine TNTAs to about 660 nm ( $E_g=1.88$  eV). Furthermore, the absorbance increased with increasing ferrite loading up to 20 mg then decreased at ferrite loading of 30 and 50 mg. this may be explained that increasing the nanoparticles inside nanotube pores may block the light penetration pathway into the inner surface area.

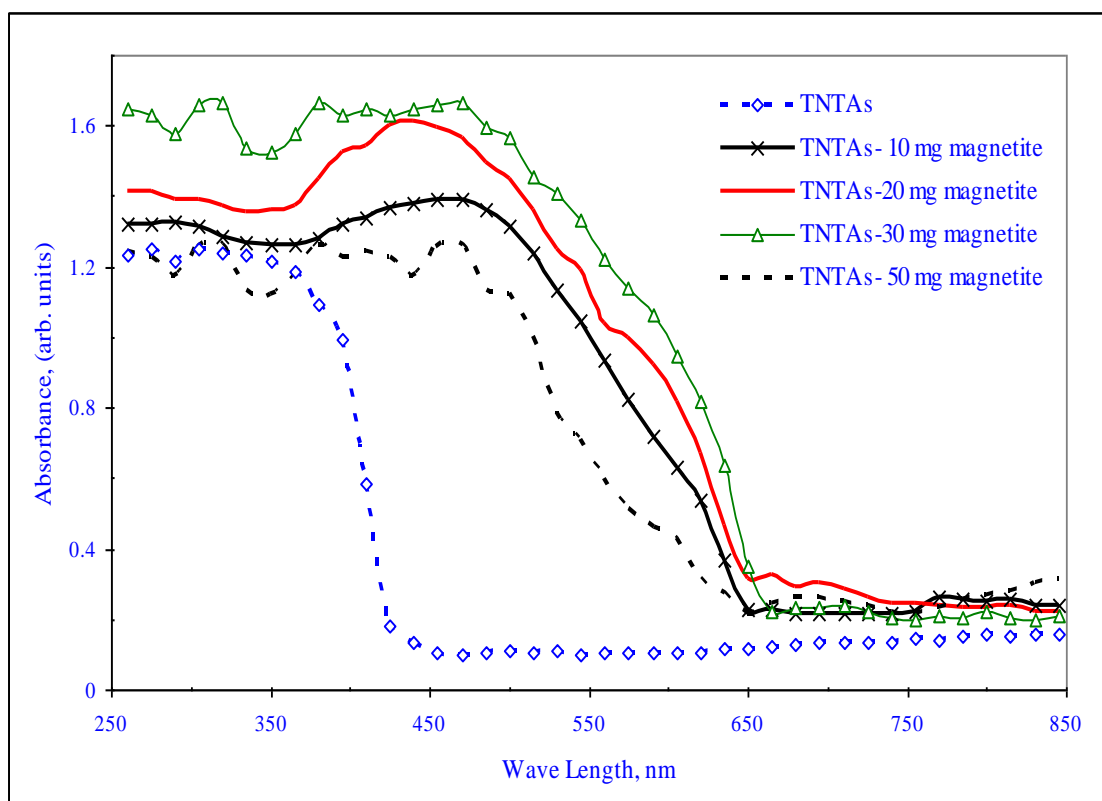


Figure 5-4 UV-vis. Diffuse reflectance spectra of ferrite encapsulated titania nanotube arrays nanocomposite.

### 5.4.3 Photoelectrochemical Performance of Ferrite-encapsulated TNTAs

Photocurrent densities were measured for ferrite-encapsulated TNTAs samples with different ferrite loading and results are shown in Figure 5-5. Photocurrent densities increased with increasing the ferrite NPs loading with the highest photocurrent density at 20 mg loading, then began to decrease with further increase in ferrite NPs loading. The photocurrent behavior was consistent with the behavior of light absorbance and can be attributed to the same reason mentioned for the explanation of light absorbance in section 5.3.2.

Figure 5-6 shows the % photoconversion efficiency, PCE, for modified and unmodified TNTAs as a function of applied potential. The percent PCE was calculated using the following equation [20, 21]:

$$\text{PCE (\%)} = [I_{\text{ph}} \times (1.23 - E_{\text{app}}) \times 100] / I_0 \quad (7)$$

$$E_{\text{app}} = E_{\text{meas}} - E_{\text{oc}} \quad (8)$$

Where:  $I_{\text{ph}}$  is the photocurrent density in  $\text{mA}/\text{cm}^2$ ,  $E_{\text{app}}$  is the external applied potential in V given in eq. (8),  $E_{\text{meas}}$  is the measured bias potential in V (vs. Ag/AgCl reference electrode), and  $E_{\text{oc}}$  is the electrode potential (vs. Ag/AgCl) of the same working electrode at open circuit conditions under the same illumination and in the same electrolyte.



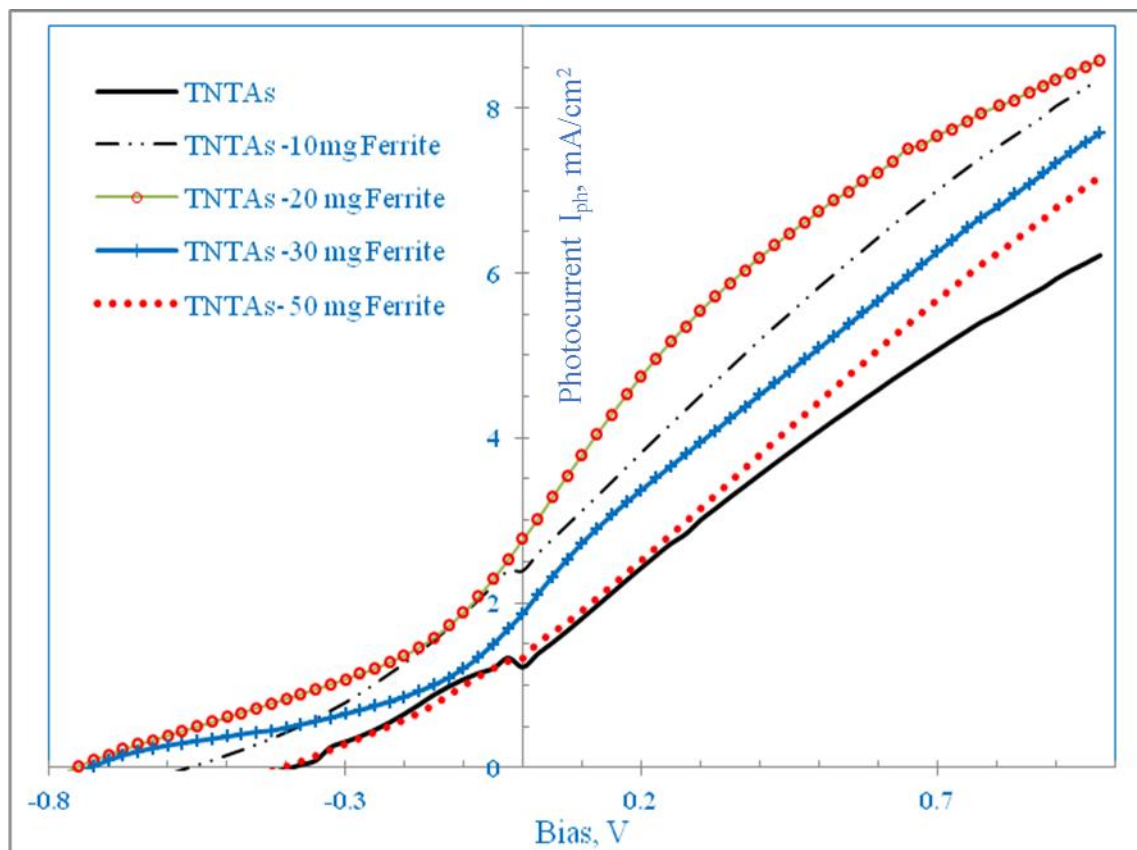
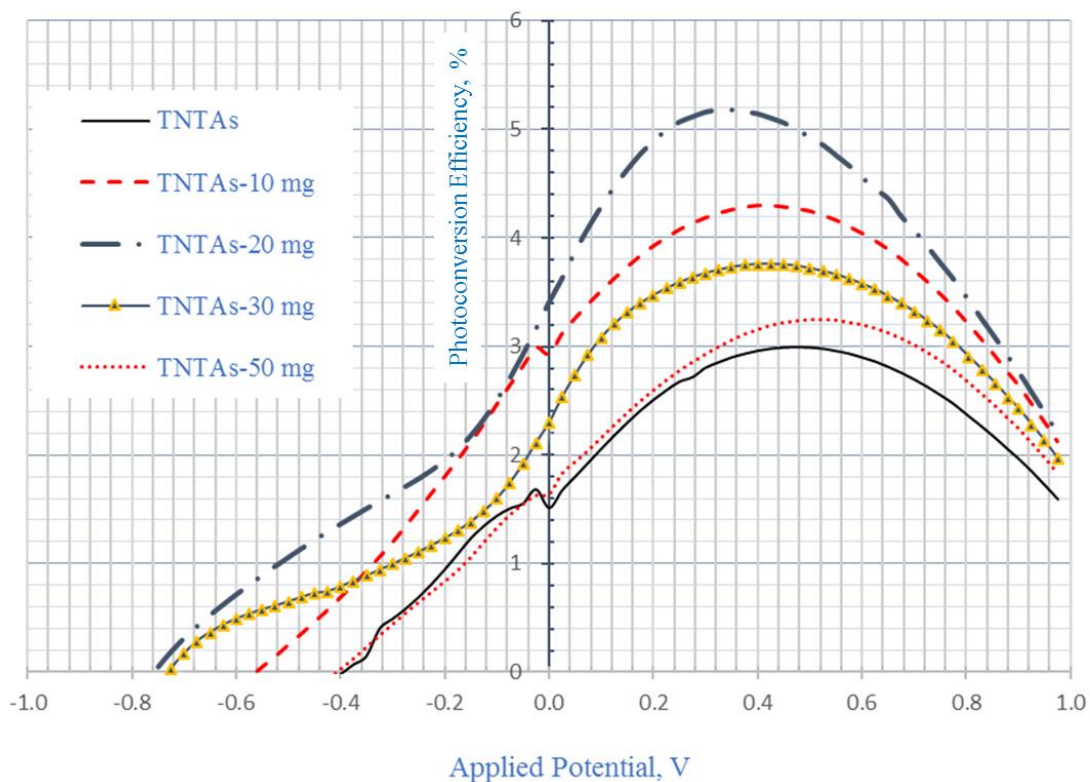


Figure 5-5 Photocurrent of ferrite-encapsulated TNTAs nanocomposite at different ferrite nanoparticles loading.



**Figure 5-6 Effect of ferrite loading on photoconversion efficiency as a function of applied potential.**

As we can see from Figure 5-6, all ferrite-encapsulated TNTAs showed enhanced photoconversion efficiency compared to pristine TNTAs. Photoconversion efficiency increased with increasing ferrite loading to reach its maximum at 20 mg ferrite loading. Further increase in ferrite loading resulted in decreasing the photoconversion efficiency. Photoconversion efficiency increased from 3% for pristine TNTAs to a maximum of 5.18% for 20 mg ferrite loading sample, with an increase of 72.6 %.

#### 5.4.4 Drug release study

The drug release mechanism was investigated to explore the application of ferrite-encapsulated TNTAs as an anti-cancer drug delivery carrier. In this study, 5-FU was selected as an anti-cancer drug model. The loading efficiency of 5-FU ranged between 60.51 and 80.26%. The ferrite loading (mg) as well as the loading techniques was characterized as a determining parameter for both drug loading and release. The drug loading efficiency was superior for the sample loaded with 50 mg of ferrite by post-synthesis freeze drying method.

The plots of 5-FU release from titania nanotubes loaded with 10, 30 and 50 mg of ferrite were exemplarily shown in Figures 5-7 and 5-8. It should be noted that the release rate of 5-FU was higher for the samples loaded with 50 mg ferrite. Figure 5-9 shows the effect of ferrite NPs-encapsulation technique on drug release from ferrite-encapsulated TNTAs at constant ferrite loading (50 mg). One also can see that post-synthesis encapsulation technique seems to be superior to in-situ encapsulation technique regarding drug delivery control as post-synthesis encapsulated samples took 14 days to release the same percentage of drug that in-situ encapsulated samples released in only 6 days.

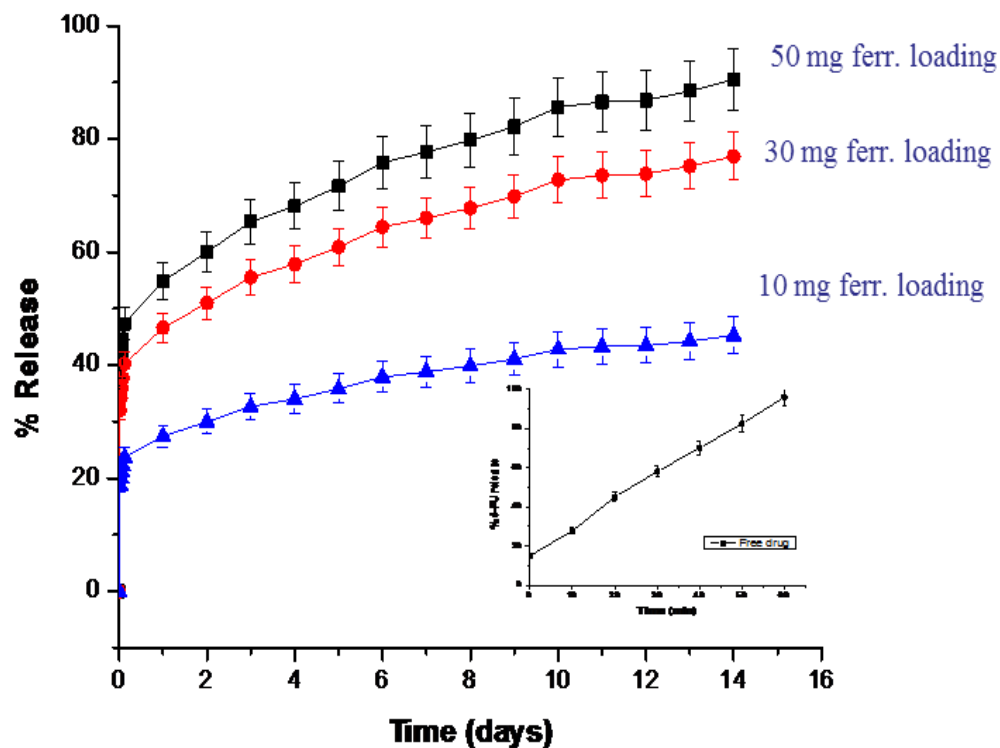


**Figure 5-7** Effect of ferrite loading on 5-FU release profile of ferrite-encapsulated TNTAs fabricated by post-synthesis encapsulation technique. The release profile for the free drug is attached.

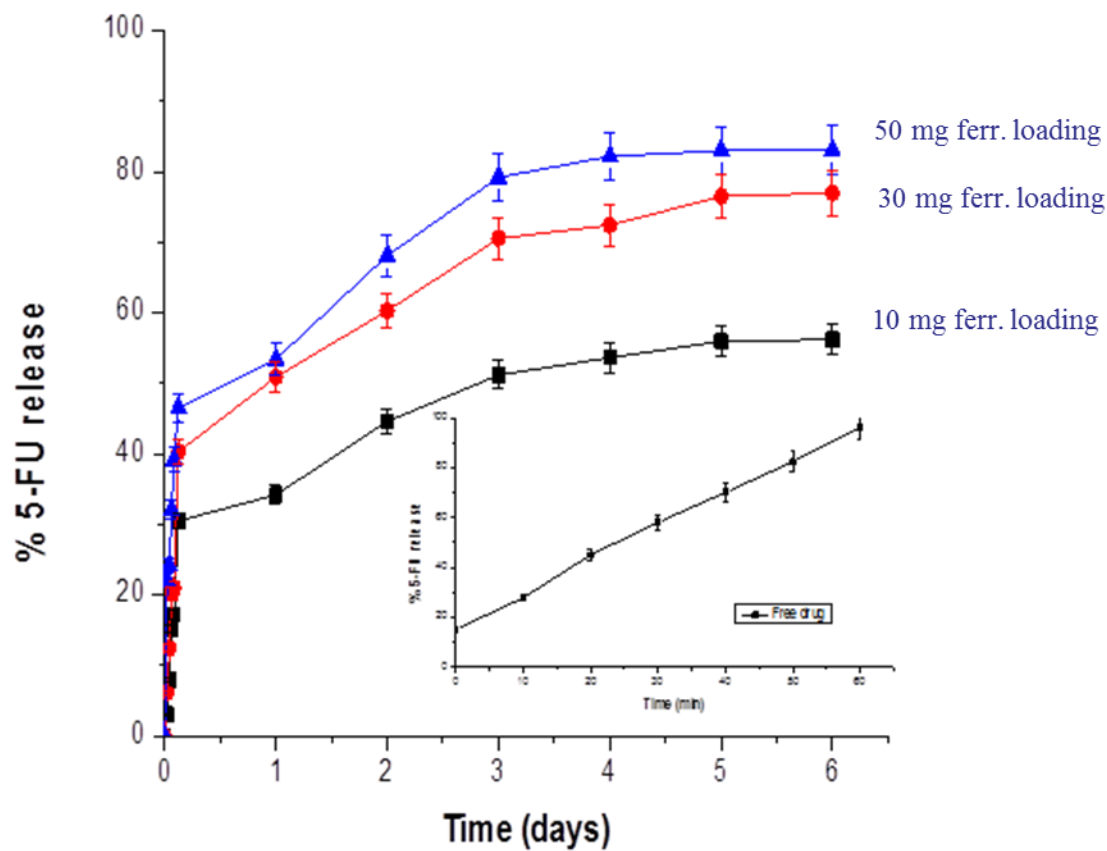


Figure 5-8 Effect of ferrite loading on 5-FU release profile of ferrite-encapsulated TNTAs fabricated by in-situ encapsulation technique. The release profile for the free drug is attached.

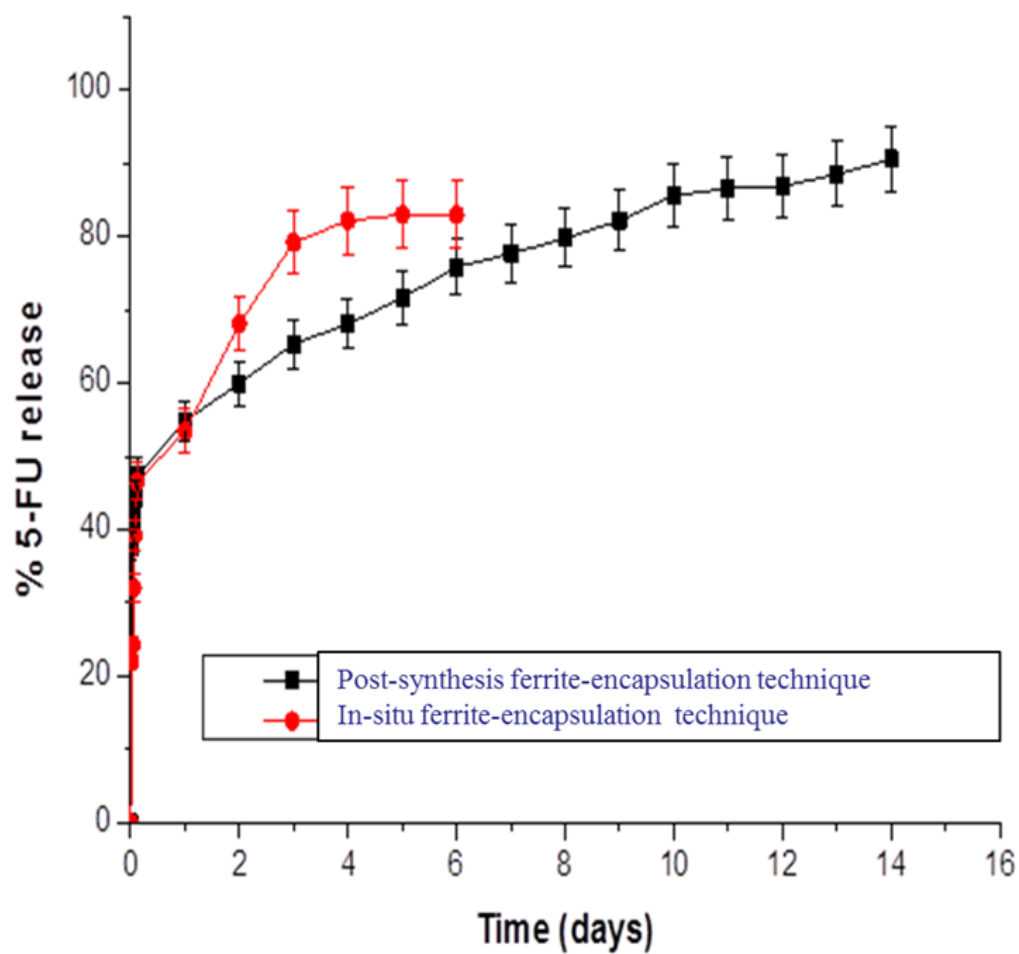
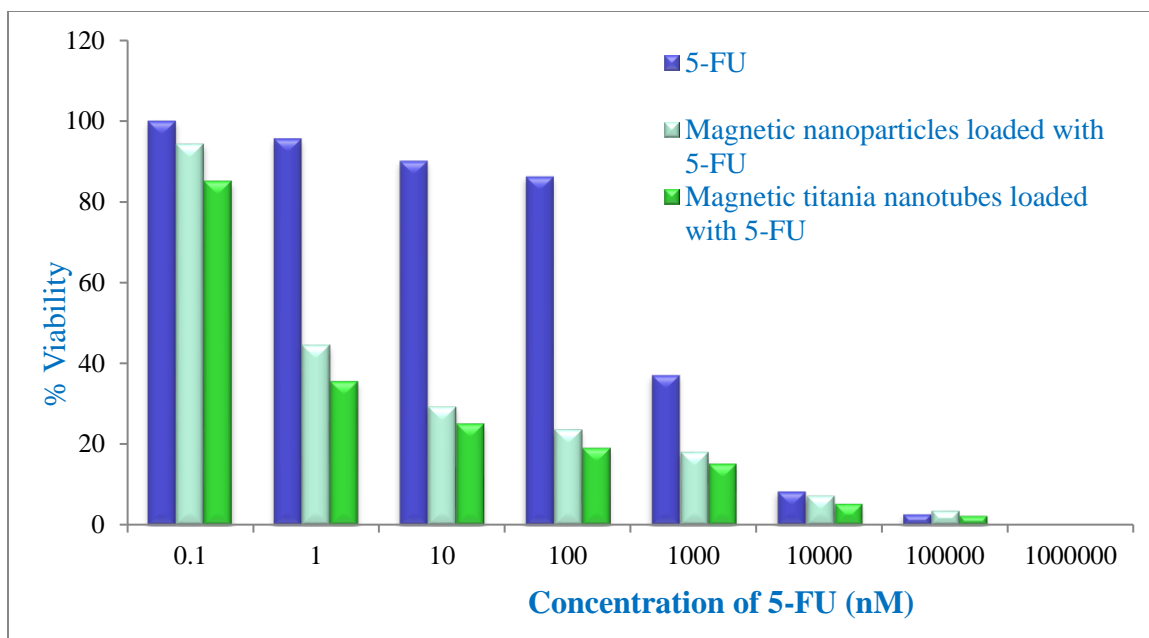


Figure 5-9 Effect of ferrite-encapsulation technique into TNTAs on 5-FU release profile at constant ferrite NPs loading (50 mg ferrite).

#### 5.4.5 Cytotoxicity of ferrite encapsulated TNTAs

A series of experiments were conducted in-vitro to compare the cytotoxicity of 5-FU loaded ferrite-encapsulated TNTAs, 5-FU loaded ferrite nanoparticles and a stand-alone 5-FU drug. Figure 5-10 shows the %viability of the three drug delivery techniques as a function of 5-FU concentration. Figure 5-10 shows clearly that the cytotoxicity increases in the order of 5-FU loaded ferrite-encapsulated TNTAs > 5-FU loaded ferrite NPs > 5-FU. The excellent cytotoxicity of 5-FU loaded ferrite-encapsulated TNTAs may be attributed to the high photo-reactivity of TNTAs as well as magnetic properties while the cytotoxicity is moderate for 5-FU loaded ferrite NPs because of the effect of magnetic properties only.



**Figure 5-10 In-vitro cytotoxicity of 5-FU loaded ferrite-encapsulated TNTAs, 5-FU loaded ferrite NPs and stand-alone 5-FU as a function of 5-FU concentration**

## 5.5 Conclusions

Magnetic ferrite NPs-encapsulated titania nanotube arrays (ferrite-encapsulated TNTAs) nanocomposite was synthesized using two different techniques, namely, in-situ encapsulation method and post-synthesis encapsulation method. Crystal structure and nanoarchitecture were characterized using x-ray and FESEM. Magnetic, optical properties and photoelectrochemical performance were characterized. Ferrite-encapsulated TNTAs enhanced photocurrent and photoconversion efficiency. Photoconversion efficiency



increased from 3 % for pristine (TNTAs) to 5.18 % for 20 mg loaded ferrite-encapsulated TNTAs with an increase of 72.6%. Magnetic ferrite-encapsulated TNTAs were used as anti-cancer drug 5-FU carrier and drug release profile was studied. Ferrite-encapsulated TNTAs showed excellent drug release profile with high controllable release over 14 days for post-synthesized encapsulation method and over 6 days for in-situ encapsulation method compared to only 60 min release time for stand-alone 5-FU anti-cancer drug. In-vitro cytotoxicity of 5-FU loaded ferrite-encapsulated TNTAs, 5-FU loaded ferrite NPs and stand-alone 5-FU was tested and compared. The cytotoxicity was increased in the order of stand-alone 5-FU < 5-FU loaded ferrite NPs < 5-FU loaded ferrite-encapsulated TNTAs.

## 5.6 References

1. Dong, L., Cao, G. -X, Ma, Y., Jia, X. -L., Ye, G. -T. and Guan, S. -K., *Trans. Nonferrous Met. Soc. China* 19, (2009), pp. 1583-1587.
2. Zhang, S., Peng, F., Wang, H., Yu, H., Zhang, S. Yang, J. and Zhao, H., *Catalysis Communications* 12, (2011), pp. 689–693.
3. Fujishima, A. and Honda, K., *Nature* 238, 1972, pp. 37–38.
4. Paulose, M., Mor, G. K., Varghese, O. K., Shankar, K. and Grimes, C. A., *J. Photochem. Photobiol., A* 178, (2006), pp. 8–15.
5. Wang, R., Hashimoto, K., Chikuni, M., Kojima, E. and Kitamura, A., *Nature* 388, (1997), pp. 388, 431.
6. Yoriya, S., Prakasam, H. E., Varghese, O. K., Shankar, K., Paulose, M., Mor, G. K., Latempa, T. J. and Grimes, C. A., *Sens. Lett.* 4, (2006), pp. 334–339.
7. Paulose, M., Shankar, K., Varghese, O. K., Mor, G. K. and Grimes, C. A., *J. Phys. D: Appl. Phys.* 39, (2006), pp. 2498–2503.
8. Hu, X., Zhang, T., Jin, Z., Zhang, J., Xu, W., Yan, J., Zhang, J., Zhang, L. Wu, Y., *Mater. Lett.* 62, (2008), pp. 4579-4581.
9. Liu, K. S., Yao, X. and Jiang, L., *Chem. Rev.* 114, (2015), p. 10044.
10. Mohamed, A. E. R. and Rohani, S., *Energy Environ. Sci.* 4, (2011), pp. 1065-1086.
11. Arias, J. L., Gallardo, V., Ruiz, M. A. and Delgado, Á. V., *European J. Pharmaceutics Biopharmaceutics* 69, (2008), pp. 54-63.
12. Pang, Y. L., Lim, S., Ong, H. C. and Chong, W. T., *ceramics International* 42, (2016), pp. 9-34.

13. Abdelaziz, H. M., Gaber, M., Abd-Elwakil, M. M., Mabrouk, M. T., Elgohary, M. M., Kamel, N. M., Kabary, D. M., Freag, M. S., Samaha, M. W., Mortada, S. M., Elkhodairy, K. A., Fang, J.-Y. and Elzoghby, A. O., *Journal of Controlled Release* 269, (2018), pp. 374-392.
14. Ragab, D. and Rohani, S., *AAPS PharmSciTech.* 14 (3), (2013), pp. 977-993. DOI: 10.1208/s12249-013-9980-y.
15. Mohamed, A. E., Kasemphaibulsuk, N., Rohani, S. and Barghi, S., *J. Nanosci. Nanotechnol.* 10, (2010), pp. 1998-2008.
16. Prakasam, H. E., Shankar, K., Paulose, M., Varghese, O. K. and Grimes C. A., *J. Phys. Chem. C* 111, (2007), pp. 7235-7241.
17. Kim, D. K., Mikhaylova, M., Zhang, Y. Muhammed, M., *Chem. Mater.* 15, (2003), pp. 1617-1627.
18. Zhang, z., Yao, G., Zhang, X., Ma, J. and Lin, H., *Ceramics International* 41, (2015), pp. 4523-4530.
19. Elzoghby, A. O., Mostafa, S. K., Helmy, M. W., ElDemellawy, M. A. and Sheweita, S. A., *International Journal of Pharmaceutics* 529, (2017), pp. 178 – 192.
20. Mohapatra, S. K., Misra, M., Mahajan, V. K. and Raja, K. S., *J. Phys. Chem. C* 111, (2007). Pp. 8677-8685.
21. Escobedo Morales, A., Sanchez Mora, E. and Pal, U., *Revista Mexicana De Fisica* S 53 (5), (2007), pp. 18-23.

## Chapter 6

### **6 Conclusions and Recommendations**

Photocatalytic reactions of TiO<sub>2</sub> have gained much interest during the past decades due to their vast applications based on solar energy conversion. More recently, during the last decade, TiO<sub>2</sub> nanotube arrays which were produced by electrochemical anodization of Ti metal in F<sup>-</sup> ions containing electrolytes have attracted more research interest due to their outstanding properties rendering them the most promising photoanode in many solar energy conversion applications including both environmental and energy production applications. The big challenge is to increase the light energy to electrical or chemical energy efficiency. There are three key factors for increasing the efficiency of solar energy applications using TiO<sub>2</sub> photoanodes. The first key factor is to increase the surface area. The second key factor is to minimize the recombination of photogenerated electron/hole charges by facilitating rapid charge separation. The third factor is to extend the photo-responsiveness of TiO<sub>2</sub> to the visible light region by modifying the band gap energy of the material. Although the high surface area could be achieved by reducing material size to nanoscale, minimizing the photogenerated electron/hole charges recombination could only be achieved through the unique architecture of highly ordered, vertically oriented titania nanotube arrays produced by electrochemical anodization of parent Ti metal foil in F<sup>-</sup> ions containing electrolytes. The nano-architecture and high surface area can be easily tuned by controlling the anodization process parameters. The present work has investigated the formation and growth of titania nanotube arrays by anodization process in viscous electrolytes. Results showed the high dependency of titania nanotubes growth and nanoarchitecture on different anodization parameters. This work has investigated the modification and functionalization of titania nanotube arrays, too. It is becoming

increasingly clear that TiO<sub>2</sub> is one of the most promising candidates for a commercial photoelectrode for solar light harvesting in a wide range of applications such as water splitting for hydrogen generation, cheap dye-sensitized solar cells and photocatalysis.

## 6.1. Challenges and limitations

Relatively wide band gap ( $E_g$ ) of TiO<sub>2</sub> limits the photoactivity to UV spectra. Surface electronic properties of TiO<sub>2</sub> nanotube arrays need to be modified to narrow  $E_g$  to enhance the visible light absorption and consequently, increase photoconversion efficiency. When choosing any modification process, the following should be considered:

- The process should not cause damage to the unique nanotubular morphology.
- The process should not decrease the huge interfacial surface area.
- The process should not block the photons penetration paths to the inner surface area of the nanotubes.

## 6.2. Objectives

The specific objectives of this research are:

1. Synthesis of titania nanotube arrays using anodization method and study the effect of different parameters on dimensionality, nanostructure and photoelectrochemical response of nanotube arrays.
2. Modification of the electronic properties to reduce band gap energy by introducing nitrogen and carbon to the surface of the nanotubes using a new, facile, low cost

and environment-friendly method and characterization of photoelectrochemical performance of the modified nanotube arrays for solar applications.

3. Functionalizing titania nanotube arrays with magnetic ferrite nanoparticle to help narrowing the band gap energy and enhance the photoelectrochemical performance for solar applications.
4. Application of magnetic ferrite-encapsulated titania nanotube arrays for controlled and magnetically-targeted drug delivery of 5-FU anticancer drug as well as evaluation of their cytotoxicity.

### 6.3. Methodology

To achieve the above general and specific objectives, the following approaches were implemented in this thesis:

- An electrochemical anodization system was set up which consists of two electrodes electrochemical cell equipped with DC power supply provided with a data acquisition system and a state-of-the-art algorithm and interface for real time monitoring of electrical current and voltage.
- Titania nanotube arrays were fabricated in different electrolytes where fabrication parameters were studied to reach the optimum conditions at which a vertically-oriented, well-organized reproducible nanotube arrays were obtained.
- A new, facile, low-cost, environment-friendly method was proposed for the first time to synthesize N- and C-modified titania nanotube arrays with excellent visible light absorbance and enhanced photoelectrochemical performance.

- Morphology and nanoarchitecture were characterized using X-Ray diffractometer and FESEM imaging. Optical properties were characterized using UV-vis. diffuse reflectance spectra. Electrochemical performance was characterized by determining photocurrent densities in a 3 electrode photoelectrochemical cell with Ag/AgCl electrode as a reference electrode.
- Titania nanotube arrays were functionalized with magnetic ferrite nanoparticles which has an excellent band gap energy of 2.2 eV. The photoelectrochemical performance was characterized the ferrite-encapsulated titania nanotube arrays. The magnetic ferrite-encapsulated TNTAs were also tested in drug delivery application as an anticancer drug carrier.

## 6.4. Conclusions

### 6.4.1. Fabrication of reproducible self-organized titania nanotube arrays

Self-organized titania nanotube arrays were successfully fabricated in glycerol, ethylene glycol and CMC-based electrolytes. Results showed that synthesis parameters play a crucial role in both nanotube arrays formation and tailoring of their nanoarchitecture. Nanotube arrays with an inside diameter ranging from 16 to 91 nm, and wall thickness ranging from 7 to 29 nm were fabricated in a glycerol-water electrolyte. Water content of at least 5 wt.%, was found to be essential for nanotubes fabrication in glycerol electrolyte. Diameter and length were influenced by varying water content above 5 wt.%. Maximum length of 900 nm was achieved at 50 wt.% H<sub>2</sub>O in glycerol. Nanotube length was found to be time-dependent at high pH values and a pH value of 6 was favorable for fabrication of highly ordered, long and continuous nanotube arrays. Using modified ethylene glycol



solution instead of glycerol, resulted in nanotubes length up to 430 nm after 1.5 h anodization time in ethylene glycol containing 2 wt.% urea and 0.5 wt.%  $\text{NH}_4\text{F}$ . Double-sided titania nanotube arrays layers with a total thickness of 9.5  $\mu\text{m}$  were fabricated for the first time with a minor modification in the anodization cell. These double-sided grown TNTAs have a very interesting layers arrangement where Ti conducting metal layer sandwiched between two semiconducting TNTAs could have a promising electronic and photocatalytic applications. Nanotube arrays were also successfully fabricated in 2 wt.% sodium carboxy methylcellulose (CMC) aqueous electrolyte which is an inexpensive viscous electrolyte compared with glycerol and ethylene glycol electrolytes.

#### 6.4.2. N- and C-modification of titania nanotube arrays

In this investigation, we report a new, facile, low cost and environmental-friendly method for N- and C-modified  $\text{TiO}_2$  nanotube arrays fabricated by immersing the as-anodized  $\text{TiO}_2$  nanotube arrays in a 10 wt.% urea solution with mechanical agitation for 30 min. The TNTAs were immersed in the solution for 6 h at room temperature. Then, TNTAs were annealed at different temperatures.  $\text{TiO}_2$  nanotube arrays with different lengths from 18  $\mu\text{m}$  to 55  $\mu\text{m}$  were synthesized in this study. The produced N- and C-modified TNTAs were characterized by FESEM, EDX, XRD, XPS, UV-Vis diffuse reflectance. Modified optical properties with narrow band gap energy,  $E_g$ , of 2.65 eV was obtained after annealing the modified TNTAs at 550°C. Modified TNTAs showed enhanced photocurrent density and photoconversion efficiency. Photoconversion efficiency, PCE, was increased from 4.35% for pristine (unmodified) TNTAs to 5.18% for modified TNTAs, an increase of 19%. The high PCE was attributed to band gap reduction due to C- and N-modification of

TNTAs and the increased surface area of long TNTAs compared to short TNTAs resulted in excellent light penetration and harvesting properties. Effect of nanotubes length of modified TNTAs on photoelectrochemical performance was studied. Photocurrent density and PCE were increased by increasing nanotube length with maximum PCE of 6.38% at nanotube length of 55  $\mu\text{m}$ . This implies excellent light penetration up to 55  $\mu\text{m}$  depth into photoanode which is about 3.6 times higher than the maximum penetration depth (15  $\mu\text{m}$ ) in the nanoparticulate photoanode. This increasing pattern of photoconversion efficiency with increasing nanotubes length also implied a high charge separation rate and lower charge recombination rate.

### 6.4.3. Multifunctional Magnetic Ferrite-encapsulated TiO<sub>2</sub> Nanotubes Nanocomposite

Magnetic ferrite NPs-encapsulated titania nanotube arrays (ferrite-encapsulated TNTAs) nanocomposite was synthesized using two different techniques, namely, in-situ encapsulation method and post-synthesis encapsulation method. Crystal structure and nanoarchitecture were characterized using X-ray and FESEM. Magnetic, optical properties and photoelectrochemical performance were characterized. Ferrite-encapsulated TNTAs enhanced photocurrent and photoconversion efficiency. Photoconversion efficiency increased from 3 % for pristine (TNTAs) to 5.18 % for 20 mg loaded ferrite-encapsulated TNTAs with an increase of 72.6%. Magnetic ferrite-encapsulated TNTAs were used as anti-cancer drug 5-FU carrier and drug release profile was studied. Ferrite-encapsulated TNTAs showed excellent drug release profile with high controllable release over 14 days for post-synthesized encapsulation method and over 6 days for in-situ encapsulation method compared to only 60 min release time for stand-alone 5-FU anti-cancer drug. In-

vitro cytotoxicity of 5-FU loaded ferrite-encapsulated TNTAs, 5-FU loaded ferrite NPs and stand-alone 5-FU was tested and compared. The cytotoxicity was increased in the order of stand-alone 5-FU < 5-FU loaded ferrite NPs < 5-FU loaded ferrite-encapsulated TNTAs.

## 6.5. Novelty and major contributions

Chapter 2: Very comprehensive critical review study has introduced a strong platform for a wide diverse academic and industrial audience to understand the latest achievements in this field.

Chapter 3: The conducted study in this chapter provided a strong understanding of the effect of each synthesis parameter such as pH, water content, anodization time and electrolyte composition. TNTAs were successfully fabricated for the first time in a very cheap viscous electrolyte composed of 2 wt.% sodium carboxy methylcellulose (CMC). Double-sided TNTAs on both sides of Ti disc were successfully fabricated with total tube length of 9.5  $\mu\text{m}$  with a unique structure composed of conducting Ti metal sandwiched between two semiconducting layers of TNTAs on each side with a new potential electronic and photocatalytic applications.

Chapter 4: N- and C-modified TNTAs were successfully fabricated using a new, facile, low cost, environment-friendly method which was also very safe on the nanostructure. The modified TNTAs showed excellent absorbance in the visible light spectra as well as enhanced photocurrent and photoconversion efficiency. Furthermore, photocurrent and photoconversion efficiency increased by increasing nanotube length in the range from 18 to 55  $\mu\text{m}$ . This implies an excellent light penetration up to 55  $\mu\text{m}$  depth into photoanode

which is about 3.6 times higher than the maximum penetration depth in the nanoparticulate photoanode. This increasing pattern of photoconversion efficiency with increasing nanotubes length also implied a high charge separation rate and lower charge recombination rate.

Chapter 5: monodispersed ferrite NPs-encapsulated TNTAs were fabricated for the first time. The fabricated nanocomposite showed a high increase of photoconversion efficiency from 3% for pristine TNTAs to 5.18% for 20 mg ferrite loading ferrite-encapsulated TNTAs which represents a percentage increase of 72.6%. Magnetic ferrite-encapsulated TNTAs were tested in drug delivery and showed excellent drug release profile and cytotoxicity capacity.

## 6.6. Recommendations and future works

- More studies are needed for fabrication of larger-area TNTAs sheets for scale up applications.
- Fabrication of different metal-ions doped TNTAs by anodizing Ti-alloys containing different metals with different concentrations.
- Fabrication of gold and silver nanoparticles-decorated titania nanotube arrays and investigation of their different modified properties for applications of CO<sub>2</sub> reduction and other photocatalytic processes.
- Applications of N- and C-modified TNTAs and ferrite-encapsulated TNTAs nanocomposite in dye-sensitized solar cell.
- Applications of N- and C-modified TNTAs and ferrite-encapsulated TNTAs nanocomposite in generating H<sub>2</sub> by water-splitting.
- Applications of ferrite-TNTAs nanocomposite in in-virtue drug delivery of selected widespread daily-used drug models.

## Curriculum Vitae

**Name:** Ahmed El Ruby A. Mohamed

**Post-secondary Education and Degrees:** **Minia** University  
El Minia, Minia Governorate, Egypt  
1992-1998, B. Chem. Eng. With honor degree.

**Minia** University  
El Minia, Minia Governorate, Egypt  
2000-2003, M. Eng. Sci.

The University of Western Ontario  
London, Ontario, Canada  
2017, Ph.D.

**Related Work Experience** Teaching Assistant  
The University of Western Ontario  
2006-2010.

Research Assistant  
CMRDI, Helwan, Cairo, Egypt  
1999-2012.

### Publications

- **Peer reviewed journals:**

1. S. Rohani, T. Isimjan, **A. Mohamed**, H. Kazemian, M. Salem, and T. Wang, "Fabrication, modification and environmental applications of TiO<sub>2</sub> nanotube arrays (TNTAs) and nanoparticles", Front. Chem. Sci. Eng. [DOI 10.1007/s11705-011-1144-6](https://doi.org/10.1007/s11705-011-1144-6).
2. **Ahmed El Ruby Mohamed** and Sohrab Rohani, "Modified TiO<sub>2</sub> nanotube arrays (TNTAs): progressive strategies toward visible light responsive photoanode, a review", Energy Environ. Sci. 4, (2011), pp. 1065-1086. (This journal is Ranked as world # 1 journal in its disciplines with **Impact factor of 29.518**). (This paper has 152 citations so far according to CrossRef and RSC Journals).
3. Tayirjan T. Isimjan, **Ahmed El Ruby**, Sohrab Rohani and Ajay K. Ray, "Fabrication of highly-ordered and visible-light responsive Fe-C-N-co-doped TiO<sub>2</sub> nanotubes", Nanotechnology **21** (2010) 055706 (6pp).
4. **Ahmed El Ruby Mohamed**, Nualjarose Kasemphaibulsuk, Sohrab Rohani and Shahzad Barghi, "Fabrication of titania nanotube arrays in viscous electrolytes", J. Nanosci. Nanotechnol. 10, (3), (2010), pp.1998-2008.

5. **Ahmed El Ruby Mohamed** and Sohrab Rohani, "Synthesis of Titania Nanotube Arrays by Anodization", AIDIC Conference Series Vol. 9, (2009) pp. 121-130. DOI:10.3303/ACOS090915.
6. Sohrab Rohani and **Ahmed El Ruby**, "Synthesis of Titania Nanotube Arrays by Anodization", Chemical Engineering Transactions 17, (2009), pp. 963-968. DOI:10.3303CET0917161.
7. **Ahmed El Ruby Mohamed** and **Sohrab Rohani**, "N and C Modified TiO<sub>2</sub> Nanotube Arrays: Enhanced Photoelectrochemical Properties and Effect of Nanotubes length on Photoconversion Efficiency" to be submitted for possible publication in a peer reviewed journal.
8. **Ahmed El Ruby Mohamed, and Sohrab Rohani**, "Multifunctional Magnetic Ferrite-encapsulated Self-organized TiO<sub>2</sub> Nanotubes Nanocomposite: Fabrication, Properties and Drug Release Control" to be submitted for possible publication in a peer reviewed journal.

- **Conferences:**

1. **Mohamed, Ahmed E.**, Ragab, Doaa and Rohani, Sohrab, "Facile Method for Fabrication of Ferrite-Encapsulated TiO<sub>2</sub> Nanotubes", 24<sup>th</sup> CMSC Canadian Materials Science Conference; Materials: Atoms to Applications, Western University, London, Ontario, Canada. June 5-8, 2012.
2. Sohrab Rohani and **Ahmed El Ruby**, "Synthesis and Characterization of highly-ordered Titania Nanotube Arrays by Anodization" ICheaP-9, "9<sup>th</sup> International Conference on Chemical and Process Engineering", 10-13 May 2009, Rome, Italy.
3. E. A. Abdel Aal, H. El-Shall, H. Cooper, **A. El Ruby** and A. K. Ismail, "Alleviation of the Environmental Impact of Black Liquor from Paper Mills Through Novel Lignin Precipitation and Separation Techniques" REWAS, 2004 Global Symposium on Recycling, Waste Treatment and Clean Technology, Sept. 26-29, 2004, Madrid, Spain.